Numerical Simulation and Analysis of High-Speed Unsteady Spiked Body Flows

Ing. Daniel Feszty

Thesis submitted to the Faculty of Engineering,

University of Glasgow, for the Degree of Doctor of Philosophy

University of Glasgow

Department of Aerospace Engineering

May 2001

Abstract

High-speed unsteady spiked body flows were simulated and analysed by using Computational Fluid Dynamics (CFD). The model geometry was a forward facing cylinder equipped with a protruding spike. Various spike lengths were considered between L/D=1.00 and 2.40 in both fixed spike and moving spike configurations. Axisymmetric, laminar flow conditions were considered at two freestreams of Mach 2.21 and Mach 6.00 and Reynolds'numbers based on the blunt body diameter of 0.12×10^6 and 0.13×10^6, respectively.

Structured, multiblock grids were generated and the PMB2D code was used as the numerical method to solve the time-dependent Navier-Stokes equations. Second order accuracy was achieved in both space and time. The numerical method was verified by grid dependence and real time step size dependence tests, which showed that medium resolution grids with maximum allowable time steps could be used in most of the cases. A validation of the results was provided in terms of the shock envelope histories and also the amplitude, frequency and characteristic shape of the pressure trace recorded at the cylinder face. The fixed spike length results were found in general good agreement with the experiment, whereas the range of the hysteresis phenomenon was overpredicted in the moving spike cases.

Two distinct flow modes, oscillation and pulsation, were identified and analysed in detail in order to reveal their driving mechanisms. It was confirmed that, in accordance with earlier literature, the oscillation flow mode was driven by the so-called "energetic shear layer hypothesis", a viscous phenomenon in nature.

The pulsation flow mode, on the other hand, was found to be driven by an entirely new driving mechanism based on the pressure imbalance arising in the triple shock system. In contrast to the oscillation flow mode, this is an inviscid phenomenon in nature.

Finally, the hysteresis simulation results were used to provide an original description of the transitions between the two flow modes. The necessary conditions of these were also established and it was found that they were driven by the movement of the separation point along the spike.

Acknowledgement

I would like to express my sincere gratitude to Dr. Ken Badcock and Prof. Bryan Richards for their excellent supervision and for the opportunity to study at the University of Glasgow. I am grateful for their constant encouragement, support and help throughout the past years and also for their continual availability when approaching them with questions and queries. I would also like to thank the other members of the CFD group, especially Brian Gribben and Laurent Dubuc, who helped me through the initial difficulties of my studies. Con Doolan, Vassilis Spathopolous, Harold Meng Chong and Fotis Tsiachris shared not only their research experiences with me, but also their friendship. Many thanks.

There were many others who helped me, in one way or another, to get this far, and it would be impossible to list them all. However, I am particularly thankful to Prof. Karol Filakovsky, Prof. Antonin Pistek, Erno Czere, Maurus Nyiredy and Istvan Szabo. Last but not least I would like to thank my family, especially my parents who always surrounded me with love and my wife, Kati, for everything.

This work was supported by a University of Glasgow Postgraduate Scholarship and an Overseas Research Student Award from the Committee of the Vice-Chancellors and Principals.

Contents

List of Tables

List of Figures

Nomenclature

a	speed of sound
$\mathbf{A}$	mean Jacobian matrix
c	speed of sound
d	spike diameter
d	diameter of the location of pressure measurement points
$d()$	diffusion term
$d\mathbf{x}$	vector of gridpoint displacement
D	blunt body diameter
e	energy
E	total energy per unit mass
E_t	total energy per unit volume
$\mathbf{F}, \mathbf{G}$	flux vector components
f	frequency
h_{aux}	auxiliary cell area
H	total enthalpy
I	inflation point
$\mathbf{I}$	unit matrix
J	jet injection point
J	Jacobian matrix
l	cavity length

L	shear layer
L	spike length
M	Mach number
M_j	Mach number on the dividing streamline
N	number of cycles
N	reattachment parameter
p	pressure
p_j	static pressure on the dividing streamline
p_{rpot}	potential reattachment pressure
p_{rr}	required reattachment pressure
p_{t2}	pitot pressure
p_x	maximum reattachment pressure in shoulder-reattaching flows
p_{Oj}	total pressure on the dividing streamline
P	separated region
$\mathbf{P}$	vector of primitive variables
Pr	Prandtl number
q_x, q_y	heat flux vector components
R	reattachment point
$\mathbf{R}$	residual
$\mathbf{R}$	matrix of right eigenvectors
$\mathbf{R^{-1}}$	matrix of left eigenvectors
$\mathbf{R}^*$	unsteady residual
Re	Reynolds' number
Re_D	Reynolds' number based on blunt body diameter
S	separation point
S	Strouhal number
t	time
t^*	pseudo time

T	time period
T	static temperature
T_0	reference temperature, 288.16[K]
u, v	velocity components
U, V	contravariant velocity components
$\mathbf{U}$	vector of state variables
v_{sp}	spike speed
v_x	velocity of a moving shock wave
V	vortical region
W	cavity depth
W	shock wave
$\mathbf{W}$	vector of conserved variables
x, y	cartesian co-ordinates
$\mathbf{x}$	gridpoint location
x_t, y_t	components of the grid speed
x_1	distance of the separation point from the spike tip
z_j	velocity ratio on the dividing streamline
α	angle of incidence
β	shock angle
γ	specific heat ratio
δ	non-dimensional longitudinal distance in a cavity
δ	deflection angle
Δ	longitudinal distance in a cavity
$\Delta(L/D)$	range of spike length change
Δp	pressure amplitude
Δt	time difference between frames
ξ, η	curvilinear co-ordinates
ϵ_r	entropy fix coefficient

λ	eigenvalue
Λ	matrix of eigenvalues
μ	laminar viscosity
μ_0	reference viscosity corresponding to T_0=288.16[K]
ρ	density
τ	stress
Φ_D	blunt body half-cone angle
Ψ, Φ	blending functions in the deforming mesh algorithm

Superscripts

i	inviscid
m	pseudo time level
n	time level
v	viscous
$+$	right hand side state
$-$	left hand side state
$*$	dimensional quantities
$\hat{}$	values in general curvilinear form

Subscripts

i, j	mesh point locations of the control volume in x,y directions
L	left hand side
min	minimum
max	maximum
n	normal component
o	stagnation values

r	radial component
R	right hand side
t	tangential component
T	values for turbulent flows
x, y, z	components in x,y,z directions
x, y, z	partial differentiation with respect to x,y,z
∞	freestream values

Acronyms

BILU	Block Incomplete Lower-Upper factorisation
GCL	Geometric Conservation Law
GSG	Conjugate Gradient Method
MUSCL	Monotone Upstream-Centred Schemes for Conservation Laws
O/P	oscillation - pulsation transition
P/O	pulsation - oscillation transition
PMB2D	Parallel Multi-Block Two-Dimensional

Chapter 1

Introduction

1.1 Literature survey

1.1.1 Spiked body applications

The family of spiked bodies, defined as those resembling the shape of a blunt body equipped with a forward protruding spike (Fig.1.1), have appeared in many different areas of aerodynamics in the past fifty years. All spiked body applications share two main features. One is a high speed freestream (ranging from approximately Mach 2.00 upwards) and the other is that the desired state of the flow around them is steady from an operational point of view. Thus, the primary aim of almost all works with a new spiked body configuration has been to study steady state flows. However, at certain combinations of flow conditions and/or geometrical parameters serious flow instabilities have been observed, endangering the safe and reliable function of a vehicle. The present section provides a review of the aerodynamic applications dominated by unsteady spiked body flows.

The first report of a spiked body type instability was from Oswatitsch in 1944 [1]. He found that the flow over axisymmetric jet inlets equipped with a conical centrebody (Fig.1.1a) can become unsteady when the engine is working at subcritical, off-design conditions. The observed phenomenon, termed as “buzz”, is known as a cause of serious combustion problems, engine surge and/or thrust loss and in some cases can even lead to the destruction of the propulsion unit. Despite it's long history and the numerous analytical models put forward in this field, “buzz” is still not properly understood. Although this is not entirely the same unsteadiness as that studied in the present work, it shows similarities in the main features of the instability observed around spiked bodies.

Increasing the effectiveness of ballistic missiles was of considerable interest in the early 50's. Large nose radii were employed to avoid excessive heat transfer rates on the missile forebody, occurring during the re-entry to the atmosphere. However, this geometry resulted in too much drag for the ascent part of the trajectory. As a compromise, a slender rod protruding from the hemispherical nose was applied (Fig.1.1b), leading to significant reductions of both the drag and the heat transfer rates, by up to 90 and 60 percent, respectively [3]. The majority of studies performed in this field aimed to understand or to improve the reduction mechanism associated with a steady flowfield. However, when examining the effect of the model geometry, highly unsteady flow occurred at certain spike lengths. This triggered the first pioneering works attempting to map and understand the unsteady spiked body flows [2] [3] [4] [6]. Their findings will be discussed in detail in the next section.

A secondary use of spiked missile foreheads originated from Album [7] and Wyborny [8], whose measurements on the aerodynamic characteristics of these bodies showed that employing a spike as a control device was a promising way of improving the stability.

In the early 1960's, another new application appeared in aerodynamics, extending further the interest in spiked body flows. Use of parachutes was considered for stabilising pilot ejection capsules and for recovering expensive test vehicles, such as space probes and satellites. Roberts [9] and Maynard [10] observed that unstable flow similar to that experienced over spiked bodies was present for such devices. These two studies led to the pioneering work of Robinson [11], the first to measure the frequencies and the amplitudes of the instability.

At the end of the same decade the problem of a future unmanned Mars landing mission was brought up. The search for possible shapes of a landing capsule made apparent that two main criteria had to be fulfilled. First, high drag characteristics were required to enable sufficient braking in the thin Martian atmosphere. Secondly, a lightweight structure capable of withstanding the large impulsive loads encountered during such a manoeuver had to be employed. As one of the suitable possibilities, concave tension shell shapes (Fig.1.1c) were considered by Jones et al. [12] in 1967. The flow over this initial option displayed instabilities similar to spiked body flows.

Ablation phenomenology obtained considerable attention in the early 70's. Investigating the flow around ablative hemisperical nosetips, created at the high Reynolds' number portions of a re-entry showed that in this particular case the peak heat transfer does not occur at the stagnation point, but near the transition from a laminar to turbulent boundary layer [13]. This resulted in the formation of a concave conical shape (Fig.1.1d), approximately resembling a spiked blunt body. Kenworthy and Richards [14] and Abbett et al. [15] demonstrated experimentally, that unstable flow similar to the spiked body instabilities is indeed present around such geometries.

The first space shuttle flights (Fig.1.2) in 1981 and 1982 experienced some new, unexpected aerodynamical phenomena also associated with spiked body flows. For example,the 3rd developmental flight (STS-3) showed problems during the ascent, associated with the initial formation of shock waves and the subsequent flow separation. This appeared in the vicinity of the Orbital Maneuvering System (OMS) pods and in the forward area of the astronauts cabin [16], and contributed to the loss of some of the Space Shuttle's heat shield tiles. During the descent, asymmetric flow problems were encountered, caused by the sporadic occurrence of the separation bubble, along with persistent aerodynamic buzzing noises from the flow separation. These latter phenomena were initiated at a flight Mach number around 3.0 and

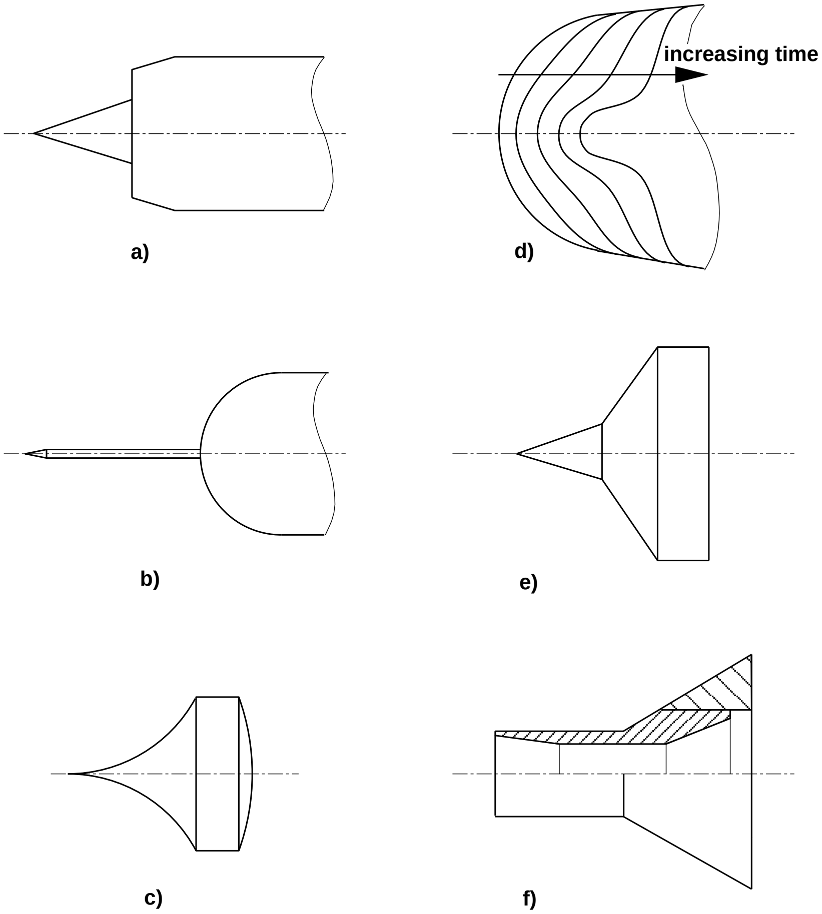

Figure 1.1: *The family of spiked bodies.*

Figure 1.2: *Launch of the Columbia Space Shuttle.*

Reynolds' number near the critical value. All these problems have been identified as spiked body flows in their fundamentals.

Finally, the most recent area of fluid dynamics exhibiting similar features involves the flow around double-cone and cylinder-flare geometries (Fig.1.1g,f). These shapes were associated with some flow separation studies around possible flame-holders in future scramjet engines [17]. Test cases considering freestream Mach numbers as high as 10 may well exhibit flow patterns typical to the spiked body flows.

1.1.2 Understanding unsteady spiked body flows

The work of Bogdonoff and Vas [3] could be regarded as the foundation- stone for studying unsteady spiked body flows. They were the first to identify two distinct forms of unsteadiness, termed as oscillation and pulsation. The basic description of these flows was also laid down, as follows. The oscillation mode is characterised by a change in the shape of the foreshock as it oscillates between a convex and a concave configuration as illustrated in Fig.1.3a. The pulsation mode, on the other hand, exhibits a somewhat more dramatic excursion between two very different shock envelopes (Fig.1.3b). One envelope consists of a conical foreshock emanating from the spike tip and intersecting the bow shock created by the blunt body (solid line) while the other is a single bow shock passing through the spike tip (dashed line). Although these instabilities were referred to by many differing adjectives in earlier works, the terms oscillation and pulsation became widely accepted later.

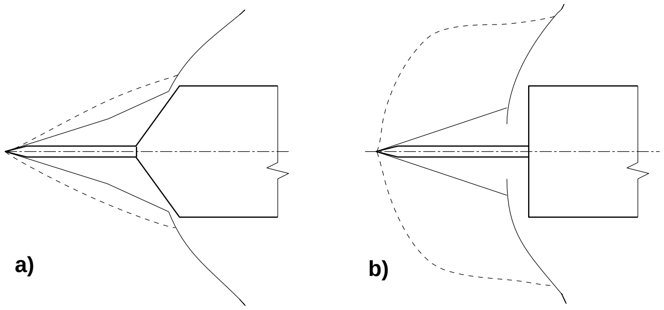

Figure 1.3: *The oscillation (a) and pulsation (b) flow modes.*

The first observation of the pulsation mode predates the work of Bogdonoff and Vas, and originated from Mair in 1952 [2]. Mair investigated the flow over both spiked hemispheres, flat cylinders and their two-dimensional counterparts at a Mach number of 1.96 ($Re_D = 1.65 \times 10^5$). Instability was observed to occur at $L/D < 1.5$ and $\Phi_D = 90^o$, and the shock-history was reconstructed using randomly sequenced photographs. Based on this it was observed that as the expanded foreshock collapses, the blunt body is as though accelerated to a supersonic speed, causing the creation of a new bow wave in front of the afterbody's face. This is characteristic of the pulsation mode [18]. However, as pointed out earlier, Mair actually used the term "oscillation" for this instability in his work, which could be explained by the relatively low Mach number he worked at. At lower speeds the pulsation mode alone is likely to occur [18] and therefore he could not be aware of the existence of another mode of unsteadiness, later termed as oscillation.

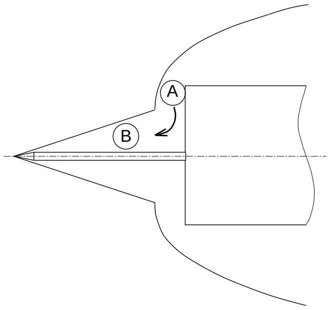

Figure 1.4: *Pressure imbalance in pulsating flow according to Maull [4].*

Maull [4], working at a larger Mach number (6.8) and examining spiked hemispheres with various shoulder radii, found the two different flow modes, but failed to distinguish between them and named both as "oscillation". However, he was the first to propose a driving mechanism for the pulsation mode by pointing out that the pressure imbalance behind the strong shock (region A in Fig.1.4) and the weak shock (region B in Fig.1.4) causes mass reversal into the separation region, which consequently becomes inflated. He substantiated this by demonstrating that a jet of air injected in front of a flat faced cylinder can produce a shock pattern similar to the one present in a spiked body flow.

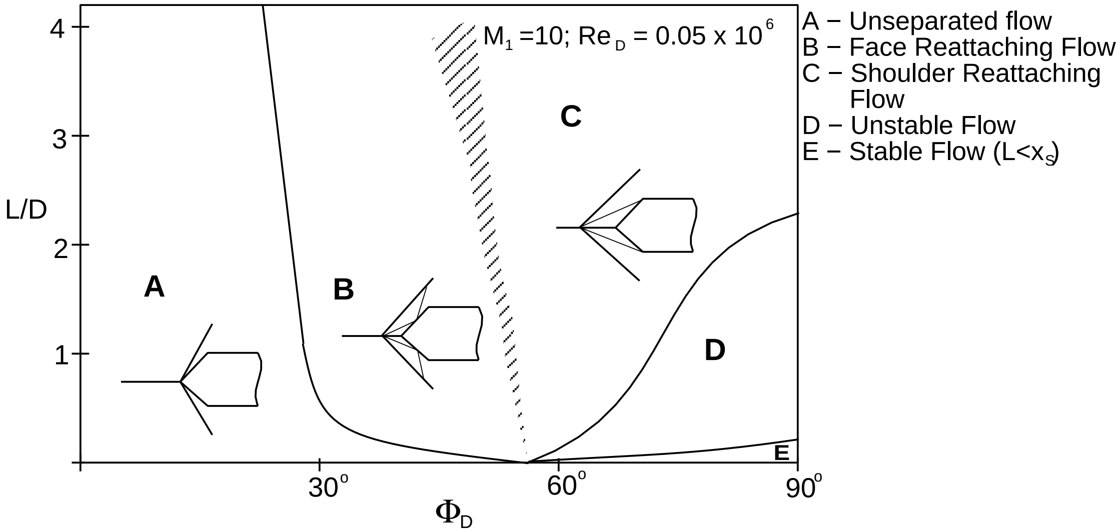

Figure 1.5: *Flow regions for spiked cones after Wood [5].*

Wood [5] and later Holden [6], working at Mach 10.00 and 15.00, respectively, conducted studies to explore the entire spectrum of all possible flow modes occurring over spiked blunt bodies. Their results plotted in the spike length-afterbody cone angle plane exhibit some interesting features (Figs.1.5,1.6). One was that the boundaries of all six regions were found to emanate from the point representing the freestream shock-detachment angle, 55.5^o [19]. As will be seen later, the shock-detachment angle has an important role in establishing unsteadiness over a spiked body. They also considered the problems associated with capturing the oscillation mode. While Wood failed to distinguish it from pulsation and labelled all unstable flows as “oscillation”, Holden managed to locate it, but, surprisingly, to a small isolated region. This is most likely due to insufficient sampling of the chosen parameters. Holden also made an important statement regarding the oscillation mode, namely that it is associated not only with the inflation of the separation region but also with the movement of the separation point along the spike.

The most relevant findings from Robinson et al. [11] concerned the onset of

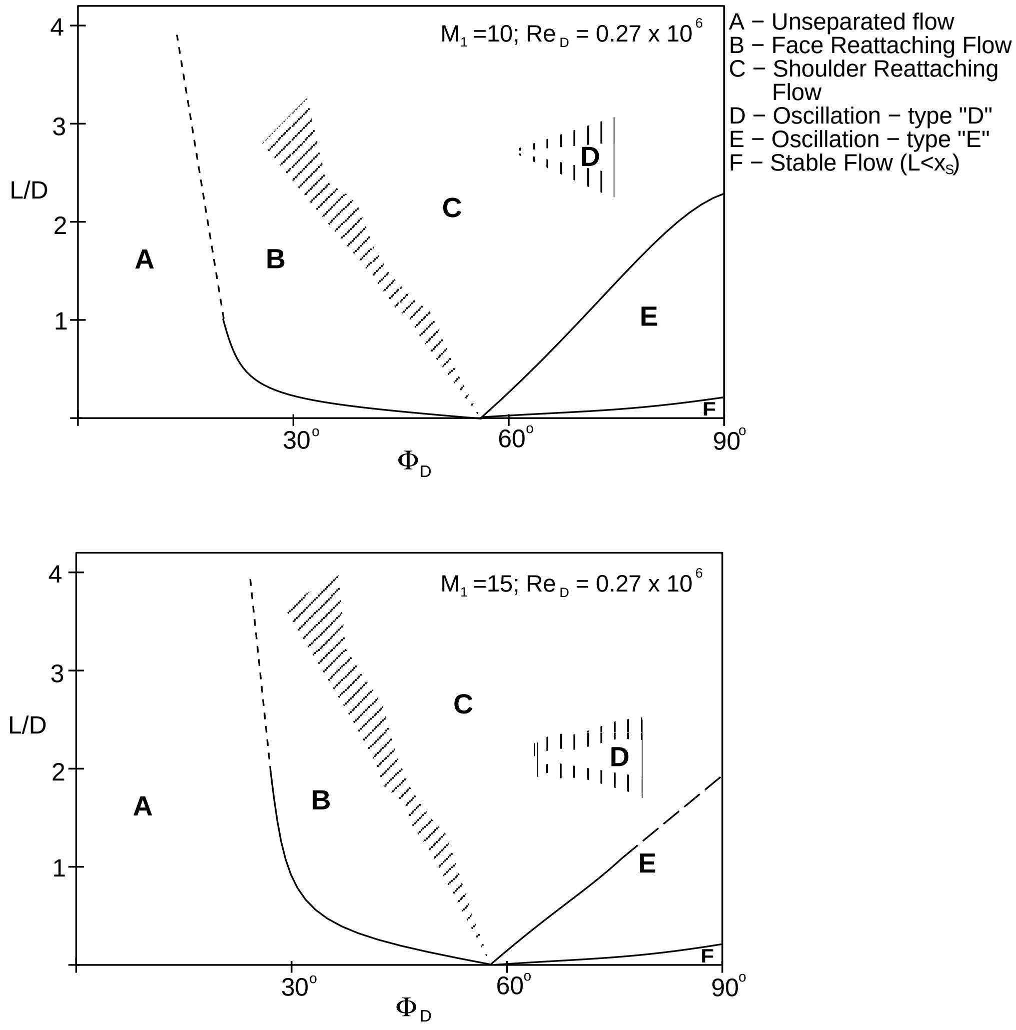

Figure 1.6: *Flow regions for spiked cones after Holden [6].*

the instability. They believed that it occurs when the angle required to turn the separated flow parallel to the model face exceeds the freestream shock-detachment angle. They also attempted to measure the pulsation upper boundary location, during which they observed a hysteresis phenomenon, depending on whether the spike length was increased or decreased. For an outward moving spike the unsteadiness disappeared at a longer spike length, than the length at which the onset appeared at an inward moving spike.

Kabelitz [20] analysed the spiked body problem by applying the small perturbation method for a simplified model of a stationary separated flow. This assumed a driving mechanism based on the shear layer entrainment and a consequent forward movement of the separation point. Although this matched the experimental observations up to a certain point, it did not deal entirely satisfactorily with either mode. Kabelitz also attempted to categorise the results, which led to the identification of another flow mode, termed vibration (Fig.1.7). Later this proved to be generated by essentially the same driving mechanism as oscillation [18].

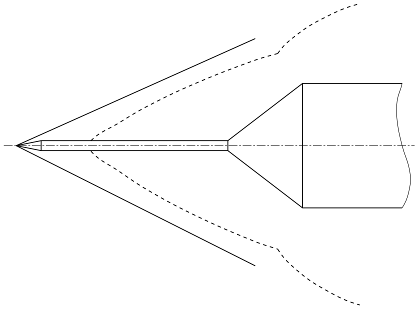

Figure 1.7: *Vibration flow mode.*

All studies mentioned up to this point assumed, that the flowfield was axisymmetric. Although photographic evidence of asymmetric shock formations existed since the earliest investigations [2] [3] [4], they were believed to be caused by the likely disturbances present in the experimental setup. However, in 1976 Demetriades conducted research on the asymmetry itself, first showing that this phenomenon may arise systematically [21]. He examined the flow over a blunted double-cone configuration exposed to a Mach 3.02 freestream (Fig.1.8). Two diametrically opposite transducers were located on the circle representing the spike base, at which point the pressure histories were simultanously recorded. Their correlation showed, that the modulations (dashed line on Fig.1.9) of the two harmonic waves were 180^o out of phase, or anticorrelated (white stripes on Fig.1.9). Further confirmation of this was given by comparison of the spectra from the individual transducers which led to a very important conclusion that three-dimensional effects could be present in an axisymmetric unsteady spiked body flow. Demetriades actually suggested that the protruding bulge rotates around the spike, completing one revolution for every two cycles of pulsation. The importance of this work lies in the detection of this three-dimensional phenomenon but the source of this remained unexplained.

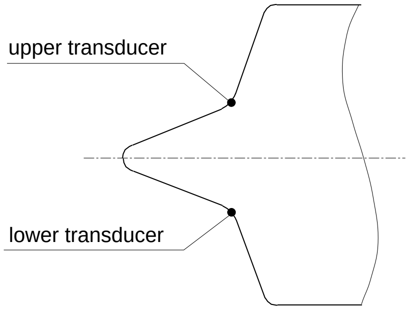

Figure 1.8: *Demetriades' model for examining shock asymmetries [21].*

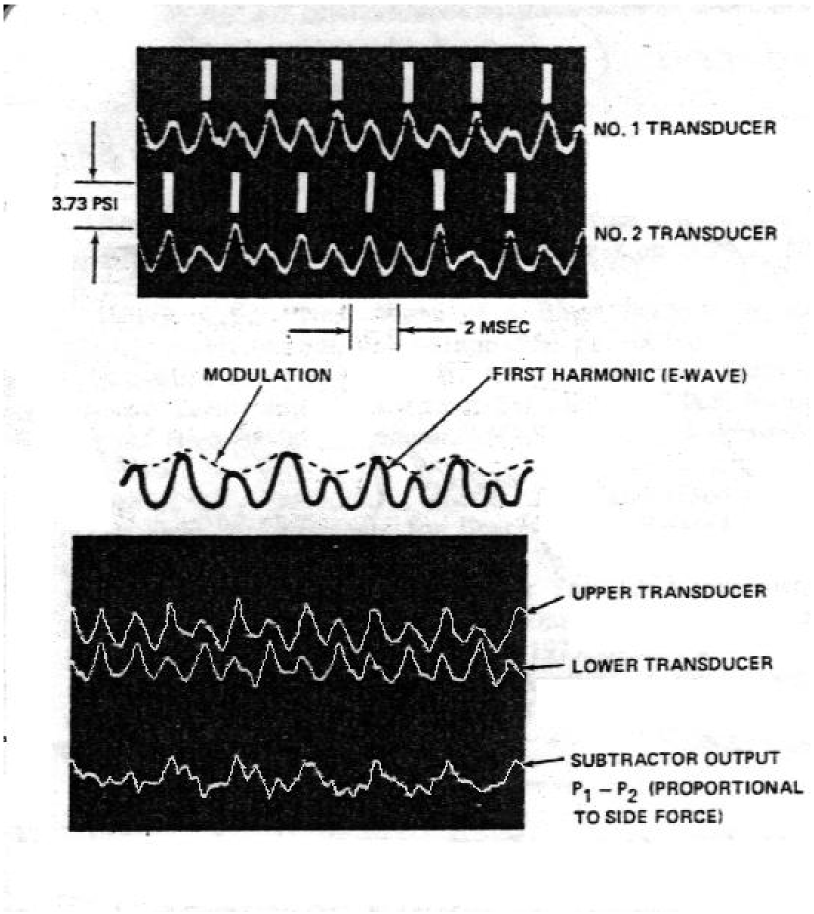

Figure 1.9: *Pressure histories recorded at two, diametrically opposite transducers located on the afterbody face by Demetriades [21].*

Understanding of the generator of the pulsation mechanism itself, however, was still not satisfactory at this time. A major breakthrough in this field came from Panaras [23], whose original idea of finding the similarity between Edney's type IV shock formation [24] and the flowfield created over a spiked body enabled the most complete explanation of this instability at the time. Edney analysed the complex shock structures arising at a weak shock-strong shock interaction, considering their various mutual positions. The shock field termed as type IV (Fig.1.10) yielded the appearance of a small supersonic jet (the supersonic feature was supported by analytical means). The jet was represented by a region of high-speed flow turned towards the separation region due to the large pressure behind the normal shock. Panaras' idea was that the same shock pattern is formed in the vicinity of a foreshock-aftershock intersection occurring in a pulsating spiked body flow (Fig.1.10). Thus, it supplies gas into the separation region, causing inflation. This led to the very important conclusion that the mass influx did not originate from the region behind the strong shock, as previously thought, but from the supersonic region bounded by the conical foreshock and the shear layer. This was further substantiated by comparing the pressure on the afterbody face and behind the normal bow shock. The former one was found to be twice as high as the latter demonstrating that the lower pressure gas would indeed not be capable of breaking through the high pressure jet region. Supporting evidence was given by sublimation tests performed on the cylinder face.

Kenworthy's extensive work [18], which aimed to investigate the unsteady flows over a wide range of spiked cones and cylinders at Mach 2.21 and Mach 6.00, already took this information into account, and expanded it further by attempting to determine the flow parameters in the individual regions. For this purpose Kenworthy constructed dynamic heart diagrams considering the actual shock collapse/growth speeds. These were determined by recording the shock position in a longitudinal

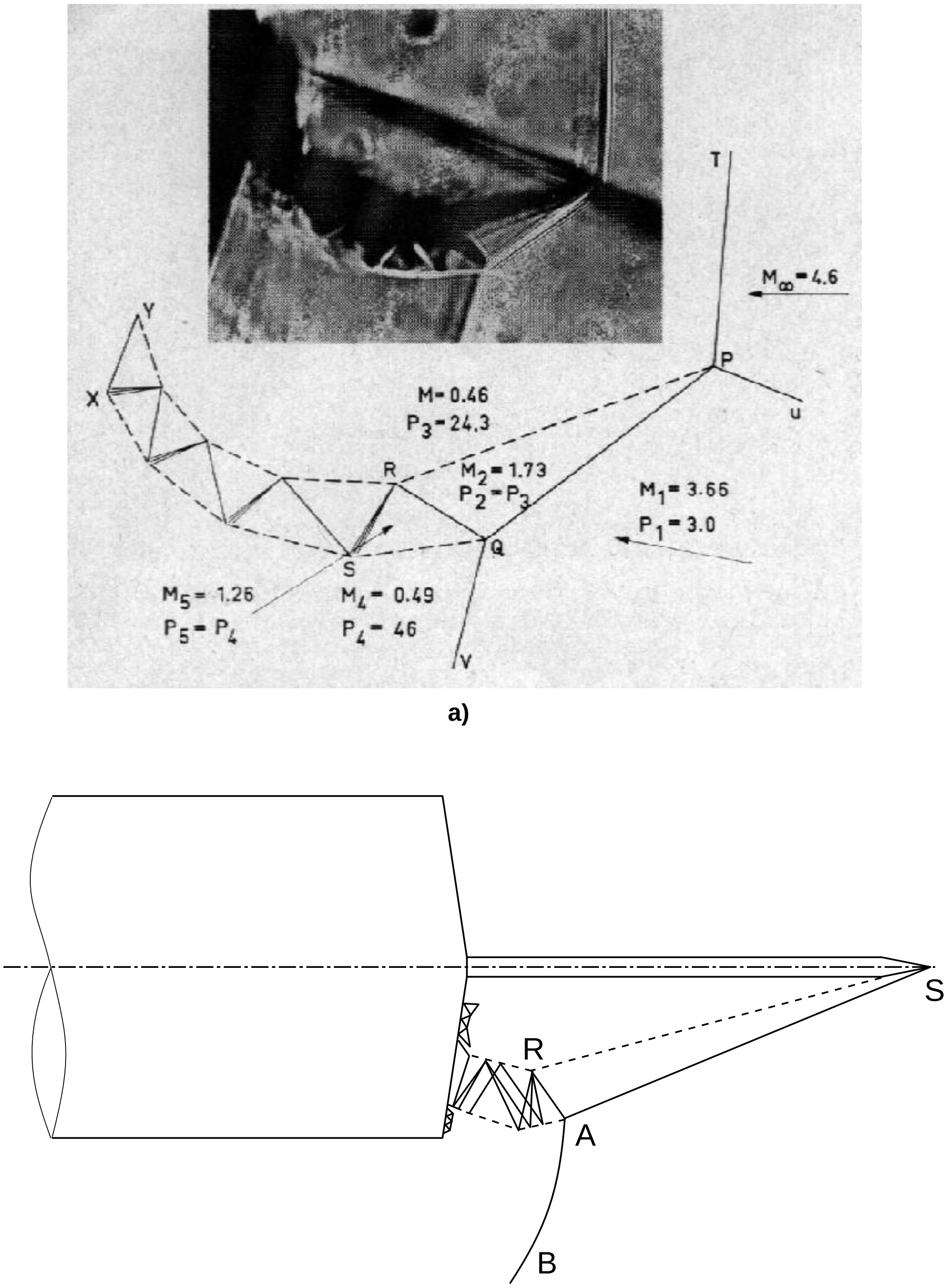

a)

b)

Figure 1.10: *Similarity between Edney's type IV shock formation [24] (a) and the flowfield corresponding to the pulsation flow mode [23](b).*

mask created at the half afterbody radius. The heart diagram analysis showed that the jet was indeed supersonic at both considered freestreams. He also built up a simplified analytical model to calculate the frequency of the event. The main contribution of this study, however, was associated with understanding the oscillation flow mode. Kenworthy established the so-called "energetic shear layer hypothesis", which essentially proved that the driving mechanisms of the two modes differ in their fundamentals. The pulsation mode is generated by a shock-shock interaction mechanism, which is inviscid in its nature, while the oscillation mode is fed through an ever-changing shoulder reattachment criterion of the shear layer, a viscous phenomenon in its nature. These hypotheses will be revealed in more detail later in this thesis.

Calarese and Hankey's research [25] from 1983 investigated the origin of the three-dimensional effects observed earlier by Demetriades [21]. The model geometry was a flat faced conical afterbody equipped with a relatively thick (d/D=0.225) blunted spike, and exposed to a Mach 3.00 freestream. Employing a thick spike enabled the implantation of transducers into the spike itself, thus providing information about the flow from within the separation region. Three equally distributed kulite pressure transducers were located on the afterbody face (see Fig.1.11). The power spectra obtained from the pressure histories at these pressure taps showed that two wave modes were present (Fig.1.12). The primary mode (even) occurred at the frequency of 2800 Hz and corresponded to the axial shock motion, which is basically the shock collapse and growth due to the pulsation. The secondary wave (odd) mode was at a frequency of 1400 Hz and was associated with the shock asymmetry. The high-speed interferometry used (44,000 frames/s) enabled the recording of four consecutive cycles, exhibiting the occurrence of asymmetry in every second cycle only. This was believed to be caused by a secondary separation and as a consequence, by a sudden pressure burst on one side of the spike only.

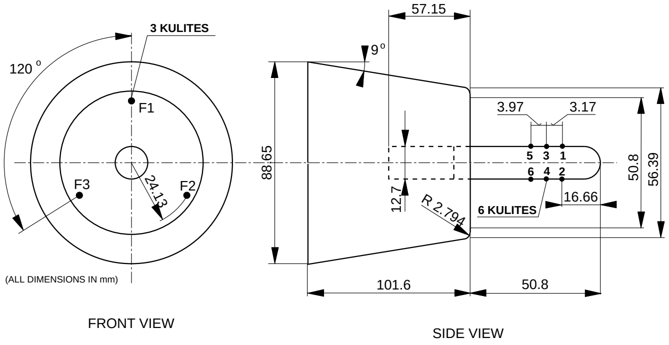

Figure 1.11: *Calarese and Hankey's model [25].*

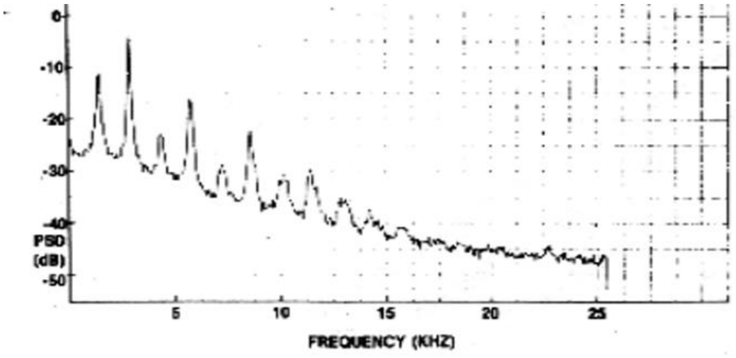

Figure 1.12: *Power spectra of the pressure at kulite F1, located on the face of the afterbody [25].*

Examining the pressure histories from the transducers located on the spike itself showed that these were in phase on one side of the spike, but out of phase on the opposite. Thus, the odd mode disturbance (i.e. the secondary separation) associated with the asymmetric shock splitting generated two distinct counter-rotating waves about the spike, proceeding downstream towards the afterbody face (Fig.1.13). These then modulated the primary mode at the cylinder face slightly on one side, but more strongly on the other, leading to the asymmetric disturbance. This new theory contradicted Demetriades' idea of having one rotational wave only, completing a revolution for every two cycles, and was substantiated by analysing the wave out of phase angles on the frustrum face. This should be 120^o according to Demetriades hypothesis (having 3 transducers), but it appeared to be 180^o instead, supporting the existence of two counter rotating waves. However, the explanation of the shock system flapping from one side of the frustrum to the other could still not be justified.

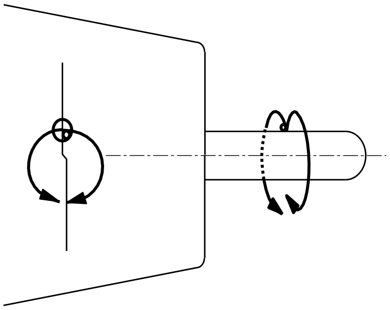

Figure 1.13: *The formation of two counter-rotating waves according to Calarese and Hankey [25].*

Among the other interesting findings of Calarese and Hankey is that the above shock-asymmetry phenomenon did not occur at the longer spike lengths, including the hysteresis range. At these configurations, very strong pulsation was experienced, but the shock system remained perfectly symmetric. This observation was accomplished at an outward moving spike, and as the measurements were recorded during the retraction as well, these authors became the first to record an entire hysteresis loop (Fig.1.14). This important information will be exploited later in the present study.

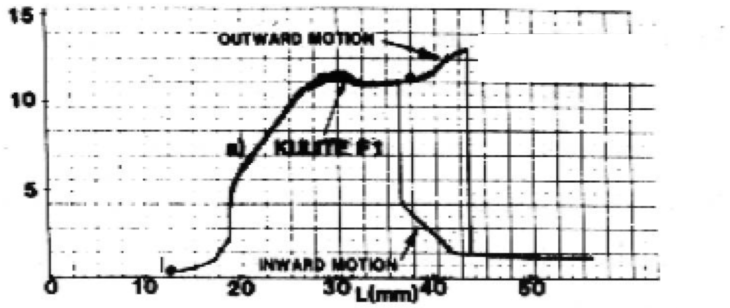

Figure 1.14: *Rms pressure - spike length diagram by Calarese and Hankey [25] showing the hysteresis phenomenon.*

The above work, representing the last significant experimental-analytical study from the field of spiked body flows, concludes the review of the commonly accessable literature. However, a number of relevant investigations could be found in the literature of the former Soviet Union as well, which remained almost completely unreferenced and unrevealed among the previously listed authors. Thus, these studies could not be considered as a chronologically integral part of the above review and therefore will be dealt with separately in the following.

Antonov et al. [26] in 1976 experimentally investigated the unsteady flows over axisymmetric spiked cylinders at freestream Mach numbers ranging from 2.10 to 6.00 (with the Reynolds' number varying between 7×10^4 and 1.6×10^6, respectively). The optical technique used was capable of recording up to 625,000 frames/s, which allowed the capture of an entire unsteady cycle instead of constructing a typical one from the frames from different cycles [21] [18]. Similarly to Kenworthy [18], a longitudinal mask located at D/4 diameter was used to measure the shock collapse/growth speeds. Using this information, a method to estimate the pulsation Strouhal number was established, which, despite the numerous simplifications involved, gave a reasonable agreement with measurements. Another new idea was introduced here. For the spike lengths larger than the blunt body diameter ($L > D$) it was suggested that the spike length was be used as a characteristic dimension in the Strouhal number calculations. Previously, this parameter was based on the cylinder diameter instead, which was retained for $L < D$ only. This formulation, but for the entire range of the spike lengths, was also suggested later by Ericcson [22]. A very good insight was given into the pulsation driving mechanism. Using standard shock relations Antonov showed that the pressure behind the normal bow shock ($p_0{}'$ in region C, Fig.1.15) is smaller than the one arising in region B, p_0". This means, that the mass influx into the separation region cannot originate from region C, but from region A, from behind the conical foreshock. This paricular point is in accordance with Panaras' finding from the same time [23]. Furthermore, the pressure behind the expanded foreshock near the spike tip could be calculated and, having the shock collapse speed already determined, the location of the new and collapsing shock waves' merge was obtained. They also experimented with the parameters affecting the frequency of the event. It was concluded that the freestream Mach number and the spike tip cone-angle, influencing the state of the boundary layer, had a significant influence on the above characteristics.

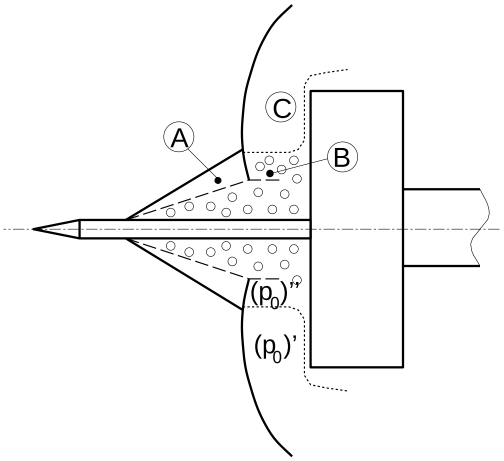

Figure 1.15: *Explanation of the pulsation mode according to Antonov et al. [26].*

As a continuation of this latest task, another investigation originating from the same authors [27] was performed. An important result of this study was that using the dual Strouhal number choice yielded a constant value for almost any afterbody half-cone angle. It is noteworthy that the latter was ranging from 45^o up to 120^o (a concave, forward facing conical cavity in the blunt body's face).

The last major experimental study was performed by Zapriagaev and Mironov in 1989 [28], also examining spiked cylinders at Mach 2.04 and Re 2.4×10^6 freestream. Contrary to the previous investigators, they suggested using the shock triple point (the intersection of the foreshock and the aftershock) location as a reference for determining the shock collapse/growth speed. Obtaining this position would normally be difficult in an experiment, but because of their high-speed camera capable of recording up to 1,000,000 frames/s this could be achieved by locating the triple point directly from the photographs. This information served as an input for the

Strouhal number calculations, exhibiting the interesting result that the above parameter appeared to be independent of the spike length at larger values, while it became dependent on it at smaller ones. The boundary of this dependence was found to be L/D=1.25, which partly justifies Antonov's dual Strouhal number choice, but also develops it further by indicating that the shift should be introduced later, beyond L/D=1.00. The driving mechanism of pulsation was described similarly, as by Antonov [26] and Panaras [23], while for the observed shock asymmetries Calarese and Hankey's explanation [25] was adopted. The new quantitative estimate on the pressure amplitude, based on standard shock wave relations, was found to be in fair agreement with the experiment. Finally, they established a calculation procedure to determine the mass influx rate into the separation region by taking a cavity hollow as a model (Fig.1.16).

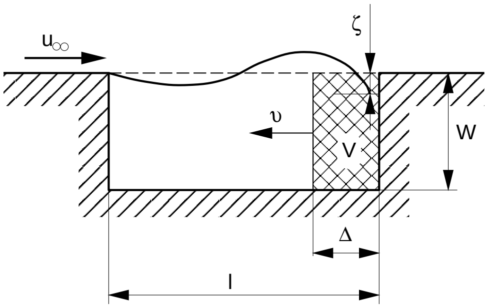

Figure 1.16: *Cavity hollow model according to Zapraigaev and Mironov [28], serving as a basis for calculating the Strouhal numbers of unsteady spiked body flows.*

Based on this result, the character of the driving mechanism could be judged, which they described either as acoustic oscillation (for $\delta < 0.1$) or as a non-mass conserving pulsation (for $\delta > 0.56$, where $\delta = \frac{\Delta}{l}$, see Fig.1.16). This criterion, however, left plenty of space for regimes in between, termed as transient instabilities.

1.1.3 Spiked bodies and CFD

The references cited above are based on experimental or analytical methods only. However, a number of numerical solutions have also been attempted, which will be reviewed in the present section.

The very first computational work from the field of unsteady spiked body flows originated from Shang and Hankey [29], who took Calarese and Hankey's experimental test case [25] as a basis. The 3-D Navier-Stokes equations were solved through an explicit, finite difference method. McCormack's predictor-corrector scheme was employed with 2nd order accuracy in space and time. The numerical evaluations were performed on a STAR 100 computer with a vectorised code and the results were found to be in a reasonable agreement with the experiment, both in terms of the pressure amplitude and the pulsation frequency. However, no further information about the flowfield was obtained from these solutions.

Another early work, from Yoshikawa in 1982 [16], represents probably the best exploitation of the opportunities offered by a numerical approach so far. He modelled the transient phenomena occurring at an impulsively started spiked body, corresponding for example to a space shuttle launch. First, based on Sears et al.'s earlier work on the separation zones near moving walls [30], Yoshikawa built up the four possible streamline patterns, which could take place in a separated flow involving the upstream/downstream movement of the separation point (Fig.1.17).

The characteristic points of the flowfield, such as the separation point (S), reattachment point (R), inflation point (I) and a jet injection point (J) were located in these figures. Then, the same points were found in the numerical results as well, identified on the basis of the zero body vorticity (Fig.1.18). The computations were achieved by applying an explicit, time-dependent method to resolve the compressible, Reynolds' averaged Navier-Stokes equations, which were discretised by second order accuracy in space and time.

These solutions showed, that a secondary separation is indeed present at an upstream moving separation bubble (Fig.1.18e), corresponding to flow type I' in Fig.1.17. This is a very important finding as it supports Calarese and Hankey's

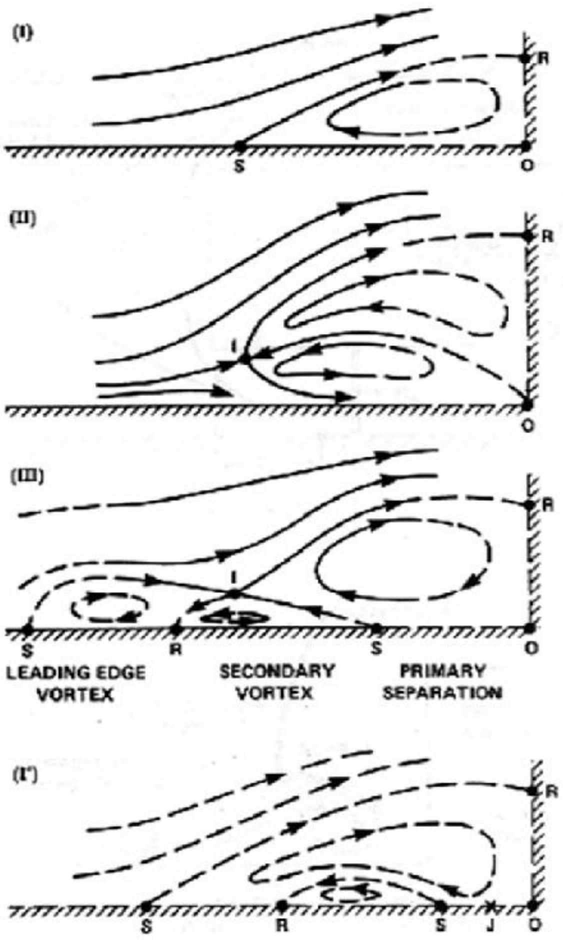

Figure 1.17: *Streamline patterns of separated flows [16]. Flow from left to right. I - fixed separation point, II - upstream moving separation point, III - downstream moving separation point, I' - upstream moving separation point generated by a jet injection at point J.*

hypothesis on the origin of 3-D effects, associated with the existence of secondary separation. The wall pressure diagrams, used alongside the vorticity diagrams and the density contour plots enabled the identification of the jet formation at the foreshock-aftershock intersection, which Yoshikawa referred to as a lambda shock structure. Thus, the numerically simulated transient flow appeared to feature the same key elements as the unsteady pulsating flow arising over spiked bodies.

Mikhail's primary aim was to investigate the drag reduction mechanism over

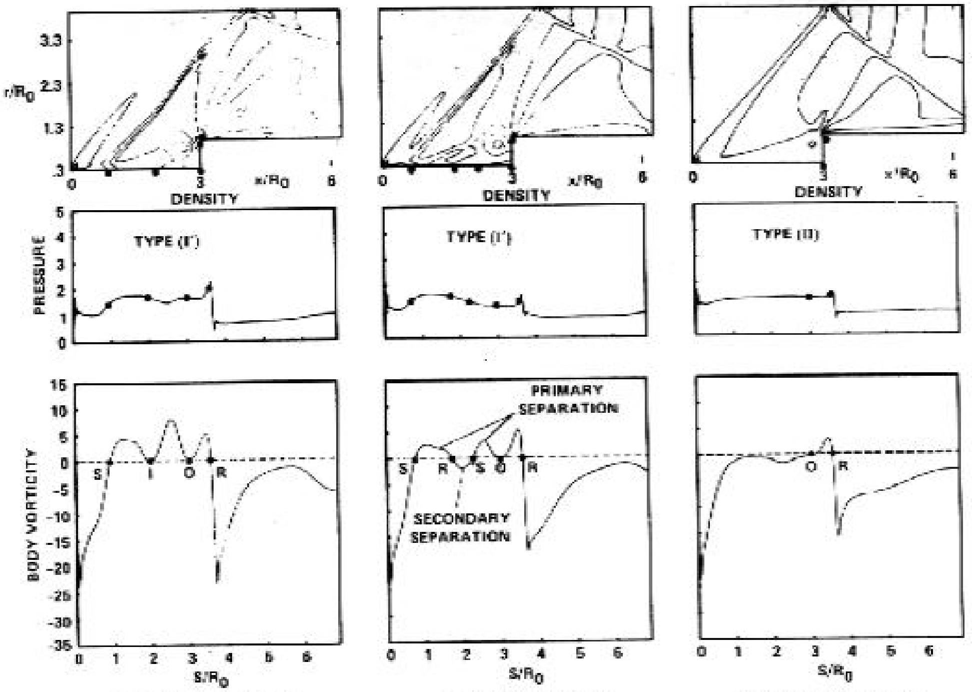

(d) TIME, $t/(R_0/C_1) = 5.4$ (e) TIME, $t/(R_0/C_1) = 6.3$ (f) TIME, $t/(R_0/C_1) = 8.5$

Figure 1.18: *Density contours, wall-pressures and body-vorticities by Yoshikawa [16].*

a spike-nosed projectile equipped with a vortex ring [31] at Mach numbers ranging between 1.90 and 3.50. The method used incorporated the solution of the compressible, Navier-Stokes equations involving a Baldwin-Lomax turbulent model. A time-dependent McCormack's scheme was used for discretisation, and the calculations were performed on a CRAY X-MP/48 supercomputer. As a secondary observation of this work, unsteady flows were reported to occur in the Mach 1.90 freestream case. Although Mikhail termed this unsteadiness as "buzz" and determined its frequency as 5333 Hz, the instability appears to be an oscillation, of which no further explanation is given in that reference.

Another computational solution on Calarese and Hankey's case [25] was performed by Ingram et al. in 1993 [32]. They employed a time accurate, explicit multi-stage Runge Kutta method to solve the full Navier-Stokes equations in an axisymmetric manner. A modified Advective Upwind Split Method (AUSM) scheme was used to express the inviscid flux vectors, with higher order accuracy being obtained through MUSCL extrapolation. Second order accuracy was achieved in both space and time. The main aim of this study was, however, to test a new solution-adaptive grid algorithm, extended to multi-block domains. The results exhibited excellent shock-resolution, showing Panaras' jet formation as well as the existence of the secondary separation during the upstream movement of the separation point (Fig.1.19). This further supported the theories of Calarese and Hankey as well as of Yoshikawa. However, apart from a brief description of the flow unsteadiness, these excellent results remained unexplored.

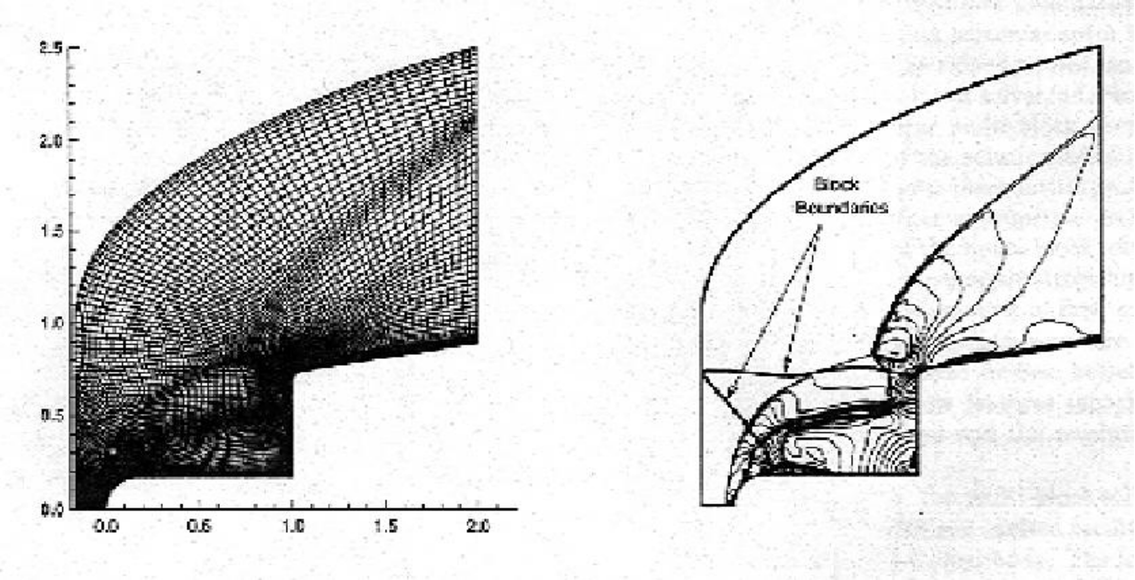

Figure 1.19: *Ingram's computation of a pulsating flow based on a solution-adaptive grid alghoritm [32].*

Yamauchi et al. [33] investigated numerically the drag reduction mechanism on spiked hemispheres. The thin layer compressible Navier-Stokes equations were resolved by an LU-ADI time integration scheme in both axisymmetric and three dimensional manner. This latter case enabled the analysis of the spike's effect on the drag reduction at incidence. The freestream Mach numbers varied between 2.05 and 6.80 (Re=0.14×10^6), and despite performing steady calculations, instabilities occurred for L/D=0.5 at all speeds. Again, as this was not the primary aim of this study, no further analysis or description was given on this phenomenon.

The few numerical studies available from the former Soviet literature will again be discussed separately.

Myshenkov [34] performed computations of spiked cylinders exposed to a range of Mach numbers up to Mach 3.00 with spike lengths varying from 1.00 to 7.00. A finite difference method was used to discretise the axisymmetric Navier-Stokes equations, applied to structured meshes consisting of 2500 points. The study aimed to investigate the drag reduction effects, during which oscillations were found at spike lengths between 2 and 3, without any detailed description.

Paskenov et al. [35] were also interested in investigating the drag reduction mechanism, considering freestream Mach numbers of 2.00 and 6.00 at fairly low Reynolds' numbers (100 and 500, respectively). Contrary to the experiments, they found steady flow to occur at the given geometries, which they attempted to explain by the extremely low Reynold numbers used. From a numerical point of view, a similar method to the one in [34] was used, with multi-block extensions.

Finally, Karlowarski et al. [39] simulated Calarese and Hankey's experiment [25], with the intention of dealing with the drag reductions only. The axisymmetric unsteady Euler equations were resolved by McCormack's predictor-corrector method employing so-called "monotonisators", representing numerical viscosity. The freestream Mach number varied between 3.00 and 8.00 while the spike length ranged from 0.25 to 1.00. It was observed, that in the absence of the "monotonisators" unsteady flow occurred in the separation region, indicating that numerical damping may significantly influence the solutions. Again, the unsteady flow features remained unexplored.

1.2 Aims and objectives

It is apparent from the above review that despite the considerable number of investigations unsteady spiked body flows are not entirely understood. Hypotheses were built up on the driving mechanisms of pulsation and oscillation modes, but their satisfactory demonstration has not been accomplished. Also, shock asymmetry was observed to occur in axisymmetric flow conditions, and an explanation on their occurrence and origin was suggested. However, it is not readily apparent whether this effect is caused by the likely imperfect axisymmetry in the experiment or is indeed a natural physical element of the flow behaviour. The hysteresis phenomenon in the onset of the different flow modes was also reported, but remained unexplained. The transition from one flow mode to another is believed to happen abruptly, but this has not been observed thus far.

The reasons for the uncertainities lie primarily in the inherent limitations of the experimental techniques, yielding difficulties in providing detailed information from inside such a complex, time-dependent flowfield. Thus, the main flow features, on which the various hypotheses are based, were obtained by an indirect deduction from the visual images, offering qualitative information only, and also from the data recorded on the model surface. Analytical methods have also been attempted, but they involved considerable simplification and therefore might be inadequate.

Computational Fluid Dynamics (CFD), on the other hand, can offer detailed insight into any part of the flowfield without interfering with the physics of the flow. It can also offer an arbitrary number of frames from within one cycle, which is an indisputable advantage at these high-frequency instabilities. The literature survey showed that although there were a limited number of CFD approaches performed in the past, the opportunities provided by a numerical solution remained unexploited.

Therefore, the purpose of the present study is to apply Computational Fluid Dynamics as a tool to enhance the understanding of the physics of unsteady spiked body flows. This will be accomplished by generating numerical results for a selected number of test cases, which will then be used to examine the existing hypotheses as well as for highlighting phenomena not observed from experiment. The numerical modelling will be restricted to axisymmetric flow conditions only, so no three-dimensional phenomena will be investigated in the present work.

In the following chapter the numerical method is described and verified. In Chapter 3, the CFD results are compared with the experimental data both qualitatively and quantitatively. Extensive validation allows then to proceed to the detailed analysis of the numerical results, which is provided in Chapter 4. This consists of three main parts: in the first one, the oscillation driving mechanism is investigated, in the second one, the driving mechanism of the pulsation mode is analysed, and in the third one the results of the hysteresis simulation are exploited to enhance the understanding of this phenomenon. Finally, conclusions are drawn in Chapter 5.

Chapter 2

Numerical approach

2.1 Test cases

The cases examined in the present work were selected from those studied in the measurements of Kenworthy [18], which were carried out at the von Kármán Institute for Fluid Dynamics in Belgium between 1974 and 1977. The results of these measurements are available for a series of spiked cones and spiked cylinders in Mach 2.21 and Mach 6.00 flows. The present work will consider only a selection from these, listed in Table 2.1. The main intention behind this choice is to provide numerical results for the configurations well suited for a detailed analysis of the phenomenon of interest. Thus, instead of aiming to cover a wide range of geometries and flow conditions, only the test cases describing best the oscillation, pulsation and the hysteresis phenomenon were selected.

Case	L/D	Mach number	Re_D
oscillation	2.0	6.00	0.13 million
pulsation	1.0	2.21	0.12 million
	1.0	6.00	0.13 million
hysteresis	1.25-2.40	2.21	0.12 million

Table 2.1: Test cases.

The model geometry in each case was a spiked forward facing cylinder, as illustrated in Fig. 2.1. The afterbody diameter in the experiment was 46 [mm], and this parameter will be used as the length scale in the numerical approach. The spike's diameter is 6.5 % of this value and is ended in a 30° angle cone. The spike length could be continuously changed in the experiment at a speed of 10[mm/s]. The model setup for these calculations is shown in Fig. 2.1. A discussion on the spike speeds chosen for the numerical method as well as on the range of spike lengths for the hysteresis simulation will be given in Chapter 3.

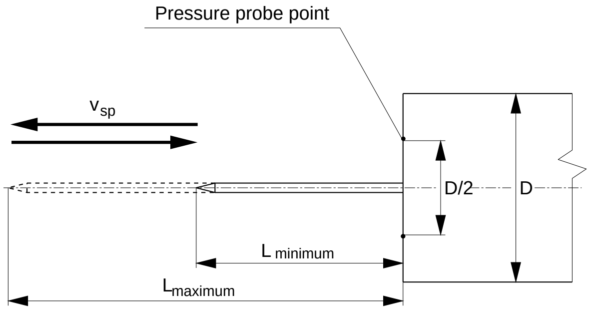

Figure 2.1: *Setup for the simulation of the hysteresis phenomenon.*

There were two pressure transducers placed at a diameter of D/2 on the face of the afterbody and the pressure was recorded at these points. To enable comparison with the experiments, the pressure history is monitored at one of these points in the numerical calculations.

Finally, in accordance with the experiment, the flow is modelled as axisymmetric, at zero angle of incidence. The pulsation flow mode will be simulated at both freestream Mach numbers of 2.21 and 6.00. Since the oscillation is typical of high Mach number freestreams, this flow mode is examined at Mach 6.00 freestream only. The hysteresis phenomenon is simulated at the Mach number of 2.21. The flow conditions are shown in Table 2.1, with the Reynolds' numbers based on the blunt body diameter.

2.2 Grid generation

Two-dimensional, structured, multiblock grids were generated for the selected test cases (Table 2.1). Because of the axisymmetry of the problem, it was sufficient to model one half of the body only. The main features of the grids used are given in Table 2.2, while the grid topologies are shown in Figs. 2.4a-e.

Grid	L/D [1]	No. of blocks	No. of cells	First spacing at the wall [1]	Application
O1	2.0	7	140,000	0.00005	Oscillation at M=6.00
P1	1.0	5	62,667	0.00100	Pulsation at M=2.21,6.00
P2	1.0	9	160,000	0.00015	Pulsation at M=2.21
H1	1.25	7	140,000	0.00050	Hysteresis lower boundary
H2	2.40	7	140,000	0.00050	Hysteresis upper boundary

Table 2.2: The basic grid parameters.

Starting with the simplest grid, P1 (Fig. 2.4) was created to simulate pulsation at both Mach 2.21 and Mach 6.00 freestreams. The mesh was structured into five blocks as shown in Fig. 2.2, from which block 1 is a relatively short one (with the horizontal dimension of $0.1L/D$), incorporating 21 cells in the x direction, and block 2 covers the entire spike length. Although this grid proved to be well suited for constant spike length calculations, it had to be altered for a hysteresis simulation.

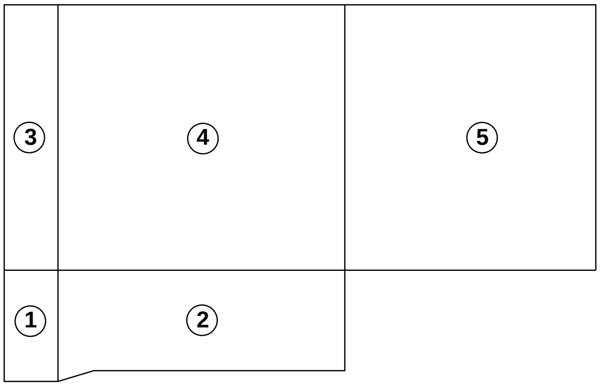

Figure 2.2: *Block structure for grid P1.*

For these calculations, the singularity problem arising at the spike tip appeared to be an important issue. In order to overcome this problem, a longer (horizontal dimension of $0.3L/D$) and more dense (50 cells in the x direction, clustered heavily near the spike tip) block 1 was employed in grids H1 and H2 (Figs. 2.4d,e), intended for moving spike calculations. Furthermore, the previous block 2 was split into two separate blocks, 2 and 3 (Fig. 2.3), to enable the modelling of a continuously changing spike length. If this was not done, then the grid around the spike cone would also change during the deforming mesh calculation (described in section A.7). Additionally, the newly created block 3 covering the spike (Fig. 2.3) was designed to accommodate more cells in the x direction, enabling a good grid resolution at both the minimum ($L/D = 1.25$) and maximum ($L/D = 2.40$) spike lengths, representing the endpoints of the hysteresis loop. This means, that the blocks of H1 and H2 are identical, apart from regions 3 and 6, which were created from the shorter version by a proportional stretching to the appropriate length.

Grid O1 (Figs. 2.4a) is analogous to H1 and H2. Finally, a special fine grid, P2 (Fig. 2.4c) was generated to enable a detailed analysis of the pulsation flow mode. The unique feature of this grid is the introduction of a fine resolution block in the region just upstream of the afterbody face (the dashed line in Fig. 2.3), where the most important elements of the pulsation flow mode are expected to occur. Hence, a locally refined grid is used in the region of interest.

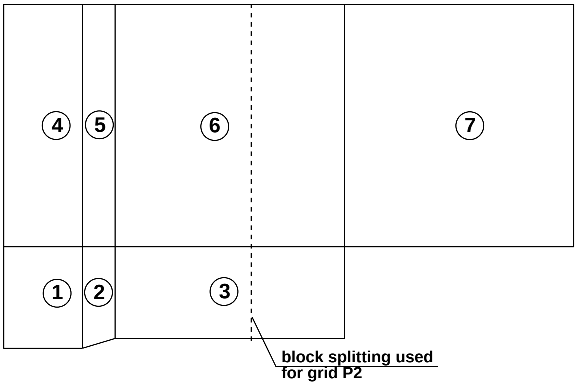

Figure 2.3: *Block structure for grids O1, H1, H2 and P2.*

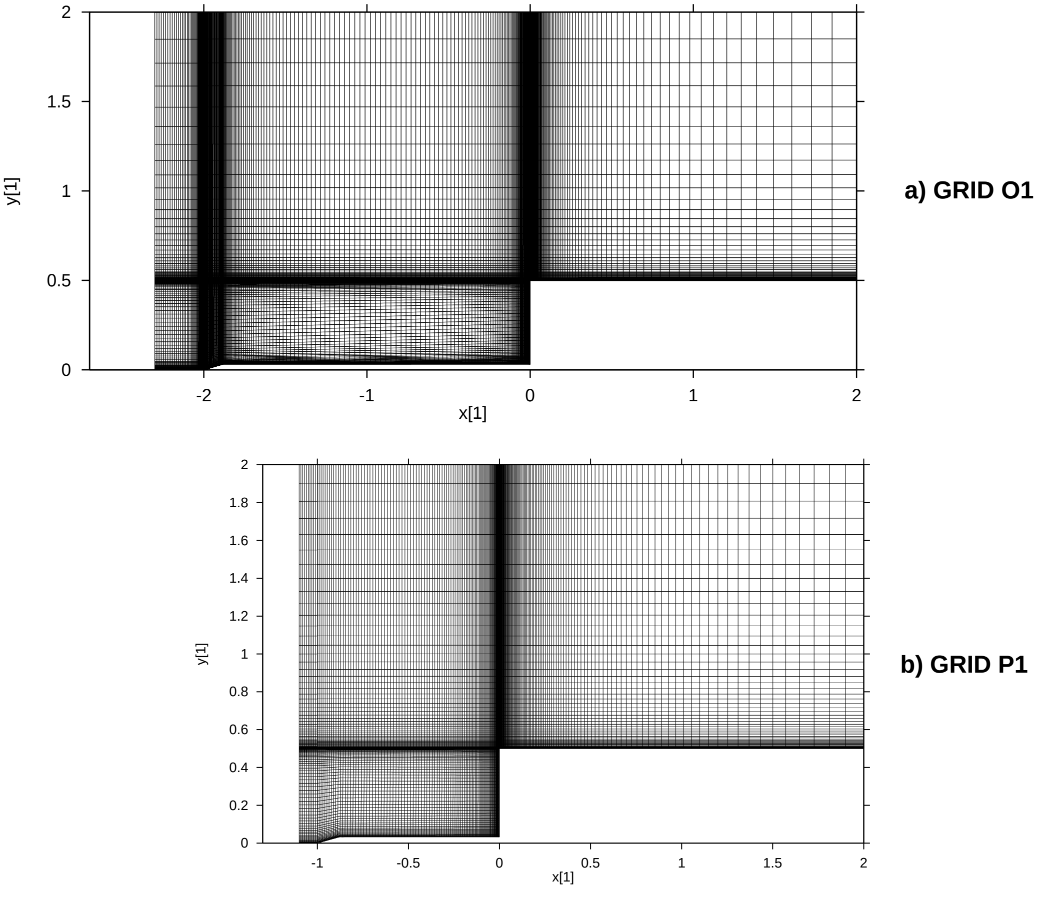

Figure 2.4: *Grid topologies, showing every second gridline only.*

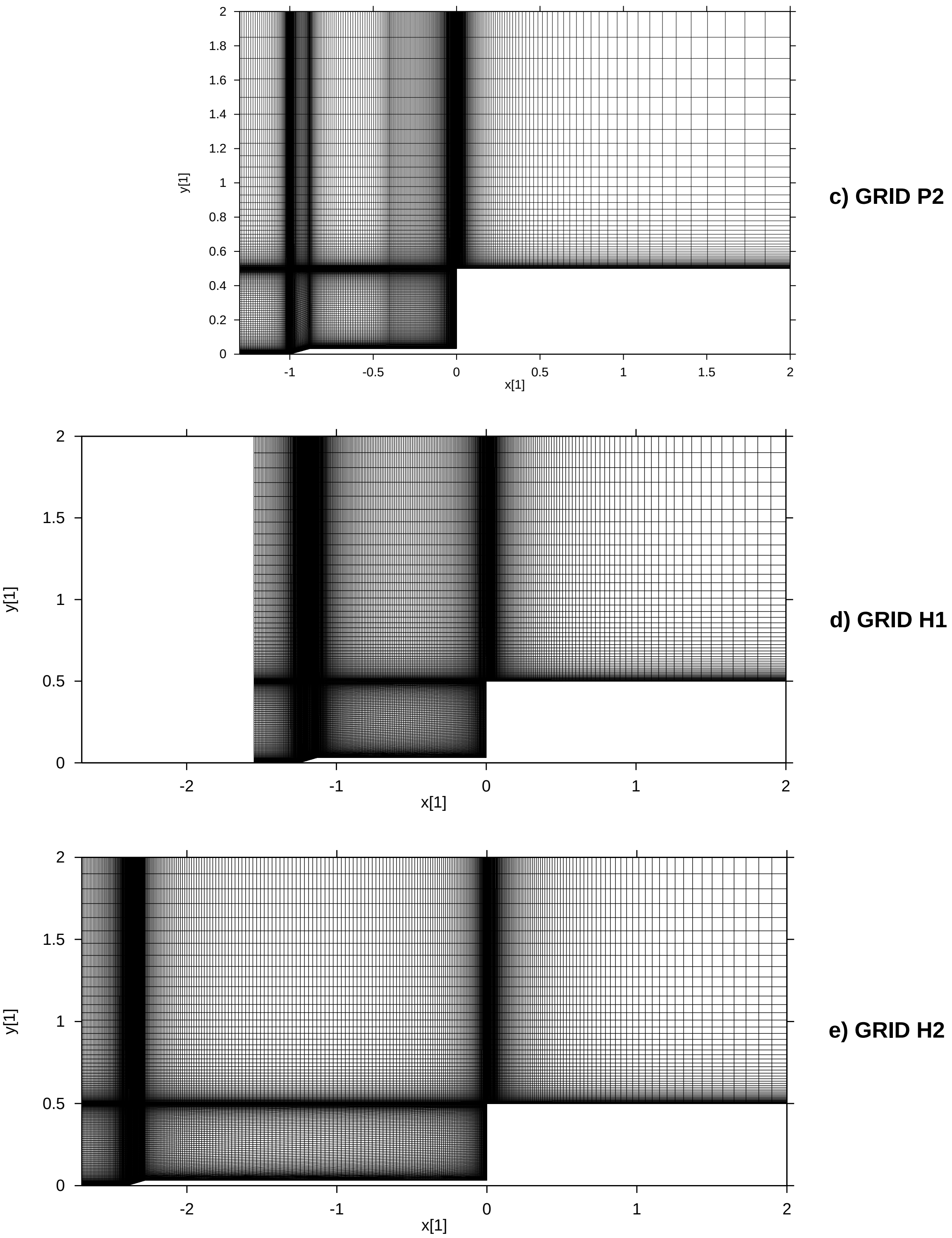

c) GRID P2

d) GRID H1

e) GRID H2

Figure 2.4: *(cont.) Grid topologies, showing every second gridline only.*

2.3 Numerical method

The PMB2D code was used for the numerical calculations. This is a generic CFD code developed at the University of Glasgow and has been used successfully to model steady and unsteady flows for a range of aerodynamic problems, such as aerofoils, cavities, nozzles and jets at both subsonic, transonic and supersonic speeds. A full description of the method is provided in Appendix A, while the most important features will be highlighted below.

The PMB2D code employs a cell-centered, finite volume discretisation for the solution of the Navier-Stokes equations. The convective terms are discretised using Osher's or Roe's scheme. All calculations in the present work were achieved by using Roe's scheme since this proved to be better suited for hypersonic freestreams. A modification to this method was introduced by applying Harten's entropy fix [50] to avoid the occurrence of non-physical expansion shocks. MUSCL variable extrapolation is used to achieve 2nd order spatial accuracy. The diffusive terms are discretised by central differencing. 2nd order time-accuracy is obtained by employing an implicit unfactored dual-time method. The linear system arising at each implicit time step is solved by a Generalised Conjugate Gradient method, using BILU factorisation as a preconditioner. An important feature of the code is the use of approximate Jacobian matrices for the left hand side of the linear system. The $k - \omega$ model is also implemented, although not used in the present work [1]. The code employs a structured, multi-block system. A deforming mesh algorithm is used to treat the simulation of moving geometry problems. This feature was specifically modified to facilitate moving spike configurations.

---

[1] An explanation of this choice will be given later, in section 2.4

2.4 Verification of the numerical method

The purpose of the verification is to ensure that the CFD results used for the validation and analysis are the correct solutions of the Navier-Stokes equations, i.e. they are independent of the quantitative parameters of the spatial and temporal discretisations. The spatial discretisation is tested in a grid dependence analysis whereas the temporal one in a real time step size dependence analysis. The parameter to be compared in these tests is the pressure history at the probe point. The length of the calculations was chosen to cover at least one properly developed cycle of the particular flow mode.

In the case of the hysteresis calculations, the tests were carried out for the minimum and maximum spike lengths only. It was assumed, that if these end-point cases of the hysteresis loop yield converged solutions, then any intermediate spike length should also.

Finally, all results presented were achieved by solving the Navier-Stokes equations, i.e. only laminar flow was assumed. This choice was supported by a number of arguments. First, the pulsation driving mechanism is expected to be inviscid in nature [18]. Hence, the simulation of this flow mode should be independent of the consideration of turbulence. Secondly, although the mechanism of the oscillation mode is expected to be viscous in nature [18], it is likely to be dominated by the shear layer's movement. As will be seen later, in Chapter 4.2, the shear layer will emanate almost always from the vicinity of the spike tip, where the boundary layer is most likely to be laminar. Thus, the shear layer should also be laminar at least in its upstream part [18]. Thirdly, the Reynolds' numbers considered in the present work appear to be middle range values, at which turbulence should not appear as a dominant feature. Thus, considering laminar simulations for the spiked body flows of the present study seem to be an acceptable approach.

2.4.1 Grid dependence tests

Three levels of grid density were considered in the grid dependence tests. A medium and a coarse grid were extracted from the original fine meshes (Table 2.2) by taking every second and every fourth point in each direction, respectively. Because of the different transients experienced on the various grid levels, the fine and the coarse grid histories were shifted along the time abscissa to allow easy comparison between the curves.

The results for the six test cases are shown in Fig.2.5 in terms of non-dimensionalised pressure $p[1]$ against non-dimensional time $t[1]$ (see section A.1.1 for the definition of the non-dimensional terms). It can be seen, that in the pulsation cases (Fig.2.5b,c,d) the three grid levels yield comparable time periods and pressure amplitudes. However, the coarse grids miss some important features, such as the existence of a pressure plateau (Fig.2.5b), the sharp pressure minima (Fig.2.5b,d) and secondary peaks on the ascending and descending parts of the curves (Fig.2.5c). The medium and the fine grid results show quite good similarity in these terms and thus the medium grids appear as sufficient for the further evaluations.

The pressure histories obtained on grid O1 (Fig.2.5a) exhibit a different situation. Firstly, the medium grid history settles to a periodic behaviour (beyond time t=60) after a substantial initial transient. Thus, only the last four cycles of this curve will be considered for the comparisons. The time periods of all three traces appear to agree well, whereas the pressure amplitudes on the coarse grid are much smaller than on the medium and fine grids. These latter ones exhibit similarities in the graph shapes as well (characterised by a double peak at the pressure maxima), and thus the medium grid can be selected for further analysis.

Similar conclusions can be drawn for the H1 grid (Fig.2.5e); the coarse grid underpredicts the pressure amplitude and the frequency whilst the medium grid again is sufficient for further use.

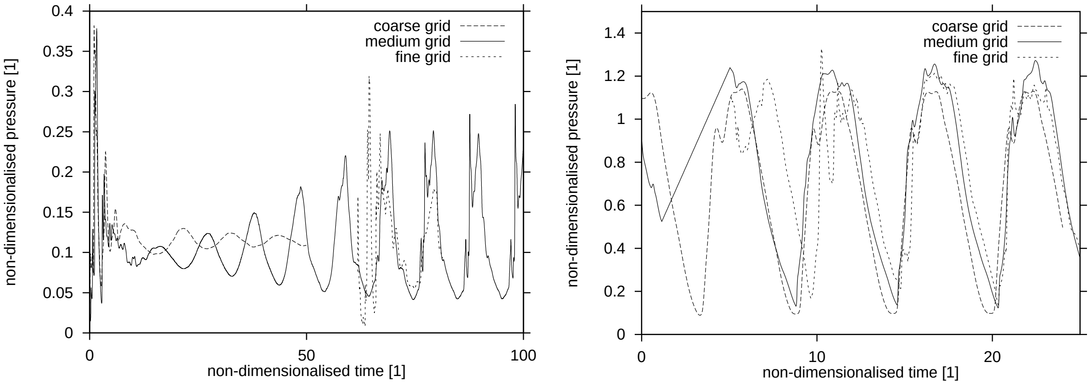

a) Grid O1 at Mach 6.00

d) Grid P2 at Mach 2.21

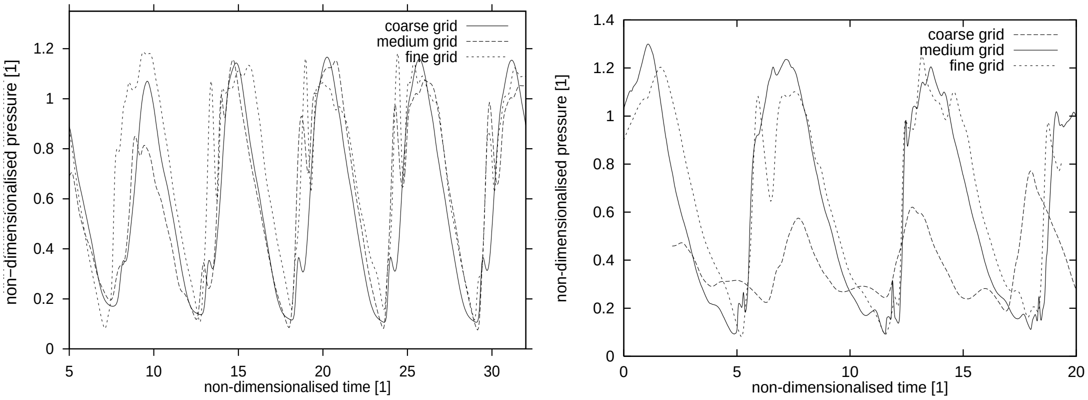

b) Grid P1 at Mach 2.21

e) Grid H1 at Mach 2.21

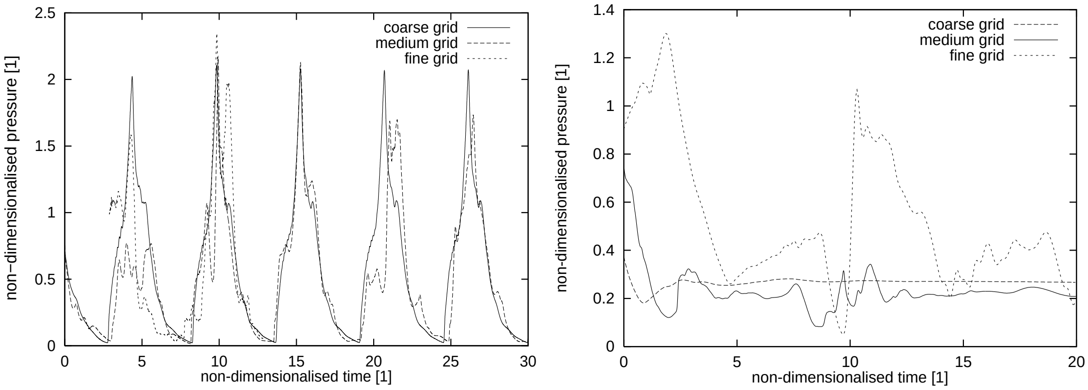

c) Grid P1 at Mach 6.00

f) Grid H2 at Mach 2.21

Figure 2.5: *Grid dependence test results.*

However, it should be noted that the H1 grid results should be examined in conjuction with the H2 grid ones, since these end-point grids will appear within one single deforming mesh calculation. Thus, the resolution of H1 and H2 are linked. The coarse grid for H2 predicts an almost steady flow (Fig.2.5f), the medium some small, irregular unsteadiness, whilst the fine one develops a clear unsteadiness characterised by pressure amplitudes of the order of unity. Hence, grid H2 results are grid dependent, which is most likely due to the large stretching of the cells in the region above the spike (blocks 3 and 6 in Fig.2.3). Thus, the formerly medium classified resolution at grid H1 becomes an effectively coarse resolution (in the longitudinal sense) at H2.

This problem could be avoided in two ways. The first is to use a finer grid for the entire simulation of the moving spike, which, however, would lead to unfeasibly costly calculations. The second option is to introduce a new deforming mesh technique, capable of dealing with very large grid stretchings. This would incorporate the addition of new gridlines during the calculation once a prescribed grid spacing is exceeded.

Since any successful CFD prediction of the hysteresis phenomenon would be a novel achievement in the field of spiked body flows, the present work will be restricted to only the qualitative prediction of the upper boundary of the hysteresis range by applying the medium grid for the entire range of the moving spike calculations. Thus, the lower boundary of this phenomenon (geometries in the vicinity of H1) are likely to be predicted correctly both qualitatively and quantitatively, whereas the upper boundary (geometries in the vicinity of H2) qualitatively only. It is believed, that these simulations can provide new and useful input into the investigation of hysteresis phenomenon.

2.4.2 Real time step size dependence tests

Initially, the maximum values of the non-dimensional real time step producing result on the medium grids were between 0.004-0.05, depending on the particular case. These values were decreased by factors of 5 and 10 to examine the effect on the results. The comparison for the various time steps is apparent from Fig.2.6. It can be seen that the smallest time steps have the general effect of shifting the curves slightly forward along the time abscissa. However, the displacement is not significant and hence the largest allowable time steps can be considered for further analyses. The only exception is for the H1 and H2 grids (Fig.2.6e,f), where the pressure amplitudes are reduced by using the largest time step size. Thus, in these two latter cases the middle time step (0.01) is used for the respective hysteresis simulations.

2.4.3 Summary

It has been shown via grid dependence and real time step size dependence tests, that the medium grid simulations achieved at the maximum allowable real time step can be used for further analyses. The only exception regards the hysteresis calculations (grids H1 and H2), where the use of a finer time step proved to be necessary. It is argued, that despite the grid dependent solutions in these cases, the medium grid will be used for the moving spike simulations. This should allow qualitatively and quantitatively correct solutions near the lower boundary of the hysteresis range, and only a qualitatively correct one at the upper boundary.

Regarding the runtimes on medium grids, the Mach 2.21 calculations required typically 5-7 days on a Pentium Pro 200 MHz processor. The Mach 6.00 pulsation, performed on a less dense grid, needed only 2 days, while the longest computation of all, the Mach 6.00 oscillation case, required 20 days.

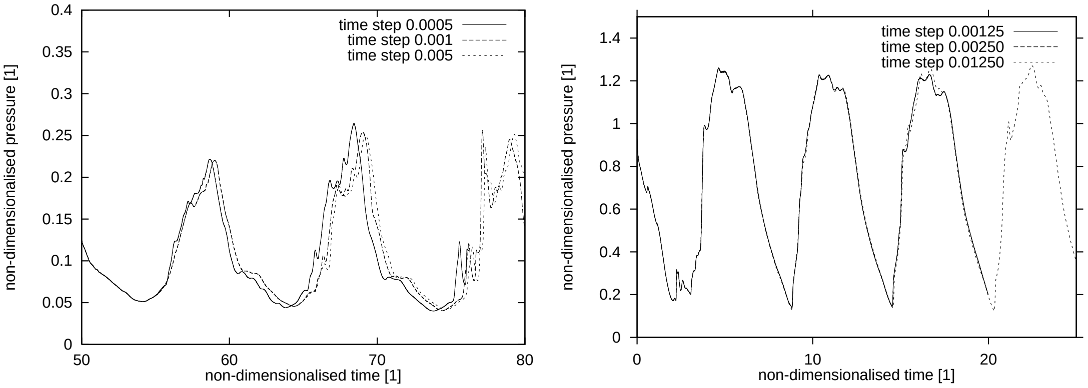

a) Grid O1 at Mach 6.00

d) Grid P2 at Mach 2.21

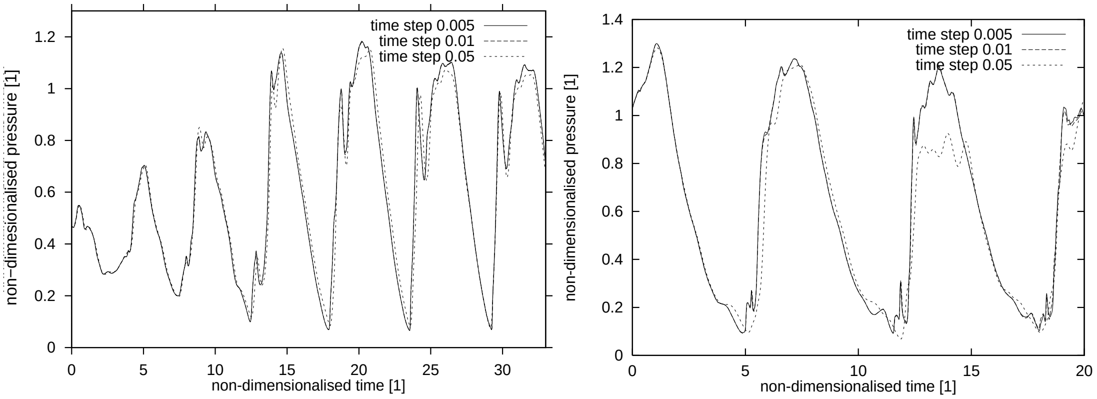

b) Grid P1 at Mach 2.21

e) Grid H1 at Mach 2.21

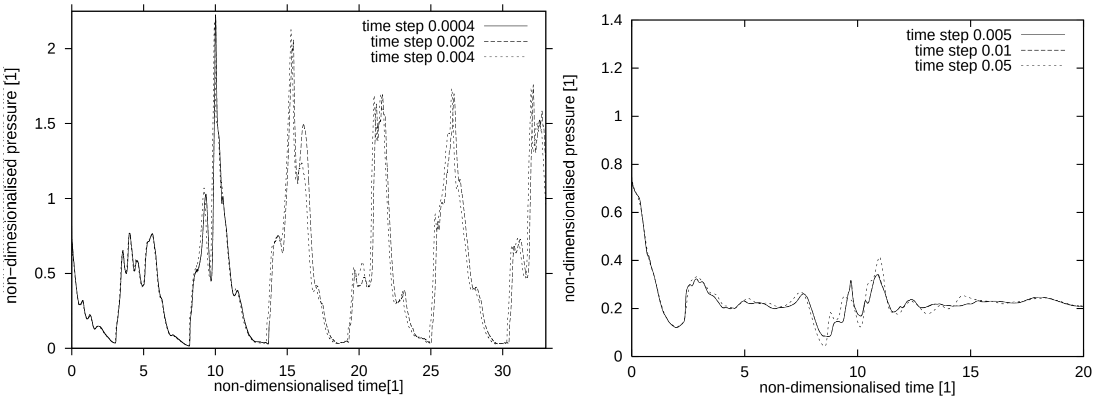

c) Grid P1 at Mach 6.00

f) Grid H2 at Mach 2.21

Figure 2.6: *Real time step size dependence test results.*

Chapter 3

Results validation

Comparison of the numerical and experimental results will be provided in the present chapter. First, the fixed spike length cases will be examined in terms of pressure amplitude, Strouhal number, characteristic shape of the pressure trace and the shock envelope history. Then, the moving spike length results will be evaluated in terms of the resultant hysteresis range.

3.1 Fixed spike length configurations

3.1.1 Data reduction

Since the experimental results for the pressure amplitudes and the frequencies are presented in time averaged form in the reference work [18], the numerical pressure histories will also be reduced via this technique. The use of time-averaging in the experiment was necessitated by the irregular cycles of the pressure traces.

For the frequency, the time-averaging has been done by measuring the time required for a known number of cycles and dividing this time by the number of cycles:

$$T = \frac{\sum\limits_{i=1}^{N} T_i^*}{N} \tag{3.1}$$

Then, using this value, the Strouhal number of the event can be determined as:

$$S = \frac{f \cdot D}{u_\infty} = \frac{D}{T \cdot u_\infty} \tag{3.2}$$

Since both the blunt body diameter (D) and the freestream velocity (u_∞) are non-dimensionalised in the numerical method, the Strouhal number from the CFD results can be obtained directly as:

$$S = \frac{1}{T} \tag{3.3}$$

The amplitudes, on the other hand, were processed by measuring the vertical distance from the first discernible trough to the adjacent peak, then the vertical distance from the peak to the next trough and so on as illustrated in Fig. 3.1. These distances were summed and divided by the total number of measurements to obtain the mean value of the amplitude:

$$\Delta p = \frac{\sum\limits_{i=1}^{N} \Delta p_i^*}{N} \tag{3.4}$$

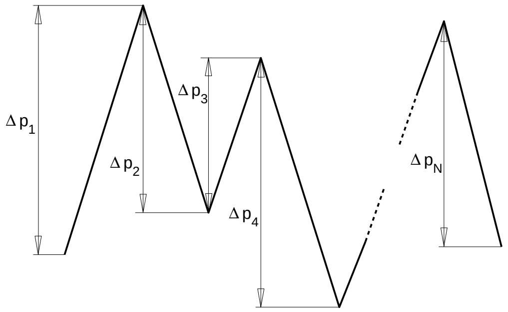

Figure 3.1: *Time-averaging data reduction.*

3.1.2 Qualitative comparison

Although the subsequent cycles were not repeated identically in the experiment, a general characteristic cycle shape could be recognised for each configuration. Thus, a cycle representative of this characteristic shape will also be provided in the pressure traces to enable qualitative comparison.

Furthermore, a set of shadowgraphs depicting the oscillation/pulsation cycle was also available for the Mach 6.00 experiment [18]. Numerically obtained flow visualisation frames will be correlated with these photographs to enable comprehensive validation of the CFD results. It has to be noted, however, that each of the photographs was taken from different cycles, since the frequency of the photographic equipment was not capable of matching the frequency of the unsteady events. The time of taking the photographs was recorded on a sample pressure history and using this information a typical sequence within a cycle was constructed [18]. CFD, on the other hand, allowed flow visualisation frames to be obtained within one particular cycle, which feature was utilised in the present work.

3.1.3 Oscillation at Mach 6.00

The oscillation mode developed at this freestream was preceeded by a quite long initial transient (time 0-60 in Fig. 3.2). Therefore, only the last 4 cycles were considered for the time-averaging process, which, along with a representative cycle from the experiment, is shown in Fig. 3.3.

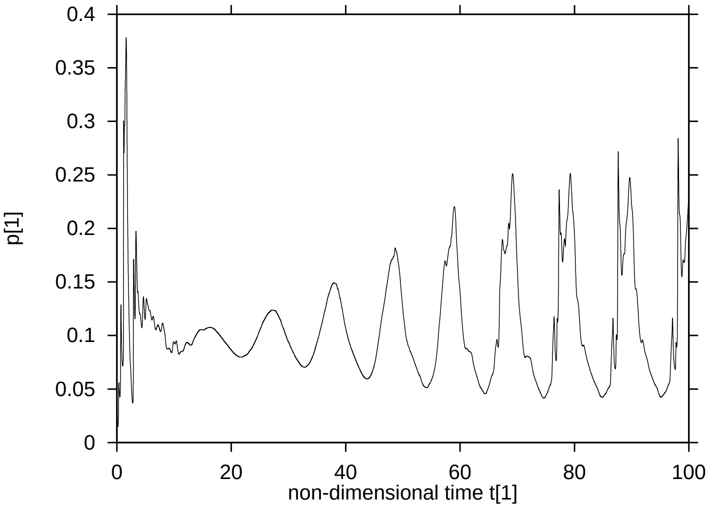

Figure 3.2: *The entire pressure history at the cylinder face (d=D/2) for the Mach 6.00 oscillation case (L/D=2.00).*

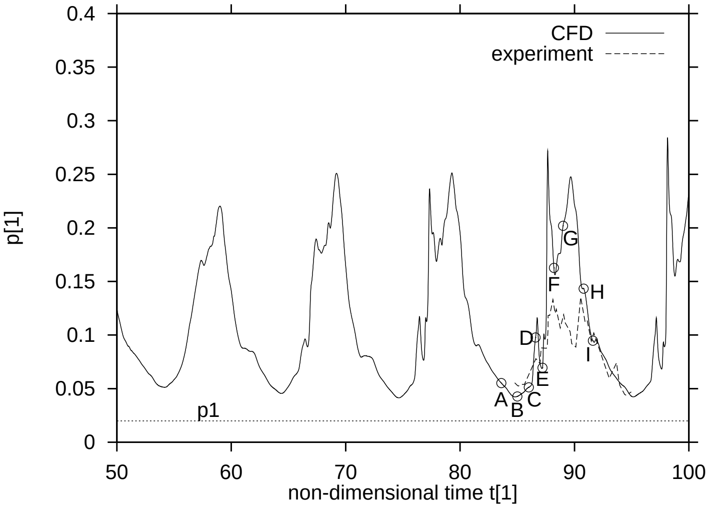

Figure 3.3: *Detail of the pressure history at the cylinder face (d=D/2) for the Mach 6.00 oscillation case (L/D=2.00). The non-dimensional value of* p_{t2} *is 0.9288 [1].*

Table 3.1: Comparison of time averaged characteristics, oscillation at Mach 6.00 freestream (L/D = 2.00).

	experiment [18]	CFD
Δp [1]	0.0745	0.2693
S [1]	0.1079	0.0983

It can be seen from this graph and also from Table 3.1, that although the pressure amplitude of the event is overpredicted by the simulation, it can be still found of the order of 0.1, which is typical of oscillation. The Strouhal numbers, on the other hand, appear to be in good agreement with the measured data. The characteristic feature of the pressure trace, the existence of a double peak, was also picked up by the CFD simulation. The magnitude of the discrepancy between the pressure amplitudes may question the validity of the numerical results. However, as recently revealed by Kenworthy [36], because of the possible errors in the experiment, the amplitude of the pressure fluctuations should be treated more qualitatively than quantitatively. This was argued by the fact, that in the experiment the pressure transducers were held in a cavity, which was likely to cause resonance and amplitude modification. Thus, the correct prediction of the Strouhal numbers and capturing the characte-

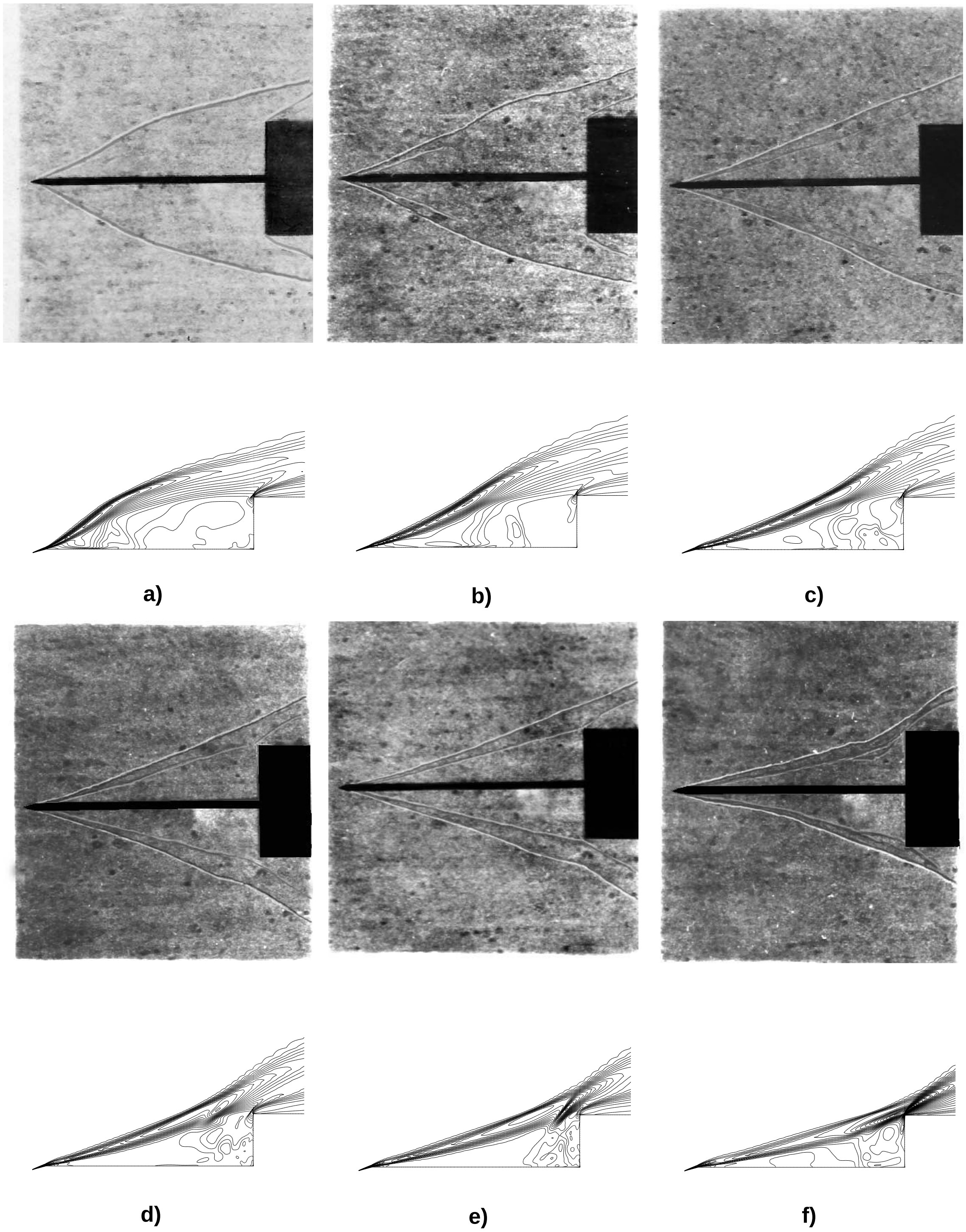

Figure 3.4: *Comparison of the shadowgraphs [18] and the density contour plots for the oscillation at the Mach 6.00 freestream (L/D=2.00).*

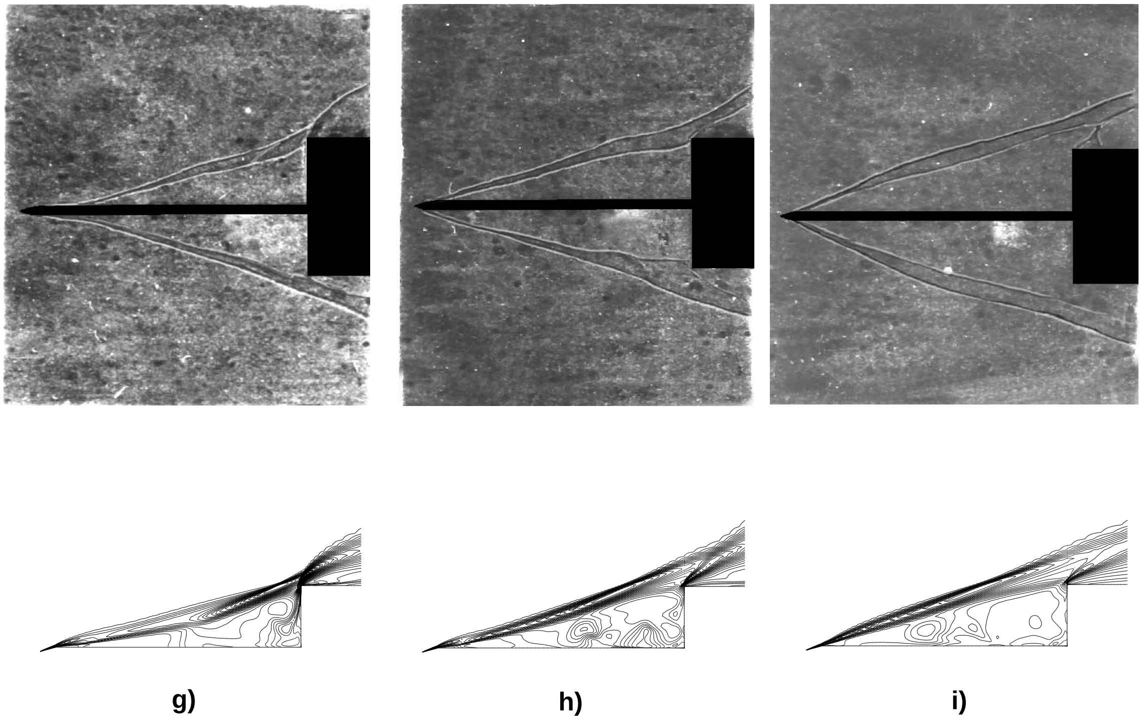

Figure 3.4: *(cont.) Comparison of the shadowraphs [18] and the density contour plots for the oscillation at the Mach 6.00 freestream (L/D=2.00).*

ristic shape of the pressure trace will appear to be far more important than the agreement of the amplitudes. Another factor contributing to the disagreement could be the difficulty of maintaining the axisymmetry at this long spike length in the experiment. These arguments are further substantiated by comparing the experimental and the numerical shock envelope histories (Fig. 3.4), showing good agreement.

Note, that the CFD results are presented in terms of density isolines, since these offer the best comparison to the density gradients captured on the shadowgraphs. The time positioning of the CFD frames is illustrated in the pressure trace shown in Fig. 3.3.

As it is evident from these figures, the numerically obtained shock envelopes are in very good agreement with the experimental ones, indicating, that the CFD prediction appears to be indeed well representative.

3.1.4 Pulsation at Mach 2.21

Results obtained on the P2 grid are considered. The pressure history for this case is shown in Fig. 3.5, and the evaluation of the time-averaged characteristics, considering the last three cycles only, is provided in Table 3.2. It can be seen from these results, that both the pressure amplitude and the frequency of the event are well predicted by the numerical method. Also, the characteristic shape of the pressure trace, featuring a pressure plateau, compares well with the measured one.

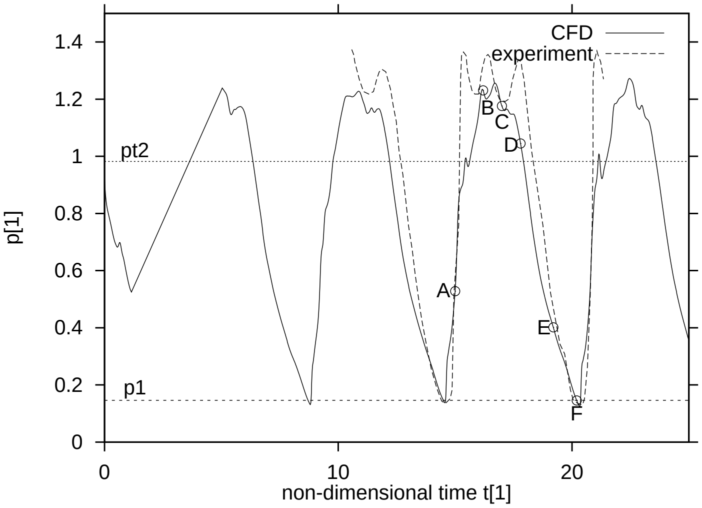

Figure 3.5: *Pressure history at the cylinder face (d=D/2) for the Mach 2.21 pulsation case (L/D=1.00).*

Table 3.2: Comparison of time averaged characteristics, pulsation at Mach 2.21 freestream (L/D = 1.00).

	experiment [18]	CFD
Δp [1]	1.1909	1.1136
S [1]	0.1725	0.1727

A set of selected frames (the time-positioning is shown in Fig. 3.5) also exhibits the typical pulsation features (Fig. 3.6). These are the inflation of the foreshock to a bow wave and its consequent downstream convection along the full length of the spike. A comparison with the shadowgraphs is not available in this case.

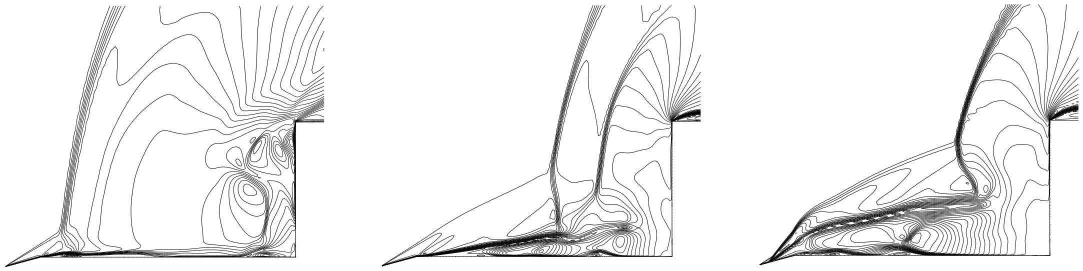

a) point A

b) point B

c) point C

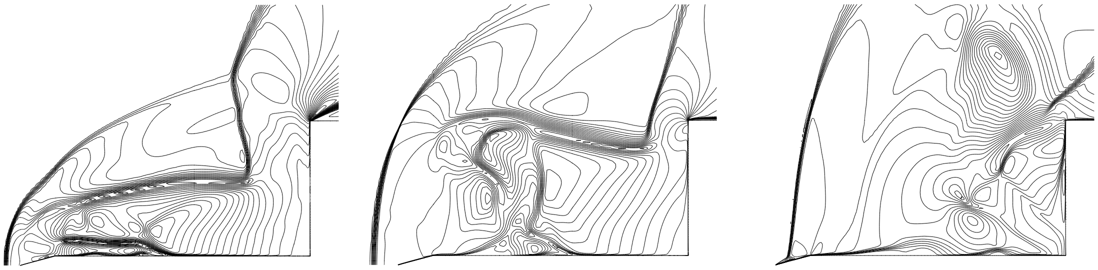

d) point D

e) point E

f) point F

Figure 3.6: *Pulsation at the Mach 2.21 freestream. Mach isolines for the frames selected from Fig. 3.5.*

3.1.5 Pulsation at Mach 6.00

The pressure history shown in Fig. 3.7 indicates, that the first three cycles can be considered as the initial transient, and were therefore excluded from the time-averaging. The results of this evaluation are shown in Fig. 3.3. It can be seen, that the pressure amplitudes are once again overpredicted by the numerical method, whereas the Strouhal number agrees very well with the experiment. Also, the shape of the pressure trace seems to feature the typical characteristic of the pulsation at this freestream, i.e. a sharp peak instead of the pressure plateau seen in the Mach 2.21 case.

Table 3.3: Comparison of time averaged characteristics, pulsation at Mach 6.00 freestream (L/D = 1.00).

	experiment [18]	CFD
Δp [1]	1.0378	1.6768
S [1]	0.1722	0.1800

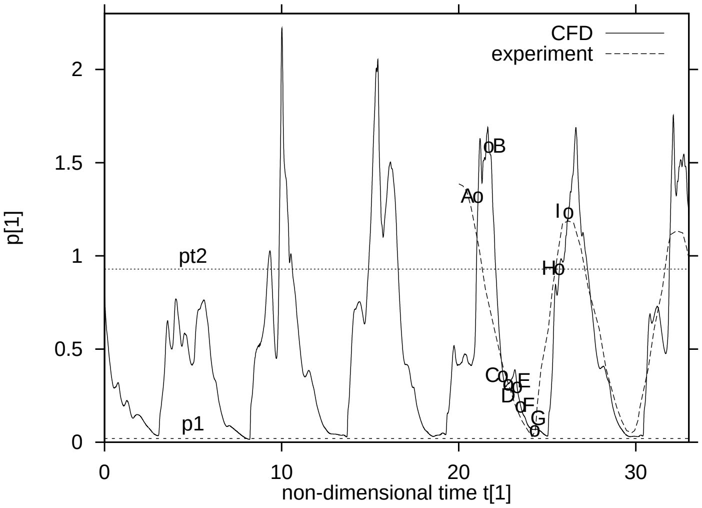

Figure 3.7: *Pressure history at the cylinder face (d=D/2) for the Mach 6.00 pulsation case (L/D=1.00).*

The comparison of the experimental and numerical shock envelope histories (Fig. 3.8) show an excellent agreement between the two sets of results, indicating that despite the discrepancy in the pressure amplitudes (for which the same argument would be true as for the Mach 6.00 oscillation case) the CFD predictions are realistic.

Finally, a comment on the point-timing of the shadowgraphs is now made. It was observed, that in the experiment the minimum pressure was recorded when the collapsing shock passed the half-spike length (Fig. 3.8h), whereas computation predicts this to happen slightly earlier, approximately at the quarter spike length. Also, the experiment reports the pressure maximum at the time instant when the separation point reaches the spike tip (Fig. 3.8c), while the computational results show this to happen earlier. Since the above processes take place very rapidly (the pulsation frequency at the Mach 6.00 freestream is around 7,600 Hz), the above deviations in timing could be caused by errors due to the complexity of synchronisation in the experiment.

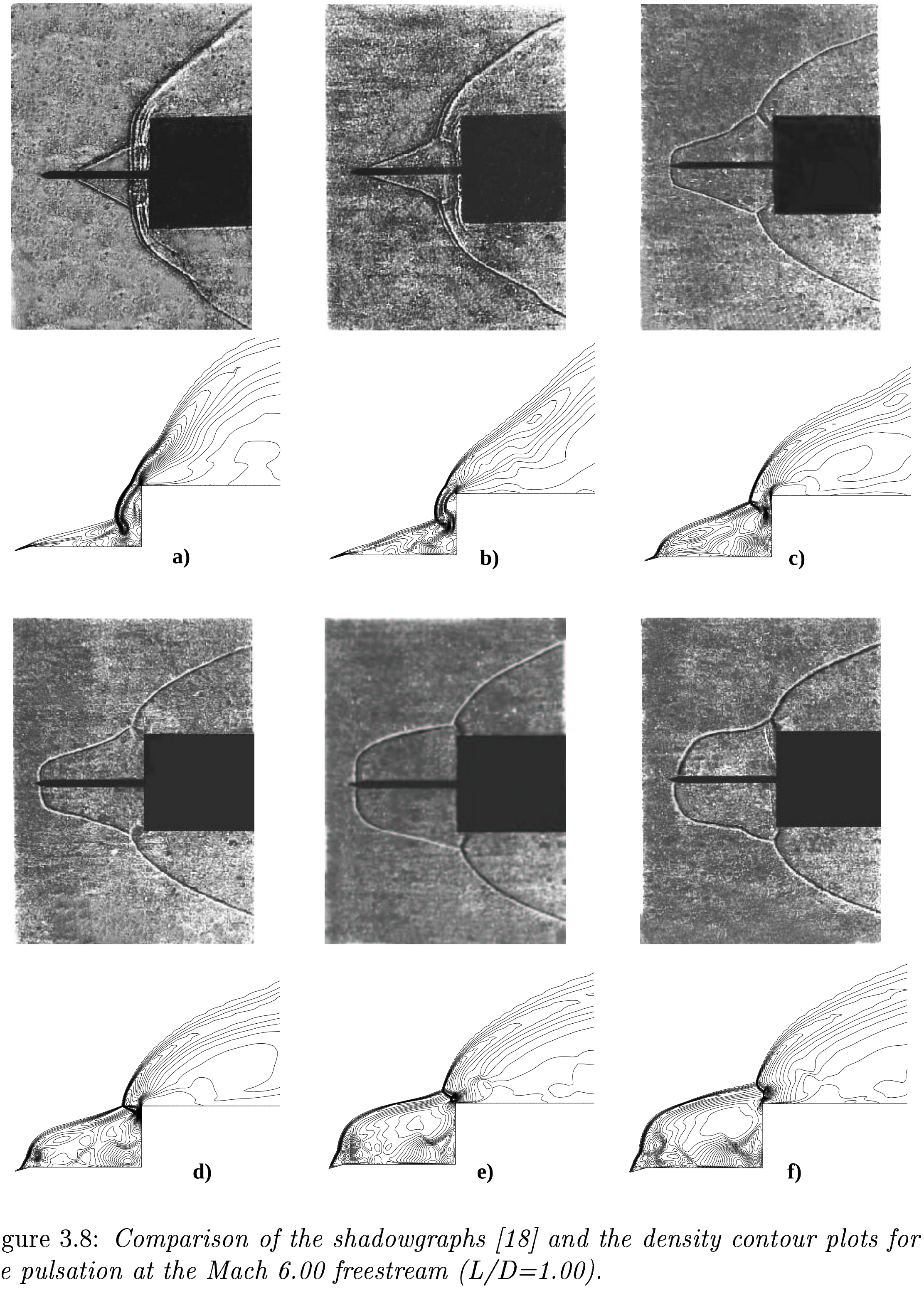

Figure 3.8: *Comparison of the shadowgraphs [18] and the density contour plots for the pulsation at the Mach 6.00 freestream (L/D=1.00).*

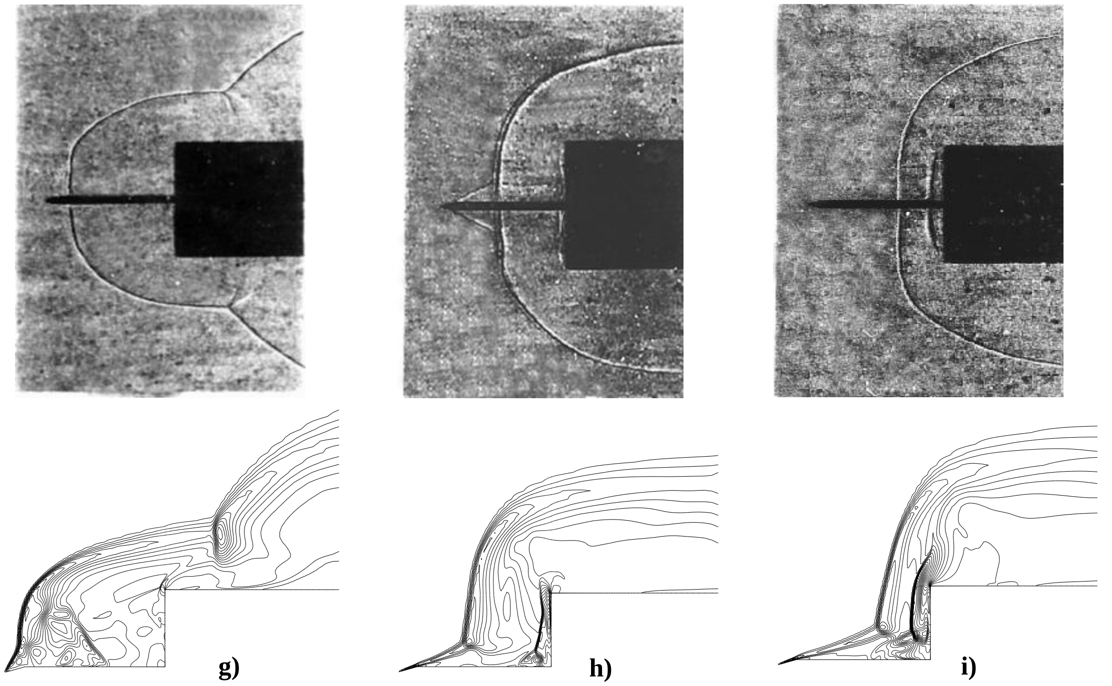

Figure 3.8: *(cont.) Comparison of the shadowgraphs [18] and the density contour plots for the pulsation at the Mach 6.00 freestream (L/D=1.00).*

3.1.6 Summary

It has been shown by comparing the numerical and the experimental results that the fixed spike length results agreed well with the measurements. The frequency of the event, the characteristic shape of the pressure trace and the shock envelope histories were found in excellent agreement, whereas the pressure amplitudes appeared to be overpredicted in the Mach 6.00 cases. However, it was argued that due to the possible errors in the pressure measurement admitted by the experiment, the correct prediction of the frequency of the event should be treated as far more important than the agreement of the amplitudes. Thus, the CFD results will be considered as valid simulations of the examined flows, and are judged as suited for further analyis.

3.2 Continuously changing spike length configurations

3.2.1 The experimental results

The results for the hysteresis phenomenon are usually expressed in graphs of pressure amplitude versus spike length. Such experimental results were reproduced in Fig. 3.9 for the test case to be considered in the numerical simulations (Tab. 2.1). The graph was obtained at the continuous retraction of the spike with a speed of $v_{sp} = 10$[mm/s] [18]. (Note, that the pressure amplitudes are expressed in time averaged sense.)

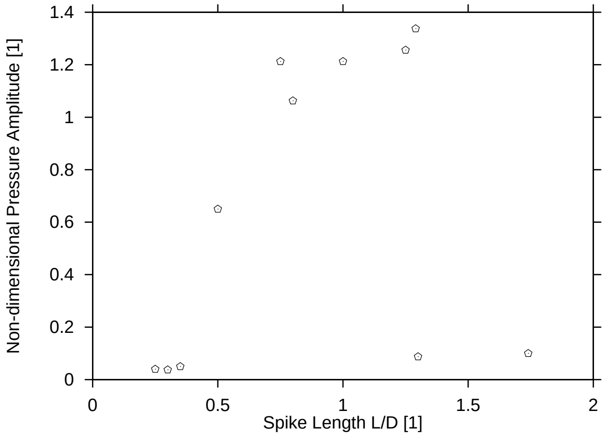

Figure 3.9: *Experimental time averaged non-dimensional pressure amplitudes plotted against spike length at continuous inward motion of the spike with the speed of* $v_{sp}{}^{*}$*=10[mm/s]. Spiked cylinder at freestream Mach number of 2.21. (Ref.[18]).*

It can be seen from this graph, that the oscillation mode, characterised by pressure amplitudes of the order of 0.1, changes abruptly to the pulsation mode at around L/D = 1.29, displayed by amplitudes of order 1.0. This is basically half of the hysteresis loop, corresponding to the inward motion of the spike. Unfortunately, there is no such graph available from the experiment for the outward moving part. It is mentioned only that the reverse change occurred at an approximately 10-15 % larger spike length than above [18]. This would correspond to an L/D around $1.42 \sim 1.48$. In order to assess this value more precisely, comparison with another experiment is made.

Calarese and Hankey [25], although using a different model geometry but comparable flow conditions ($M = 3.0, Re_D = 0.39 \times 10^6$), did record the pressures for the outward motion of the spike as well. They found the upper boundary of the hysteresis range (P/O transition), to be 19% larger than at the inward motion (see Fig. 1.14). This suggests, that the 15% spike length range from Kenworthy's measurement is a more likely value for the particular configuration, and hence in the following the value of $L/D = 1.48$ will be referred to as the experimental P/O boundary of the hysteresis phenomenon.

The two end-points of the numerical hysteresis loop (see Table 2.1) were selected on the basis of this information. The minimum spike length, $L/D_{min} = 1.25$, lies just below the experimental value 1.29. The maximum one, $L/D_{max} = 2.40$, however, is well beyond the corresponding parameter from the measurement, 1.48. This choice was made following the resulting larger range of hysteresis in preliminary CFD simulations. An explanation for this might be connected with the imposed axial symmetry for the calculations, at which the pulsation can be maintained longer than in the experiment.

3.2.2 Spike speeds

The choice of the spike speed in the numerical method is important. First, it is difficult to perform the same number of cycles as in the experiment during a desired spike length change. Given the 10[mm/s] spike speed in the experiment and the 2000[Hz] frequency of the pulsation mode (the model diameter was D^*=46[mm] in the experiment), there should be a total of 10,000 cycles performed for a spike length change between L/D=1.25 and 2.40. This would lead to a very long computation. Therefore a much faster motion of the spike needs to be imposed in the numerical simulation.

Secondly, the movement of the spike in the measurement appears to be quasi-steady when related to the flow unsteadiness. Only this important property has to be maintained in the numerical method to get a valid simulation of the experiment. In fact, it is suggested that the maximum spike speed, at which the transition and the hysteresis effect occur as a quasi-steady phenomenon is much higher than the one used in the measurements. The choice of this speed is believed not to be based on the criterion of quasi-steadiness, but rather on the limitations of the experimental equipment.

Therefore, two spike speeds will be considered and tested in the numerical method. The values are selected as 0.008 and 0.004, which are expressed as

$$v_{sp} = \frac{\Delta(L/D)}{t}.$$

Here $\Delta(L/D)$ represents the dimensionless spike length change (1.15 in the present case) and t the non-dimensional real time used by the numerical method. Expressing the experimental 10[mm/s] spike speed in these terms gives $v_{sp,exp}$=0.00001903, which means that the spike's movement is approximately 400 and 200 times faster, respectively, in the simulation than in the experiment.

3.2.3 Initial conditions

The hysteresis calculations were initiated from the flow modes occurring at the end points of the hysteresis range.

Pulsation at L/D=1.25. The outward motion is started from a pulsating flow occurring at $L/D = 1.25$. This flow mode was generated by performing an unsteady calculation on the corresponding fixed spike length, allowing 3 cycles of pulsation to develop. The pressure history corresponds to the medium grid curve in Fig. 2.5e. The dominant pressure amplitude and the Strouhal number (which is expressed as the reciprocal value of the time period) compared to the experiment shows excellent agreement (see Tab.3.4).

Table 3.4: Comparison of time averaged characteristics, pulsation at Mach 2.21 freestream (L/D = 1.25).

	experiment [18]	CFD
Δp [1]	1.25	1.20
S [1]	0.150	0.143

Oscillation at L/D=2.05. In order to decrease the computational cost, the inward moving spike calculations are initiated from a solution at L/D=2.05. This was the shortest spike length at which oscillation could be obtained from a calculation involving a fixed spike. The pressure history is shown in Fig.3.10. Unfortunately, there are no values available from the experiment for this case, but the trend of the time averaged pressure amplitudes in Fig.3.9 allows us to deduce that the value should remain of order 0.1, which would be in good agreement with the numerical results.

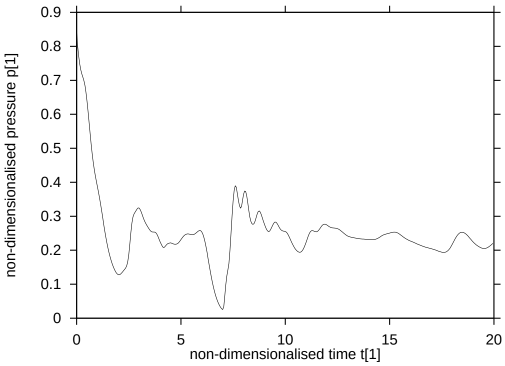

Figure 3.10: *Pressure history at the probe point for an L/D=2.05 spiked cylinder at Mach 2.21.*

3.2.4 Hysteresis loop at $v_{sp} = 0.008$

The pressure histories (plotted against the spike length) are shown in Fig.3.11 for the inward and the outward motion, respectively.

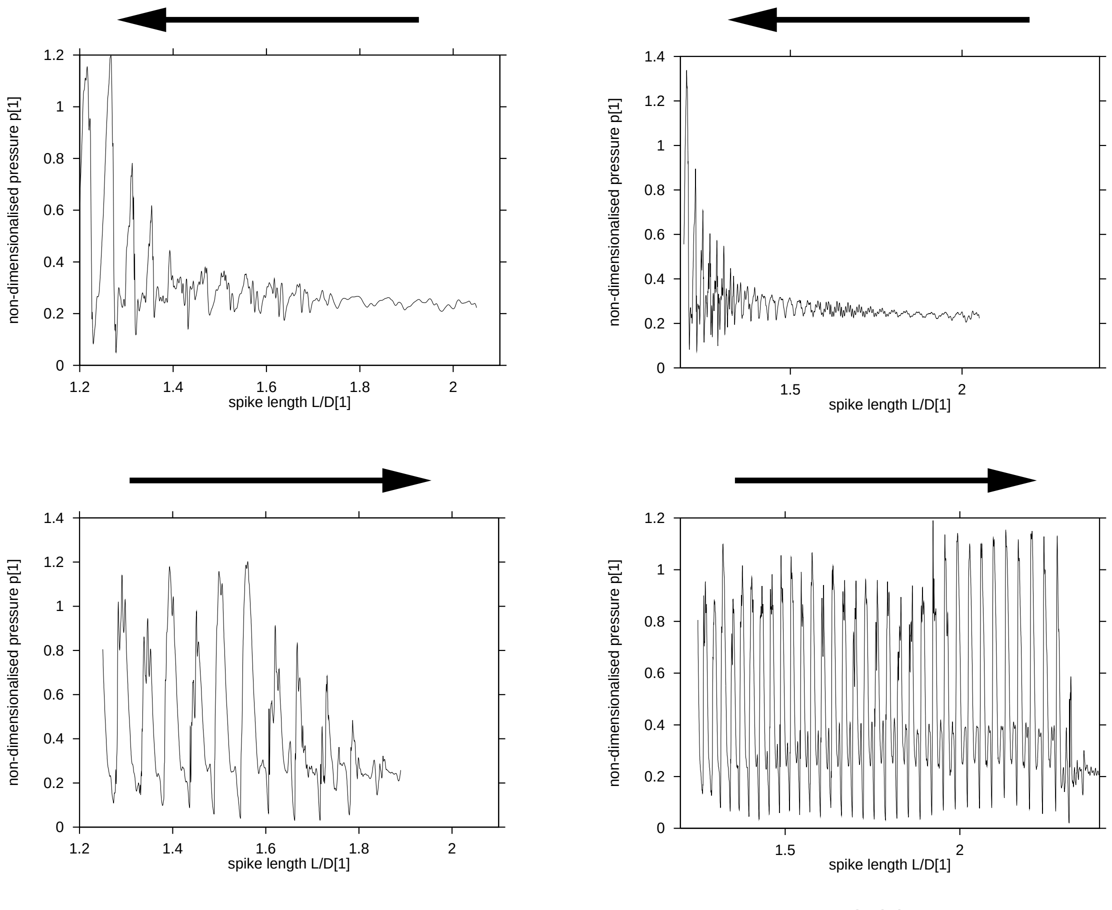

$v_{SP} = 0.008$ $v_{SP} = 0.004$

Figure 3.11: *Hysteresis effect shown by the pressure histories at the probe point for two different spike speeds.*

The inward motion was initiated from the oscillation solution at L/D=2.05 and it can be seen that this regime is clearly maintained for the spike lengths between 2.05 and 1.43. Then, three transitional cycles follow, apparently as a consequence of the excitation started at L/D=1.70. The first one could be characterised as a very irregular cycle, with an obvious disturbance to the previously regular time periods. The frequency of the peak values becomes again regular afterwards. The first properly developed pulsation cycle starts at L/D=1.27, and the amplitude of this cycle is found to be in excellent agreement with the experiment (Fig.3.9). The O/P boundary, defined by the first properly developed pulsation cycle in the present work, could be determined therefore as L/D=1.27, which is also in excellent agreement with the experimental value of L/D=1.29.

The outward motion, started from the pulsation solution for L/D=1.25, shows this flow mode to be preserved up to L/D=1.60 as the spike length is increased. This is a clear display of the hysteresis phenomenon - two different flow modes could be obtained for the same spike length, depending on the direction of approach. At L/D=1.60 four transitional cycles follow, gradually decreasing the amplitude from 1.2 to 0.1. The P/O boundary defined by the first properly developed oscillation cycle (i.e with the first amplitude in the order of 0.1) appears at L/D=1.83. This means, that the upper boundary of the hysteresis range is overpredicted by the numerical approach.

3.2.5 Hysteresis loop at $v_{sp} = 0.004$

This case was initiated from the same initial conditions as above. The pressure history results are shown in Fig.3.11, clearly displaying the hysteresis phenomenon again. However, the range of the dual flow mode region is much larger this time.

The inward motion history displays the O/P boundary to occur at a slightly smaller spike length than before. The first properly developed pulsation cycle could be identified at L/D=1.20, which still agrees well with the experiment (L/D=1.29). The number of transitional cycles is 6 in this case, double of that observed earlier. The first one shows similarity to the above described “irregular” cycle, but appears later, at L/D=1.33 (previously 1.43).

The outward motion history represents more dramatic changes than its faster spike speed counterpart. Firstly, the O/P boundary occurs much later, at L/D=2.29 (to be discussed later, in a section on the P/O transition) and secondly, it happens abruptly, through a single transitional cycle only (there were four transitional cycles in the earlier case). Furthermore, it appears that there are some secondary harmonic waves present at the cycles’ declining portions, which are gradually amplified in time.

A detail of the last few cycles, plotted against the time instead of the spike length, is provided in Fig.4.42. Note, that the time periods are almost doubled in comparison with the short spike lengths (see for example Fig. 2.5e), which indicates, that the speed of the shock wave collapse/growth remains unchanged regardless of the spike length.

3.2.6 Summary

The hysteresis phenomenon occurring over a spiked cylinder exposed to Mach 2.21 freestream was simulated at two spike speeds. On both occasions, the hysteresis phenomenon was predicted qualitatively. The lower boundary of the hysteresis range (O/P boundary) was found to be in good agreement with the measured data. However, the upper limit of the hysteresis range (P/O boundary) was overpredicted by the numerical method at both spike speeds. Note that these results are not grid independent near the upper (P/O) boundary. An even larger hysteresis range is likely to be obtained if grid convergent solutions could be ensured at very long spike lengths. Regarding the effect of the spike speed, it appears that applying a faster spike decreases the hysteresis range, although a definitive conclusion on this should be drawn only after understanding the driving mechanisms of spiked body flows.

Nevertheless, as the slower, $v_{sp} = 0.004$, spike speed results seem to represent a quasi-steady spike movement better, these results will be used for the further analysis of the hysteresis phenomenon.

Chapter 4

Theoretical analysis and discussion

4.1 Analysis method and flow visualisation

The high complexity of the flowfield associated with the oscillation and pulsation modes necessitates the use of a detailed approach in the analysis of the driving mechanism. This means, that if all the elements of the mechanism are to be revealed, then one might question whether in past analyses there have been sufficient data available for this purpose. A typical number of frames per cycle from experiments is around 10 [18] [23] [25]. In Kenworthy's work [18], which serves as a comparison for the present study, the frames were obtained from different cycles because the photographic equipment was not capable of matching the high frequency of the flow modes, which ranges between 1000-7500 Hz, depending on the particular configuration. In this latter work, the snapshots taken from the subsequent cycles had been re-arranged to produce a so called 'typical' cycle. However, as it has been seen in the previous chapter, the measured pressure histories, which are related to the shock envelopes, were not repeatedly identical. This means that some important details of the flowfield might have been overlooked in past studies.

All these facts lead to the conclusion, that for the purpose of analysing the oscillation and pulsation driving mechanisms, the number of frames per cycle must be substantially larger than 10 and also that frames should preferably originate from the same cycle. Thirty frames for each case have been extracted from the CFD simulations for the analysis of the mechanisms. These are shown in Fig. 4.2 for the oscillation and in Figs. 4.12 and 4.31 for the pulsation flow modes, respectively.

Three different types of flow visualisation are presented simultaneously: the pressure isolines, enabling the identification of the presence of shock waves and vortices in the flowfield; the Mach number isolines, which can reveal shear layers and boundary layer separations; and an array of 7 (10 in the case of pulsation), instantaneous streamlines, which also represent the local instantaneous flow path directions, and which are shown superimposed on the Mach contour plots. Extra streamlines are introduced in the flowfield when this is useful to explain interesting phenomena. Detailed vector plots will also be used where necessary. It is sometimes difficult to identify the streamlines, but the animations given in the enclosed CD-ROM (see Appendix B) help in the interpretation of the flow.

4.2 The oscillation mode

4.2.1 The shock envelope history

A sequence of 28 frames, covering an entire cycle of oscillation is shown in Fig. 4.2. The non-dimensional time difference between each of the frames is $\Delta t = 0.4[1]$ and the times shown are as indicated on the pressure history plot recorded at the probe point (Fig. 4.1), which was located at the $D/2$ diameter on the cylinder face.

Note, that this choice of the pressure trace was made since it provides a link with the experiment, in which this was the position where the sole pressure measurement was taken. This, as will be seen later, is not necessarily the best position to characterise the oscillation behaviour. The numerical analysis, in contrast to the experimental data, can provide pressures at all points on the surface as well as in the flow field. This feature will be used extensively in the analysis of the oscillation flow mode.

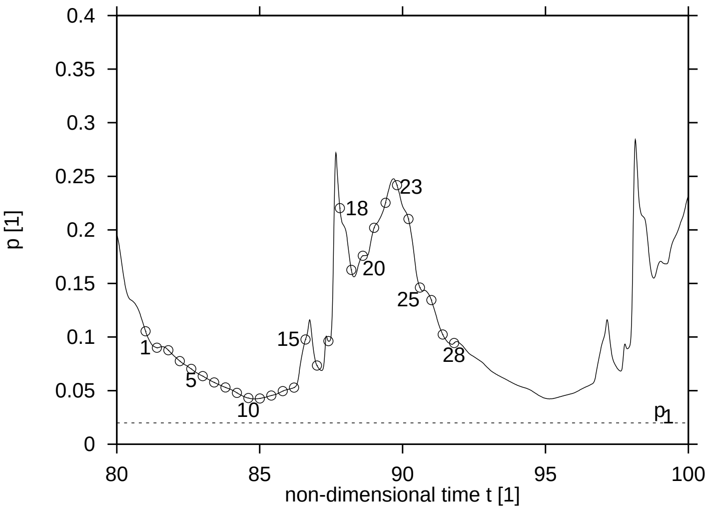

Figure 4.1: *Detail of the pressure history at the cylinder face (d=D/2) for the Mach 6.00 oscillation case.*

Based on the frame sequence in Fig. 4.2, a description of an oscillation cycle can be constructed. However, before doing so it has to be noted, that the examined unsteady flow is not liable to quasi-steady analysis. According to East and Wilkinson [38], unsteady flows occurring over forward facing steps and possessing a Strouhal number ($S = \frac{fD}{u_\infty}$) larger than 0.01 are not amenable to quasi-steady analysis. It has beeen seen in Chapter 3, that the Strouhal number of the considered oscillation flow mode is an order of magnitude larger and therefore strict attention need to be paid to the dynamics of the event. It will be seen soon, that the dynamics of the oscillation will indeed play its part in the analysis.

Starting with frames 1 and 2, the separation point has nearly reached its most upstream position as it is pushed forward by an upstream moving pressure gradient (evident from the pressure plots). All of the introduced streamlines appear to be positioned at their highest point over the afterbody shoulder, which implies that no flow originating from the freestream is reversed into the separation zone. The time delay of the particles in the streamlines is comparable to those in the freestream. These travel the length of the spike during $(L/D) \times S$ portion of the cycle, i.e. it

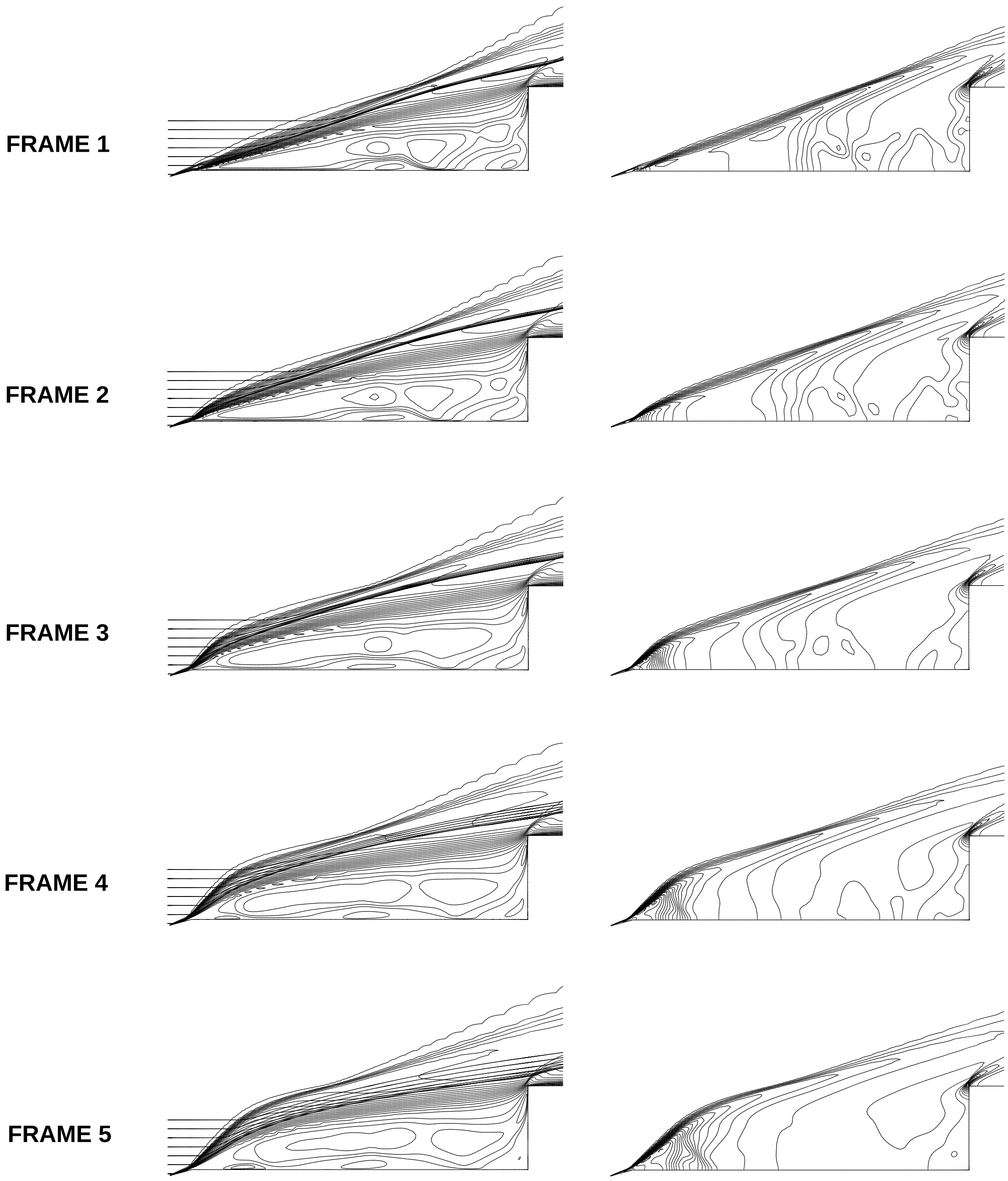

Figure 4.2: *Oscillation at Mach 6.00, L/D=2.00. Shown are the Mach isolines superimposed with instantaneous streamlines (left column) and the pressure isolines (right column).*

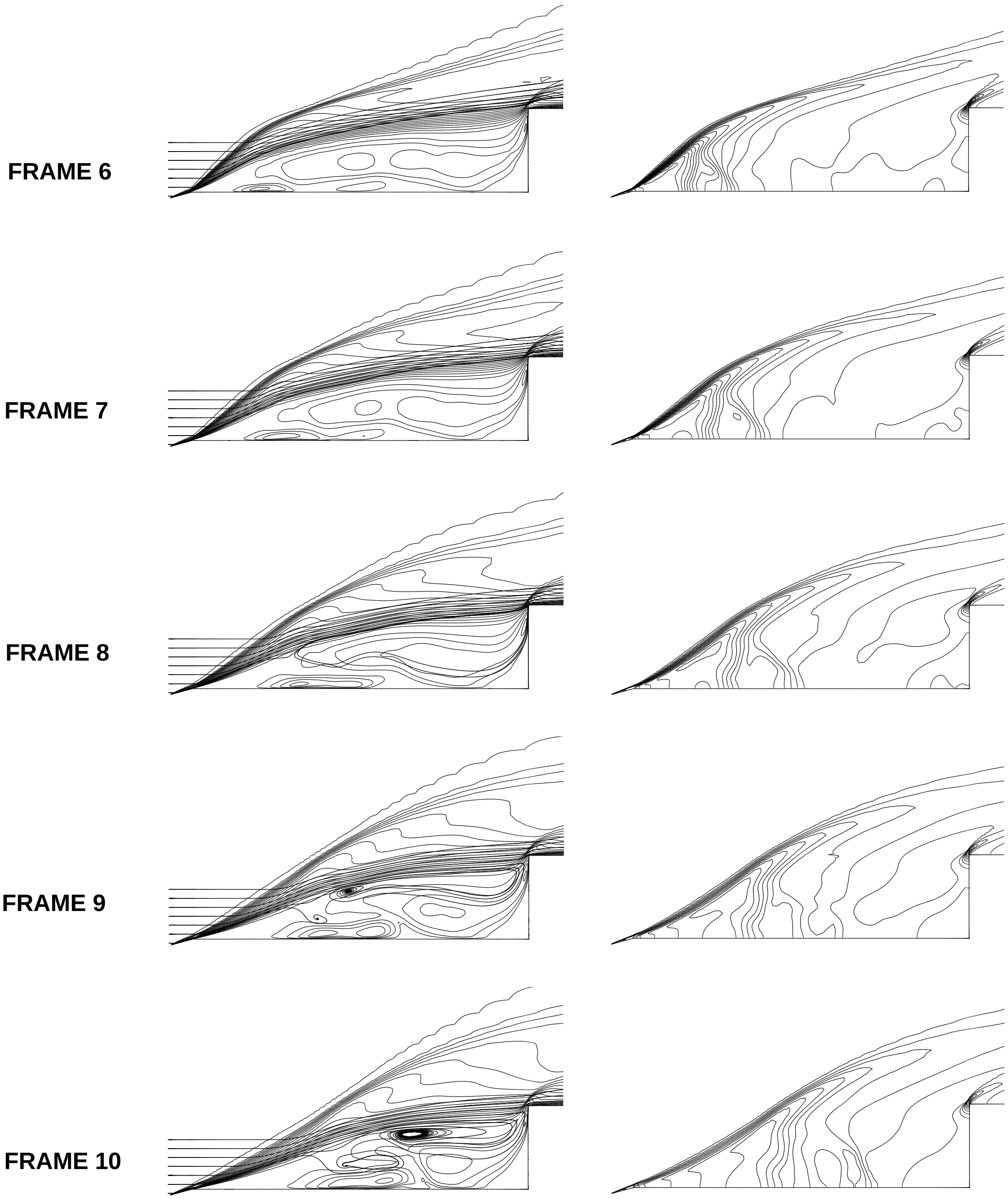

Figure 4.2: *(cont.) Oscillation at Mach 6.00, L/D=2.00. Shown are the Mach isolines superimposed with instantaneous streamlines (left column) and the pressure isolines (right column).*

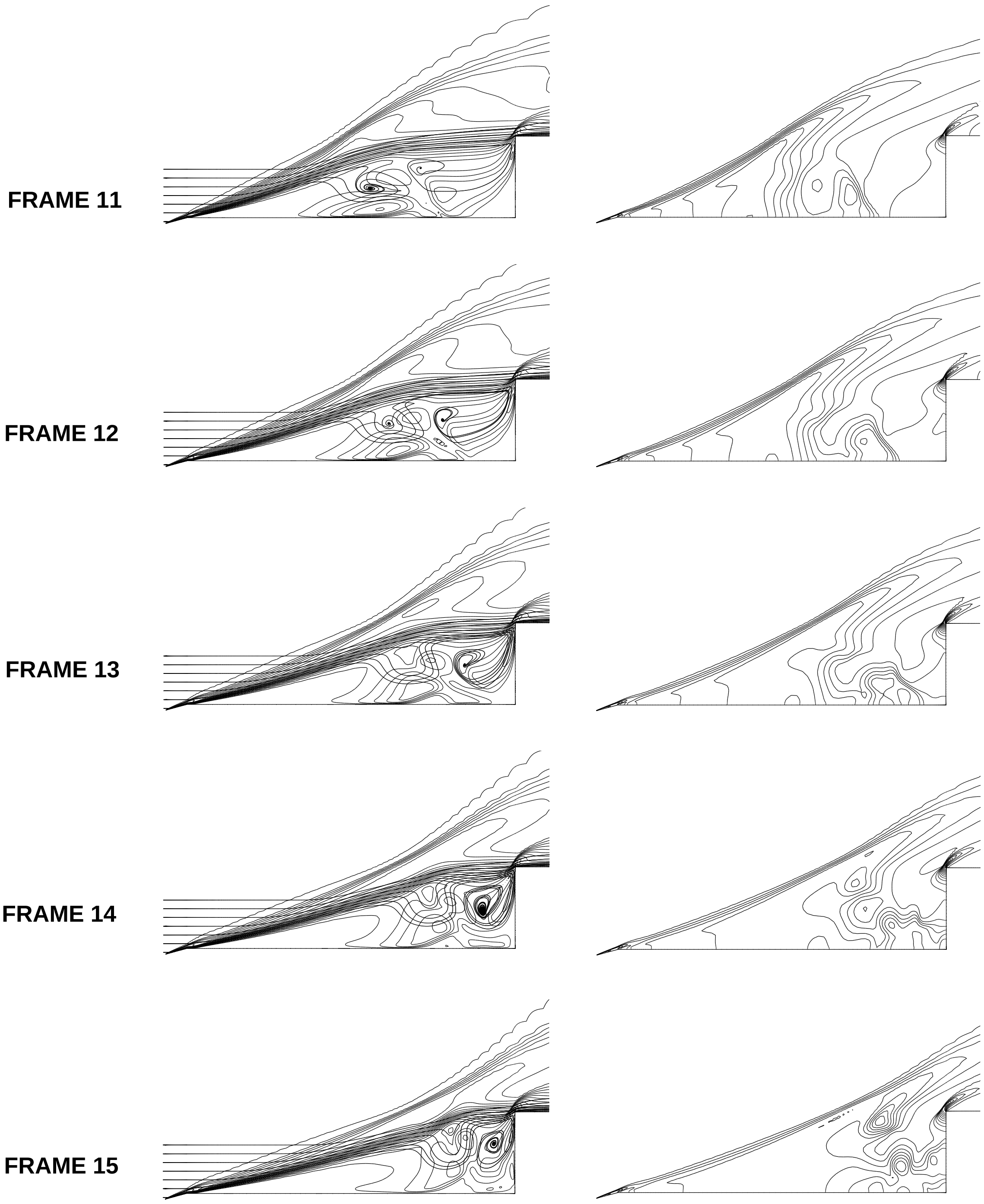

FRAME 11

FRAME 12

FRAME 13

FRAME 14

FRAME 15

Figure 4.2: *(cont.) Oscillation at Mach 6.00, L/D=2.00. Shown are the Mach isolines superimposed with instantaneous streamlines (left column) and the pressure isolines (right column).*

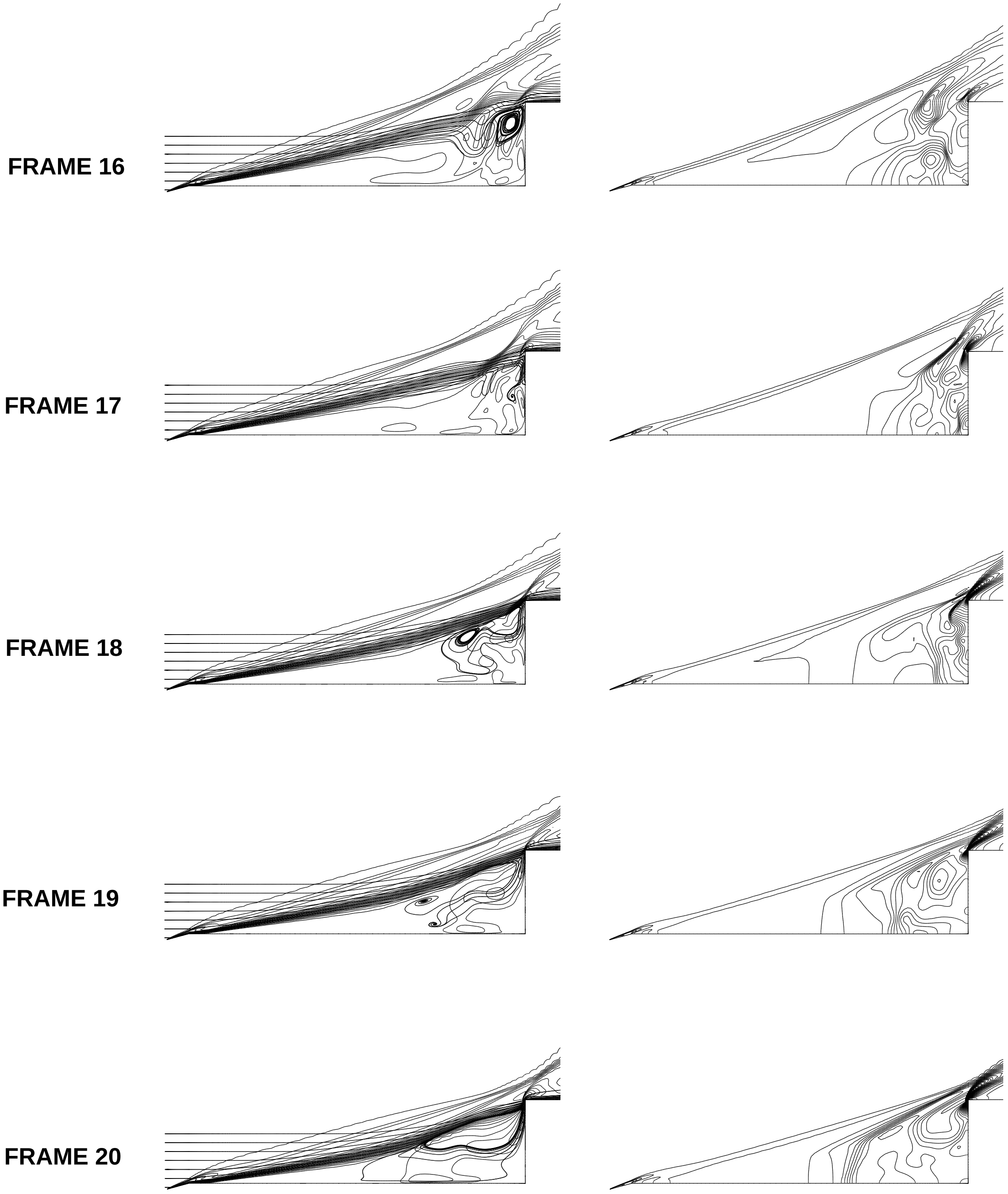

Figure 4.2: *(cont.) Oscillation at Mach 6.00, L/D=2.00. Shown are the Mach isolines superimposed with instantaneous streamlines (left column) and the pressure isolines (right column).*

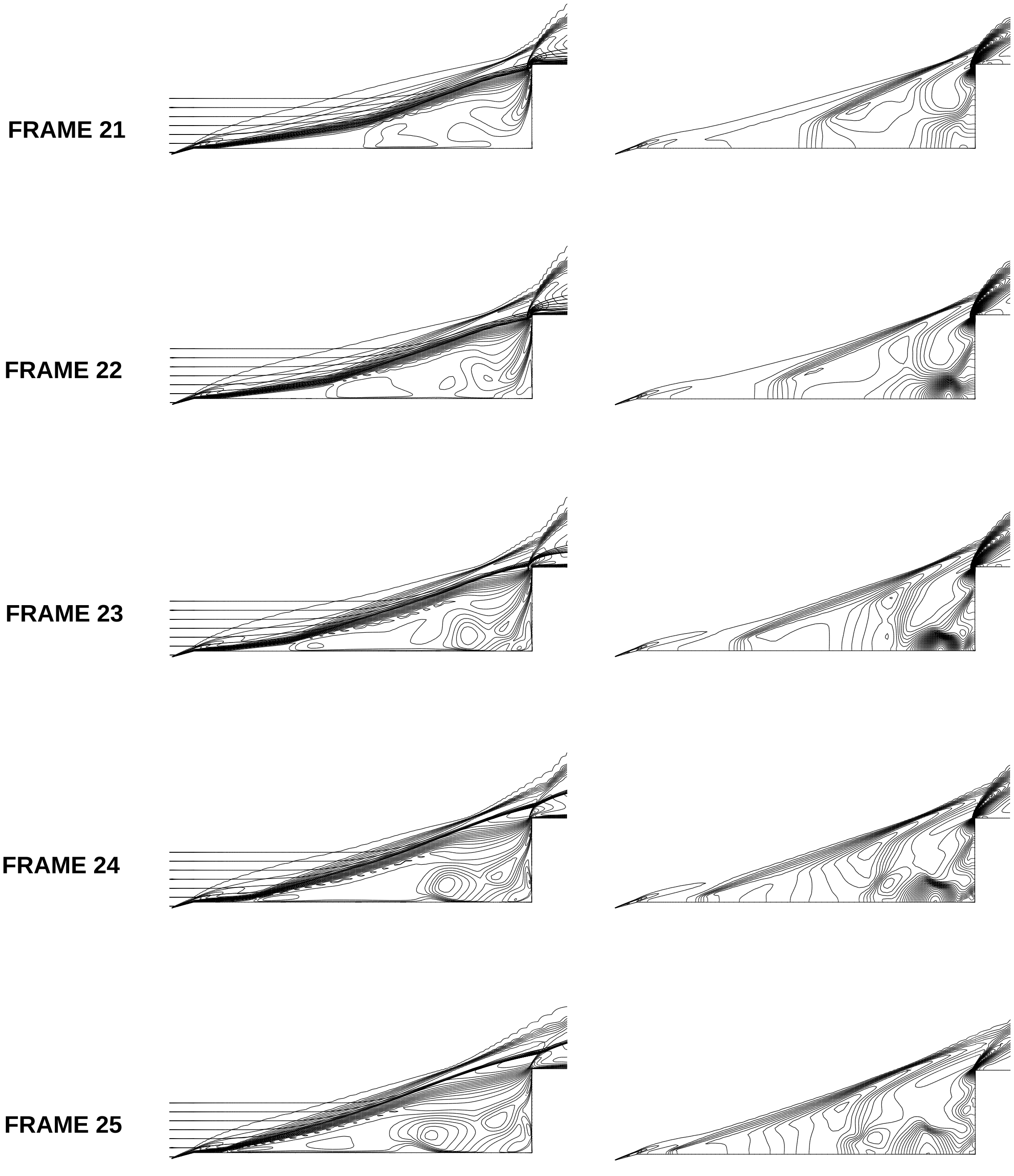

Figure 4.2: *(cont.) Oscillation at Mach 6.00, L/D=2.00. Shown are the Mach isolines superimposed with instantaneous streamlines (left column) and the pressure isolines (right column).*

FRAME 26

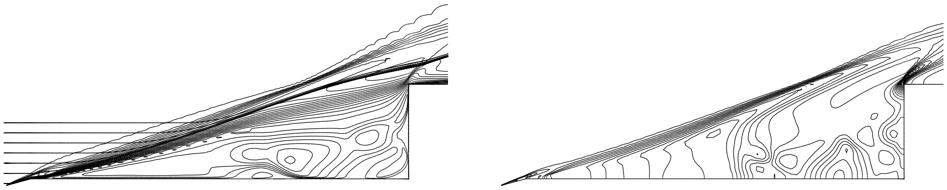

FRAME 27

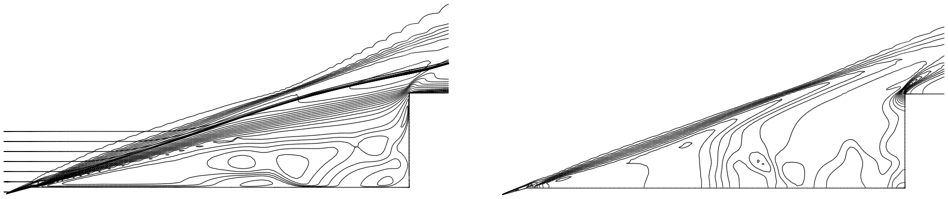

FRAME 28

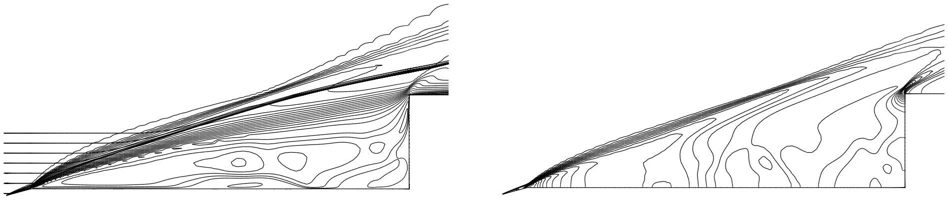

Figure 4.2: *(cont.) Oscillation at Mach 6.00, L/D=2.00. Shown are the Mach isolines superimposed with instantaneous streamlines (left column) and the pressure isolines (right column).*

takes approximately 1/5 time period for a particle to travel from the spike tip to the corner. The high position of the streamlines also means, that mass is escaping from the separation region, since the flow bounded by the array of the introduced streamlines was entrained by the shear layer from the separated region. In frame 3, both the separation point and the region of the pressure gradient seem to complete their motion in the upstream direction. As a consequence, the pressure builds up in the vicinity of the spike tip shoulder and a waviness occurs in the shape of the shear layer as it is deformed due to the slight lateral expansion (frame 4). Then, the high pressure region starts to migrate downstream towards the cylinder face, dragging along the waviness in the shear layer (frames 5, 6, 7). Note, that the pressure wave is nearly perpendicular relative to the spike, which is caused by the zero pressure gradient across the shear layer ($\frac{\partial p}{\partial y} = 0$). The introduced streamlines now seem to take on a lower position around the afterbody shoulder and the lower two reattach on the cylinder face (frame 8), indicating that mass escape from the separation zone alters to a mass influx. However, the pressure at the cylinder face continues to drop (see the pressure history in Fig. 4.1), which phenomena is most likely a consequence of the dynamics of the event.

Frames 9-15 illustrate that the filling mechanism intensifies as the number of streamlines reattaching on the shoulder increases. An interesting feature, not observed in the experiment, is that the lowest of these streamlines leaves the shear layer to enter the separation region. The location, where this happens coincides with the position of the downstream travelling pressure gradient. This effect is believed to occur due to the conflict between the flow coming from upstream and that being reversed.

When the downstream convecting pressure gradient finally impacts on the cylinder face (frame 18), it is reflected from the wall, starting a new upstream migration (see the pressure plots of frames 19 and 20). However, this upstream movement seems to be generated this time by the flow reversal. When the mass influx stops (frame 21), the pressure wave has only reached the half-distance of the spike. However, frames 22-28 show its migration to continue to the spike tip. Hence, this effect must be supported by the continuing expansion of the gas already trapped in the separation region, which indicates the importance of the dynamics in the oscillation analysis.

Another interesting observation concerns the existence of the pressure gradient. The pressure plots of frames 21-23 show that as soon as the mass influx stops, a low pressure region appears behind the upstream travelling high pressure zone. Thus, a low pressure will exist both in front of and behind the pressure gradient, showing a pressure wave within the separation zone.

A final important note regarding the above description is that all the above phenomena are associated with the upstream/downstream excursion of the separation point along the forward portion of the spike, which is in accordance with the experimental observations of Holden [6] and Kenworthy [18].

Summarising the above findings, the fundamental element of the oscillation flow mode is the shear layer's ever-changing shoulder reattachment condition. This phenomena is solely responsible for the mass influx or mass escape from the separation region. Mass influx occurs when the shear layer is at its lowest position whereas mass escape takes place when the highest location is achieved. Because of the dynamics of the event, the subsequent expansion/contraction of the separation zone and the associated excursion of the separation point takes place with a certain time lag.

4.2.2 The pressure imbalance at the reattachment

The most complete analysis attempting to tackle the explanation of the driving mechanism of oscillation originates from Kenworthy [18], who constructed a working hypothesis on this phenomena, termed as the "energetic shear layer" hypothesis. As many elements of this concept seemed to match the description performed on the basis of the numerical results, this hypothesis will be taken as the basis for the further analysis. It will be reviewed in the light of the CFD results, with the primary aim of filling the gaps which could not be sufficiently supported by theoretical or experimental means.

According to Kenworthy [18], the key feature in the driving mechanism of the oscillation is the appearence of a pressure imbalance between the pressure supplied by the shear layer and that required by the afterbody. The former will be referred to as the potential reattachment pressure, p_{rpot}, which can be defined as the pressure which would occur if the dividing steamline of the shear layer would be brought to rest on the afterbody shoulder. On the other hand, the latter one will be referred to as the required reattachment pressure, p_{rr}, and represents the pressure corresponding to that experienced on the afterbody shoulder in a steady, shoulder reattaching separated flow.

Kenworthy proposed, that if

- $\mathbf{p_{rpot}} > \mathbf{p_{rr}}$, then the particles in the dividing streamline are able to overcome the pressure rise at the afterbody shoulder and will pass downstream. In this case, **mass escape** occurs.
- $\mathbf{p_{rpot}} < \mathbf{p_{rr}}$, the particles in the dividing streamline are not able to overcome the pressure rise at the afterbody shoulder and will be reversed into the separation zone, then **mass influx** takes place.

The relationship of these two characteristics is constantly changing during a time-dependent, shoulder reattaching separation, such as oscillation. In order to understand the behaviour of these two pressures, however, the steady separated flows have to be examined first.

4.2.3 Steady separated flow

4.2.3.1. The required reattachment pressure

Non-shoulder reattaching flows

Consider a steady separated flow occurring over a forward facing step exposed to a supersonic freestream (Fig. 4.3a). The shear layer emanates from the separation point (S), located at a distance x_1 from the leading edge, and reattaches at the point of reattachment (R) on the afterbody face, which is assumed to be below the shoulder in the first instance.

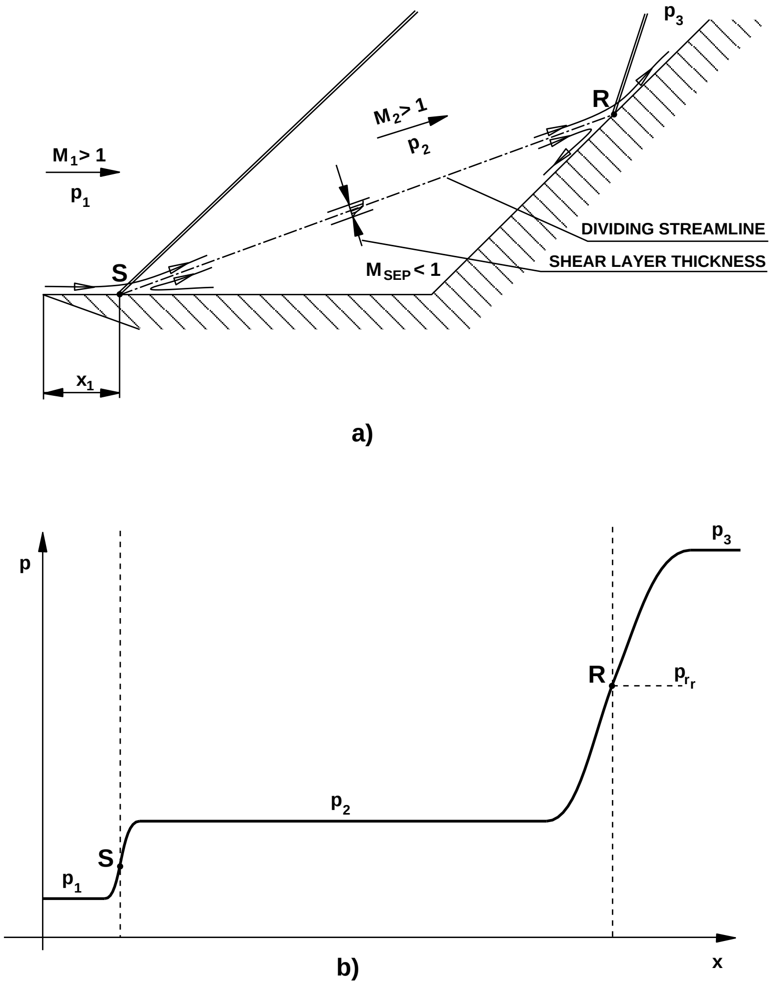

Figure 4.3: *Scheme of a steady, face-reattaching separated flow (a) and the corresponding surface pressure distribution (b).*

At the point of reattachment (R), part of the flow in the shear layer will be reversed into the separation region and part of it will pass downstream. In order to satisfy the steady nature of the separation, the mass reversed at point R must equal the mass entrained by the shear layer from the separated region at point S [40] [18]. Thus, a dividing streamline is formed within the shear layer, which can be defined as the streamline dividing the mass in the separated region from that coming from upstream of the separation point.

The dividing streamline must possess a pressure when brought to rest at the reattachment point which is equal to the required reattachment pressure [41]:

$$p_{rpot} = p_{rr} \tag{4.1}$$

In earlier works, such as Chapman [41], it was thought, that p_{rr} is equal to the static pressure of the external inviscid flow,

$$p_{rr} = p_3 \tag{4.2}$$

However, later experimental observations [42] [43] showed that p_{rr} is somewhat smaller than this, in fact lying somewhere between p_2 and p_3, as illustrated in Fig. 4.3b.

Nash [42] proposed a reattachment parameter N, which relates the required reattachment pressure to the pressure rise

$$N = \frac{p_{rr} - p_2}{p_3 - p_2} \tag{4.3}$$

and concluded, that N is a nearly constant value for a wide range of Mach numbers. He determined N as 0.35 for turbulent reattaching flows, whereas Sirieix [44] and Cooke [45] found N to be 0.5 for the laminar counterparts. However, the above approximations do not fully stand for the oscillatory flows, since they feature shoulder-reattachment different from the situation depicted above.

Shoulder reattaching flows

Wood [5] and Kenworthy [18] concluded, that the necessary condition of the oscillation flow mode is leading edge separation and shoulder reattachment. This point is emphasized in Figs. 1.5 and 1.6, in which the region of unstable flow (region D in Fig. 1.5 and region E in Fig. 1.6) is bounded by shoulder reattaching flow (apart from the unimportant region of the stable flow, in which the spike length is shorter than the shock detachment distance).

Therefore, understanding the process of shoulder reattachment is of prime importance in the investigation of oscillation.

Wood [5] argued, that although the dividing streamline itself impacts on the afterbody face in a shoulder reattaching flow, the part of the shear layer from above the dividing streamline may pass the blunt body shoulder (illustrated in Fig. 4.4a) instead of turning parallel to the face. Hence, the pressure on the afterbody shoulder will be considerably less than at a non-shoulder reattaching flow, because the low pressure occurring due to the expansion downstream of the shoulder will communicate upstream via the boundary layer.

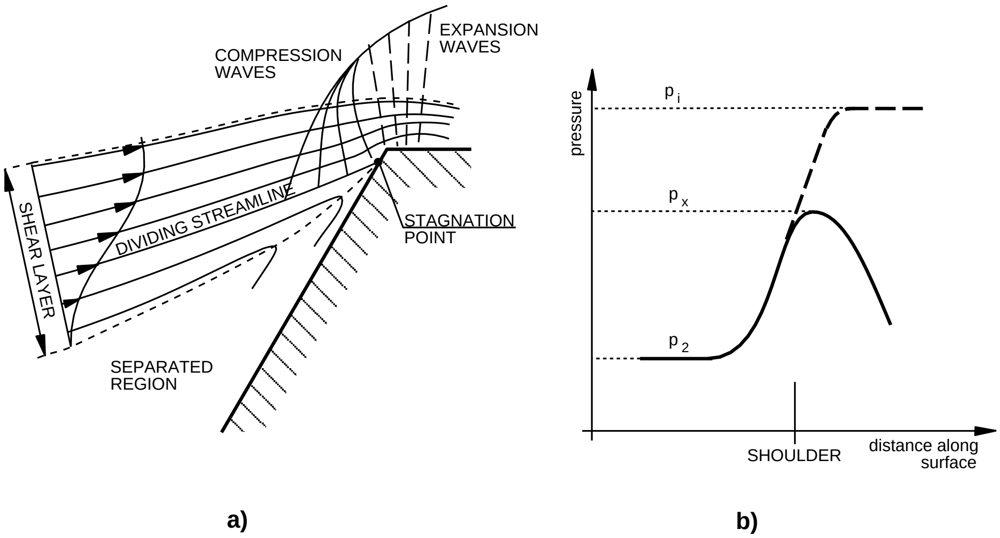

Figure 4.4: *Shoulder reattachment after Wood [5] (a) and the corresponding surface pressure distribution according to Kenworthy [18].*

This situation is illustrated in Fig. 4.4b, showing the surface pressure distribution for a shoulder reattaching steady separation after Kenworthy [18]. Here, the dashed line marks the imaginary case of the flow being turned parallel to the face, while the solid line shows the assumed pressure distribution for the shoulder reattaching case. As there were no experimental or theoretical data available to Kenworthy on the maximum pressure in the vicinity of the shoulder, p_x, he used an approximation to determine this important characteristic of the energetic shear layer hypothesis [18].

This information can be recovered from a CFD simulation of the steady separation case. The flow conditions of the Mach 6.00 oscillation case were chosen with $L/D = 2.75$ spike length case. This spike length is the nearest geometrical configuration to the examined L/D=2.00 case, which yields steady separation (see Fig. 4.5 showing the shock envelope).

The flow in the vicinity of the shoulder as well as the corresponding detail of the surface pressure distribution are shown in Fig. 4.6. Comparing these figures to the original scetches of Wood and Kenworthy (Fig. 4.4) shows how well the sketches capture the essence of the shoulder reattachment process. In particular, the existence of the compression and expansion waves was well predicted. The compression waves appear because of the upstream propagation of the high stagnation pressure, and a small shock wave can be observed at the outer regions of the shear layer, where the particles already travel with supersonic velocity.

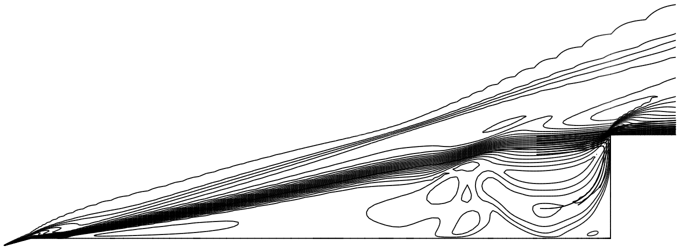

Figure 4.5: *Mach number isolines for the L/D-2.75 spike length case.* $M = 6.00$, $Re_D = 0.13 \times 10^6$.

The shape of the surface pressure distribution also matches very well the CFD results, although a small difference in the location of p_x can be observed. Kenworthy

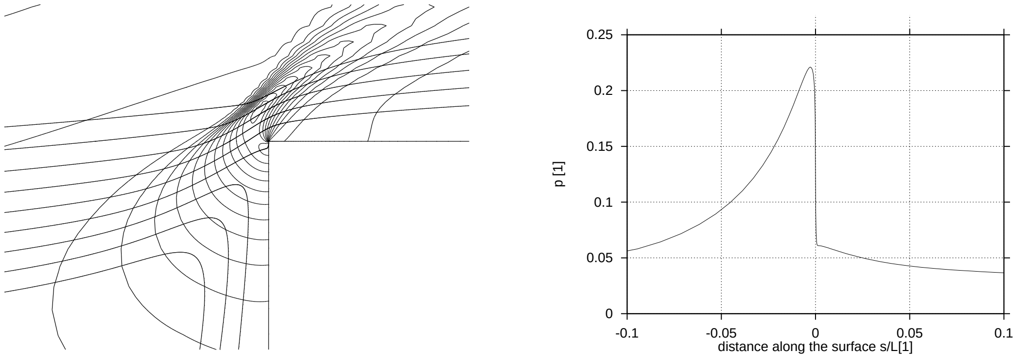

a) **b)**

Figure 4.6: *CFD results of the shoulder reattachment (a) and the corresponding surface pressure distribution in the vicinity of the shoulder.* $M = 6.00$, $Re_D = 0.13 \times 10^6$, $L/D = 2.75$.

predicts the peak pressure to occur just beyond the shoulder, whereas in the simulation it occurs in front (Fig. 4.6b, where 0 marks the corner of the afterbody). It can be seen, that the value of the non-dimensional maximum pressure is $p_x = 0.22$, and since this can be understood as the upper limit of p_{rr} [18], this value will be used for the required reattachment pressure.

$$p_{rr} = p_x = 0.22 \tag{4.4}$$

4.2.3.2. The potential reattachment pressure

Chapman et al. [41] proposed, that the pressure supplied by the shear layer, p_{rpot} is equal to that achieved by an isentropic compression of the dividing streamline if it would be brought to rest on the blunt body shoulder. Hence the term "potential reattachment pressure". Although this appears to be a very simplified model, Burgraf [46] showed by numerical techniques, that this is indeed a valid assumption. Thus [18],

$$p_{rpot} = p_0 j - p_2 \left(1 + \frac{\gamma - 1}{2} M_j\right)^{\frac{\gamma}{\gamma - 1}} \tag{4.5}$$

where p_0j is the total pressure on the dividing streamline, p_2 is the static pressure above the shear layer (see Fig. 4.3) and M_j is the Mach number on the dividing streamline.

Kenworthy [18] performed an analysis of the variation of the length of the attached boundary layer x_1 (Fig. 4.3), the velocity ratio on the dividing streamline, $z_j = \frac{M_j}{M_2}$, and the potential reattachment pressure, p_{rpot}, depending on the spike length, L/D. These calculations were performed for the freestream conditions of the current case and involved axisymmetric and laminar considerations as well. The results of this analysis are shown in Fig. 4.7, from which x_1 decreases as L/D decreases and z_j and p_{rpot} increase with decreasing L/D. Use will be made of these information later in the explanation of the energetic shear layer hypothesis.

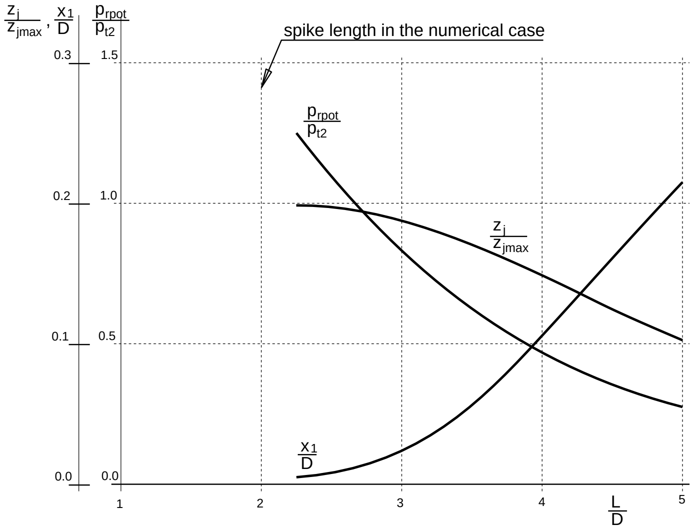

Figure 4.7: *Results of the free interaction calculation by Kenworthy [18].* $M = 6.00$, $Re_D = 0.13 \times 10^6$ *freestream considered.*

4.2.4 Unsteady separated flows

4.2.4.1. The bounding and escape streamlines

So far we have dealt with steady separation only. The term "dividing streamline" has been introduced, providing a valid description of the shear layer both in the vicinity of the separation point as well as the reattachment. However, in the case of the unsteady separations this definition will no longer stand since the shear layer is changing its position constantly, causing different streamlines to reattach on the blunt body face. This process has been demonstrated in section 4.2.1. Therefore, it seems useful to introduce two new terms to describe the shear layer separately in the vicinity of the separation point and the reattachment. These terms are identical to the ones used by Kenworthy [18] and East and Wilkinson [38].

The term "bounding streamline" will be used to describe the shear layer in the vicinity of the separation point. It will be defined as the streamline which bounds the flow entrained by the shear layer originating from the separation zone from that coming from upstream.

The term "escape streamline", on the other hand, serves to describe the situation in the vicinity of the reattachment point. The escape streamline will be defined as the highest streamline still impacting on the afterbody shoulder, i.e. reattaching.

The interpretation of these two new terms is clearly demonstrated in Fig. 4.8. In the case of mass escape, the bounding streamline lies above the escape streamline (Fig. 4.8a), whereas at mass influx, the opposite will be true (Fig. 4.8b). It is also clear from these definitions, that the bounding streamline and the escape streamline coincide in the case of a steady separation, thus forming the classical dividing streamline.

4.2.4.2. The energetic shear layer hypothesis

Kenworthy's energetic shear layer hypothesis [18] will be introduced in the present section, along with a direct comparison to the results obtained from the numerical simulation (see Fig. 4.2, M=6.00, L/D=2.00).

The core of the hypothesis is shown in Fig. 4.9, in which the first column of figures shows the original sketches of Kenworthy [18], which were prepared solely on

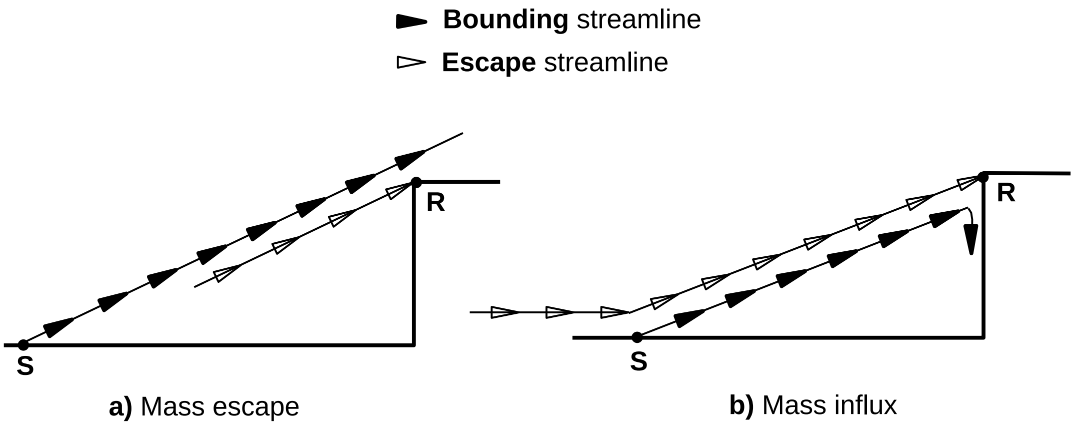

Figure 4.8: *Demonstration of the bounding and escape streamlines.*

the basis of the experimental observations and the concepts of the hypothesis. They show the representative shape of the bounding streamline in five characteristic time instants. The magnitude of the streamline vectors indicate the magnitude of the local velocity.

The remaining columns show the results obtained from the present simulation. First, the numerically obtained bounding streamlines are presented. These were obtained by launching a streamline from the separation point. Similar to Kenworthy's illustration, the magnitude of the dashes indicate the local velocity on the bounding streamline.

Next, the distribution of the Mach number M_j along the bounding streamline is provided, obtained again from the CFD results. These can be compared with the results in the second column and also serve as one of the inputs for the calculation of p_{rpot}.

Finally, the distribution of the potential reattachment pressure (p_{rpot}) along the bounding streamline is shown in the last column. These values were calculated by using equation 4.5, where p_2 was substituted by the static pressure on the bounding streamline, p_j (since $\frac{\partial p}{\partial y} = 0$ across the shear layer). The stagnation pressure on the

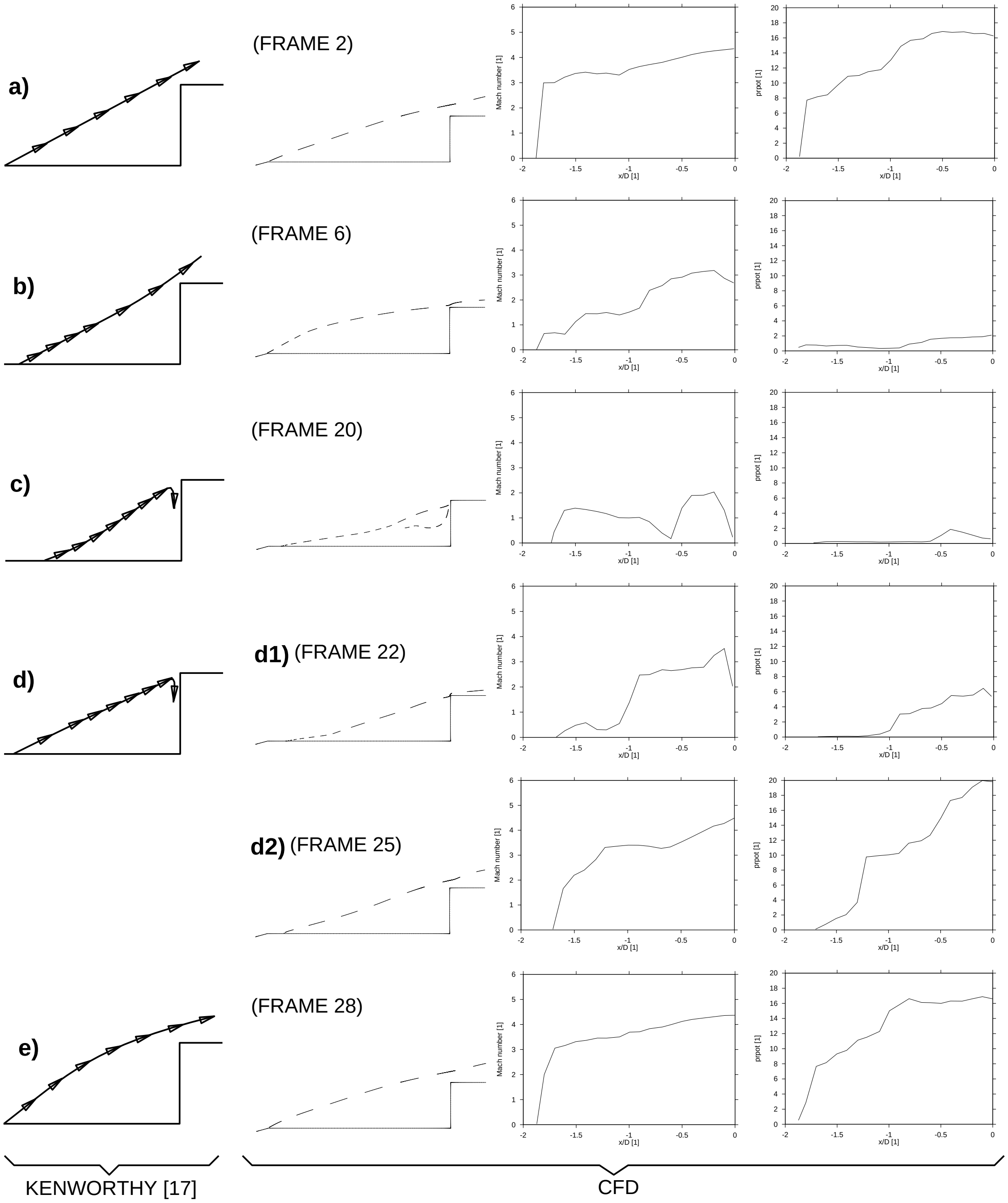

Figure 4.9: *Schematic of the energetic shear layer hypothesis applied to M=6.00, L/D=2.00 case (Fig. 4.2). First column shows Kenworthy's original sketches [18], second column the corresponding bounding streamline obtained by CFD, while the third and the fourth columns show the Mach number and the potential reattachment pressure distributions along the bounding streamline.*

bounding streamline, p_{0j}, is determined as [19]:

$$p_{0j} = \frac{p_j}{\left(1 + \frac{{M_j}^2}{5}\right)^{\frac{-\gamma}{\gamma-1}}} \tag{4.6}$$

It is noteworthy to emphasize here, that presenting the CFD results in the above fashion is new, enabling a direct quantitative evaluation of p_{rpot} and p_{rr}. This was not achievable earlier, since no data could be collected directly from the bounding streamline.

The analysis begins with frame 2 (Fig. 4.2), which is shown schematically in Fig. 4.9a. According to Kenworthy's sketch (first column), the velocity is fairly uniform and high along the bounding streamline . This is argued by the very small value of x_1, which implies a large z_j and p_{rpot} on the basis of Fig. 4.7.

It can be seen from the CFD results, that all these features are predicted by the numerical method. The velocity distribution along the bounding streamline is fairly uniform with M_j reaching values as high as 4. The potential reattachment pressure is also high ($p_{rpot} >> p_{rr}$), although not as uniform as the velocity. This is due to the apparent pressure gradient along the spike, shown in the pressure plot of frame 2 (Fig. 4.2).

This configuration, i.e. the bounding streamline lying above the escape streamline, yields mass escape from the separation zone. Thus, according to Kenworthy, after an interval of time required for this to be felt upstream, the separation recedes towards the model face (Fig. 4.9b). As x_1 increases, z_j and p_{rpot} will decrease as shown in Fig. 4.7. However, as the particles on the bounding streamline travel with a finite velocity between the separation and the reattachment, this effect will not be felt uniformly along the entire bounding streamline, but with a certain time lag. This means, that while the upstream part of the bounding streamline accommodates to the new p_{rpot} and M_j, the downstream one remains unaffected.

Once again, the CFD results agree very well with this part of the hypothesis.

It is clearly demonstrated in the numerically obtained bounding streamline that a smaller velocity appears near the separation, whereas a still larger one is present over the afterbody shoulder. The distribution of M_j further substantiates this trend. As a consequence, a small p_{rpot} is travelling downstream along the bounding streamline, while the value near the reattachment remains just high enough to maintain mass escape ($p_{rpot} > p_{rr}$).

Returning to Kenworthy's description, by Fig. 4.9c, the last of the over energetic fluid has passed downstream, and now the energy deficient fluid is beginning to arrive in the reattachment region and is being reversed into the separated region.

CFD shows a relatively small velocity present along the entire length of the bounding streamline (see the magnitude of the dashes in the second column of Fig. 4.9c and the M_j distribution), which agrees well with the hypothesis. Also, a small p_{rpot} dominates the entire length of the streamline, with the value just in front of the cylinder face being approximately one fifth of that seen in the previous frame, which leads to a mass influx ($p_{rpot} < p_{rr}$).

Up until this point, Kenworthy's hypothesis and the CFD results were found in very good agreement. However, the first major difference could be observed in the comparison of Fig. 4.9d with the numerical results.

Kenworthy argued that after a certain time lag the separation point will react to the mass influx and be pushed forward towards the spike tip. By this, as x_1 is decreased, z_j and p_{rpot} will increase according to Fig. 4.7 and this will be felt first at the separation point, and later, after the particles have travelled downstream, at the reattachment as well. This would mean, that the larger velocity magnitudes would propagate in the downstream direction, from the separation point towards the reattachment (see Fig. 4.9d).

However, the CFD results show this propagation to occur in the opposite sense, i.e. the larger velocity magnitudes appearing first at the reattachment and then propagating upstream towards the separation point. This process is illustrated via two frames, Fig. 4.9d1 and d2. The same trend can be observed in the corresponding M_j and p_{rpot} plots. The larger Mach number values (of the order of Mach 3) and the high pressure propagate upstream instead of downstream. The explanation of this phenomena lies in the behaviour of the upstream/downstream travelling wave, which was described in section 4.2.1.

The pressure wave impacts on the cylinder face and the reflection starts to travel upstream (frames 19-22 in Fig. 4.2). However, this upstream movement cannot be realised without influencing the static pressure in the bounding streamline (p_j), since the pressure gradient through the shear layer is zero ($\frac{\partial p}{\partial y} = 0$). This sudden increase in p_j will be responsible for the rapid growth of M_j and p_{rpot}, first near the reattachment and later at the separation, when the pressure wave reaches there.

The most important point is, however, that because of the increased p_{rpot} at the reattachment, no mass influx can occur in Fig. 4.9d, but instead, mass escape will take place ($p_{rpot} > p_{rr}$). This is in contrast to Kenworthy's hypothesis.

Finally, when the upstream moving pressure wave reaches the separation point, this moves forward to the spike tip and a new cycle starts again (Fig. 4.9e).

4.2.4.3. The actual reattachment pressure

As a final part of the oscillation analysis, the actual reattachment pressure will be examined. The graph showing the variation of the reattachment pressure in time during the oscillation will be used for this purpose (Fig. 4.10). The time positioning of the flow visualisation frames (Fig. 4.2) is also provided.

Kenworthy proposed in his hypothesis [18], that when the bounding streamline does not coincide with the escape streamline, a lower (or higher) streamline of the shear layer will achieve $p_{rpot} = p_{rr}$, and will therefore stagnate on the afterbody face.

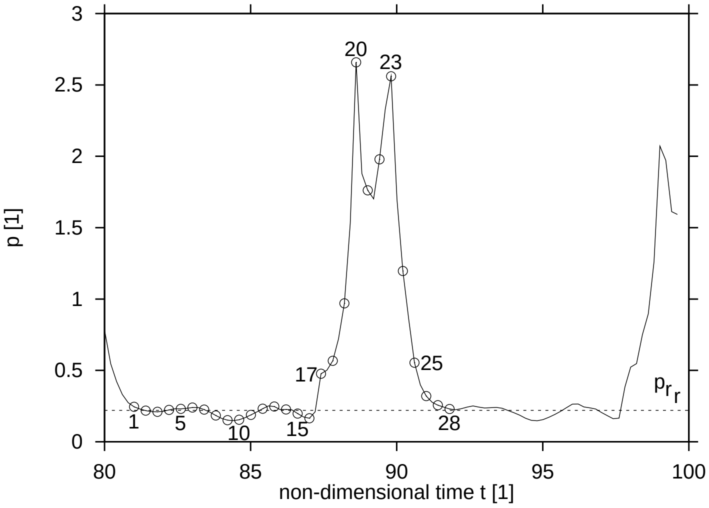

Figure 4.10: *History of the reattachment pressure (recorded at* $d = 0.99D$ *on the cylinder face) occuring during the Mach 6.00 oscillation.*

However, it can be seen from Fig. 4.10, that this is true for a certain period of the oscillation cycle only. Correlating the frame sequence of Fig. 4.2 with Fig. 4.10 shows, that the actual reattachment pressure equals p_{rr} during the shear layer's downward movement only (frames 2-16). (The required reattachment pressure $p_{rr} = 0.22$ was recovered earlier, in Eq. 4.4, section 4.2.3). However, when the shear layer moves upward (frames 17-28), the actual reattachment pressure takes on much larger values than $p_{rr} = 0.22$. This could be explained by the high pressure occurring behind the small bow wave, which is formed in front of the shoulder when the shear layer attains its lowest position. Thus, the outer portion of the afterbody becomes exposed to supersonic stream.

Inevitably, the intersection of the $p_{rr} = 0.22$ line with the pressure history yields the highest and the lowest positions of the shear layer (frames 2 and 16).

This observation further substantiates, that the shear layer's lateral movement is indeed related to the reattachment pressure of the actual escape streamline.

4.2.5 Summary

The results of the simulation largely confirm the energetic shear layer hypothesis of Kenworthy [18] apart from some minor modifications. According to this theory, the ever changing shoulder reattachment condition is driven by the mutual relationship of the pressure supplied by the shear layer, p_{rpot} and that required by the afterbody, p_{rr}. When $p_{rpot} > p_{rr}$ then the shear layer is lifted off from the afterbody shoulder and mass escape from the separation zone occurs, whereas in the opposite case the shear layer reattaches below the afterbody shoulder and mass influx into the separation zone takes place.

The conditions at the separation point change as a reaction to this effect with a certain time lag, which leads to a non-uniform distribution of the velocity and potential reattachment pressure in the shear layer.

The first minor modification concerning Kenworthy's concept is, that a high pressure (in terms of p_{rpot}) and high velocity fluid can never precede a low pressure and low velocity fluid within the bounding streamline.

The second modification regards the value of the actual reattachment pressure: it was found to be substantially larger than the required reattachment pressure, when the shear layer was moving laterally upwards.

4.3 The pulsation mode

4.3.1 Method of analysis

The methodology described below refers primarily to the pulsation obtained at the Mach 2.21 freestream, since this case will be analysed first. The corresponding Mach 6.00 results will be presented in a similar fashion separately later.

The sequence of 30 flow visualisation frames is shown in Fig. 4.12. The non-dimensional time difference between each of the frames is $\Delta t = 0.2$ [1] and the times from one cycle of the pressure history are shown in Fig. 4.11. Similar to the oscillation analysis, the pressure history was recorded at a probe point located at the D/2 diameter on the cylinder face. The following detailed description of the flowfield has been developed and thought to be accurate on the basis of the successful validation of the simulation given in Chapter 3.

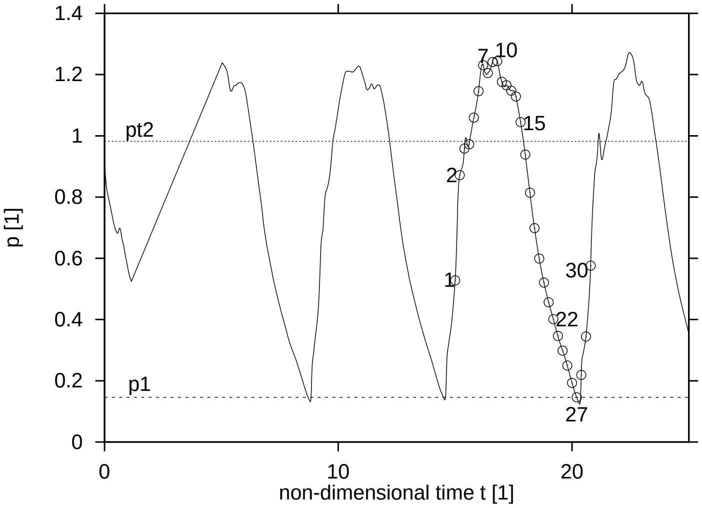

Figure 4.11: *Pressure history at the cylinder face (d=D/2) for the Mach 2.21 pulsation case.*

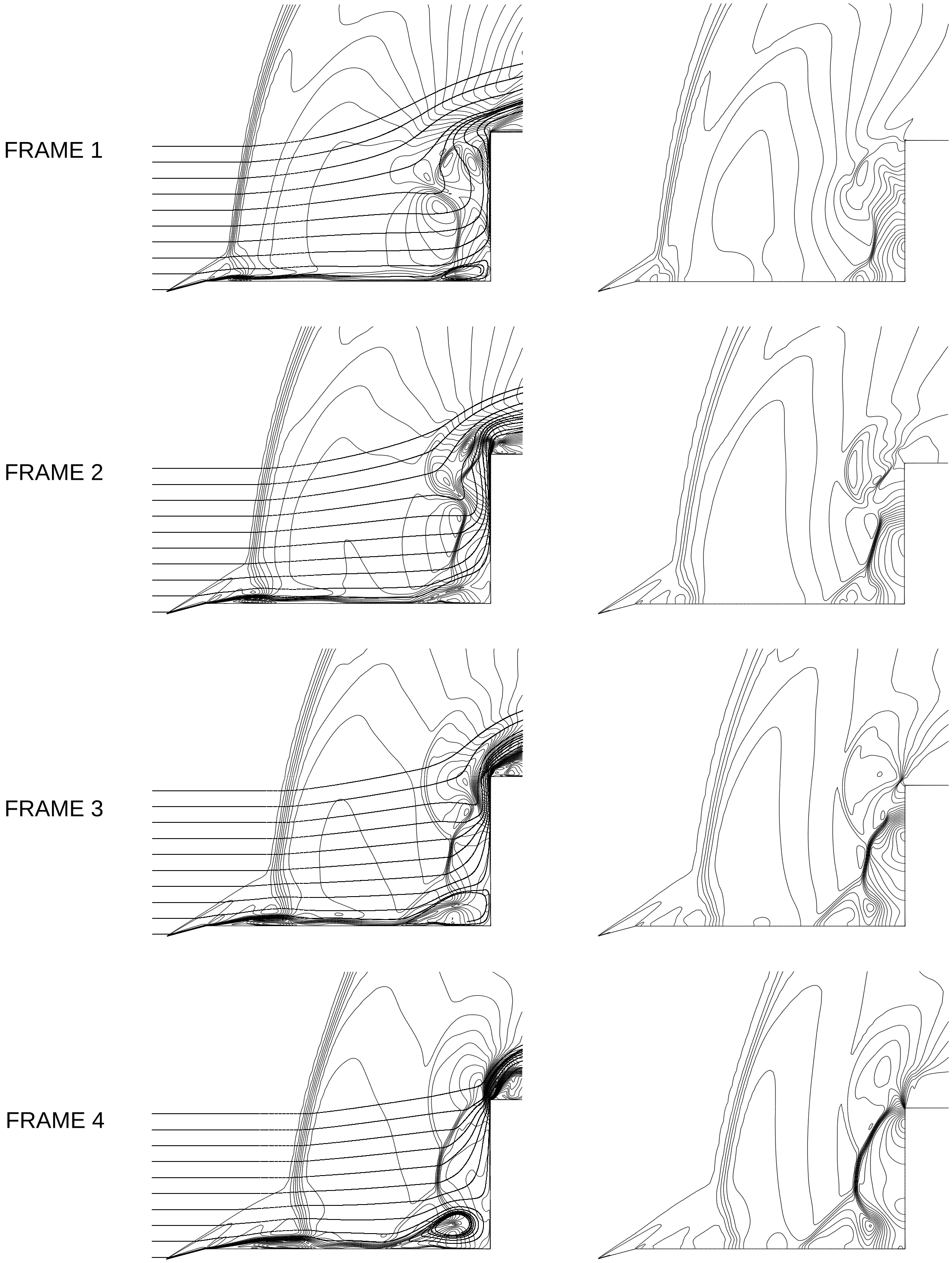

Figure 4.12: *Pulsation at Mach 2.21, L/D=1.00. Shown are the Mach isolines superimposed with instantaneous streamlines (left column) and the pressure isolines (right column).*

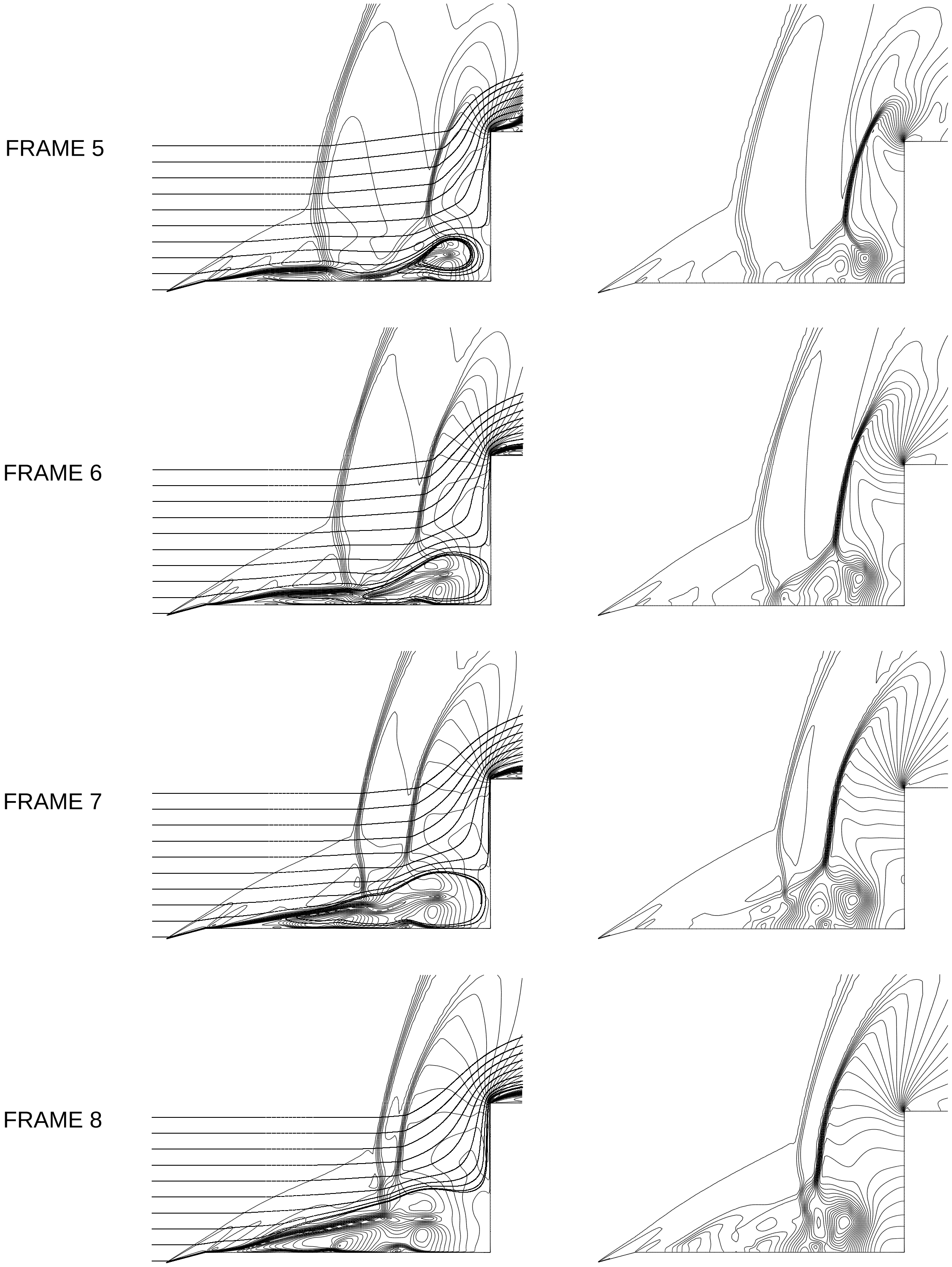

Figure 4.12: *(cont.) Pulsation at Mach 2.21, L/D=1.00. Shown are the Mach isolines superimposed with instantaneous streamlines (left column) and the pressure isolines (right column).*

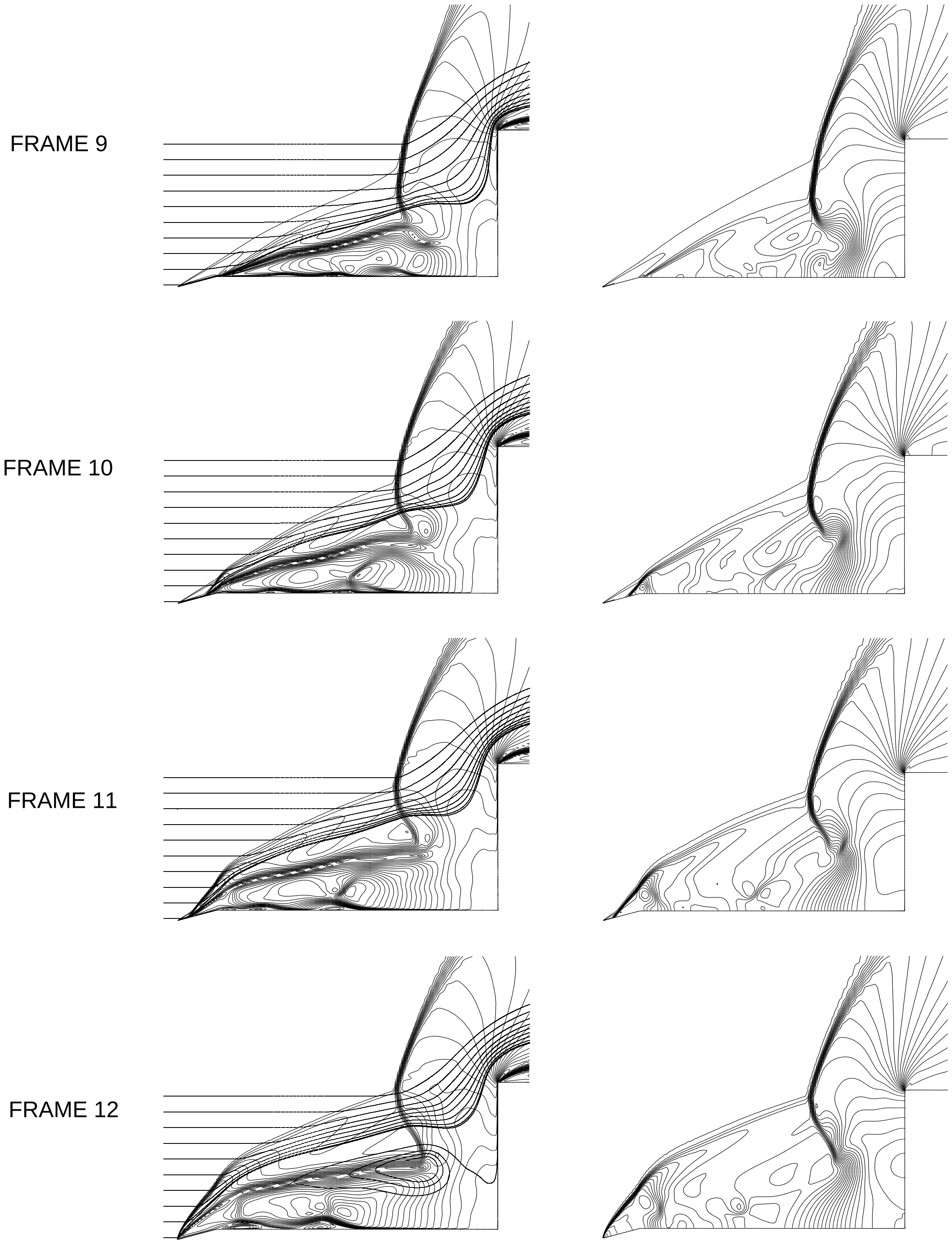

Figure 4.12: *(cont.) Pulsation at Mach 2.21, L/D=1.00. Shown are the Mach isolines superimposed with instantaneous streamlines (left column) and the pressure isolines (right column).*

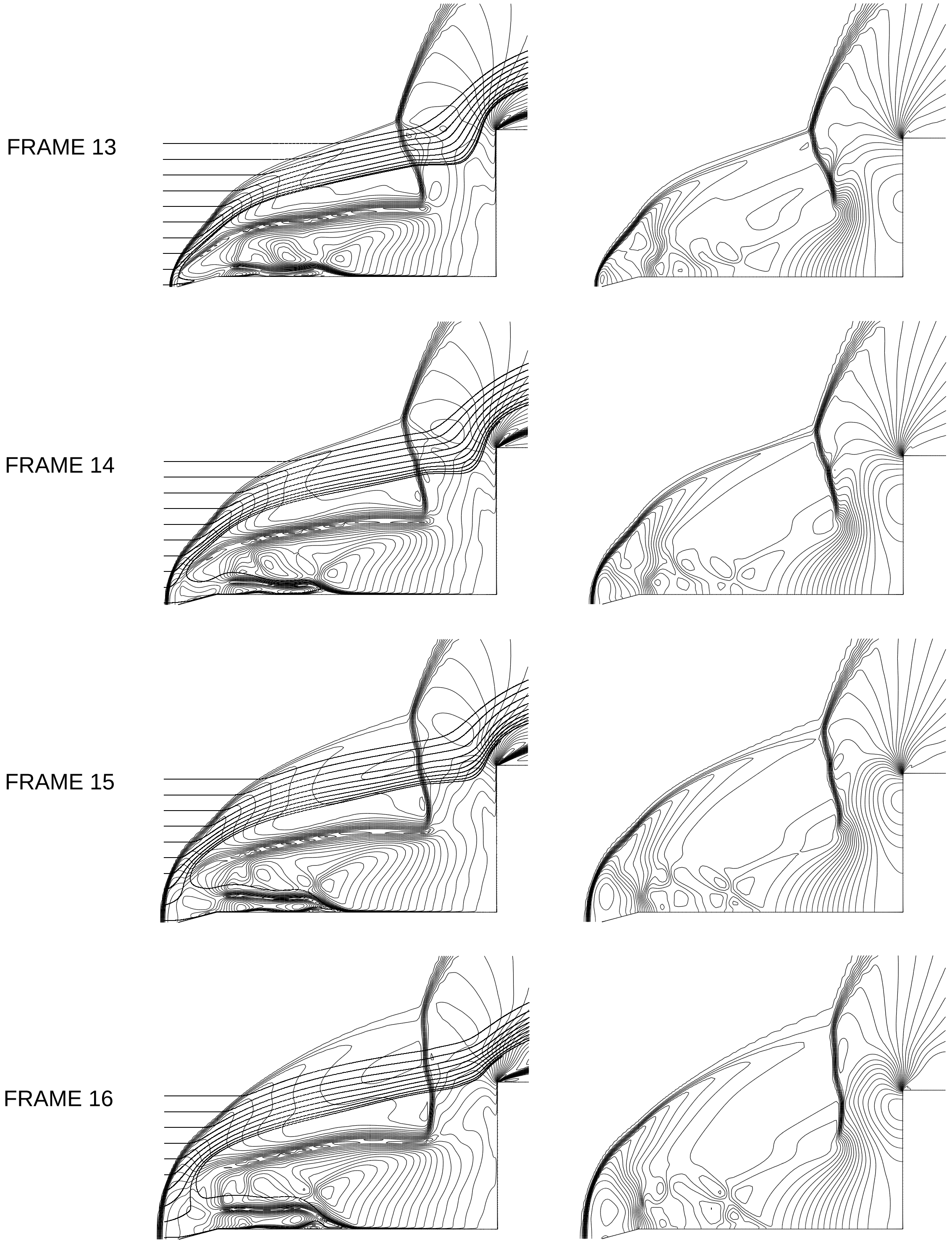

Figure 4.12: *(cont.) Pulsation at Mach 2.21, L/D=1.00. Shown are the Mach isolines superimposed with instantaneous streamlines (left column) and the pressure isolines (right column).*

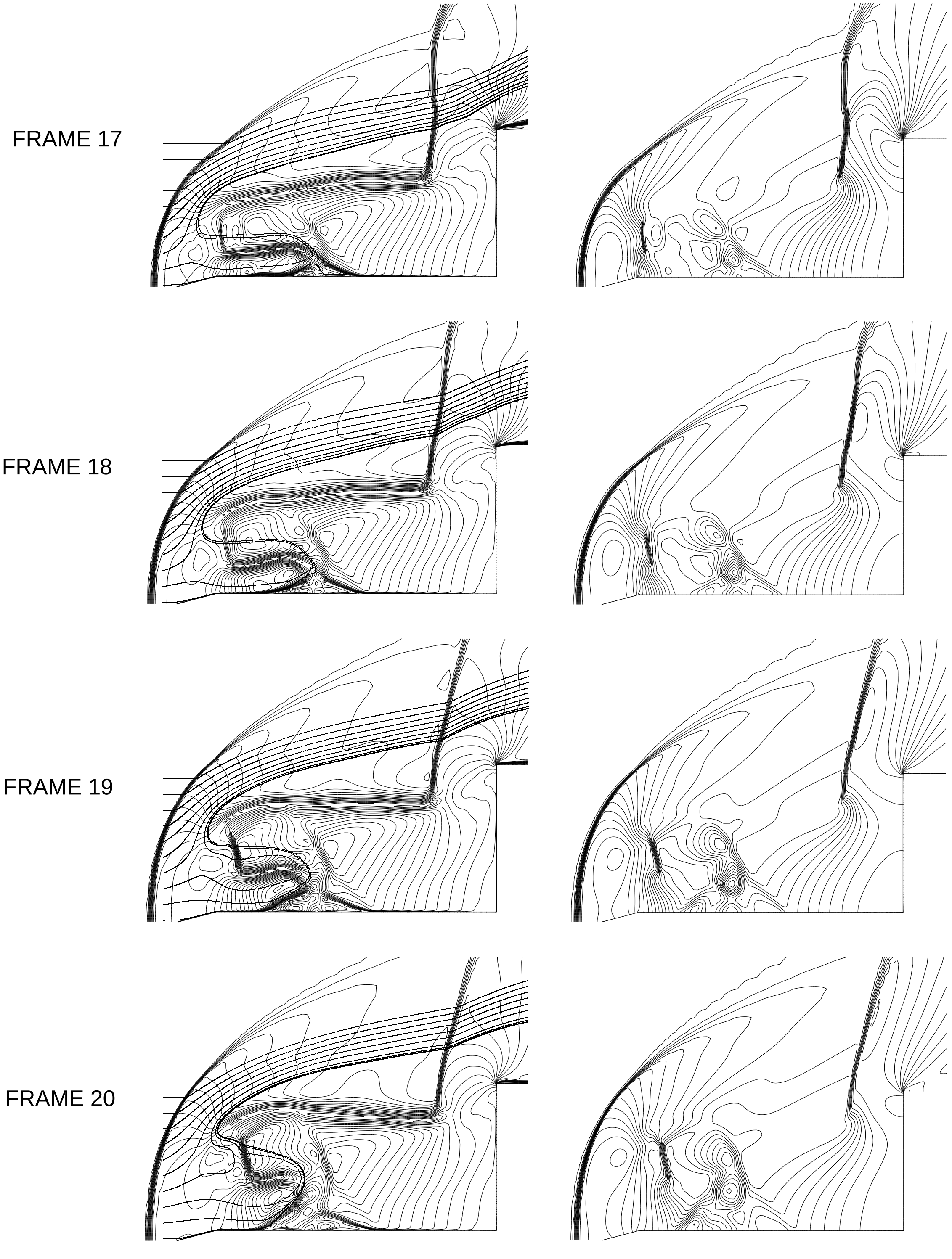

Figure 4.12: *(cont.) Pulsation at Mach 2.21, L/D=1.00. Shown are the Mach isolines superimposed with instantaneous streamlines (left column) and the pressure isolines (right column).*

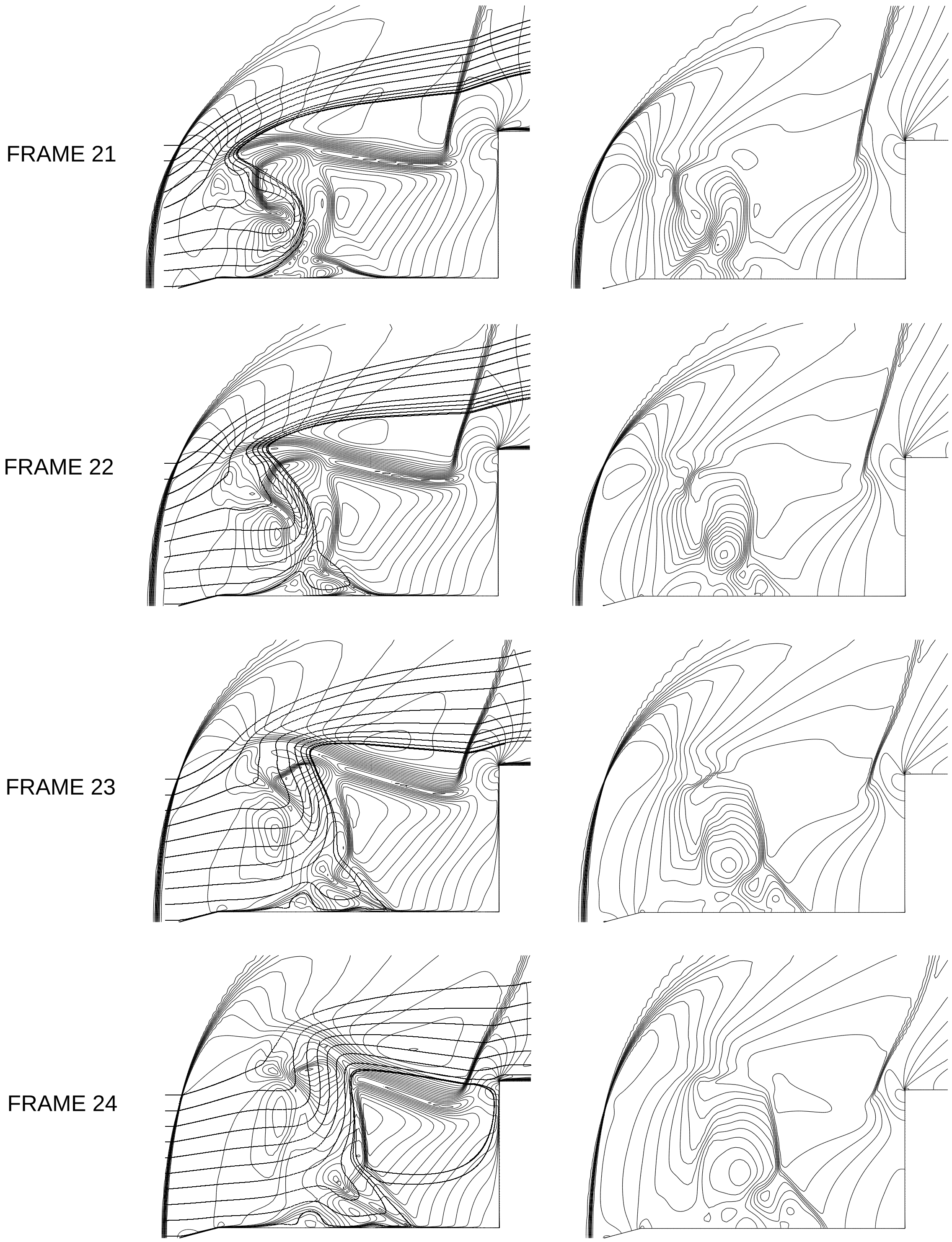

Figure 4.12: *(cont.) Pulsation at Mach 2.21, L/D=1.00. Shown are the Mach isolines superimposed with instantaneous streamlines (left column) and the pressure isolines (right column).*

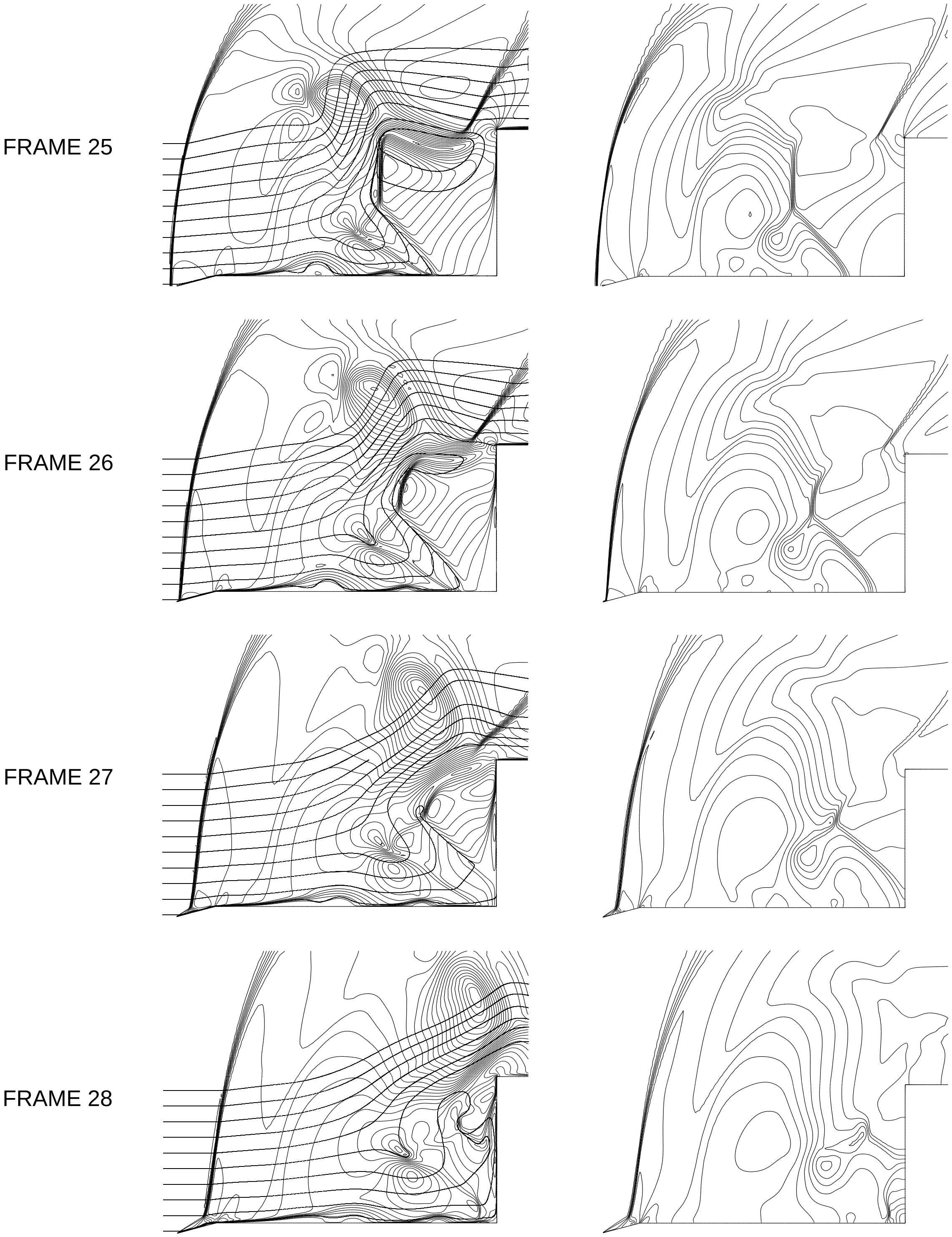

Figure 4.12: *(cont.) Pulsation at Mach 2.21, L/D=1.00. Shown are the Mach isolines superimposed with instantaneous streamlines (left column) and the pressure isolines (right column).*

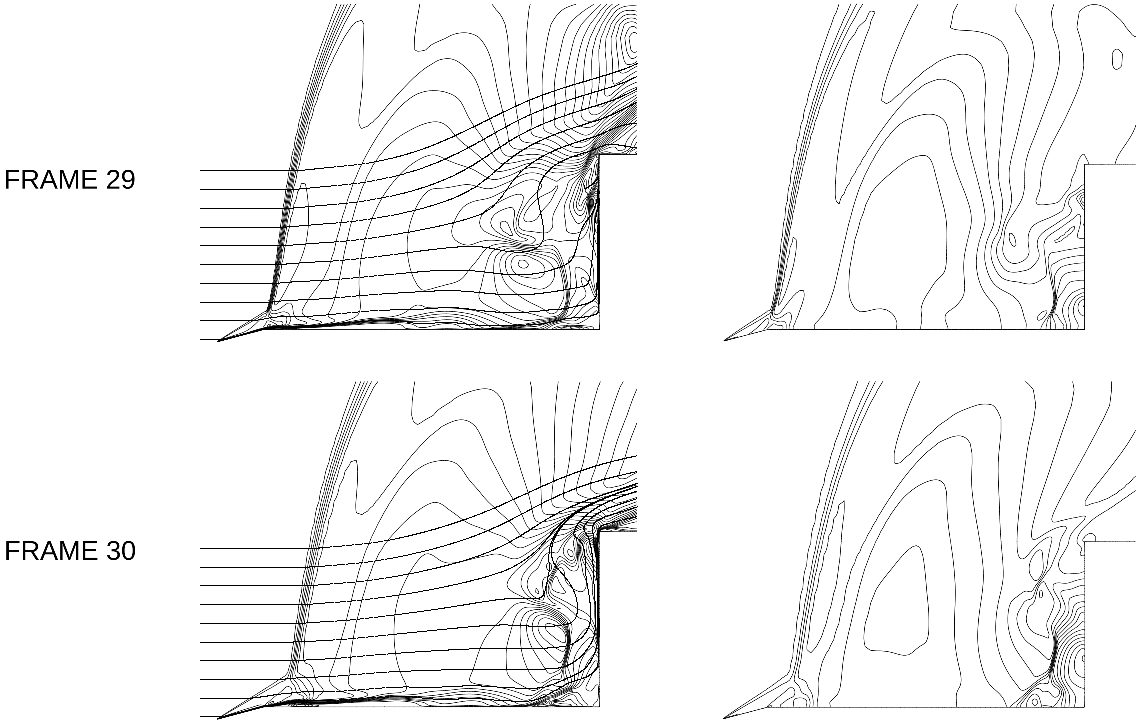

Figure 4.12: *(cont.) Pulsation at Mach 2.21, L/D=1.00. Shown are the Mach isolines superimposed with instantaneous streamlines (left column) and the pressure isolines (right column).*

In order to identify the dominant movements of the complex shock system, a reference point relating to the shock envelope has been selected. Following Zapriagaev and Mironov [28] the triple point (corresponding to the foreshock - aftershock intersection) was chosen for this purpose, as it incorporates both the longitudinal movement as well as the rate of the lateral expansion of the bow wave. The position of this reference point in time was tracked and plotted in Figs. 4.13, 4.14, 4.15. The origin of the co-ordinate system of these plots was set to the centre of the afterbody face and the triple point was monitored only while in the region of interest, i.e. in front of the cylinder face. For some of the cycle there were two triple points present, one in the collapsing shock system and one in the growing one. After the two merged, the second triple point disappeared. Finally, the foreshock angle (at the point of the attachment to the triple shock system) was also recorded (Figs. 4.16).

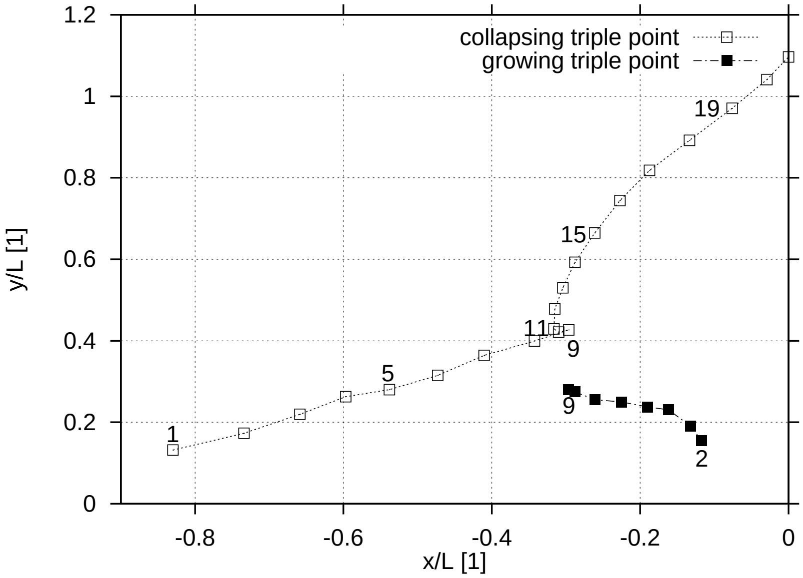

Figure 4.13: *Location of the triple point in time, with the frame numbers indicated.*

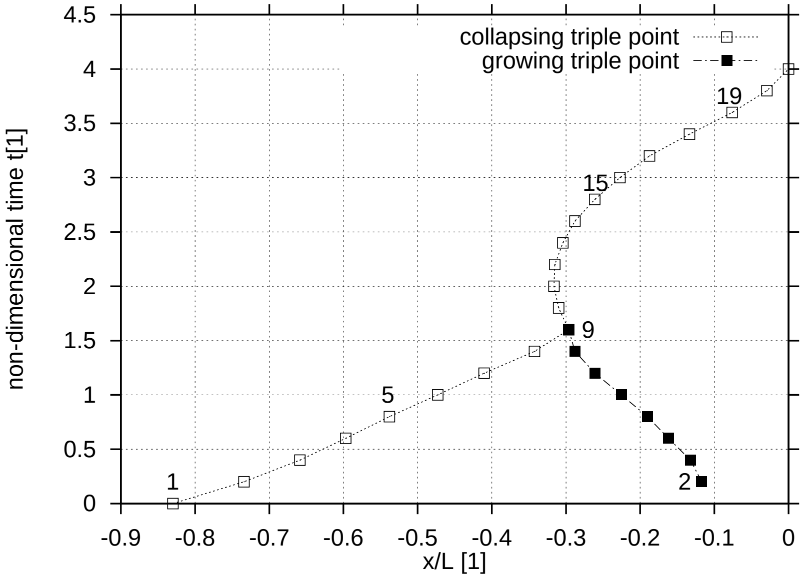

Figure 4.14: *X position of the triple point in time.*

Based on these graphs and the frame sequence, it was found appropriate to divide the pulsation cycle into three main sections (the frame numbers are presented for the Mach 2.21 case, Fig. 4.12):

(i) the section of collapse (frames 1-9), during which the rapid horizontal move-

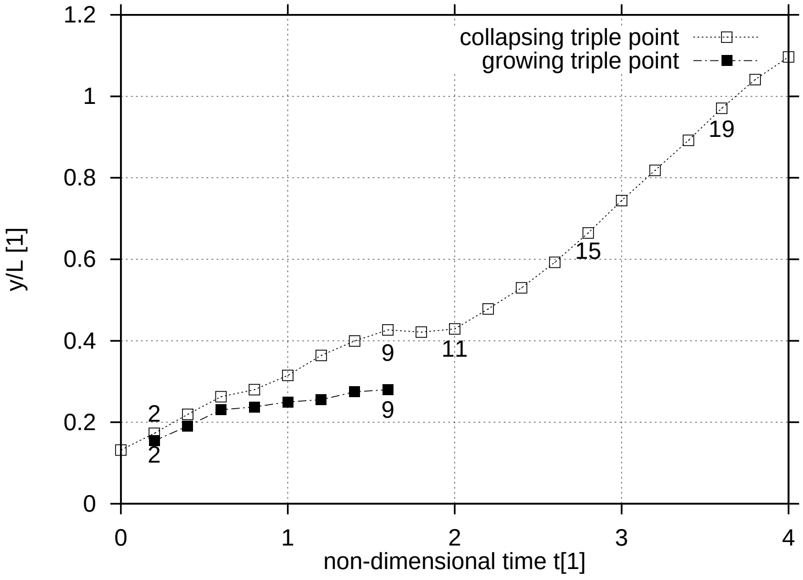

Figure 4.15: *Y position of the triple point in time.*

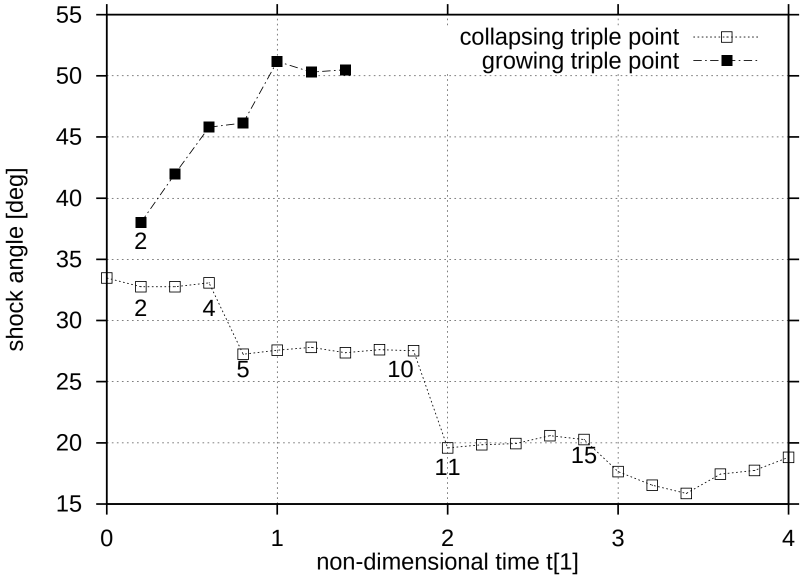

Figure 4.16: *Variation of foreshock angle in time.*

ment of the reference point is dominant,

(ii) the section of inflation (frames 10-20), during which the fast lateral movement of the foreshock-aftershock intersection is dominant, and

(iii) the section of withhold (frames 21-30), during which the expanded foreshock is almost stationary and for the earlier part of this section detached from the spike tip.

The above sections of pulsation will be analysed in detail later.

4.3.2 Flow conditions behind unsteady shock waves

The knowledge of the flow conditions behind moving shocks is of particular importance to the explanation of pulsation in section 4.3.3, in which complex shock systems are created due to this effect. The following is an analysis of this type of flow.

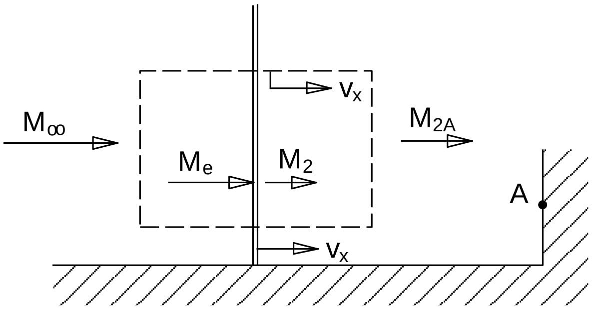

Figure 4.17: *Schematic of a moving normal shock wave.*

Consider a flowfield characterised by a freestream Mach number of M_∞ and involving a normal shock wave moving along the x axis with the velocity of v_x (Fig. 4.17). Such a flow could be interpreted in a co-ordinate system with a speed of v_x and featuring a standing shock wave. Then, the shock wave will be exposed not to the freestream Mach number M_∞, but to an effective one, M_e, which can be determined as:

$$M_e = M_\infty - \frac{v_x}{a_\infty} = M_\infty - M_{x\infty}.$$

This means, that if the shock wave is moving downstream, then the flow Mach number upstream of the wave will be less than the freestream one. For an upstream motion of the shock wave, the opposite would be true. Using the standard shock relations [19], the Mach number behind the moving shock wave, M_2 can be calculated from

$$M_2 = \sqrt{\frac{{M_e}^2 + 5}{7{M_e}^2 - 1}}.$$

Note, that as this value was determined from M_e, it represents the Mach number behind the shock wave, relative to the shock wave. In order to obtain the absolute Mach number M_{2A}, which is relative to the stationary point A in Fig. 4.17, M_2 has to be increased by v_x. However, because of the different speed of sound behind the normal wave, M_{x2} will be different from $M_{x\infty}$:

$$M_{2A} = M_2 + \frac{v_x}{a_2} = M_2 + M_{x2},$$

where a_2 could be obtained from the following relation [19] (note that a_2 is based on the conditions corresponding to M_e and not M_∞):

$$\frac{{a_2}^2}{{a_e}^2} = \frac{(7{M_e}^2 - 1)({M_e}^2 + 5)}{36{M_e}^2}.$$

4.3.3 Pulsation at Mach 2.21

Because of the numerous flow features emerging and dispersing during the pulsation cycle, flow schematics helping their identification were produced during each section (Figs.4.18, 4.23, 4.25, 4.27). In these figures, shock waves are noted as ‘W’, separated regions as ‘P’, shear layers as ‘L’ and vortical regions as ’V’. They will be numbered in the order that they appear during the cycle.

The process of collapse: frames 1-9

In frame 1 (seen in Fig. 4.12) the bow wave (W2) has already accomplished its expansion and starts to migrate towards the afterbody. The minimum pressure on the cylinder face has just been passed (Fig. 4.11) and starts to rise as shock W2 approaches the afterbody. As it exposes the most forward portion of the spike to the supersonic freestream during the collapse, an oblique conical foreshock, W1, emanates from the spike tip, intersecting W2. The angle of W1 is 33^o (Fig. 4.16), which is basically the value expected from the 15^o cone semivertex angle of the spike tip [19]. The flow behind the oblique wave is supersonic, so it is decelerated yet again through another oblique shock wave (W3) emanating from the point of intersection, i.e. the triple point (T1). As this oblique wave interacts with the boundary layer on the spike, a separated region (P1) is formed. The first sign of this is visible in frame 1 and it is further developed in frame 2.

The speed of the collapsing bow wave is represented by the slope of curve 1-9 in Fig. 4.14 which appears to have an almost constant value for the whole section of collapse. Therefore, it can be determined as

$$v_x = \frac{x_9 - x_1}{t_9 - t_1} = 0.3335[1]$$

According to section 4.3.2, $M_{x\infty}$ will be 0.737 and hence the effective Mach number, which acts on the shock, can be calculated as

$$M_e = M_\infty - M_{x\infty} = 2.21 - 0.737 = 1.473$$

Using the standard shock relations, M_2 (based on M_e) takes a value of $M_2 = 0.711$. This is the relative Mach number behind the shock wave. The absolute Mach number relative to the body can then be obtained as (see section 4.3.2)

$$M_{2A} = M_2 + M_{x2} = 0.711 + 0.646 = 1.357$$

This agrees exactly with the value predicted by the numerical simulation and it means that although the afterbody is lying downstream of a normal shock, it is nevertheless still exposed to a supersonic stream. Hence, a new normal shock (W5) is created in front of the cylinder face, whose first signs are visible in frame 1 (Fig. 4.12). This new bow wave interacts with the boundary layer on the spike and creates another separation (P2). The first (i.e. lowest) shown streamline entering the shock system is seen to be reversed by the cylinder face and as a consequence separation

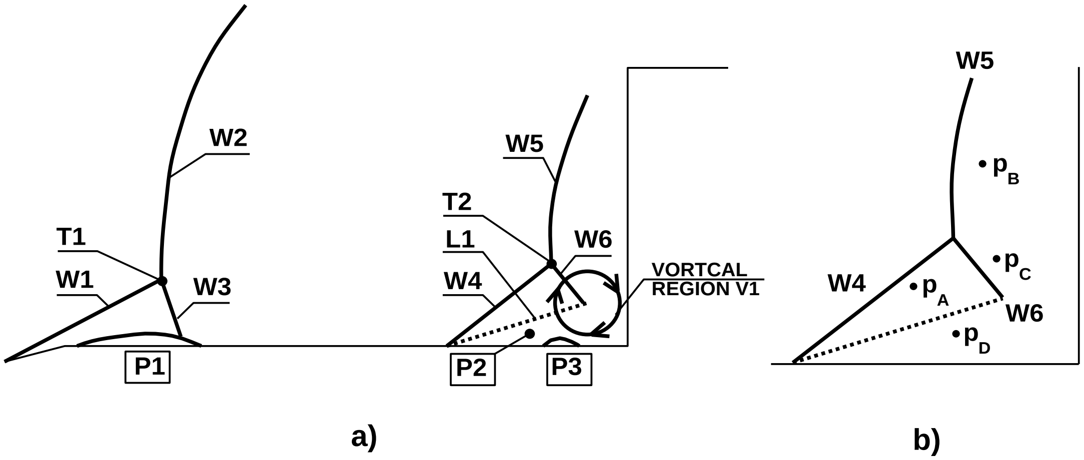

Figure 4.18: *Scheme of the shock system during collapse (based on frames 3/4).*

point P2 is induced forward (frame 2). The rest of the streamlines pass the afterbody shoulder helping the bow wave (W2) to continue its migration downstream.

By frame 2, separation region P1 has grown downstream, tracking the collapsing bow wave. Separated region P2 on the other hand, has moved further forward ahead of the growing bow wave (W5), and a weak oblique shock (W4) is generated from it. The new W4 intersects the growing W5 and, similar to the flow field at the spike tip, another triple shock system is formed (T2, W6). In frames 3 and 4, the two separated regions (P1, P2) gradually grow and move closer to each other and the secondary triple shock system becomes more clearly developed.

As a consequence of this, a shear layer (L1) is being formed, bounding separation zone P2 from the supersonic region behind shock wave W4. Assuming a zero pressure gradient through the shear layer (i.e. $\frac{\partial p}{\partial y} = 0$) then the pressures in these two regions will be equal and of a relatively low value ($p_A = p_D$, see Fig. 4.18b). However, the pressure behind shock W6 (p_C) will be high because it will tend to equal the high pressure arising behind the normal wave W5 ($p_B = p_C$). Thus, the pressure imbalance between p_C and p_D will lead to a strong favourable pressure gradient in the direction of the separation zone and thus, in an upstream direction. This combined with the immediate flow reversal by the shear layer (L1) results in the appearance of a significant vortical region (V1) at the bottom part of shock W6. The vortical region can be clearly recognised in the pressure plot of frame 3, characterised by concentric, nearly circular isolines and a low pressure in the centre. Although the appearance of such vortical region seems obvious in the present shock system, it has not been identified in any previous work, although, as it will be seen shortly, has a vital role in the pulsation driving mechanism.

The primary effect of the vortical region V1 is the flow reversal of the lowest streamlines, such as streamline 1, into the lower pressure separation zone, from where it reverses and re-enters the supersonic zone (behind foreshock W4) through shear layer L1. The filling effect intensifies with elapsing time as the next introduced streamline becomes involved in this process in frame 4. The introduced streamlines outside these, although being deflected downwards from their original direction, reach the face at an angle larger than zero and hence eventually flow outward.

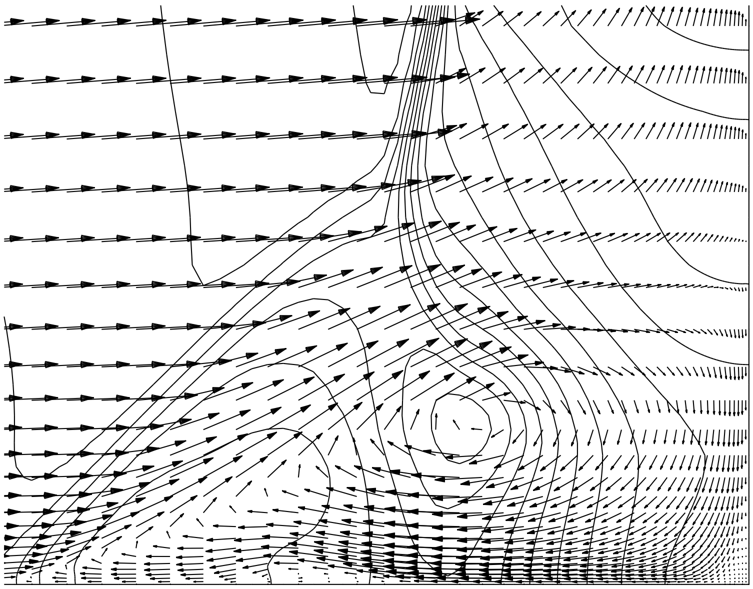

Figure 4.19: *Vector plot detail and pressure isolines for frame 3 from Fig. 4.12, Mach 2.21 freestream (every second vector shown only).*

Secondly, as a consequence of the pressure gradient created by V1 the spike boundary layer becomes affected. On the downstream side of V1 a favourable (relative to the reversed flow) pressure gradient arises, causing the thinning of the boundary layer on that side (see the vector plot detail of frame 3, Fig. 4.19). On the other hand, the adverse pressure gradient (again relative to the reversed flow) present on the upstream side of the vortex will result in a thickening effect and eventually the separation of the boundary layer there (Fig. 4.19). Thus, a new separated region (P3) of reverse direction to P1 and P2 and embedded in the latter appears just in front of the vortical region and below P2. It will be shown later, that P3 will be maintained and grow for almost the entire pulsation cycle and, similar to V1, will have a crucial importance in the driving mechanism of pulsation.

As the primary shock system (W1-W2-W3) continues to collapse, the secondary one (W4-W5-W6) strengthens (frames 4 and 5). This leads to the growth of vortical region V1, causing the enlargement of separated region P3. Note, that the position of P3 remains stationary and connected to V1.

By frames 6 and 7 separation regions P1 and P2 merge to form an enlarged region we will call P1 with a resultant merged shear layer L2 (Fig. 4.23). This event paves the way to an enlargened zone for the reversed high pressure flow to fill. The separation point of P1 will remain stationary during this period until frame 7. The induced flow field of the vortical region and associated pressure gradient is sufficient for the reversed flow to achieve supersonic speeds locally (around Mach 2).

Also during this period (frames 5,6,7) the angle of W1 drops rapidly from 33^o to 27^o (Fig. 4.16). This is due to the expansion waves emanating from the spike tip shoulder weakening the foreshock. The shock wave angle of 27^o is the smallest allowable for the Mach 2.21 freestream. The flow thus has zero deflection through this oblique shock which is further confirmed from the flow visualisation frames (frames 5,6,7).

By frame 8, the secondary foreshock (W4) has almost disappeared as the growing shock system starts to merge with the collapsing one. Although the vortical region remains active and continues to reverse the flow in the separation zone, this process no longer involves flow originating directly from the freestream.

This important finding means, that the whole of the forthcoming inflation of the separation zone is not due to a mass influx, but is in fact an expansion of the gas already trapped in this zone at high pressure (generally above p_{t2} - see Fig. 4.11). This is in contradiction to previous suggestions (Antonov [26], Panaras [23] Kenworthy [18]) of a continuous filling of the separation region *from* the freestream, for example through the mechanism of Edney's jet. Note, that the very first point of separation zone P1 has still not advanced.

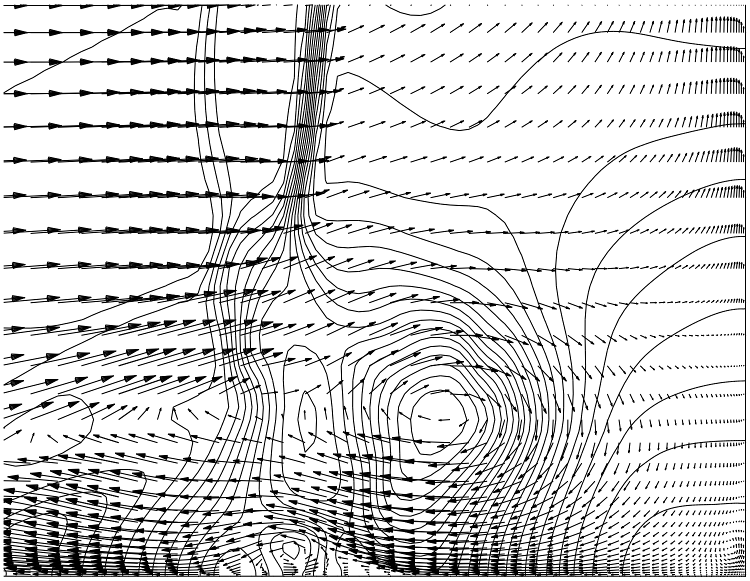

Figure 4.20: *Vector plot detail and pressure isolines for frame 8 from Fig. 4.12, Mach 2.21 freestream (every second vector shown only).*

At this stage the reversed flow is impeded by the oncoming pressure wave associated with the first triple shock region. However, by frame 9, the two bow waves merge. The position where they meet corresponds to the shock-detachment distance of the blunt body in the freestream. This is explained by the collapsing bow shock

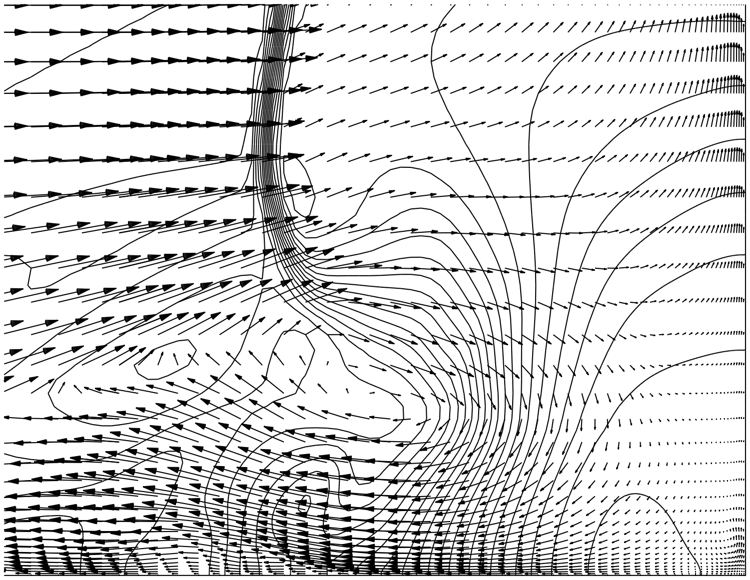

Figure 4.21: *Vector plot detail and pressure isolines for frame 9 from Fig. 4.12, Mach 2.21 freestream (every second vector shown only).*

(W1) becoming sufficiently weak to have little effect on the flow field at this stage. Thus the growing bow shock (W5) is then fully exposed to freestream conditions.

The most important feature of frame 9 concerns the behaviour of the vortical region itself. The oncoming pressure wave passes through the region to leave a strong favourable upstream pressure gradient. This process can be closely observed in the vector plots, Figs. 4.20 and 4.21, showing also how the separation region P3 is affected by this. In the sudden lack of the adverse pressure gradient the flow within the boundary layer will now be accelerated in the upstream direction, slowing the flow reversal. Hence, instead of the term 'separated region' the term 'thickened boundary layer' would be more appropriate to this particular frame. However, the notation P3 will be kept, as this flow feature will later change back to a separated region.

Demonstrated in the x-t plot of the triple point movement (Fig. 4.14) is that the axial velocity of the point becomes suddenly very small at this moment ($v_x = 0$ and thus $M_{x\infty} = M_{x2} = 0$). This leads to an instant drop of the Mach number behind the shock wave from supersonic (at M=1.473) to a fully subsonic value. Another interpretation of this situation is, that the resulting normal shock adopts a position as though it was the growing bow wave.

Note, that by frame 9 the separation region P1 has started to move forward and reaches the spike tip shoulder. This is associated with the maximum pressure recorded at the cylinder face (Fig. 4.11), which maximises the flow escape to the separation zone which thus becomes deformed.

The process of inflation: frames 10-20

Frame 10 shows the beginning of the lateral expansion of the foreshock. The lowest part of shock W3 has just reached its most rearward position due to the dynamics of the collapse.

This unique shape means, that W3 will act as a weak oblique shock on the internal streamlines involved in the recirculation (see the sketch in Fig. 4.23), and thus a supersonic pocket (reaching Mach 1.2) appears behind shock W3 for a short period of time (frame 10 only). This zone was fully subsonic before. The pressure field of the residual of the vortical region starts to enlargen (and weaken) as the high pressure gas accumulated at the cylinder face (the pressure reaches its maximum in frames 9 and 10) escapes upstream with supersonic speeds. This is the only possible path of flow as the direction of the pressure field does not allow any other solution. The growing region of pressure gradient will also cause the thickened boundary layer (P3) to move upstream, which seems to have large enough inertia to maintain its existence. It eventually causes the highly accelerated flow (Mach 2) flowing over it to be channelled causing a weak oblique shock (W7) to appear (see the pressure isolines of frame 10 and Fig. 4.23). This in turn interacts with the locally thickened boundary layer and separates it again (see the vector plot of frame 10, Fig. 4.22).

This is an important feature because although P3 will play a role later, it could have disappeared without the re-vitalising effect of W7.

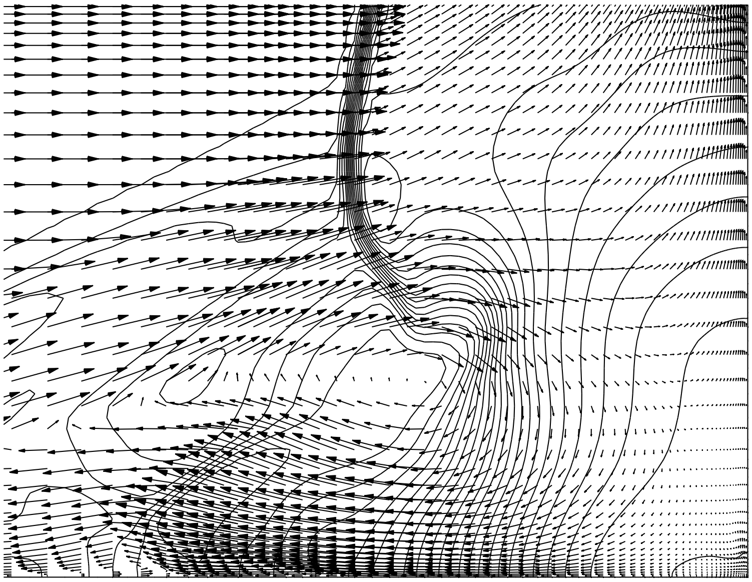

Figure 4.22: *Vector plot detail and pressure isolines for frame 10 from Fig. 4.12, Mach 2.21 freestream (every second vector shown only).*

As the recirculated gas re-enters the downstream going supersonic region (behind wave W1) through shear layer L2, it collides with the flow originating from the freestream. This results in the flow being recirculated again and re-energised by the outer flow. This effect is visualised in frame 12 by introducing an additional streamline originated near the bottom part of shock W3.

This demonstrates that the expansion process is internally fed, rather than originating from outside. It means that the resulting flow recirculation enables the high-pressure gas, accumulated at the cylinder face during the collapse to expand upstream into the separation zone. As a consequence of this, separation point P1 advances from the spike shoulder towards the tip. The shear layer originating from it (L2) seems however to keep the same angle relative to the spike surface, so when the spike tip shoulder is passed (frame 11) a break in the shape of the shear layer appears.

An interesting feature appears when examining the angle of the foreshock at the triple point at this time instant. It takes on a value, 20^o, which could not exist normally in a freestream of Mach 2.21 [19]. The weakest possible shock angle at this speed is 27^o, which suggests that another factor has to be taken into account. Fig.4.16 further demonstrates this sudden drop from 27^o to 20^o at frame 11, and the value is then preserved through the next four frames. These correspond to the period when the triple point starts to move laterally, which therefore has a bearing on this apparent anomaly concerning the foreshock angle.

Indeed, adding the lateral Mach number to that of the freestream flow, a new resultant Mach number could be obtained (see Fig. 4.15), i.e.

$$M_e = \sqrt{{M_\infty}^2 + {M_{y\infty}}^2} = 2.28$$

acting at an angle of $\alpha = 14.1^o$. Now, the effective angle between the foreshock and the resultant flow will be

$$\beta_e = \beta + \alpha = 20^o + 14.1^o = 34.1^o$$

These conditions (upstream Mach number 2.28, shock angle 34.1^o) result in a Mach number behind the foreshock of 1.89 and a deflection of 10.2^o, which are in very good agreement with the CFD results, which give 1.92 for the Mach number and 10.1^o for the deflection. (Note, that the deflection is measured from the freestream direction.) This analysis confirms Kenworthy's suggestion [18], that shock systems during the pulsation mode should be considered as unsteady instead of quasi-steady.

By frame 11 and 12 the separation region at P1 reaches the spike tip and expands laterally. The recirculated flow also moves forward. As a consequence of this, the cross-sectional area at P3 will increase, leading to the disappearance of shock W7 (frames 11 and 12). However, as the separation zone at P1 continues to grow laterally, the foreshock (W1) angle near the spike tip also grows and strengthens (frames 13, 14). This results in an increase of the pressure behind the shock. The recirculated supersonic flow is thus decelerated to these conditions before re-entering shear layer L2, and hence an internal normal bow wave (W8) is created in the vicinity of the spike tip shoulder (frames 11,12 and also Fig. 4.23). As this shock interacts with the boundary layer, another separation region (P4) embedded in and of reverse direction to P1 occurs.

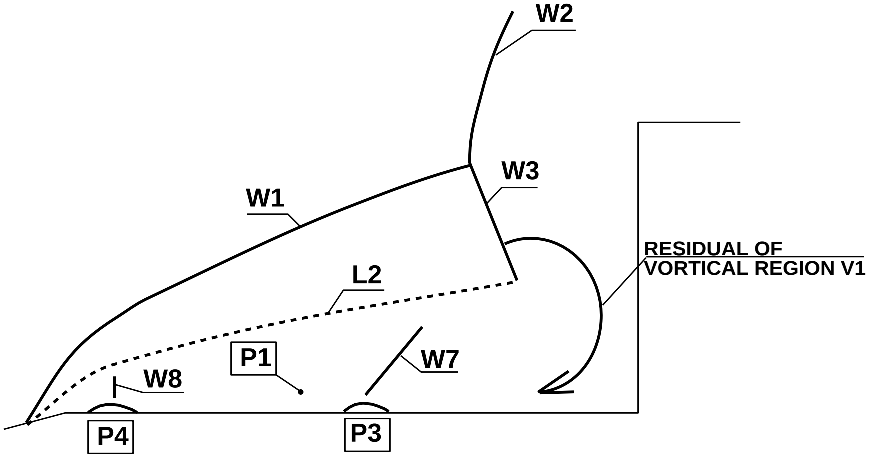

Figure 4.23: *Scheme of the shock system during the final phase of collapse and initial phase of inflation (based on frames 10/11).*

Frame 13 marks the first occurrence of foreshock W1 becoming normal near the centre line as it detaches from the tip. This means the creation of a sizeable high pressure region behind this bow wave portion, causing shear layer L2 to be lifted off from the spike tip. The first introduced streamline is thus able to penetrate more deeply below the separation zone, absorbing P4 and even reaching the location of the other internal separated region P3 (the resultant of the two will be called as P3) and creating another shear layer (L3) originating from it (frames 13-16 and Fig. 4.25). It is interesting to follow the path of this streamline: it enters the recirculation region via shear layer L3 to turn back to a direction opposite to the freestream (see the vector plot detail of frame 14, i.e. Fig. 4.24). Then it enters the supersonic flowfield behind the oblique part of W1 through the internal normal wave (W8) and finally

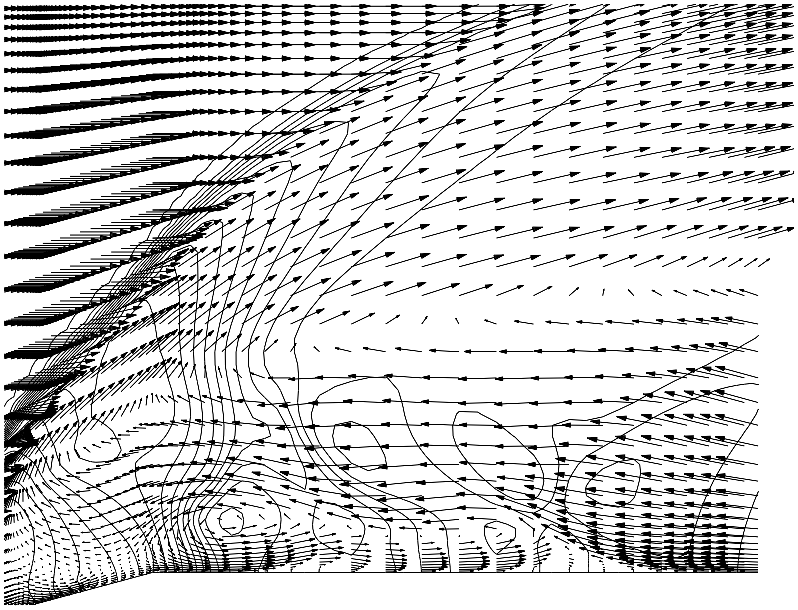

Figure 4.24: *Vector plot detail and pressure isolines for frame 14 from Fig. 4.12, Mach 2.21 freestream (every second vector shown only).*

passes the afterbody shoulder via the triple shock system. Also note that as shear layer L2 moves away from the centre, the triple point is gradually displaced in the lateral direction.

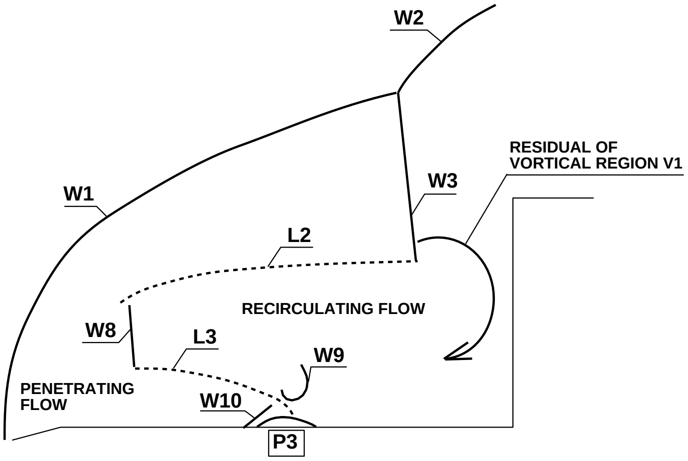

Figure 4.25: *Scheme of the shock system during the late phase of inflation and initial phase of withhold (based on frames 18/19).*

By frame 17, the second introduced streamline joins the first one in passing below the newly formed shear layer, L3. A high-pressure pocket can be observed at around the half spike length (or the location of the separation point of P3), which appears due to the collision of the penetrating and recirculating streams as they are almost brought to a standstill there. The first sign of the pocket actually appears 2 frames earlier, on frame 15, and it gradually grows until frame 22. Because it is created in a relatively low pressure environment, it will be surrounded by a curved shock wave W9 (frames 17,18,19 and Fig. 4.25). The collision of the flows is well illustrated in the vector plot detail of frame 19, Fig. 4.26.

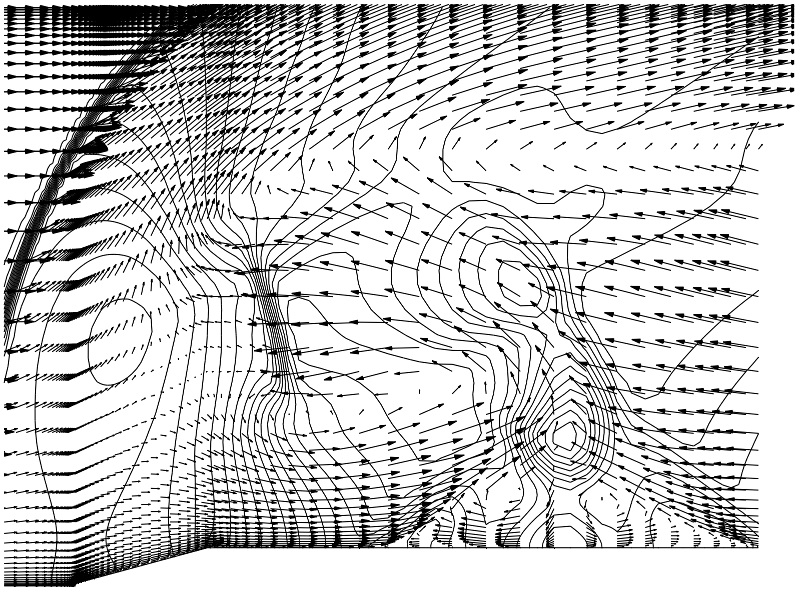

Figure 4.26: *Vector plot detail and pressure isolines for frame 19 from Fig. 4.12, Mach 2.21 freestream (every second vector shown only).*

Another interesting feature apparent from this figure is the effect of shock W8 on the penetrating flow. Because shock W8 determines the direction of the pressure gradient locally (high to low in a downstream direction), the same gradient will act as an expansion ray on the penetrating flow as well. Hence, it will experience an expansion from high pressure to low pressure, strong enough to accelerate it to supersonic speed (Mach 1.8) before colliding with the recirculated flow (frame 19).

By frames 18-20 the number of the introduced streamlines participating in this penetration process increases to three, causing a continuing lift off of the shear layer L3. Shock W8 moves downstream, rotates and also moves radially outward because of the high pressure behind the expanded foreshock W1 and also because of the shifting shear layer L3. It also weakens with little evidence of it by frame 24.

For a short period of time (frames 19-21) an oblique wave (W10) appears in front of the high pressure pocket, because separation region P3 has been so much enlargened that it will dictate large flow deflections.

The above observations are original. All previous publications (for example Antonov [26], Panaras [23], Kenworthy [18]) believed that the streamlines through the bow wave will actually enter the separation zone, reach the afterbody face and then pass by the cylinder shoulder. Instead, as it has been shown, they all turn back against the freestream direction via the secondary shear layer (L3) and then enter the supersonic conical flow region. The more flow that become involved in this process, the larger the normal portion of the foreshock becomes (frames 18-22). This enables the volume dominated by high pressure (generated by the normal shock) to greatly grow in the vicinity of the spike tip.

The withhold: frames 23-30

Frames 21 and 22 mark the most forward position of the bow wave (W1) and even when it starts to move downstream in frame 23, it continues to expand laterally (frames 23-25). This justifies the use of term “withold” for this section. By this process shock (W1), seen in frame 22 and consisting of a normal and an oblique part, becomes gradually transformed to a predominantly normal bow wave (frames 25-30).

The withhold and the actual lateral expansion occurs because of the equilibrium between the high-pressure zone behind the foreshock and the lower pressure separation region. In these frames (frames 23-25) therefore, it is as though a conflict between the two zones (separated by wave W9 which has now grown) takes place for supremacy. However, because of the lift off of the primary shear layer L2 currently in process, the prospects of the new high-pressure zone to prevail are better. Shear layer L2's deformation leads to the growth of the size of the high-pressure subsonic region, until it becomes so large that it cannot be held back by the lower pressure recirculation zone (frame 25). Hence, the collapse starts again and continues until frame 30, which leads back to the beginning of the cycle (frame 30 is identical to frame 1). It is true, that for a short time (frames 25 and 26) the mass influx into the collapsing separation zone is renewed (happening in a region involving as many as four streamlines), but is able to delay the ongoing processes only. When this feature disappears, the collapse suddenly accelerates and a new cycle starts again.

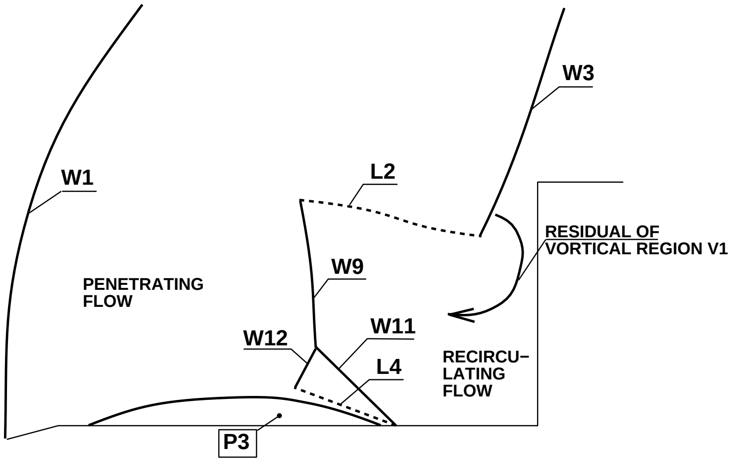

Figure 4.27: *Scheme of the shock system during the late phase of withold and initial phase of collapse (based on frames 24/26).*

An interesting feature of the withhold section is that another triple shock system, the third during a single pulsation cycle, appears inside the separation region. Its normal shock portion is formed from the originally curved W9 shock, which has been gradually opened as the number of penetrating streamlines increase. By this, the extent of the collision has also increased, which is well demonstrated on the vector plot details of frames 22 and 24, i.e. Figs. 4.28, 4.29, where the deflection of the recirculated flow is nearly 90^o. Such change in the flow direction is normally impossible through a shock wave, which further substantiates that wave W9's existence is induced by a need for a boundary between two very different flow states.

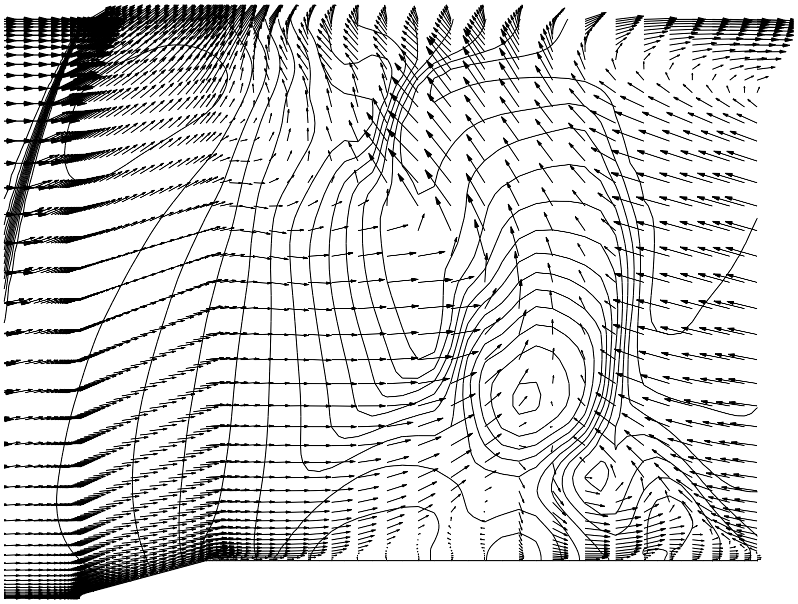

Figure 4.28: *Vector plot detail and pressure isolines for frame 22 from Fig. 4.12, Mach 2.21 freestream (every second vector shown only).*

As the collapse starts in frames 23,24, the whole system (shocks W1, W9 and also P3) starts to move downstream. As separation point P3 is moving in the opposite direction to the local stream (recirculation), an oblique shock wave (W11) will emanate from it (see the pressure isolines of frames 23 and 24 and also Fig. 4.27). As a consequence of this, a shear layer (L4) and an oblique wave (W12) is being formed, which has the role of decelerating the supersonic flow behind W11 to the conditions corresponding to the collision. The collapse also means the displacement of shock W3, which strongly weakens the residual of the vortical region V1. As W3 passes the cylinder shoulder, V1 suddenly disperses resulting in the recirculation process terminating. Thus, the third triple shock system becomes strongly weakened even before reaching the afterbody face (frames 26,27).

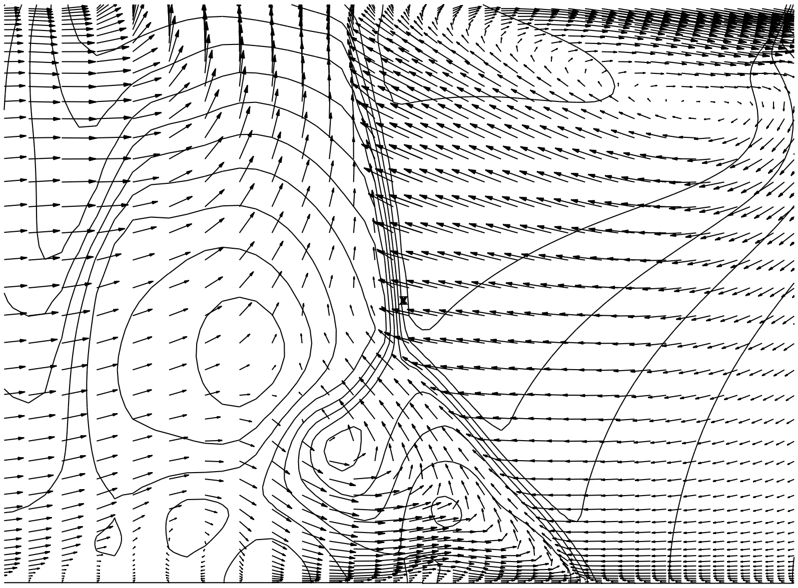

Figure 4.29: *Vector plot detail and pressure isolines for frame 24 from Fig. 4.12, Mach 2.21 freestream (every second vector shown only).*

It is also interesting to note that in frame 27 the pressure on the face reaches its lowest point and is then approximately equal to the freestream static pressure (see Fig. 4.11).

4.3.4 Pulsation at Mach 6.00

The pulsation appearing at the Mach 6.00 freestream was found to be driven by essentially the same mechanism as was revealed in the Mach 2.21 case. Thus, instead of providing a detailed description once again, only the differences arising from the hypersonic nature of the freestream will be discussed.

Similar to the previous section, a sequence of 28 frames covering an entire cycle of pulsation was selected for the purposes of the analysis (Fig. 4.31). The time-positioning of the frames is indicated from the pressure trace shown in Fig. 4.30. The non-dimensional time difference between each of the frames is again $\Delta t = 0.2[1]$.

The start of the frame sequence was chosen to enable direct comparison with the supersonic case and was based on the longitudinal location of the collapsing

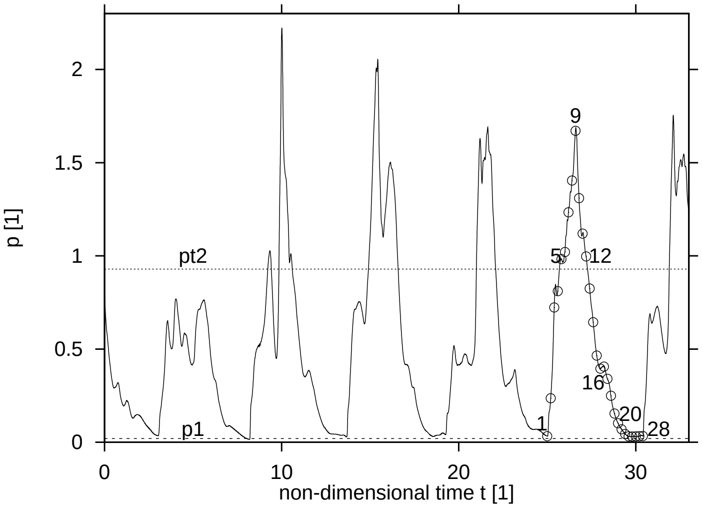

Figure 4.30: *Pressure history at the cylinder face (d=D/2) for the Mach 6.00 pulsation case.*

foreshock. This means that the position of the expanded foreshock in frame 1 of the Mach 6.00 case (Fig. 4.31) is identical to the one seen in the corresponding frame in the Mach 2.21 case (Fig. 4.12).

Finally, the triple point's location (Fig. 4.32, 4.33) was used again to identify the three characteristic sections of the pulsation mode. Interestingly, the length of the individual sections proved to be exactly the same as seen in the Mach 2.21 case, i.e.

(i) the section of collapse corresponds to frames 1-9,

(ii) the section of inflation, corresponds to frames 10-20, and

(iii) the section of withhold, corresponds to frames 21-28

This suggests that the fundamental processes of the pulsation take place at the same rate (relative to the time period of the cycle) as for the lower Mach number.

Starting with the examination of the discrepancies between the supersonic and the hypersonic freestream cases it can be seen, that the first difference occurs in the first frame. While in the Mach 2.21 case the new bow wave was already clearly developed by this time, it has just started to show its first sign in the present analysis, lying very near to the afterbody face. This means, that the new bow wave

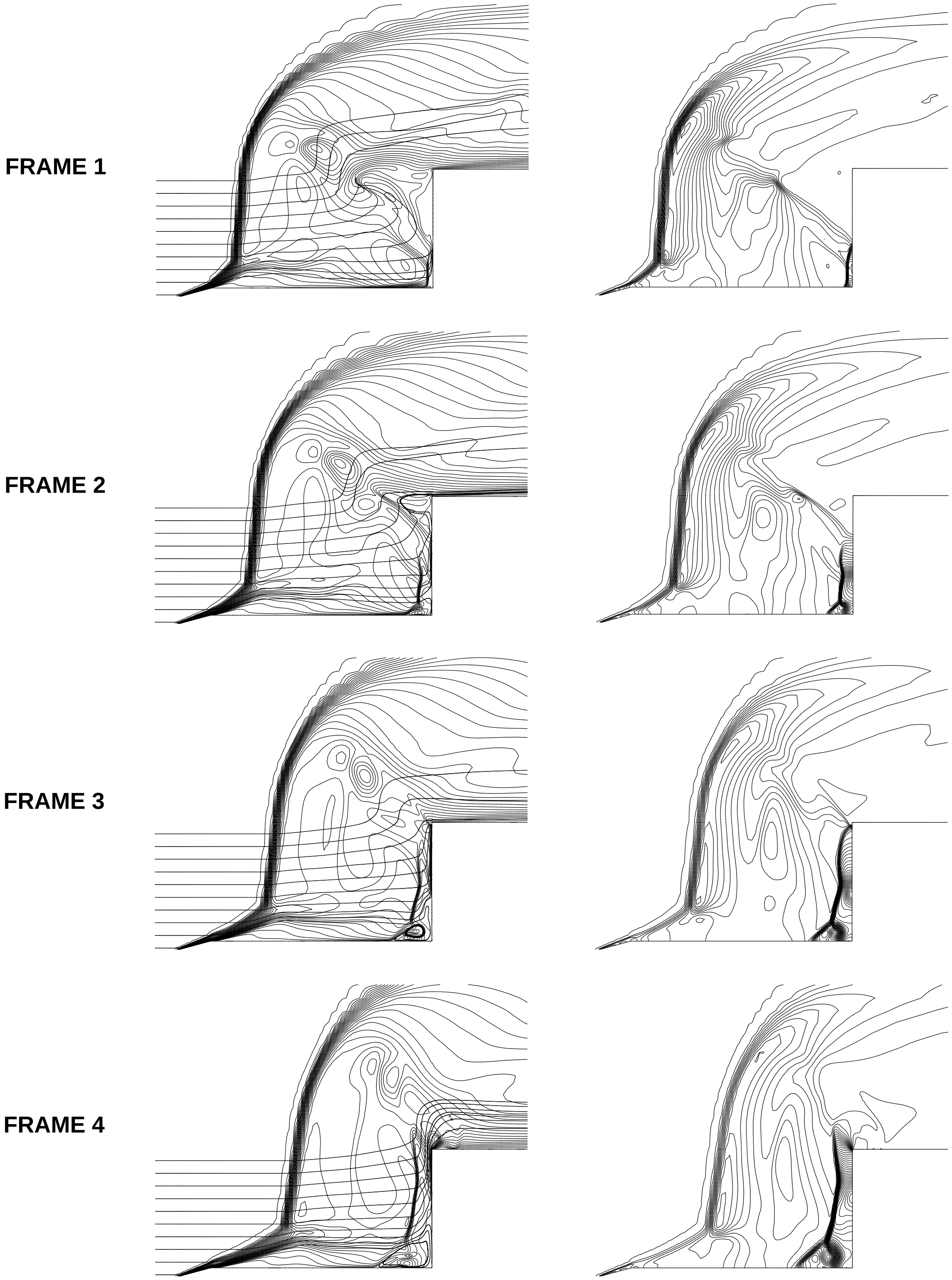

Figure 4.31: *Pulsation at Mach 6.00, L/D=1.00. Shown are the Mach isolines superimposed with instantaneous streamlines (left column) and the pressure isolines (right column).*

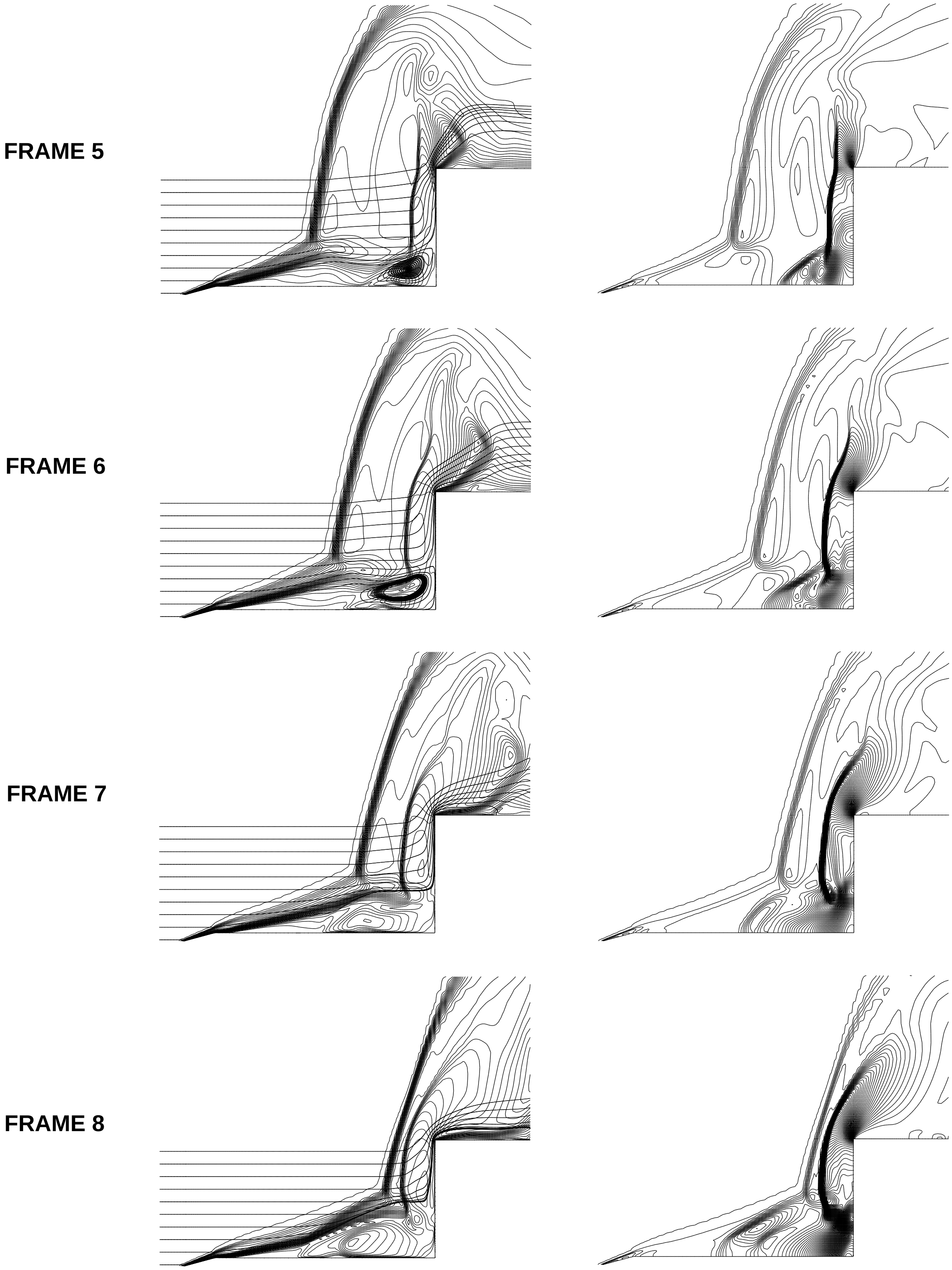

Figure 4.31: *(cont.) Pulsation at Mach 6.00, L/D=1.00. Shown are the Mach isolines superimposed with instantaneous streamlines (left column) and the pressure isolines (right column).*

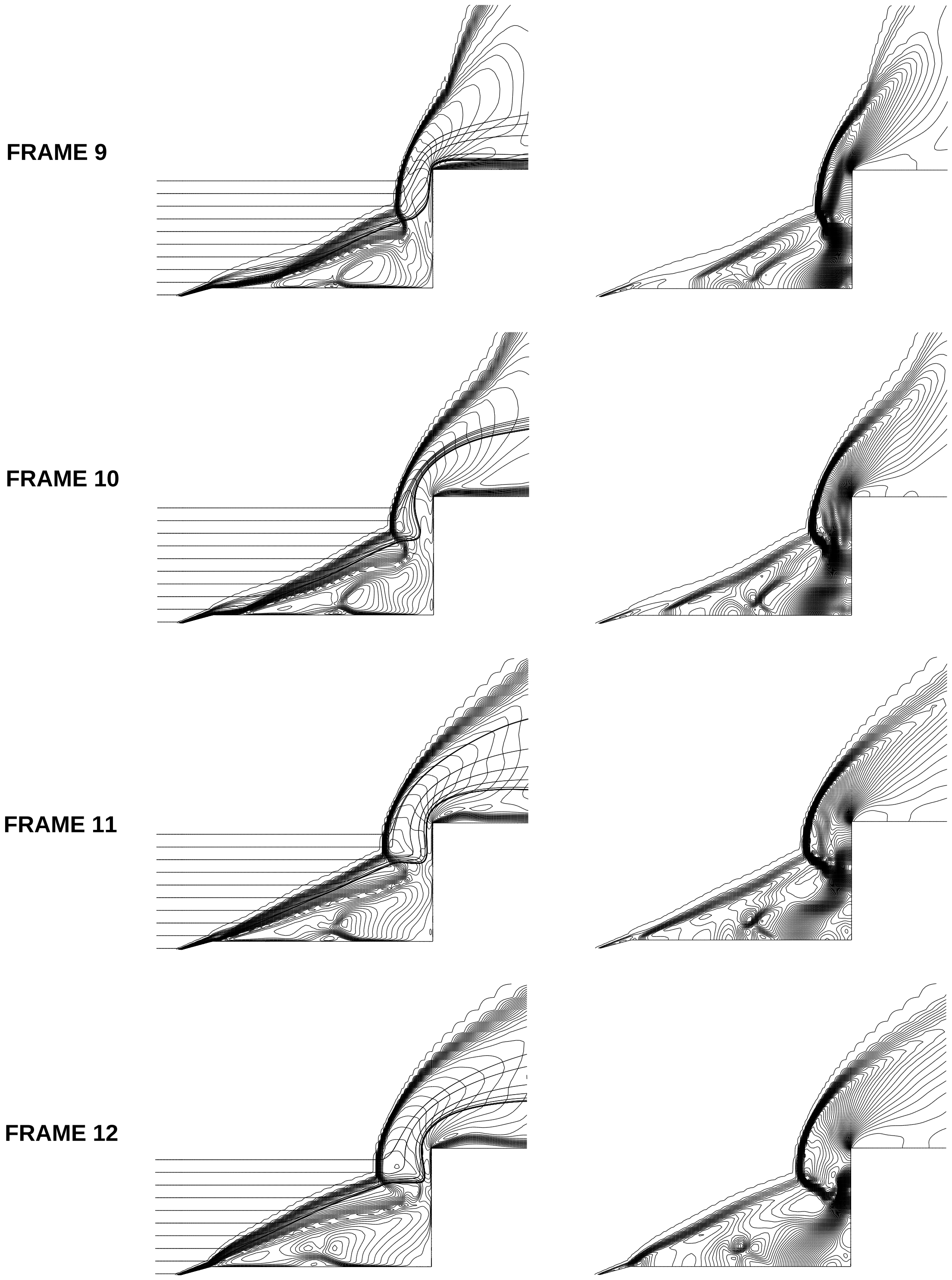

Figure 4.31: *(cont.) Pulsation at Mach 6.00, L/D=1.00. Shown are the Mach isolines superimposed with instantaneous streamlines (left column) and the pressure isolines (right column).*

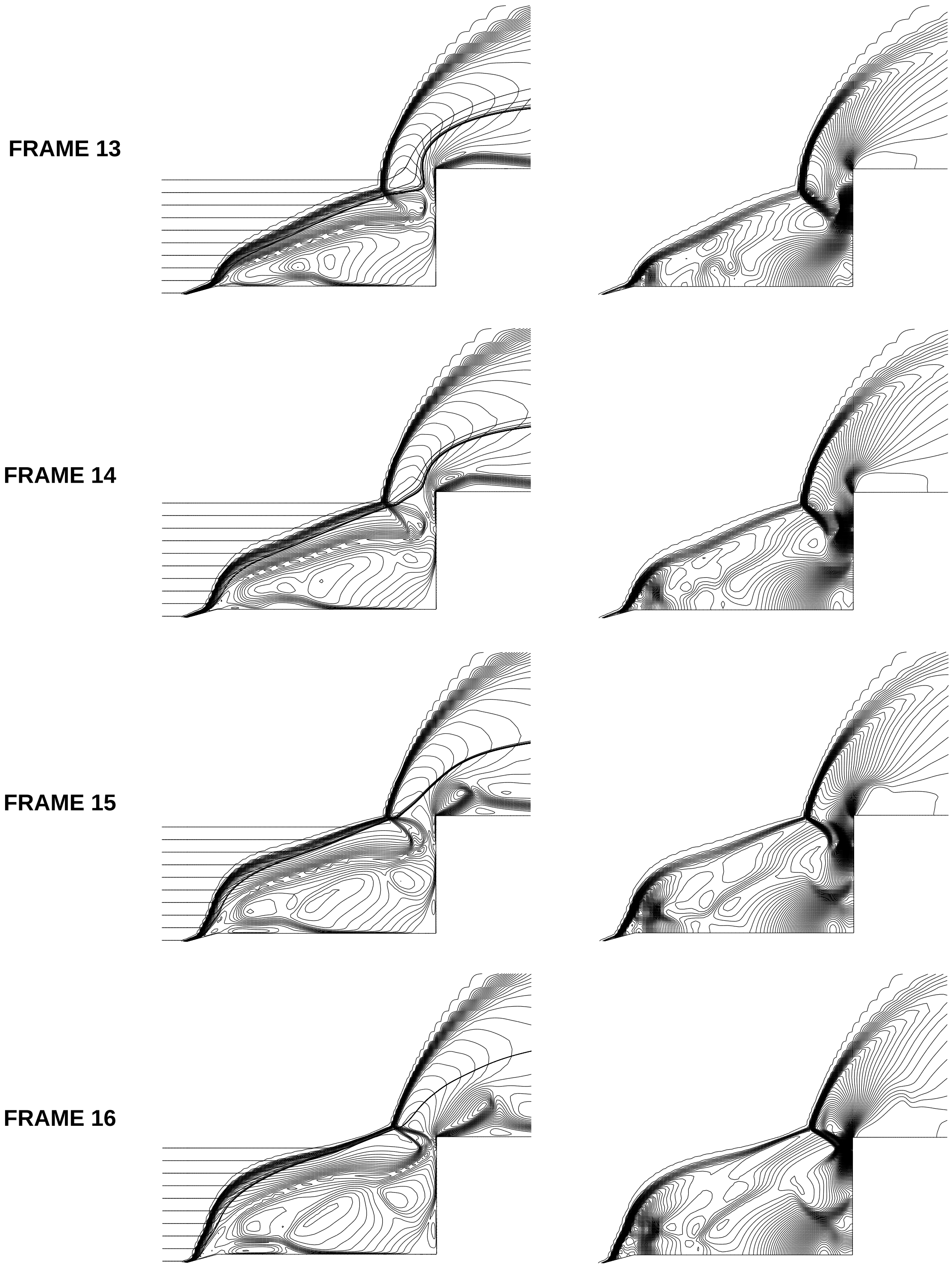

Figure 4.31: *(cont.) Pulsation at Mach 6.00, L/D=1.00. Shown are the Mach isolines superimposed with instantaneous streamlines (left column) and the pressure isolines (right column).*

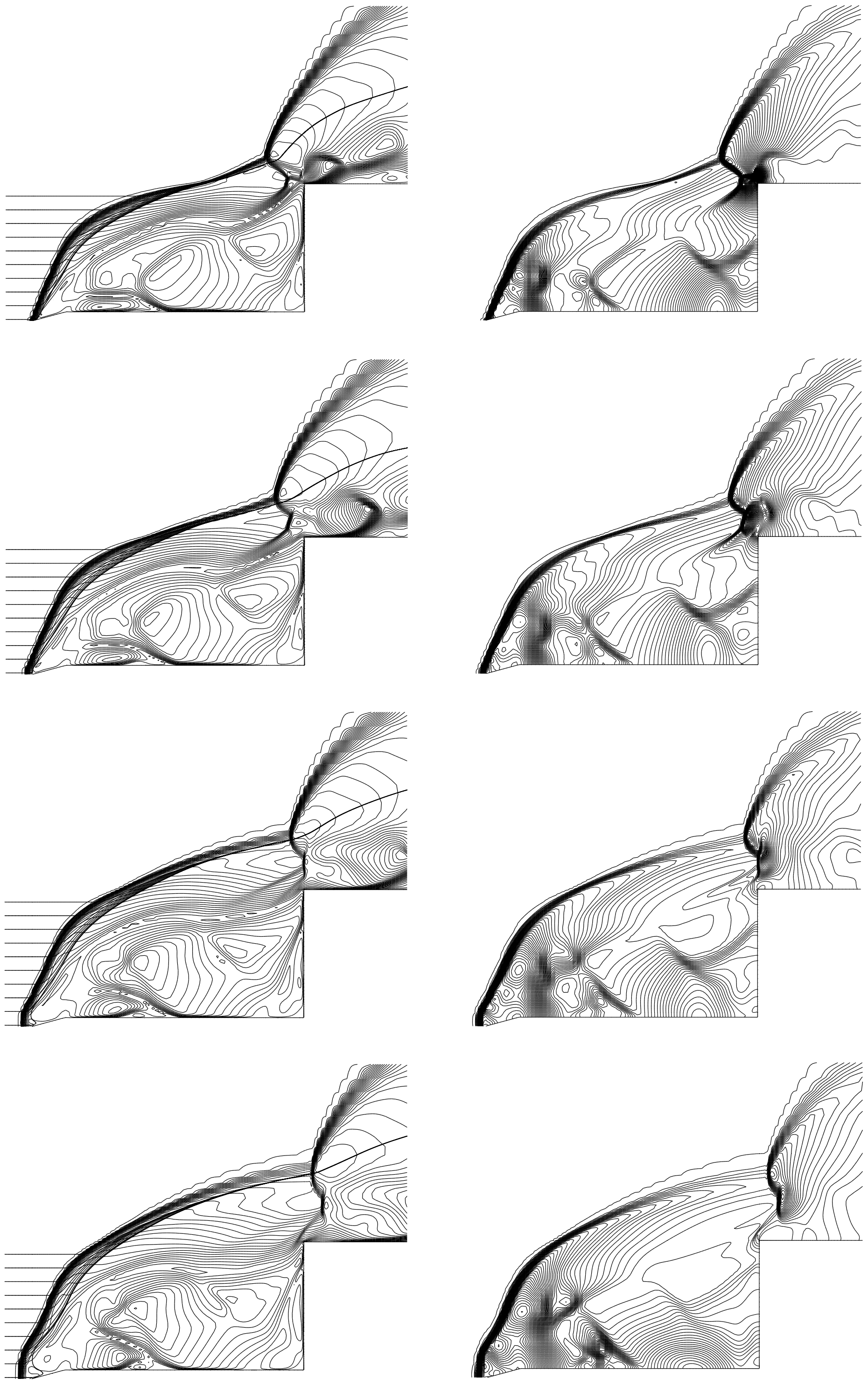

Figure 4.31: *(cont.) Pulsation at Mach 6.00, L/D=1.00. Shown are the Mach isolines superimposed with instantaneous streamlines (left column) and the pressure isolines (right column).*

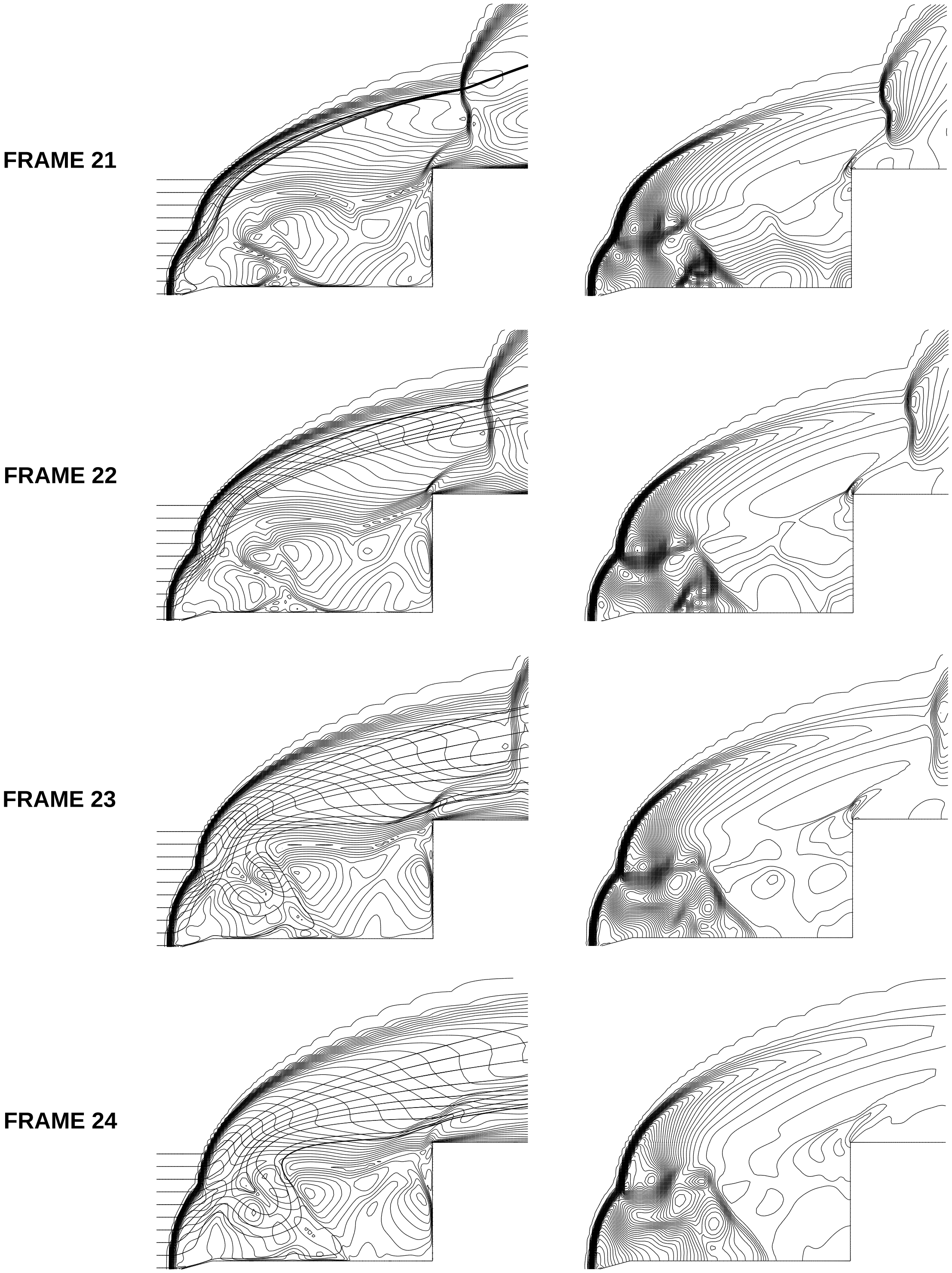

Figure 4.31: *(cont.) Pulsation at Mach 6.00, L/D=1.00. Shown are the Mach isolines superimposed with instantaneous streamlines (left column) and the pressure isolines (right column).*

FRAME 25

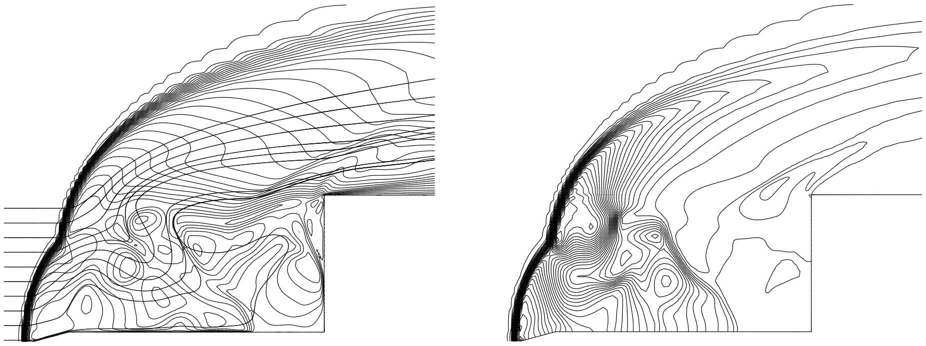

FRAME 26

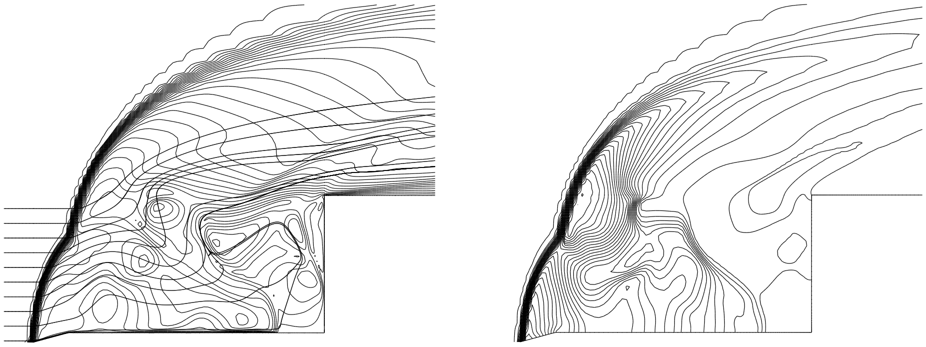

FRAME 27

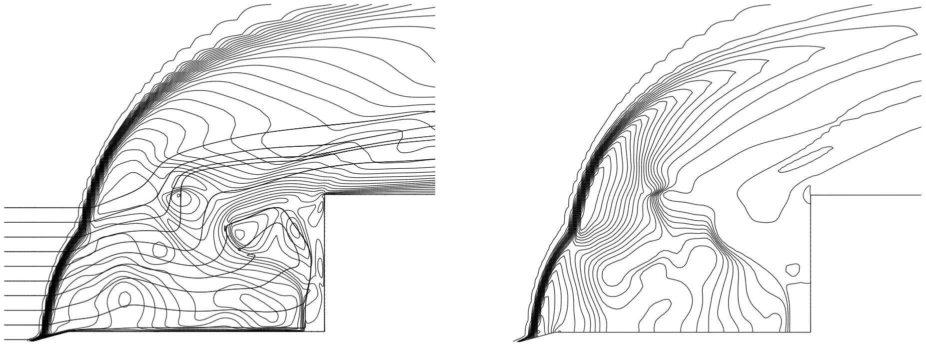

FRAME 28

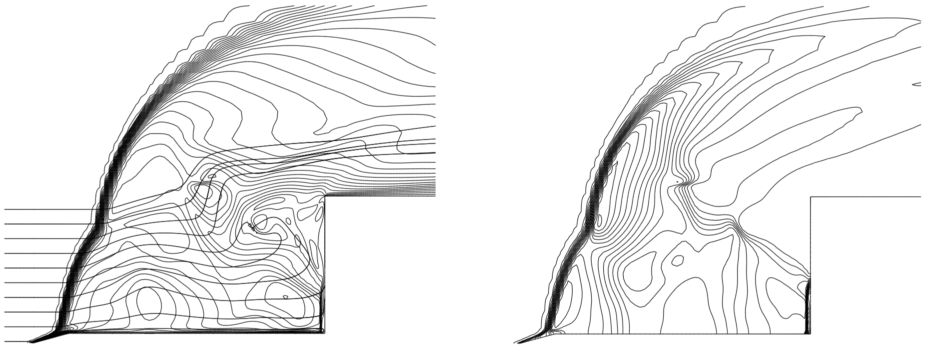

Figure 4.31: *(cont.) Pulsation at Mach 6.00, L/D=1.00. Shown are the Mach isolines superimposed with instantaneous streamlines (left column) and the pressure isolines (right column).*

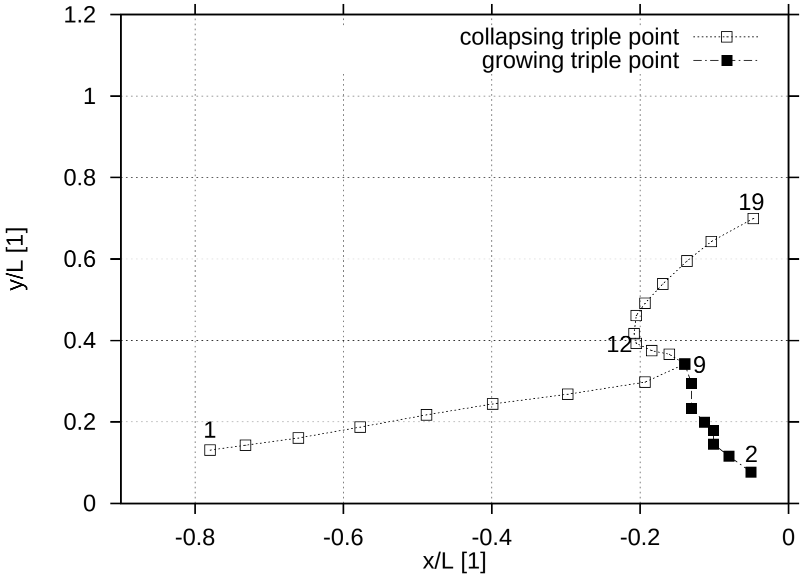

Figure 4.32: *Location of the triple point in time, pulsation at Mach 6.00 freestream.*

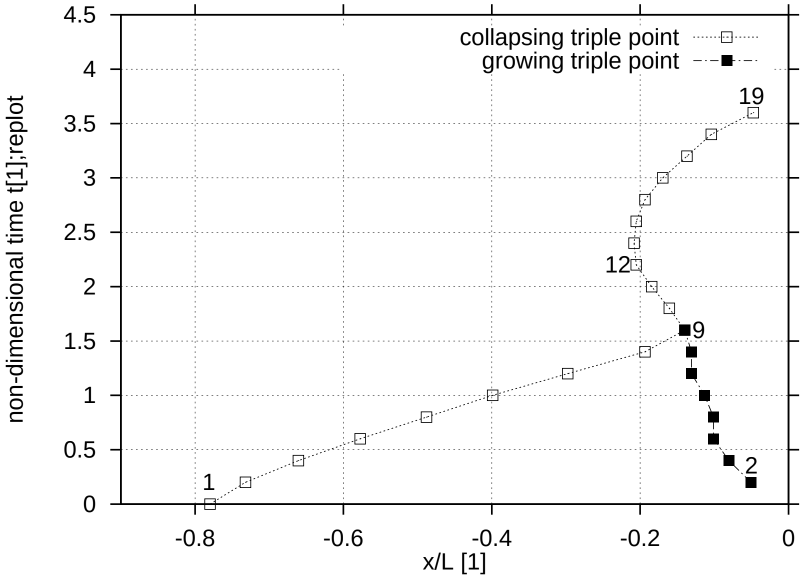

Figure 4.33: *X position of the triple point in time, pulsation at Mach 6.00 freestream.*

starts its growth with a certain delay in comparison to the supersonic freestream case. Interestingly, however, the collapse itself does not appear to happen significantly faster than before (to be discussed below), and thus the merging of the collapsing and growing bow waves will occur at a location well behind the freestream shock stand-off distance (frame 9). However, this effect becomes compensated as soon as the merged bow shock becomes pushed upstream to reach the shock stand-off position (frames 10-12). This was not observed in the Mach 2.21 case.

The speed of the collapse does not change significantly, even though the freestream Mach number becomes nearly three times larger than before. This is evident from Fig. 4.33, which shows the slope of the curve 1-9 to be $v_x = 0.4000[1]$, compared with value $v_x = 0.3335$ from the previous section. Based on the calculation procedure given in section 4.3.2, one can obtain $M_{2A} = 1.738$ for the value of the Mach number to which the afterbody is exposed behind the moving bow wave (with the intermediate results of $M_{x\infty} = 2.40$, $M_e = 3.60$ and $M_2 = 0.45$). This is again not much larger than the $M_{2A} = 1.357$ seen earlier, indicating, that the value of the freestream Mach number does not affect significantly either the conditions on the afterbody surface or the speed of the collapse.

Another difference implied by the high freestream nature is, that although the foreshock angle appears to be of the same order as in the Mach 2.21 case (compare Figs. 4.16 and 4.34), the foreshock itself will lie much closer to the shear layer. Thus, the triple point is kept in a lower position than before during the entire sections of inflation and withhold, having a dual effect on the evolution of the shock system. First, the expanded foreshock will appear as a more bell-like shape, with better pronounced curvature above the spike tip region (frame 16). Secondly, because of the closeness of the triple point to the afterbody, shock W3 (Fig. 4.23) interacts with the cylinder surface, leading to the appearance of complex shock structures as the triple point passes the shoulder (frames 17-20).

Finally, the Mach 2.21 and Mach 6.00 cases do not share the same trend regarding the foreshock angle (Figs. 4.16 and 4.34). While the former one is characterised by periods of constant values changing in discrete jumps, the latter one exhibits a rather

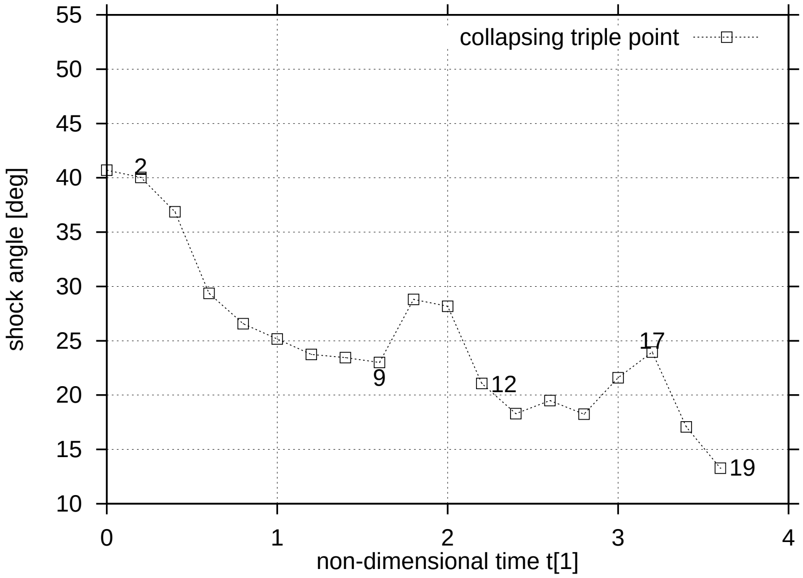

Figure 4.34: *Variation of foreshock angle in time, pulsation at Mach 6.00 freestream.*

continuous variation. This is because of the different minimum allowable shock angle appearing at the particular freestream and also because of the different separation zone thickness during the collapse. In fact, the foreshock angle cannot reach its minimum allowable value (9.6° at the Mach 6.00 freestream [19]) as it was seen in the Mach 2.21 case, since the separation zone's thickness is much larger due to the stronger normal shock causing the interaction. Thus, the angle of the foreshock will be guided by the shear layer angle. An increase in the shock angle occurs as the two bow waves merge (frames 10,11), which is the effect of the upstream movement of the merged shock wave. Then, the continuation of the previous decreasing trend follows, which is disrupted by the triple point passing the afterbody shoulder. The appearance of complex shock structures in the vicinity of the triple shock (discussed above) will also alter temporarily the foreshock angle.

Apart from these deviations, the rest of the characteristic flow features, and indeed the major ones such as the existence of the vortical region responsible for the mass influx, or the lift off of the shear layer by the streamlines penetrating into the separation zone, takes place by exactly the same manner as described earlier in the Mach 2.21 case.

4.3.5 The driving mechanism of pulsation

As a summary of the above analyses, the following picture of the driving mechanism of pulsation has been built up.

During the collapse of the expanded foreshock, a vortical region is generated within the growing triple shock system. This region feeds the separation zone with gas originating from the freestream for about the quarter time period of pulsation (7 out of 28 frames). When the growing and collapsing bow waves merge, the pressure at the afterbody face reaches a maximum. Also, the pressure field of the vortical region interacts with the merged shock to leave a strong pressure gradient decreasing in the upstream direction. This forces gas to be reversed rapidly into the separation region, from which it re-enters the supersonic stream behind the oblique foreshock via a shear layer. However, this recirculated flow is confined to the lower layers of the supersonic region by the flow coming from the freestream and hence will again be entrained by the vortex. This means a repeated recirculation of the flow and also that the mass of the gas trapped in the separation zone will be fairly constant. Thus, the original vortex and its residual pressure field have two different roles: the former one fills the separation zone with a certain amount of gas, whereas the latter one ensures that this gas does not escape.

The combination of these three factors: a nearly constant mass of gas in the separation zone, a recirculation driven by the residual pressure field and the high pressure accumulated at the cylinder face will drive the inflation/expansion process. The constant mass of gas increases its volume (the volume of the separation zone) as the high pressure near the cylinder face is relieved.

This leads to a lateral expansion of the foreshock and ultimately to its transformation to a bow wave. The high pressure arising at the bow wave will lift off the shear layer and will allow the flow to penetrate below the separation region. However, it does not possess enough energy to stop the recirculated flow, so after they collide it turns back in a direction opposite to the freestream flow to enter the supersonic region behind the oblique portion of the foreshock. As the shear layer is lifted off, more streamlines become involved in this process. Therefore, the size of the high pressure subsonic zone behind the expanded foreshock grows until it overwhelmes the recirculation zone's resistance. Then, the whole shock system collapses again.

4.3.6 Review of former pulsation concepts in the light of numerical results

The described driving mechanism represents a new explanation of the pulsation phenomenon. It has been enabled because of an important advantage of CFD in offering a detailed insight into all regions of the flowfield. It has been seen, that at some frames, the analysis of as much as four physical features (pressure, Mach number, instantaneous streamlines and velocity vectors) have been used to provide a 'richness' of information hardly achievable in the experiments. The previous explanations are now reviewed in light of the newly available data.

It had been recognised in the earliest investigations that the pulsation flow mode happens due to some sort of mass influx from the freestream into the separated region, which then inflates and collapses. All concepts, however, assumed that the mass influx takes place during the entire inflation process. In other words, that the pressure in the separation zone remains constant and that the volume change is caused by a mass added by some sort of flow reversal mechanism. (It has been seen from the CFD results, that the mass influx from the freestream does not operate for the entire process of inflation, i.e. the inflation is caused by a nearly constant mass of gas expanding into the forebody flow.) The major question was, however, how this mass influx is realised and from where the flow reversal originates? Three major concepts on this were put forward.

The earliest theory on the mass influx was suggested by Maull [4] assuming that it appeared because of the pressure imbalance between the region behind the bow wave and the separation zone (regions 3 and 5 in Fig. 4.35).

It is interesting to see that how this very first and simple explanation captures the essence of the driving mechanism revealed in the present work. The pressure imbalance does play an important role in the creation of the vortex. However, the mass inflow does not originate from region 3, but instead from region 4. This concept did recognise that the pressure in the separation zone was indeed considerably lower than that of the region behind the normal wave because of the zero pressure gradient across the shear layer ($\frac{\partial p}{\partial y} = 0$), dividing the supersonic region of the conical foreshock (region 2) and the separation zone itself (region 5 in Fig. 4.35).

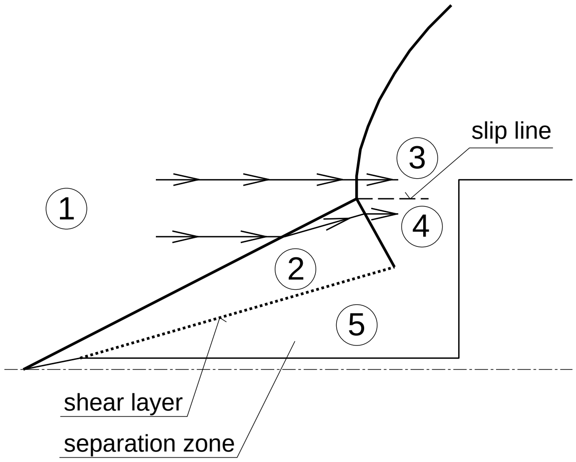

Figure 4.35: *Flow regions in pulsation.*

Antonov [26], Panaras [23] and Kenworthy [18] all showed that the mass entering the separation zone cannot originate from the subsonic zone behind the bow wave (region 3), but instead from the supersonic one behind the conical foreshock (region 2). Two different approaches appeared to substantiate this.

First, Antonov [26] claimed in his work, that the pressure in region 4 (Fig. 4.35) will actually be larger than in region 3, thus preventing the streamlines from this latter passing to the separation region (region 5). Although the latter conclusion itself proved to be true, the analysis of shock-shock interactions and CFD results show the pressures in regions 3 and 4 to be equal.

Secondly, Panaras [23] associated the shock system with Edney's type IV shock pattern (Fig. 1.10), also suggesting that the reversed flow originates from region 2 and not from region 3. Panaras termed region 4 as a 'supersonic annular jet', which, according to Edney's solution, is deflected and curved towards the body axis, thus inflating the separation zone (Fig. 1.10). In order to prove that region 4 is supersonic, he constructed a shock hodograph, more commonly called a 'heart diagram', to account for the behaviour in the vicinity of the foreshock-bow shock intersection (triple point [18]). As heart diagrams are normally suited to analyse only steady flows, Panaras assumed the pulsation to be a quasi-steady event. However, by considering region 4 to be supersonic, a slip-line will be formed between regions 3 and 4 (Fig. 4.35), along which the deflections (δ_3 and δ_4) and the pressures (p_3 and p_4) should be the same. This is only true just downstream of the triple point, but not necessarily over the whole regions of 3 and 4.

Based on the foreshock angle β, measured from the Schlieren pictures, Panaras was able to demonstrate that supersonic flow existed in region 4 (and simultaneously subsonic in region 3) for the Mach 6.00 freestream case. This solution is reproduced in Fig. 4.36a. Here, the positive deflection angles (δ) correspond to deflections away from the body axis, and thus any deflection of a left-running wave appears on the right-hand side of the heart diagram [37]. For example, the conical foreshock is a left-running wave, capable of causing positive deflections only (away from the body axis) and therefore, its heart diagram representation appears on the right-hand side of the shock hodograph. This means, that curve "a", corresponding to foreshock "A" in Fig. 4.36b is correctly plotted. Curve "c" is also correct, as shock "C" represents a right running wave relative to streamline 1. However, curve "b" appears on the left-hand side of the hodograph, meaning that if intersection "X" is to be achieved, then streamline 2 should experience a right-running wave in shock "B" (showed by a dashed line in Fig. 4.36b). Examining the numerical solutions or the shadowgraphs (Fig. 3.8) show that this is never the case. The bow wave is always left running (or normal at the worst) to the freestream. Therefore, a negative deflection in region 4 (or intersection "X" in Fig. 4.36) appears to be an unlikely representation of the flowfield taking place in pulsation. Examining the CFD results (for example Frame 9 in Fig. 4.12) shows also positive deflections in both regions near the triple point.

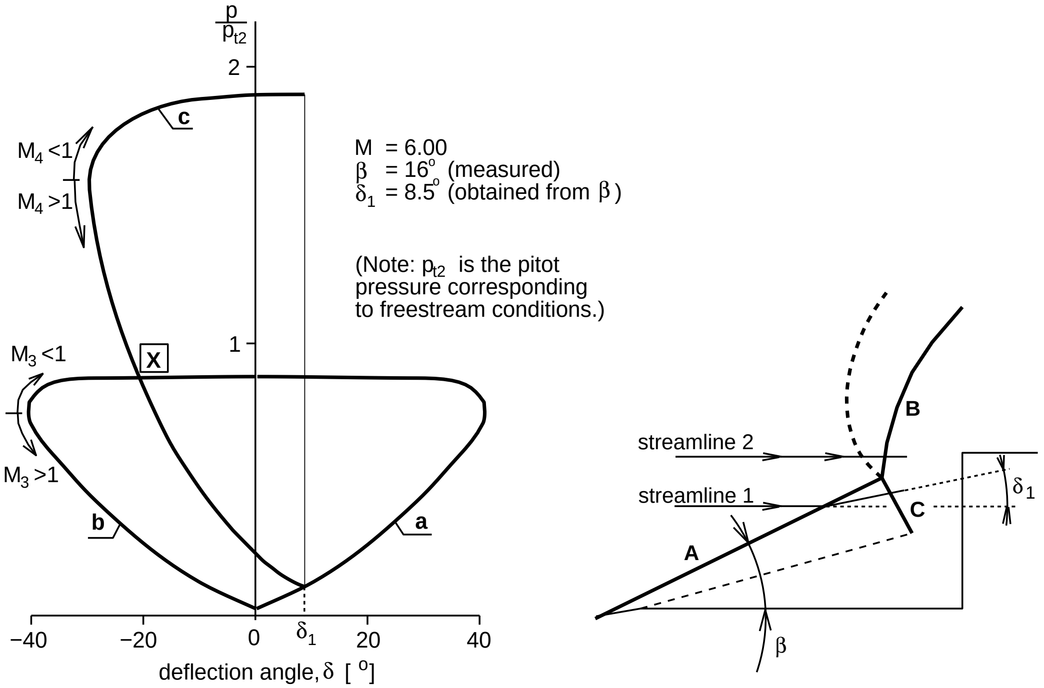

a) b)

Figure 4.36: *Panaras' quasi-steady heart diagram for the Mach 6.00 pulsation.*

Interestingly, if returning to the original idea of Panaras, which assumed that Edney's type IV shock system takes place in region 4, the same trend can be observed. A closer look on the shock pattern (Fig. 1.10) shows, that the strong shock (V-Q) is indeed left-running relative to the flow P_1, representing the freestream in our case. The flow behind this wave as well as in the jet region is initially deflected away from the freestream (or from the body axis in spiked body terms) and is turned back later, after experiencing a substantial number of reflections and curvature.

Another point related to this issue is that the previous effect occurs in a longitudinal distance almost twice as large as the length of the supersonic region P-Q-R (Fig. 1.10). As this latter corresponds to the conical foreshock in the spiked body case, it can be seen that the curvature of the supersonic annular jet is quite unlikely to occur in the pulsation flow mode, simply because the distance between the triple point and the cylinder face is too short to realise this rapid turning at the jet region (see frame 10 in Fig. 4.12 for the Mach 2.21 freestream, where this distance is only around 30 % of the foreshock length). This is especially true for the Mach 6.00 case, where the collapsing and growing bow waves merge well behind the freestream shock detachment distance (frame 9 of Fig. 4.31). This means, that even if Edney's type IV shock pattern was formed in spiked body flows, it would most likely reattach to the afterbody face at an angle yielding rather an outflow than a mass reversal to the separation region.

Inspired by Panaras' idea on the driving mechanism, Kenworthy [18] attempted to show that the same annular jet concept drives the lower Mach number pulsation cases as well. However, when constructing a heart-diagram for the Mach 2.21 freestream, subsonic flow was obtained in the jet region (see intersection 'X' in Fig. 4.38a). As it was feared that Edney's jet could not take place at such conditions, Kenworthy decided to re-examine the methodology of using heart-diagrams in the pulsation analysis.

Using East and Wilkinson's findings [38] he argued that unsteady flows characterised by Strouhal numbers larger than 0.01 should not be treated as quasi-steady. As the Strouhal number of the pulsation mode was found to be around 0.2 [18], he introduced 'dynamic' heart diagrams instead of Panaras' steady ones, taking into account shock movement as well.

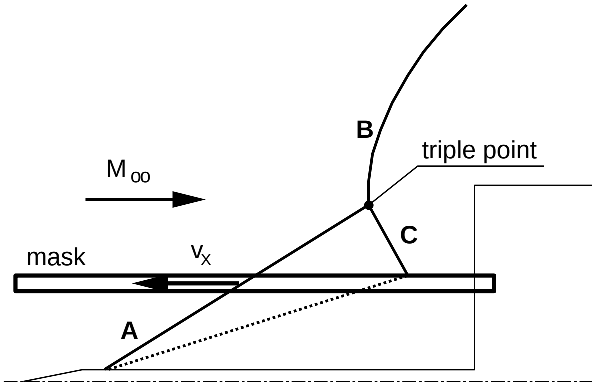

Figure 4.37: *Kenworthy's [18] measurement of the shock growth/collapse speed.*

In order to obtain the required shock movement speeds, Kenworthy recorded the foreshock's position in time experimentally through a mask located at the diameter D/2 (Fig. 4.37). By adding the obtained speed v_x to the freestream velocity v_∞, an effective Mach number, acting on the foreshock, could be obtained:

$$M_e = \frac{v_\infty + v_x}{a_\infty} = M_\infty + \frac{v_x}{a_\infty}$$

This value proved to be almost 30 % higher during the inflation than the freestream Mach number (Mach 2.80 instead of Mach 2.21). Thus, Kenworthy's reconstructed heart-diagrams were similar to Panaras' but with the difference, that his curve 'a' (Fig. 4.38b), corresponding to foreshock A in Fig. 4.37) was not calculated from the freestream Mach number 2.21, but from the above calculated effective one, Mach 2.80, instead. This yielded indeed a supersonic flow in region 4 (Fig. 4.35) even for the Mach 2.21 freestream (intersection 'X_{dyn}' in Fig. 4.38).

As it has been seen in the previous sections, the CFD results do not predict supersonic flow in region 4 for the Mach 2.21 freestream case. (In fact, a supersonic pocket did appear for a very short time only, but near the lower part of region 4, far from the triple point, close to which this analysis refers). So, Kenworthy's first quasi-steady graph (Fig. 4.38a) seems actually to predict a better solution at least

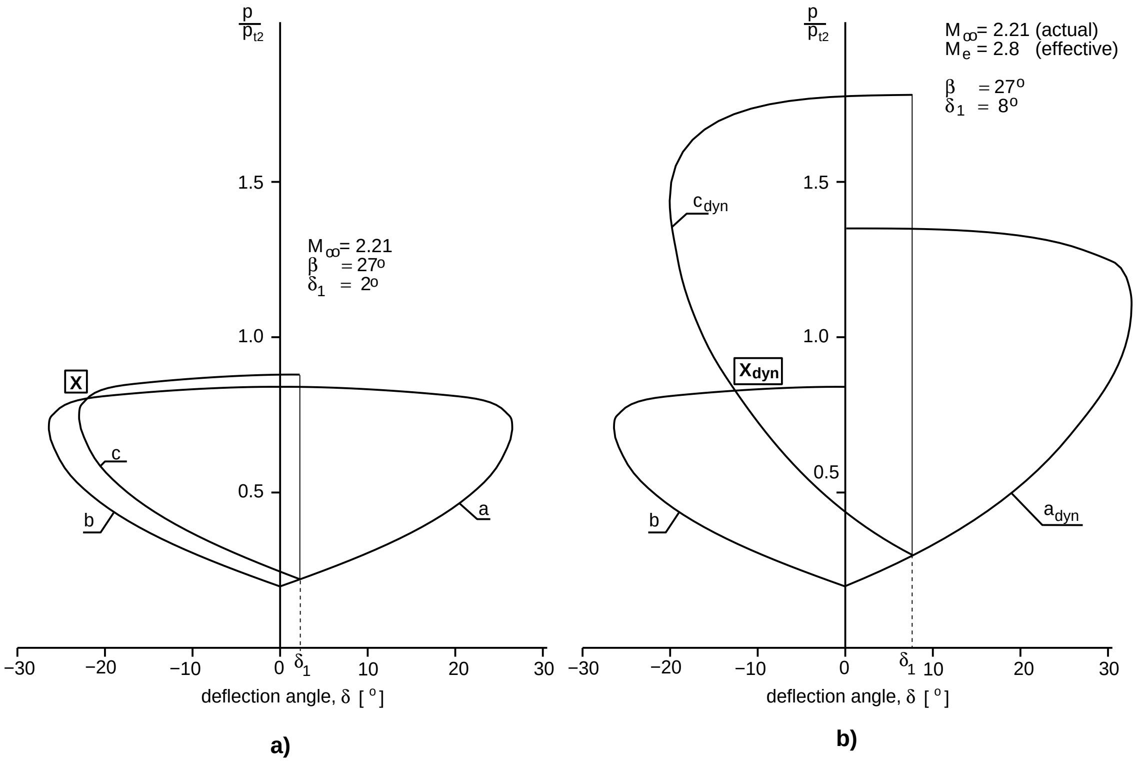

Figure 4.38: *Heart diagrams for the Mach 2.21 pulsation mode according to Kenworthy [18]. Quasi-steady (a) and 'dynamic' (b) solutions.*

in terms of the Mach number. Although the deflections seem to be in the opposite direction than the CFD results show, this finding inspired the re-evaluation of the role of shock motions using this methodology.

In Kenworthy's approach, the separation point moved rapidly forward, pulling along the foreshock. This was the reason for his assumption that the shock growth speed is important in the analysis. However, examination of the numerical and experimental results shows that at the moment when the two bow waves merge, i.e. when Edney's jet is supposed to be created, the separation point has almost already reached the spike tip shoulder and that for most of the jet's suggested existence it is actually completely still (frames 9 and 11 in Fig. 4.12)

This means, that the movement of the separation point and the creation of the jet are events taking place subsequently rather than simultaneously and therefore it seems to be quite unlikely that there is a connection between the two. Hence, if unsteady motions are to be involved in the the heart diagram analysis, then another point of reference should be considered.

As it was pointed out earlier, heart diagrams are suitable for the description of the situation in the vicinity of shock-shock intersection only and therefore, recording the movement of the triple point seems to be a reasonable approach. Zapriagaev and Mironov [28] were the first to track the triple point's position. However, they did not really exploit the information gained. The triple point has been used as a point of reference in the present work as well. The results showed (Figs. 4.14, 4.15 and frames 10-16 in Fig. 4.12), that its position is longitudinally almost fixed during the supposed jet creation, meaning that the very upper portion of the foreshock (the one closest to the triple point) will not experience any forward movement at all. Instead, the lateral movement appears to be more significant, which fact has already been exploited in the present work decribed earlier.

As a summary of this section it can be concluded, that all previous concepts involved elements which appeared in the driving mechanism revealed by the current results. These include the pressure imbalance first recognised by Maull [4], the fact that the flow originates from the supersonic region from behind the oblique foreshock by Antonov [26], Panaras [23] and Kenworthy [18], the importance of the unsteady shock motions by Kenworthy [18] and the need for taking the triple point as a point of reference by Zapriagaev and Mironov [28].

However, the assumption of continuous filling from the freestream during the entire process of inflation and the concept of Edney's type IV shock system as the source of flow reversal proved to be incorrect in the light of the numerical results. The main evidence regarding the latter issue is the lack of supersonic flow behind the triple shock system at the lower Mach number case, in which conditions the existence of Edney's jet seems to be doubtful.

Nevertheless, in the light of the information available from the experimental data all these hypotheses represented reasonable concepts based on the available data. They also offered a rich background and inspiration for the present research.

4.4 The hysteresis phenomenon

The numerical results of the hysteresis phenomenon are analysed in the present section. There are two principal aims of the analysis: to provide a description of the transition processes from one flow mode to another and to establish the necessary conditions for the onset of a new flow mode. The $v_{sp} = 0.004$ spike speed results will be used for this purpose, which appear to correspond better to a quasi-steady spike movement.

4.4.1 The oscillation/pulsation transition (O/P)

It has already been shown in the previous sections, how a single oscillation and pulsation cycle work. The basic concepts of these mechanisms are expected to remain unchanged even in the case of a continuously changing spike length. However, slight cycle to cycle deviations in the mechanism are anticipated to occur as the spike length increases/decreases, leading ultimately to the transformation to another mode. In order to illustrate these changes, a comparative approach has been chosen. This means, that frames corresponding to the same phase (for example, the ones representing the minimum and the maximum pressures) of the cycles will be visualised and compared. The subsequent cycles are marked as A-K and the points selected from them as 1-3.

The pressure history detailing the cycles of transition is shown in Fig. 4.39. The flow visualisation frames corresponding to these points are shown in Fig. 4.41. Mach number contours superimposed with seven, originally equally distributed instantaneous streamlines will be used for the purposes of the analysis.

The first obvious sign of the O/P transition is a rapid, almost exponential growth of the pressure amplitudes in the pressure history, starting at around $L/D = 1.33$ (Fig. 3.11). Although a slight growth of this parameter has also been displayed earlier, at longer spike lengths, it is not readily apparent what triggers the rapid

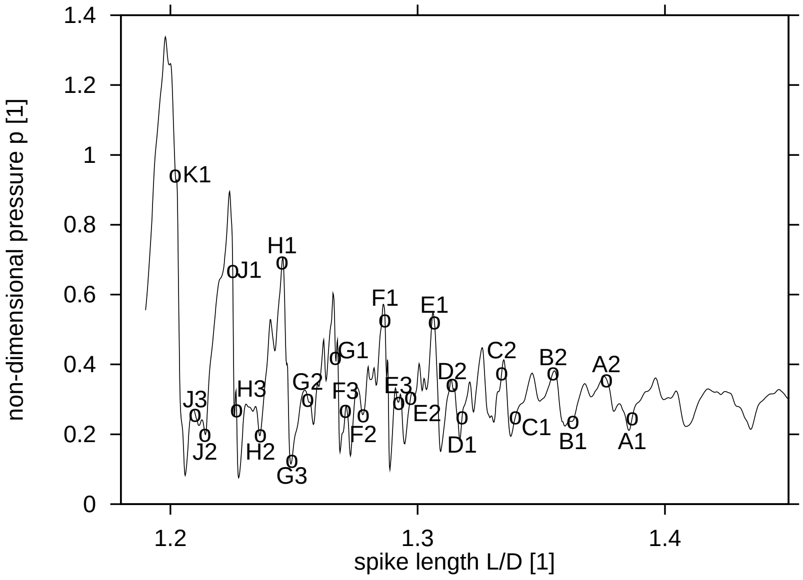

Figure 4.39: *Pressure history detail of the O/P transition for a continuously decreasing spike length. Freestream Mach number 2.21, spike speed* $v_{sp} = 0.004$.

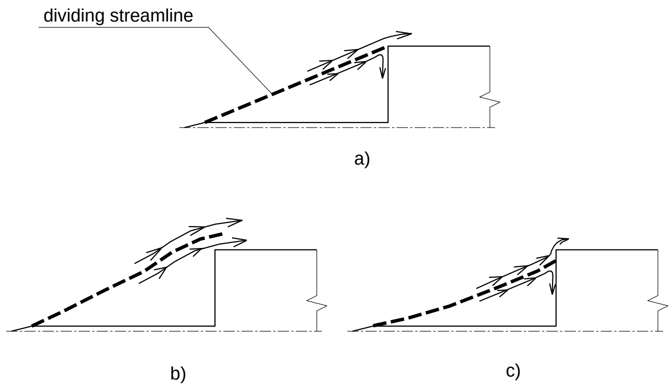

Figure 4.40: *Schematic of the oscillation mechanism.*

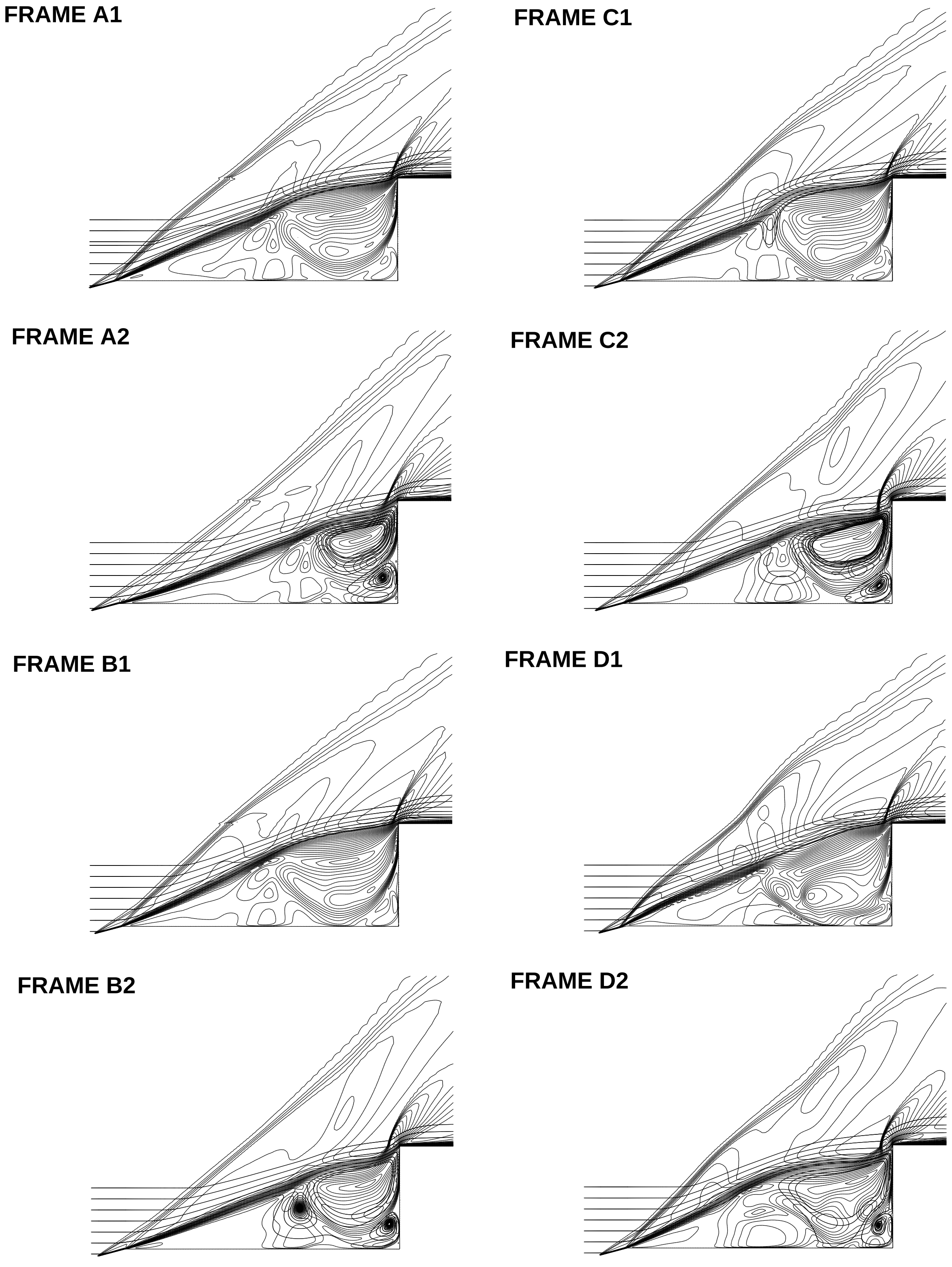

Figure 4.41: *The O/P transition occurring at a continuously decreasing spike length. Spike speed* $v_{sp} = 0.004$*, freestream Mach number 2.21. Mach number isolines and instantaneous streamlines shown for the frames from Fig. 4.39.*

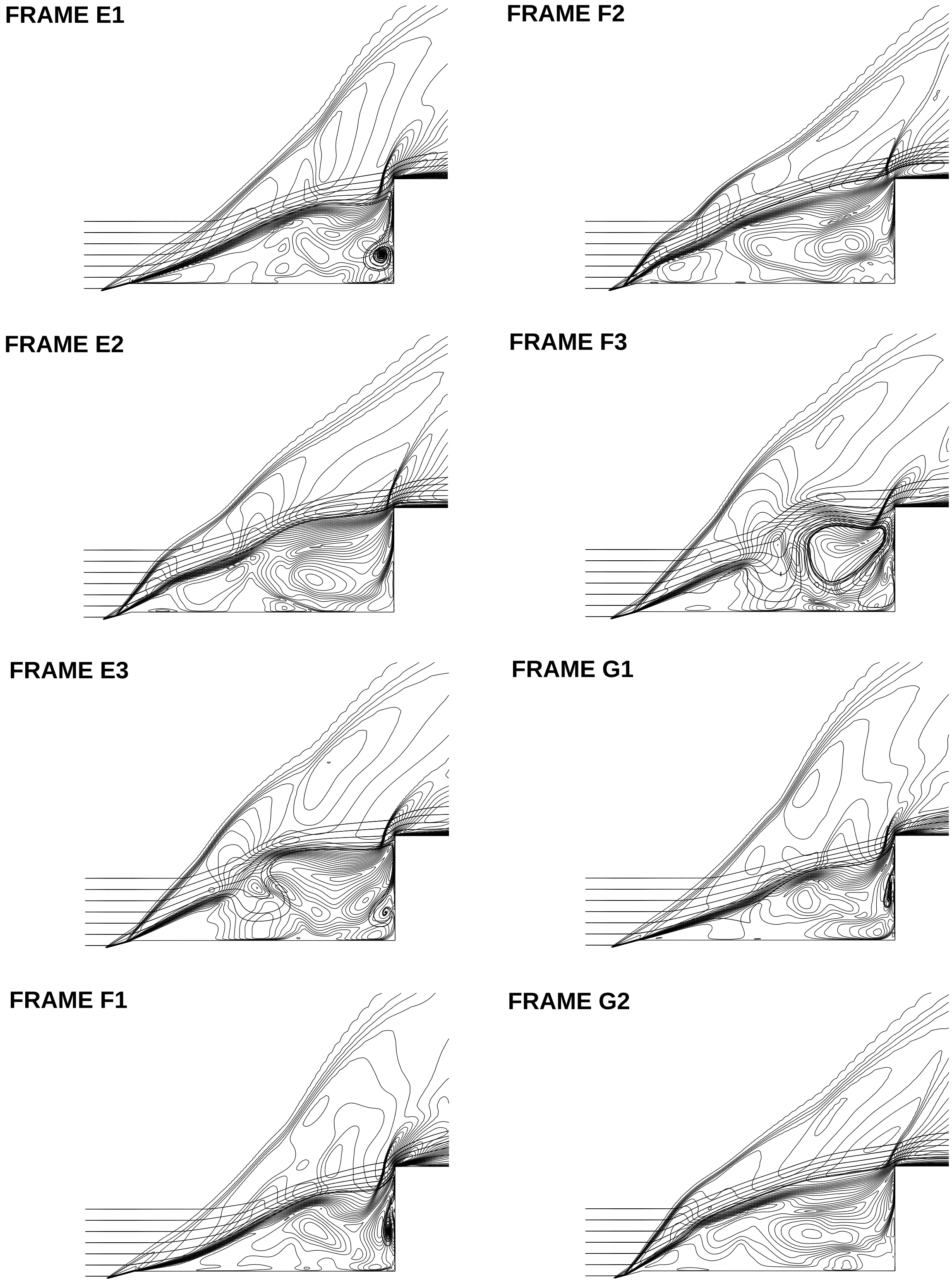

Figure 4.41: *(cont.) The O/P transition occurring at a continuously decreasing spike length. Spike speed* $v_{sp} = 0.004$, *freestream Mach number 2.21. Mach number isolines and instantaneous streamlines shown for the frames from Fig. 4.39.*

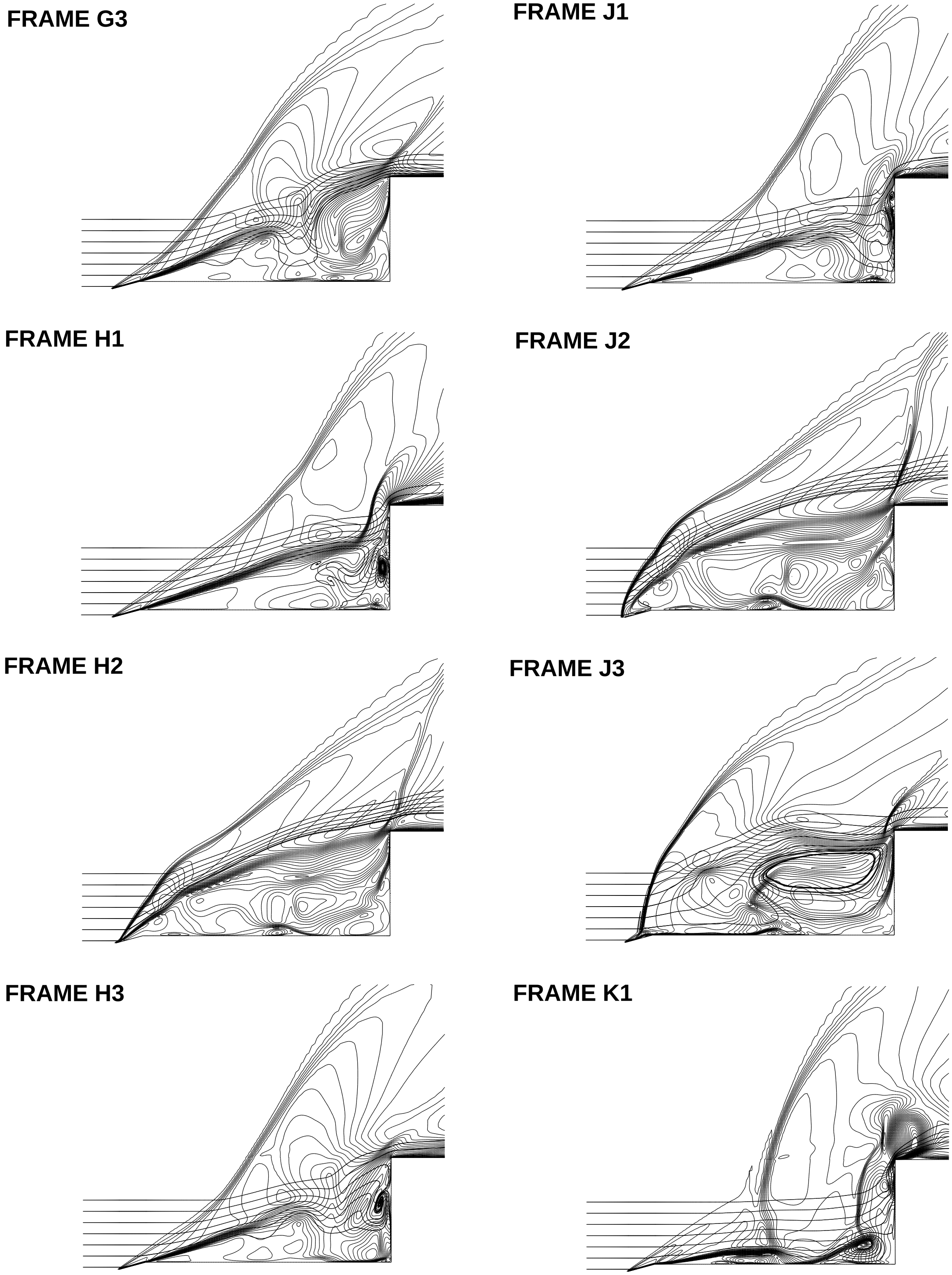

Figure 4.41: *(cont.) The O/P transition occurring at a continuously decreasing spike length. Spike speed* $v_{sp} = 0.004$*, freestream Mach number 2.21. Mach number isolines and instantaneous streamlines shown for the frames from Fig. 4.39.*

growth and why it appears exactly at this spike length? The answer could be found in the nature of the oscillation mode. As it has been shown previously (section 4.2), the oscillation mode is driven by an ever-changing shoulder reattachment condition of the shear layer. As the latter swings radially near the afterbody shoulder, it is either lifted to allow the gas to escape from the separation zone (Fig. 4.40b), or it is reattached to the cylinder face so that most of the shear layer flow is reversed, causing influx into the separation region (Fig. 4.40c). It has also been pointed out, that the separation point reacts to this mechanism with a certain delay, i.e. it moves downstream during the filling and is pushed upstream during the flow escape from the separation zone. This anomaly can be explained by the fact, that the filling can only take place when the shear layer reaches its lowest position (angle). In such a situation, a low pressure is present in the separated zone, meaning that the separation point will be forced downstream (suction effect). As the filling stops, the gas trapped in the separation zone starts to expand, forcing the separation point forward.

The delay in the timing of the separation point appears to play a crucial role in the growth of the pressure amplitude during the changing spike length. In fact, the amount of gas supplied into the separation zone depends on the geometrical conditions present at the instant when the shear layer is at its lowest position. A mass influx arising at this point would be sufficient to maintain a self sustained oscillation if the spike length was constant. However, by the time the information about the quantity of the mass influx reaches the separation point, the spike tip has already moved downstream, closer to the afterbody, by a small portion. Thus, the separation point is pushed more forward relative to the spike, than in the earlier cycle, because the amount of gas producing this effect proves to be more than required. For the same reason, the shear layer's lateral expansion will also be larger, allowing more gas to escape from the separation zone as the shear layer waviness propagates downstream. Therefore, the pressure loss appears to be more substantial than would be necessary to maintain a regular, self-sustained oscillation, and the shear layer will deflect down to a much lower position than before. This effect is well illustrated by frames A1-A2, B1-B2, C1-C2, showing the lowest and the highest positions of the shear layer in three consecutive cycles. Note, that since the outer portion of the cylinder face will no longer be exposed to a subsonic flow, an annular bow wave appears in front of it. This grows gradually in the subsequent cycles as the minimum angle of the shear layer decreases. The lower down the face that the shear layer reattaches, the more streamlines are reversed into the separation zone, intensifying the filling mechanism and pushing the separation point further forward.

In the next cycle, the separation point passes the spike tip shoulder for the first time (frame D1). However, as the shear layer emerging from the separation point aims to maintain its relative angle to the spike tip surface, a sudden break appears in its shape. This becomes more apparent later, when the waviness in the shear layer, caused by passing the spike tip shoulder, propagates downstream (frame D2). The evidence of the shear layer disintegrating is well demonstrated by the first three streamlines introduced, leaving it at around the half-distance of the spike. This is the first ‘pulsation-like’ feature of the flow, at which the lift-off of the shear layer was accomplished also by the streamlines penetrating into the separation zone.

Frame E1 shows the number of introduced streamlines participating in the filling mechanism to be increased to four in contrast to the two seen in the first cycle (frames A1-A2). The separation point reaches further upstream in the subsequent cycle (frame E2) and the break of the shear layer takes place in a more violent manner (frame E3).

These features are gradually enhanced in the next three cycles (frames F1-F3, G1-G3 and H1-H3). By the last one of them (H), the five lowest introduced streamlines are involved in the flow reversal (frame H1) and the separation point nearly reaches the spike tip (frame H2). The shear layer's second half almost completely disappears at this time, and because there is nothing to guide the streamlines emerging from it, they impact on the cylinder face as though in a random fashion (frame H3).

With the convection of the shock system downstream, a straight shear layer is re-established (frame J1), intersecting the annular bow wave. This has now become fairly large. Then, the separation point reaches the spike tip for the first time, detaches from it and a small bow wave is formed as a consequence of that (frame J2). This is the first clear sign of the pulsation mechanism.

As it has been shown earlier, in section 4.3.3, the streamlines penetrating through the initial bow wave will eventually lift off the shear layer from the spike and expand the previously oblique foreshock to a bow wave. As this is being convected downstream (frame J3), it is as though the afterbody accelerated to a supersonic speed, leading to the appearance of an entirely new bow wave in front of it (frame K1). This implies the creation of a triple shock system with the vortical region inside it, which starts the full pulsation mechanism.

4.4.2 The necessary condition of the O/P transition

Based on the above description, the necessary condition of the O/P transition can be established. The oscillation mode will transform to the pulsation only when the separation point reaches the spike tip. This transformation is preceeded by a transitional process characterised by a rapid growth of the pressure amplitude, triggered by the separation point passing the spike tip shoulder for the first time.

This finding implies an interesting conclusion, namely, that different spike tip functions (for example, Calarese and Hankey [25] used a hemisphere spike ending) could exhibit different transitional processes in terms of their duration.

4.4.3 The pulsation/oscillation (P/O) transition

The P/O transition exhibits a rather different behaviour in its pressure history than the previously seen O/P one. The two main differences are the following.

Firstly, the transition takes place abruptly (see Fig. 3.11), with no sign of prior “preparation” as it has been seen in the case of the O/P transition case. Secondly, the last twelve cycles exhibit somewhat larger pressure amplitudes than those of the preceeding ones. This latter observation was found to be in accordance with the available experimental hysteresis data of Calarese and Hankey [25], where the pulsation amplitudes were measured to be approximately 15 % higher just before the P/O transition than those outside the hysteresis region (see Fig. 1.14). In the numerical method, the last cycles differ by 18% from the preceeding ones, confirming that the computational solution is likely to be qualitatively correct. This is an important feature as it means, that despite the overprediction of the P/O transition value, the description of the transformation itself should be valid.

The detail of the pressure history is provided in Fig. 4.42. Note, that the graph in this instance is given not in terms of spike length but in time instead. This enables to illustrate later the increase of the time periods. Flow visualisation frames of the selected points are shown in Fig. 4.43.

First, let us examine the pulsation mode operating at this extremely large spike length. Frame A1 shows the time at the instant of the collapse. However, along with the two triple shock systems seen at the short spike length pulsation (the collapsing and the growing bow wave, section 4.3.3), a third triple shock system could also be observed (illustrated by the pressure isolines plot in frame A1 of Fig. 4.44). It appears at approximately the half-distance between the two waves and by consid-

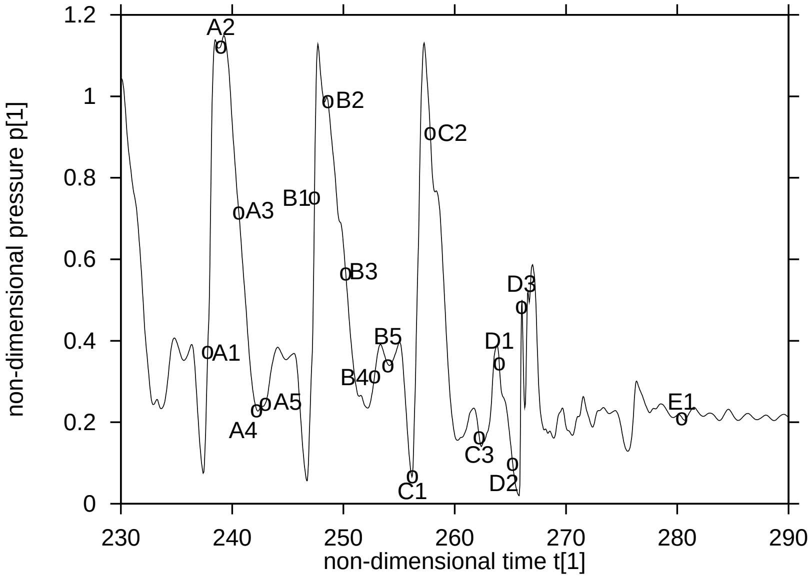

Figure 4.42: *Pressure history detail of the P/O transition for a continuously increasing spike length. Freestream Mach number 2.21, spike speed* $v_{sp} = 0.004$.

ering the direction of its movement it is collapsing. This triple shock system could not be observed earlier since it is created by shock wave W9 overtaking separation region P3 (see Fig. 4.16) during the convection downstream. This process could not take place at shorter spike lengths, because W9 strikes the wall much sooner.

As this central shock system merges with the growing triple shock, the vortical region already formed in the latter one transforms to a residual (frame A2 in Figs. 4.43 and 4.44). This is another difference from the shorter L/D case, where the residual of vortical region appeared because of the merger with the collapsing bow wave.

As this feature contributes to the filling and expansion processes, the separation point is pushed upstream along the spike (frames A3, A4) until it eventually reaches the spike tip. Then, the foreshock expands to a small bow wave, allowing the streamlines to lift off the shear layer (frame A5). Note, that a small annular bow wave remains present at the afterbody shoulder, keeping the vortical region residual, and thus the flow recirculation in the separation zone operational.

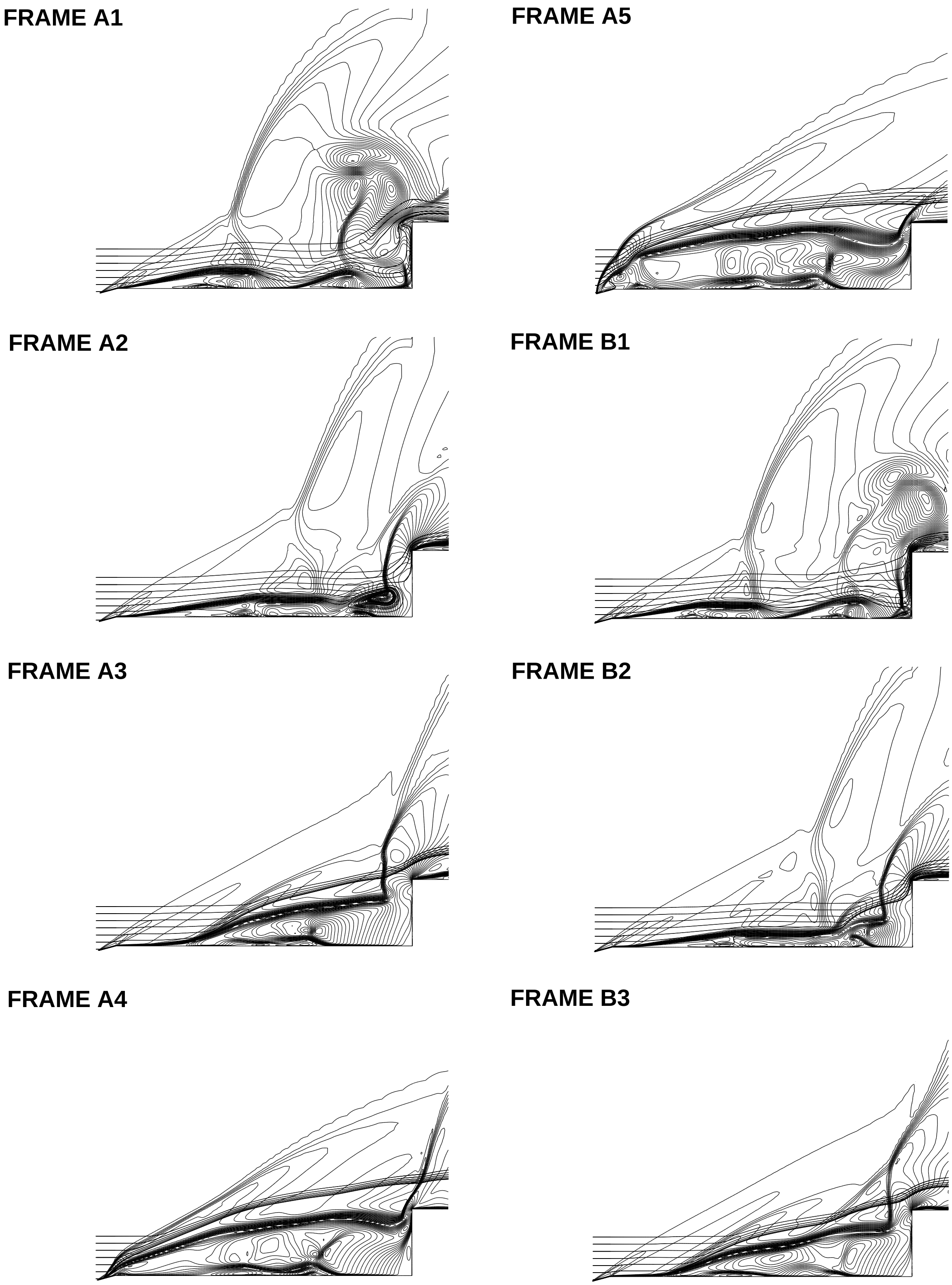

Figure 4.43: *The P/O transition occurring at a continuously increasing spike length. Spike speed* $v_{sp} = 0.004$*, freestream Mach number 2.21. Mach number isolines and instantaneous streamlines shown for the frames from Fig. 4.42.*

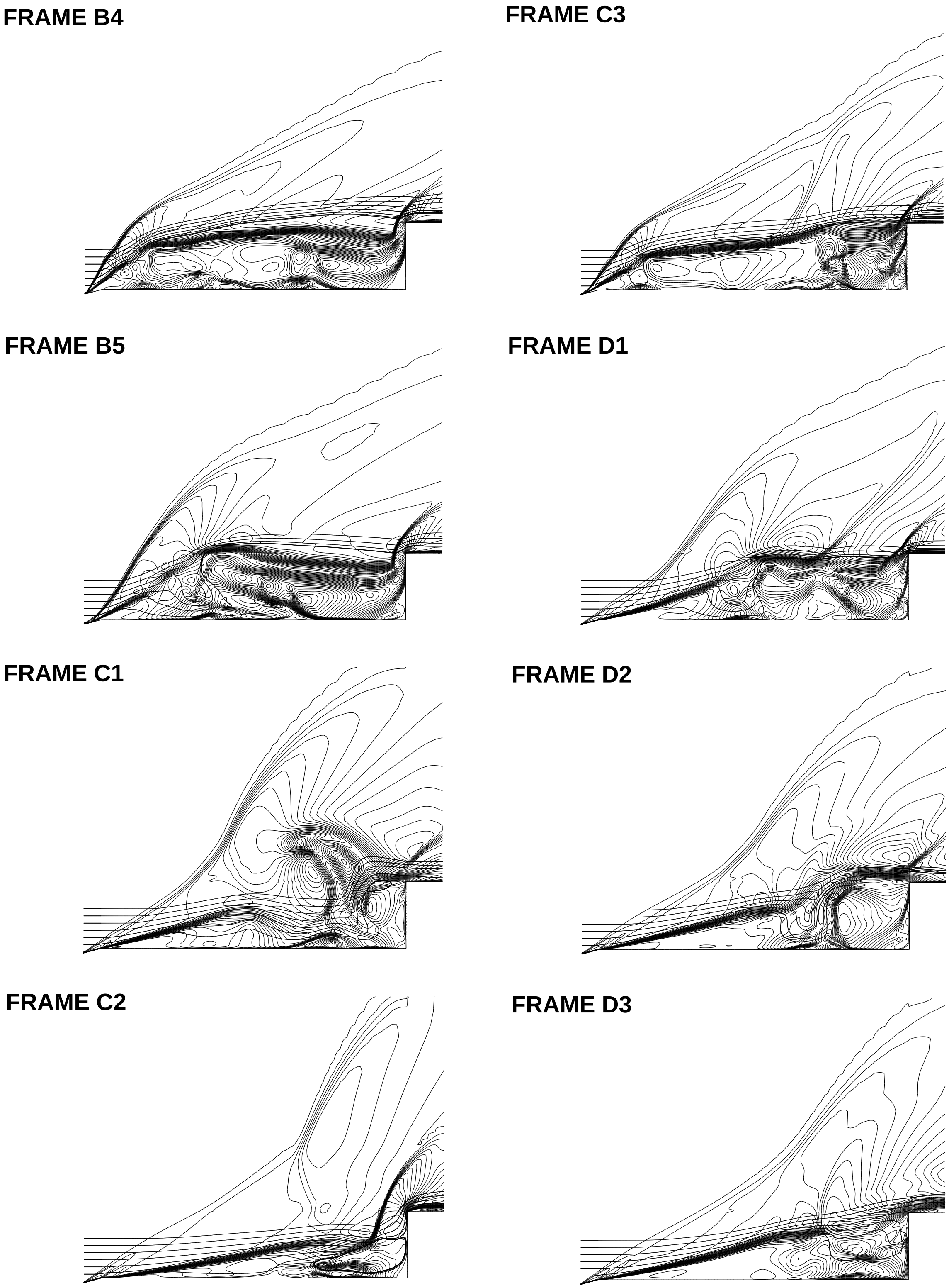

Figure 4.43: *(cont.) The P/O transition occurring at a continuously increasing spike length. Spike speed* $v_{sp} = 0.004$, *freestream Mach number 2.21. Mach number isolines and instantaneous streamlines shown for the frames from Fig. 4.42.*

FRAME E1

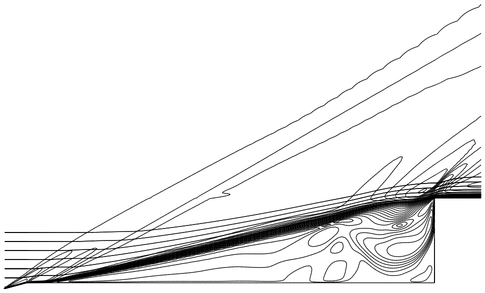

Figure 4.43: *(cont.) The P/O transition occurring at a continuously increasing spike length. Spike speed* $v_{sp} = 0.004$*, freestream Mach number 2.21. Mach number isolines and instantaneous streamlines shown for frames from Fig. 4.42.*

The same processes take place in the next cycle (frames B1, B2, B3), however, this time with the difference that the bow wave cannot be formed at the spike tip (frame B4). This is due to the increased spike length, meaning, that although the separation point can still reach the spike tip, there is not enough energy left in the flow to accomplish the lateral expansion fully. Hence, the shear layer remains attached to the spike tip, not allowing the streamlines to penetrate into the separation zone immediately. However, most likely due to the dynamics of the event, the shear layer is torn apart once again causing the streamlines to leave it and to enter below the secondary shear layer within the separation zone (frame B5). During the collapse, the recirculation zone is squeezed for the last time in a pulsation like manner (frame C1). Meanwhile, the downstream convection causes the attached shear layer to be lengthened, creating a shallow but long separation zone. This does not allow the growing triple shock system's lower part to be properly developed, causing a lack of the vortical region inside it (frame C2 and also Fig. 4.44). Without this generator of pulsation, the separation zone cannot be filled to its full extent and the separation point looses its ability to reach the spike tip. This is further enhanced by the increased spike length (frame C3).

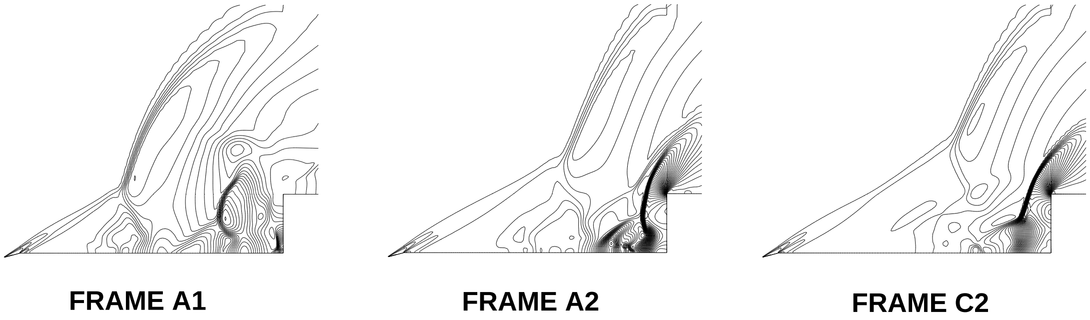

Figure 4.44: *Pressure contour plots for frames A1, A2 and C1 from Fig. 4.42. P/O transition at a continuously increasing spike length, spike speed* $v_{sp} = 0.004$*, freestream Mach number 2.21.*

Due to the poor expansion, the angle of the foreshock will be smaller than in the previous cycle (compare frames C3 and B4), meaning less pressure behind it. Thus, the streamlines emerging from this region will not possess enough energy to lift the secondary shear layer off (frames D1, D2) and as the collapse is completed, the entire cylinder face will lie in the wake of a subsonic separation zone (frame D3). As no bow wave can be formed in front of the afterbody, the pulsation generator vortical region will be missing in this cycle.

Hence, in the subsequent cycle, the separation point will be unable to reach the spike tip shoulder, and the flow soon becomes steady (frame E1).

4.4.4 The necessary condition of the P/O transition

Summarising the above findings it can be stated, that the P/O transition occurs at the spike length at which the separation point cannot reach the spike tip. This also implies the conclusion, that from the numerous elements of the pulsation mechanism revealed in the earlier sections, the most crucial one is the lift off of the primary shear layer. If this element cannot be realised, the pulsation transforms abruptly to oscillation/steady flow.

Chapter 5

Conclusions

The primary aim of the present work has been to investigate the driving mechanisms of high-speed unsteady spiked body flows by using Computational Fluid Dynamics as a tool. Three main issues were addressed: the oscillation and pulsation flow modes and the hysteresis phenomenon. Conceptually, the numerical results were first verified and extensively validated before proceeding to their analyses.

The numerical method was described and verified in Chapter 2. Axisymmetric, laminar modelling was chosen as an acceptable description of the examined problems. It should be acknowledged, however, that the role of turbulence effects cannot be entirely neglected in spiked body flows. The large vortical regions appearing in the pulsation flow mode are likely to provoke turbulent flow/large eddies within the separated region. Also, it is uncertain whether the shear layer remains fully laminar during the oscillation mode or it undergoes transition to a turbulent one, which would enhance the mixing. These issues could not be addressed in this thesis since the $k - \omega$ model available in the used numerical method exhibited robustness problems during the preliminary calculations. Thus, future computational work should aim to provide turbulent simulations in order to assess the effect of the turbulence on the results. Such simulations will possibly necessitate the use of a Large Eddy Simulation (LES) method tailored for high-speed applications.

The main findings of the verification of the numerical method can be summarised as follows:

For the fixed spike length cases

- medium grids yielded grid convergent solutions,
- the use of maximum time step was possible.

For the moving spike cases

- medium grid yielded grid convergent solution at the lower (O/P) boundary of the hysteresis range,
- finer resolution grid would be required at the upper (P/O) boundary of the hysteresis range,
- the use of reduced time steps was necessitated

In order to keep the computational costs of the moving spike calculations at an acceptable level, the medium grid was applied for the entire range of the hysteresis phenomenon. This means, that the numerical results should be treated as both qualitatively and quantitatively correct at the lower boundary of the hysteresis range only, and only qualitatively correct at the upper one. This deficiency of the numerical simulation was compensated to a certain extent by the originality of such results and hence a qualitative evaluation was still considered valuable. If a fully grid convergent solution was achieved, then this would lead to further increase of the hysteresis range. The most promising way of achieving grid convergence near the P/O boundary appears to be the development of a special deforming mesh technique capable of maintaining optimal grid resolution (for example by introducing extra gridlines in a suitable manner).

In Chapter 3, the numerical results were validated. A comprehensive comparison with the experiment was provided and the main results are:

- in accordance with the experiment, the pulsation flow mode is characterised by pressure amplitudes of the order of the pitot pressure (p_{t2});
- oscillation is found to exhibit pressures an order of magnitude smaller than those in pulsation, which agrees with the experiment;
- the frequency, the characteristic shape of the pressure trace and the shock envelope history were found in very good agreement with the measurements;
- the pressure amplitudes agreed in the Mach 2.21 cases only, but were overpredicted in the Mach 6.00 cases
- the hysteresis phenomenon was qualitatively successfully predicted;
- quantitatively, the lower boundary of the hysteresis range was found in good agreement with the experiment, but the upper one was well overpredicted.

The disagreement of the pressure amplitudes is most likely due to the suggested errors in the measurement. The small scale of the model ($D^* = 20$[mm]) could mean difficulties in maintaining perfect axisymmetry, while the use of cavity-like pressure transducers and the high frequency of the event were likely to yield resonance and pressure amplification. The latter argument was supported by the fact, that larger frequencies yielded larger deviations from the experiment (Mach 6.00 cases). Thus, the agreement of the pressure amplitudes proved to be less important than the correct prediction of the frequencies and the other characteristics of the flow modes [18]. The high frequency of the instabilities was also responsible for the most striking difference between the CFD simulation and the experiment: measurements capture a large number of cycles which could hardly provide data from one particular period (hence the shock envelopes were constructed from frames obtained from different cycles), whereas CFD is advantageous for simulating few cycles only. These are ideal for detailed analysis but not well suited for comprehensive time-averaged or power spectra evaluations. Therefore, if the observations of a CFD analysis should be confirmed experimentally, then advanced measurement techniques, such as the capability of recording as much as 10^5 frames/s and taking pressure measurements from more locations on the model surface, would be required.

The significant disagreement of the upper boundary of the hysteresis range was not fully understood but it is most probably caused by some other features as well as the possible axisymmetry issue. From the two spike speeds considered the lower one seemed to correspond better to a quasi-steady phenomena and hence was judged as qualitatively realistic. Although the set of available results does not allow a strong conclusion on this, it appears that the hysteresis range can be significantly reduced by applying a very fast spike speed.

The runtimes for fixed spike length calculations were of the order of days (considering a Pentium Pro 200 MHz processor) which times are likely to be reduced to order of hours by the rapid development of computational facilities. Thus, CFD simulations of spiked body flows appear attractive for engineering purposes as well, offering quick response to the designer. The runtimes for the hysteresis calculations were of the order of weeks, which are also likely to be reduced to order of days.

Following the verification and the validation, the numerical results were used to investigate the driving mechanisms of oscillation, pulsation and the hysteresis phenomenon in Chapter 4.

The main results from the oscillation analyses are:

- the oscillation was found to be driven by the shear layer's ever changing shoulder reattachment condition, a viscous phenomena in nature

- unique results were revealed from the CFD simulations for:
  - the required reattachment pressure (p_{rr}), and
  - the potential reattachment pressure (p_{rpot}),
  showing very good agreement with the theory
- based on these results, Kenworthy's "energetic shear layer hypothesis" was confirmed as the driving mechanism of the oscillation flow mode
- the value of the actual reattachment pressure (experienced on the afterbody) was found to be linked to the direction of the shear layers lateral movement.

The capability of CFD to gain quantitative information from any part of the flowfield was exploited in this analysis and provided the main input to the understanding of the oscillation flow mode. Data, such as the Mach number distribution and the pressure distribution along the bounding streamline of the shear layer (which is moreover unsteady) are virtually inaccessible by measurement and thus it seems that without a CFD analysis the hypothesis could never be confirmed. It is remarkable, however, how well the theoretical and experimental researchers were able to capture the essence of the oscillation driving mechanism, with their concepts based on the limited data available from the measurements.

In contrast to the oscillation, an entirely new driving mechanism was revealed for the pulsation flow mode. The mechanism is based on a number of new elements, not observed in any previous work. These are:

- the existence of a vortical region in the growing triple-shock system, causing flow reversal into the separation zone,
- the duration of the filling mechanism being only one fourth of the time period,

- the inflation and expansion of the separation zone continuing even after the filling has stopped,
- the appearance of supersonic flow and shock waves within the separated region,
- the detachment of the expanded bow wave from the spike tip,
- the lift off of the shear layer,
- the flow penetrating through the expanded bow wave being reversed instead of impacting on the afterbody face.

Since the filling mechanism is realised through a vortical region generated by the pressure imbalance in the triple-shock system, the pulsation mechanism could be regarded as inviscid in nature. This is another striking difference between the oscillation and pulsation flow modes. In accordance with previous researchers ([16] [25], multiple separated zones were observed along the spike. These are believed to be the source for the shock asymmetry in the experiments. Since 3-D effects could not be investigated by the present axisymmetric simulation, future numerical studies should aim to tackle this problem. The majority of spiked body experiments were conducted more than two decades ago. Hence, new techniques that have emerged during this period, such as Particle Image Velocimetry (PIV), could be utilised to confirm the observations of the CFD analysis.

A final note on the fixed spike length calculations regards the irregularity of the pressure traces. These have been observed in both the experiment and the present numerical simulation. However, while in the former one it was believed to occur because of the 3-D effects or the measurement inaccuracies, this could certainly not be the case in the latter one. Thus, it is suggested that the irregular CFD cycles appear due to the relatively small number of cycles performed, which were thus still affected by the initial transient. This raises the question of whether a very large number of cycles would result in a perfectly periodic pressure history.

In the final part of Chapter 4, the hysteresis phenomenon was examined. The main findings can be summarised as:

- the O/P transition takes place gradually through a finite number of cycles and is triggered by the separation point passing the spike tip shoulder,
- the P/O transition takes place abruptly through a single cycle, and occurs at the spike length at which the separation point is not capable to reach the spike tip.

The hysteresis phenomenon is an area which requires further numerical and experimental investigations. Experimental results are needed for the outward moving spike portion of the hysteresis loop and it would be useful if the pressure history instead of the time-averaged amplitudes would be available in the vicinity of the transitions. Although the exact source of the hysteresis phenomenon is yet to be fully understood, the description of the transitions and the establishment of the necessary conditions for their occurrences could be interpreted as a step in the right direction towards this goal.

Appendix A

The PMB2D code

A detailed description of the PMB2D code is given here, focussing particularly on the features employed in the spiked body calculations. Some of the descriptions are adopted from [47] [53] [54] and [55].

A.1 Governing equations

A.1.1 Two-dimensional form

The two-dimensional, compressible Navier-Stokes equations written in a Cartesian frame are given by

$$\frac{\partial \mathbf{W}}{\partial t} + \frac{\partial \mathbf{F}^i}{\partial x} + \frac{\partial \mathbf{G}^i}{\partial y} = \frac{1}{Re} \left(\frac{\partial \mathbf{F}^v}{\partial x} + \frac{\partial \mathbf{G}^v}{\partial y} \right) \tag{A.1}$$

Here, the vector $\mathbf{W}$ is the vector of conserved variables:

$$\mathbf{W} = \begin{pmatrix} \rho \\ \rho u \\ \rho v \\ \rho E \end{pmatrix} \tag{A.2}$$

where ρ denotes the density, u, v are the two components of the Cartesian velocity vector and E is the total energy per unit mass.

The flux vectors $\mathbf{F}$ and $\mathbf{G}$ are decomposed into an inviscid, or convective, contribution denoted by $(^i)$ and a viscous, or diffusive, conribution denoted by $(^v)$ Written in full these are:

$$\mathbf{F}^i = \begin{pmatrix} \rho U \\ \rho u U + p \\ \rho v U \\ U(\rho E + p) + x_t p \end{pmatrix}$$
$$\mathbf{G}^i = \begin{pmatrix} \rho V \\ \rho u V \\ \rho v V + p \\ V(\rho E + p) + y_t p \end{pmatrix} \tag{A.3}$$

$$\mathbf{F}^\nu = \begin{pmatrix} 0 \\ \tau_{xx} \\ \tau_{xy} \\ u\tau_{xx} + v\tau_{xy} + q_x \end{pmatrix}$$
$$\mathbf{G}^\nu = \begin{pmatrix} 0 \\ \tau_{xy} \\ \tau_{yy} \\ u\tau_{xy} + v\tau_{yy} + q_y \end{pmatrix} \tag{A.4}$$

In the above expressions, U and V are the contravariant velocities, defined as

$$U = u - x_t \qquad V = v - y_t \tag{A.5}$$

where x_t and y_t are the components of the grid speed in a Cartesian sense. The components of the stress tensor and of the heat flux vector are modelled in the following way:

$$\begin{aligned} \tau_{xx} &= -\mu\left(2\frac{\partial u}{\partial x} - \frac{2}{3}\left(\frac{\partial u}{\partial x} + \frac{\partial v}{\partial y}\right)\right) \\ \tau_{yy} &= -\mu\left(2\frac{\partial v}{\partial y} - \frac{2}{3}\left(\frac{\partial u}{\partial x} + \frac{\partial v}{\partial y}\right)\right) \end{aligned} \tag{A.6}$$

$$\begin{aligned} \tau_{xy} &= -\mu\left(\frac{\partial u}{\partial y} + \frac{\partial v}{\partial x}\right) \\ q_x &= -\frac{1}{(\gamma-1)M_\infty^2}\frac{\mu}{Pr}\frac{\partial T}{\partial x} \\ q_y &= -\frac{1}{(\gamma-1)M_\infty^2}\frac{\mu}{Pr}\frac{\partial T}{\partial y} \end{aligned} \tag{A.7}$$

Here, γ is the specific heat ratio, equal to 1.4 for air, Pr is the laminar Prandtl number set to 0.72, T is the static temperature and M_∞ and Re are the freestream Mach number and Reynolds number, respectively. Furthermore, the various flow quantities are related to each other by the perfect gas relations:

$$\begin{aligned} E &= e + \frac{1}{2}\left(u^2 + v^2\right) \\ p &= (\gamma - 1)\,\rho e \\ \frac{p}{\rho} &= \frac{T}{\gamma M_\infty^2} \end{aligned} \tag{A.8}$$

Finally, the laminar viscosity μ is evaluated using Sutherland's law:

$$\frac{\mu}{\mu_0} = \left(\frac{T}{T_0}\right)^{3/2} \frac{T_0 + 110}{T + 110} \tag{A.9}$$

where $\mu_0 = 1.7894 \times 10^{-5}[\frac{kg}{m.s}]$ and $T_0 = 288.16[K]$ represent the reference viscosity and temperature, respectively. All terms used in the numerical method are non-dimensionalised as follows:

$$x = \frac{x^*}{L^*}, \qquad y = \frac{y^*}{L^*}, \qquad t = \frac{t^*}{L^*/V_\infty^*},$$

$$u = \frac{u^*}{V_\infty^*}, \qquad v = \frac{v^*}{V_\infty^*}, \qquad \mu = \frac{\mu^*}{\mu_\infty^*},$$

$$\rho = \frac{\rho^*}{\rho_\infty^*}, \qquad p = \frac{p^*}{\rho_\infty^* V_\infty^{*2}}, \qquad T = \frac{T^*}{T_\infty^*}, \qquad e = \frac{e^*}{V_\infty^{*2}}$$

where * denotes dimensional quantities and $_\infty$ denotes free-stream values.

A.1.2 Axisymmetric form

Spiked body flows are modelled in the current work in an axisymmetric fashion. The modelling equations for such case are the Navier-Stokes equations rewritten in cylindrical coordinates with the symmetry in the azimuthal direction. These equations written in Reynolds' averaged and non-dimensional form are given as:

Mass continuity

$$\frac{\partial \rho}{\partial t}+\frac{\partial}{\partial r}\left(\rho v_r\right)+\frac{\partial}{\partial z}\left(\rho v_z\right) = -\frac{\rho v_r}{r} \tag{A.10}$$

Momentum

$$\begin{aligned}\frac{\partial}{\partial t}\left(\rho v_r\right)+\frac{\partial}{\partial r}\left(\rho v_r^2+p\right)-\frac{\partial}{\partial r}\left[\frac{\mu+\mu_T}{Re}\left(2\frac{\partial v_r}{\partial r}-\frac{2}{3}\left(\frac{\partial v_z}{\partial z}+\frac{\partial v_r}{\partial r}\right)+\frac{2}{3}\rho k\right)\right]& \\ +\frac{\partial}{\partial z}\left(\rho v_r v_z\right)-\frac{\partial}{\partial z}\left[\frac{\mu+\mu_T}{Re}\left(\frac{\partial v_z}{\partial r}+\frac{\partial v_r}{\partial z}\right)\right] &= -\frac{\rho v_r^2}{r}+\frac{4\left(\mu+\mu_T\right)}{3Re}\left(\frac{1}{r}\frac{\partial v_r}{\partial r}-\frac{v_r}{r^2}\right)\end{aligned} \tag{A.11}$$

$$\begin{aligned}\frac{\partial}{\partial t}\left(\rho v_z\right)+\frac{\partial}{\partial r}\left(\rho v_r v_z\right)-\frac{\partial}{\partial r}\left[\frac{\mu+\mu_T}{Re}\left(\frac{\partial v_z}{\partial r}+\frac{\partial v_r}{\partial z}\right)\right]+\frac{\partial}{\partial z}\left(\rho v_z^2+p\right)& \\ -\frac{\partial}{\partial z}\left[\frac{\mu+\mu_T}{Re}\left(2\frac{\partial v_z}{\partial z}-\frac{2}{3}\left(\frac{\partial v_z}{\partial z}+\frac{\partial v_r}{\partial r}\right)+\frac{2}{3}\rho k\right)\right] &= -\frac{\rho v_r v_z}{r}+\frac{\mu+\mu_T}{rRe}\left(\frac{1}{3}\frac{\partial v_r}{\partial z}+\frac{\partial v_z}{\partial r}\right)\end{aligned} \tag{A.12}$$

Energy

$$\begin{aligned}&\frac{\partial E_t}{\partial t}+\frac{\partial}{\partial r}\left(v_r\left(E_t+p\right)\right)+\frac{\partial}{\partial z}\left(v_z\left(E_t+p\right)\right)\\ &\quad-\frac{\partial}{\partial r}\left\{v_r\left[\frac{\mu+\mu_T}{Re}\left(2\frac{\partial u_r}{\partial r}-\frac{2}{3}\left(\frac{\partial u_r}{\partial r}+\frac{\partial u_z}{\partial z}\right)+\frac{2}{3}\rho k\right)\right]+v_z\left[\frac{\mu+\mu_T}{Re}\left(\frac{\partial u_r}{\partial z}+\frac{\partial u_z}{\partial r}\right)\right]\right\}\\ &\quad-\frac{\partial}{\partial z}\left\{v_z\left[\frac{\mu+\mu_T}{Re}\left(2\frac{\partial u_z}{\partial z}-\frac{2}{3}\left(\frac{\partial u_r}{\partial r}+\frac{\partial u_z}{\partial z}\right)+\frac{2}{3}\rho k\right)\right]+v_r\left[\frac{\mu+\mu_T}{Re}\left(\frac{\partial u_r}{\partial z}+\frac{\partial u_z}{\partial r}\right)\right]\right\}\\ &\qquad-\frac{\partial}{\partial r}\left\{\frac{1}{\left(\gamma-1\right)M_\infty^2}\left(\frac{\mu}{Pr}+\frac{\mu_T}{Pr_T}\right)\frac{\partial T}{\partial r}\right\}-\frac{\partial}{\partial z}\left\{\frac{1}{\left(\gamma-1\right)M_\infty^2}\left(\frac{\mu}{Pr}+\frac{\mu_T}{Pr_T}\right)\frac{\partial T}{\partial z}\right\}\\ &\qquad\qquad=\frac{1}{r}\left[-v_r\left(E_t+p\right)+\frac{\mu+\mu_T}{Re}\left(v_z\frac{\partial u_z}{\partial r}+\frac{v_z}{3}\frac{\partial u_r}{\partial z}-\frac{4v_r}{3}\frac{\partial u_z}{\partial z}+\frac{2v_r}{3}\rho k\right)\right.\\ &\qquad\qquad\qquad\left.+\frac{1}{\left(\gamma-1\right)M_\infty^2}\left(\frac{\mu}{Pr}+\frac{\mu_T}{Pr_T}\right)\frac{\partial T}{\partial r}\right]\end{aligned}$$

In the above equations, subscripts ($_z$) and ($_r$) represent the tangential and the radial components of the velocity, respectively, whereas subscripts ($_T$) indicate values corresponding to turbulent flows. E_t is the total energy per unit volume. The above equations are treated analogously to the planar equations in the rest of the code. For more details see [47].

A.2 Spatial discretisation

The Navier-Stokes equations are discretised using a cell-centered finite volume method, which transforms the partial differential equations into a set of ordinary differential equations which can be written as

$$\frac{d\mathbf{W}_{i,j}}{dt} = -\mathbf{R}_{i,j} \tag{A.13}$$

and where $\mathbf{R}_{i,j}$ represents the discrete approximation of the convective and diffusive flux integrals. Subscripts (i, j) are the coordinates of the control volume in the generalised coordinate system.

The control volumes are obtained by dividing the computational domain into a finite number of non-overlapping cells, to which the Navier-Stokes equations are applied in turn. The PMB2D code employs a structured multiblock approach, which means that each cell is represented by four edges and that the cells could be organised into a finite number of non-overlapping blocks, assembling the entire computational domain.

A.2.1 General curvilinear form

Since the method is based on using body-conforming grids of arbitrary density and orientation, the Navier-Stokes equations are first rewritten into a curvilinear coordinate system (ξ,η). This is achieved by performing a space transformation from the Cartesian coordinate system (x, y) to the local coordinate system (ξ,η)

$$\begin{aligned} \xi &= \xi\,(x, y) \\ \eta &= \eta\,(x, y) \\ t &= t \end{aligned}$$

The Jacobian matrix of the transformation is given by

$$J = \frac{\partial(\xi, \eta)}{\partial(x, y)}$$

The equations (A.1) can then be written as

$$\frac{\partial \hat{\mathbf{W}}}{\partial t} + \frac{\partial \hat{\mathbf{F}}^i}{\partial \xi} + \frac{\partial \hat{\mathbf{G}}^i}{\partial \eta} = \frac{1}{Re}\left(\frac{\partial \hat{\mathbf{F}}^v}{\partial \xi} + \frac{\partial \hat{\mathbf{G}}^v}{\partial \eta}\right) \tag{A.14}$$

where

$$\begin{aligned} \hat{\mathbf{W}} &= \frac{\mathbf{W}}{J} \\ \hat{\mathbf{F}}^i &= \frac{1}{J}\left(\xi_x \mathbf{F}^i + \xi_y \mathbf{G}^i\right) \\ \hat{\mathbf{G}}^i &= \frac{1}{J}\left(\eta_x \mathbf{F}^i + \eta_y \mathbf{G}^i\right) \\ \hat{\mathbf{F}}^v &= \frac{1}{J}\left(\xi_x \mathbf{F}^v + \xi_y \mathbf{G}^v\right) \\ \hat{\mathbf{G}}^v &= \frac{1}{J}\left(\eta_x \mathbf{F}^v + \eta_y \mathbf{G}^v\right) \end{aligned} \tag{A.15}$$

A.2.2 Discretisation of the convective terms

The convective terms are discretised by either Roe's or Osher's upwind scheme. Since numerical experiments showed Roe's scheme to be more robust for high-speed applications than Osher's, the calculations of the present work were obtained using this method.

A.2.3 Roe's scheme

Roe's scheme [48] serves to determine the numerical flux at a cell interface if an upwind discretisation is used. This is accomplished by solving the Riemann problem (shock wave propagation in a tube [49]) in an approximate manner at each cell interface.

The upwind numerical fluxes can be generally written as:

$$\mathbf{F}(\mathbf{U}_L, \mathbf{U}_R) = \frac{1}{2}\left(\mathbf{F}(\mathbf{U}_L) + \mathbf{F}(\mathbf{U}_R) - d(\mathbf{U}_L, \mathbf{U}_R)\right) \tag{A.16}$$

where $\mathbf{U}_L$ and $\mathbf{U}_R$ are the left hand side and right hand side state variables, respectively, $\mathbf{F}(\mathbf{U}_L)$ and $\mathbf{F}(\mathbf{U}_R)$ are the fluxes at the left and right states and $d(\mathbf{U}_L, \mathbf{U}_R)$ is a diffusion term arising at the interface. The difference between the various Riemann solvers lies in the solution of this last term only.

The method proposed by Roe [48] is a flux difference splitting approach for the solution of $d(\mathbf{U}_L, \mathbf{U}_R)$ and it was suggested that the interaction between the left and right states in the Riemann problem can be replaced by an average shock. According to Roe, the diffusion term can be expressed as:

$$d(\mathbf{U}_L, \mathbf{U}_R) = |\mathbf{A}(\mathbf{U}_L, \mathbf{U}_R)|(\mathbf{U}_R - \mathbf{U}_L) \tag{A.17}$$

where matrix $\mathbf{A}$ is the mean Jacobian matrix defined to satisfy the following properties:

(i) $\mathbf{A}(\mathbf{U}, \mathbf{U}) = \mathbf{A}(\mathbf{U})$

(ii) for any $\mathbf{U}_L, \mathbf{U}_R, \mathbf{A}(\mathbf{U}_L, \mathbf{U}_R)(\mathbf{U}_R - \mathbf{U}_L) = \mathbf{F}_L - \mathbf{F}_R$ and

(iii) the eigenvectors of $\mathbf{A}$ are linearly independent.

Condition (i) guarantees consistency, (ii) ensures a conservative algorithm and (ii) alongside (iii) guarantees, that the shock waves are captured with the correct speed, i.e. the Rankine-Hugoniot jump conditions are satisfied.

Matrix $|\mathbf{A}(\mathbf{U}_L, \mathbf{U}_R)|$ is then defined as:

$$|\mathbf{A}| = \mathbf{R}|\Lambda|\mathbf{R}^{-1} \tag{A.18}$$

where $\mathbf{R}$ is the matrix of the right eigenvectors of $\mathbf{A}$, Λ is the diagonal matrix of absolute values of the corresponding eigenvalues and $\mathbf{R}^{-1}$ is the matrix of the left eigenvectors. These matrices are expressed as:

$$\mathbf{R} = \begin{pmatrix} 1 & 1 & 1 & 0 \\ u - cn_x & u & u + cn_x & -n_y \\ v - cn_y & v & v + cn_y & n_x \\ H - U_n c & \frac{1}{2}(u^2 + v^2) & H + U_n c & V_t \end{pmatrix} \tag{A.19}$$

$$|\Lambda| = \begin{pmatrix} |U_n - c + n_t| & 0 & 0 & 0 \\ 0 & |U_n + n_t| & 0 & 0 \\ 0 & 0 & |U_n + c + n_t| & 0 \\ 0 & 0 & 0 & |U_n + n_t| \end{pmatrix} \tag{A.20}$$

$$\mathbf{R}^{-1} = \begin{pmatrix} \frac{1}{2}(b_1 + \frac{U_n}{c}) & \frac{1}{2}(-b_2 u - \frac{n_x}{c}) & \frac{1}{2}(-b_2 v - \frac{n_y}{c}) & \frac{b_2}{2} \\ 1 - b_1 & b_2 u & b_2 v & -b_2 \\ \frac{1}{2}(b_1 - \frac{U_n}{c}) & \frac{1}{2}(-b_2 u + \frac{n_x}{c}) & \frac{1}{2}(-b_2 v + \frac{n_y}{c}) & \frac{b_2}{2} \\ -V_t & -n_y & n_x & 0 \end{pmatrix} \tag{A.21}$$

In matrices A.19, A.20, A.21 n_t is the corresponding component of the grid speed in the (ξ, η) plane, and U_n and V_t are the normal and tangential components to a side of the velocity. These are defined as:

$$U_n = un_x + vn_y \qquad\qquad V_t = -un_y + vn_x \tag{A.22}$$

with $n(n_x, n_y)$ denoting the outward unit vector normal to a side. Furthermore, in matrix A.19, H is the total enthalpy, defined as

$$H = \gamma E - (\gamma - 1)\frac{u^2 + v^2}{2} \tag{A.23}$$

and in equation A.21

$$b_2 = \frac{\gamma - 1}{c^2} \qquad\qquad b_1 = b_2 \frac{u^2 + v^2}{2} \tag{A.24}$$

In order to satisfy the conditions stated for matrix $|\mathbf{A}|$, the flow variables in expressions A.19-A.24 are replaced by an average value weighted by the square root of the densities. These particular averages, termed as the Roe averages, are defined by setting

$$R = \sqrt{\frac{\rho_R}{\rho_L}} \tag{A.25}$$

$$\rho = \sqrt{\rho_R \rho_L} \tag{A.26}$$

$$u = \frac{\sqrt{\rho_L} u_L + \sqrt{\rho_R} u_R}{\sqrt{\rho_L} + \sqrt{\rho_R}} = \frac{u_L + R u_R}{1 + R} \tag{A.27}$$

$$v = \frac{\sqrt{\rho_L} v_L + \sqrt{\rho_R} v_R}{\sqrt{\rho_L} + \sqrt{\rho_R}} = \frac{v_L + R v_R}{1 + R} \tag{A.28}$$

$$H = \frac{\sqrt{\rho_L} H_L + \sqrt{\rho_R} H_R}{\sqrt{\rho_L} + \sqrt{\rho_R}} = \frac{H_L + R H_R}{1 + R} \tag{A.29}$$

while the corresponding (average) speed of sound will be

$$c^2 = (\gamma - 1)\left(H - \frac{u^2 + v^2}{2}\right) \tag{A.30}$$

Finally, the numerical fluxes $\mathbf{F}(\mathbf{U}_L)$ and $\mathbf{F}(\mathbf{U}_R)$ used in equationA.16 are:

$$\mathbf{F}(\mathbf{U}_L) = \begin{pmatrix} \rho_L U_L \\ \rho_L u_L U_n + p_L n_x \\ \rho_L v_L U_n + p_L n_y \\ \rho_L U_n H_L - p_L n_t \end{pmatrix}$$

$$\mathbf{F}(\mathbf{U}_R) = \begin{pmatrix} \rho_R U_R \\ \rho_R u_R U_n + p_R n_x \\ \rho_R v_R U_n + p_R n_y \\ \rho_R U_n H_R - p_R n_t \end{pmatrix}$$

A.2.4 The entropy correction

An undesired property of Roe's scheme is that it cannot see a sonic point in the interval $(\mathbf{U}_L, \mathbf{U}_R)$. In this case, an eigenvalue of matrix A will vanish and the flux function (equation A.16) will lead to a non-physical expansion shock instead of a physically correct expansion fan. This characteristic of the Roe solver violates the second principle of thermodynamics, which states that in any physically realisable adiabatic evolution the entropy can only increase during the transformation of the system. Hence, only compression shocks should be retained whereas expansion shocks, corresponding to a negative entropy variation, should be excluded [49].

A common technique for avoiding expansion shocks consists of introducing a local expansion fan when an expansion is detected through a sonic point. This could be realised through a so-called entropy fix, which modifies the modulus of the diagonal elements of matrix $|\Lambda|$. There are a number of different entropy fixes available for Roe's scheme, from which Harten's [50] proved to be the most suitable for the calculations of the present work. This entropy fix is specially suited for problems involving hypersonic freestream, and is defined as:

$$|\Lambda_i| = \begin{array}{ll} |\Lambda_i| & if|\Lambda_i| \geq 2\varepsilon_r \\ \dfrac{|\Lambda_i|^2}{4\varepsilon_r} + \varepsilon_r & if|\Lambda_i| < 2\varepsilon_r \end{array} \tag{A.31}$$

Here, ε_r is in the range (0.1 to 0.4), with the larger values used when strong normal shocks are present in the flowfield. Since this is the case at the spiked body flows, the value of ε_r was set to 0.4 in all calculations presented in this study.

A.2.5 Higher-order spatial accuracy

A MUSCL extrapolation method is used to improve the formal accuracy to second-order in the numerical scheme. Additionally, von Albada's limiter is employed to ensure monotonic solutions around shock waves.

A.3 Discretisation of the diffusive terms

Regardless of the convective discretisation, the viscous terms are always centrally discretised. This requires the knowledge of the velocity components and their derivatives, as well as the derivatives of the static temperature, at the edges of each cell. Cell-edge values of the velocity components are approximated by the average of the two adjacent cell-centre values, for example:

$$u_{i+\frac{1}{2},j} = \frac{1}{2}\left(u_{i,j} + u_{i+1,j}\right) \tag{A.32}$$

Cell-edge values of the derivatives are obtained using Green's formula applied to an auxiliary cell surrounding the considered edge, for example:

$$\begin{aligned} \frac{\partial u}{\partial x} &= \frac{1}{h_{aux}} \oint_{\Omega_{s_{aux}}} u dy \\ \frac{\partial u}{\partial y} &= \frac{-1}{h_{aux}} \oint_{\Omega_{s_{aux}}} u dx \end{aligned} \tag{A.33}$$

where h_{aux} is the area of the auxiliary cell. The values at the four points a, b, c, d are obtained using the neighbouring cell-centre values (see Fig.A.1):

$$\begin{aligned}
u_a &= u_{i,j} \\
u_b &= \frac{u_{i,j-1} + u_{i,j} + u_{i+1,j-1} + u_{i+1,j}}{4} \\
u_c &= u_{i+1,j} \\
u_d &= \frac{u_{i,j} + u_{i,j+1} + u_{i+1,j} + u_{i+1,j+1}}{4}
\end{aligned} \tag{A.34}$$

The choice of the auxiliary cell is guided by the need to avoid odd-even point decoupling and to minimise the amount of numerical viscosity introduced in the discretised equations.

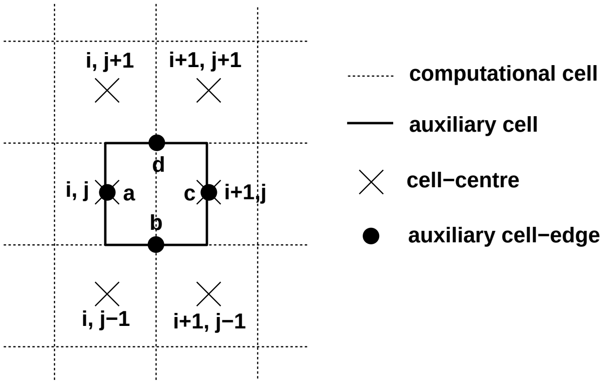

Figure A.1: *Typical auxiliary cell for viscous flux evaluation.*

A.4 Boundary conditions

The boundary conditions are set by using ghost cells on the exterior of the computational domain. In the far field, ghost cell values are set at the freestream conditions. At solid boundaries, ghost values are extrapolated from the interior, ensuring that the normal component of the velocity on the solid wall is zero.

A.5 Time-marching scheme

A.5.1 Steady state solver

A steady state solution is obtained by integrating equation A.13 in time using an implicit time marching scheme:

$$\frac{\mathbf{W}^{n+1} - \mathbf{W}^{n}}{\Delta t} = -\mathbf{R}^{n+1} \tag{A.35}$$

where n is the current time level, $n+1$ is the new time level, and subscripts (i, j) are neglected for clarity. The above equation represents a system of non-linear algebraic equations and to simplify the solution procedure, the flux residual $\mathbf{R}^{n+1}$ is linearised in time as follows:

$$\begin{aligned}\mathbf{R}^{n+1} &= \mathbf{R}^{n} + \frac{\partial \mathbf{R}}{\partial t}\Delta t + O(\Delta t^2) \\ &\approx \mathbf{R}^{n} + \frac{\partial \mathbf{R}}{\partial \mathbf{W}}\frac{\partial \mathbf{W}}{\partial t}\Delta t \\ &\approx \mathbf{R}^{n} + \frac{\partial \mathbf{R}}{\partial \mathbf{W}}\Delta W \end{aligned} \tag{A.36}$$

where $\Delta\mathbf{W} = \mathbf{W}^{n+1} - \mathbf{W}^{n}$. Equation (A.35) now becomes the following linear system:

$$\left(\frac{\mathbf{I}}{\Delta t} + \frac{\partial \mathbf{R}}{\partial \mathbf{W}}\right)\Delta\mathbf{W} = -\mathbf{R}^{n} \tag{A.37}$$

Equation A.37 can now be rewritten in terms of the vector of primitive variables $\mathbf{P}$:

$$\left(\frac{1}{\Delta t}\frac{\partial \mathbf{W}}{\partial \mathbf{P}} + \frac{\partial \mathbf{R}_{\xi}}{\partial \mathbf{P}} + \frac{\partial \mathbf{R}_{\eta}}{\partial \mathbf{P}}\right)\Delta\mathbf{P} = -\mathbf{R}^{n} \tag{A.38}$$

where the terms $\frac{\partial \mathbf{R}_{\xi}}{\partial \mathbf{P}}$ and $\frac{\partial \mathbf{R}_{\eta}}{\partial \mathbf{P}}$ denote the flux Jacobians associated with the discretised flux in the ξ and η direction, respectively.

The above linear system is solved by using a Generalised Conjugate Gradient method (GSG) [51], preconditioned by a Block Incomplete Lower-Upper Factorisation (BILU).

In the present work, steady state solutions obtained by the above implicit method were used to start an unsteady calculation. However, as implicit schemes require particular treatment during the early stages of the iterative procedure, the following approach has been employed. First, the initial flow was smoothed out by performing some explicit iterations (a typical number of explicit steps was around 1000) to switch then to the implicit algorithm to obtain fast convergence.

A.5.2 Unsteady flow solver

Unsteady solutions of equation A.13 are obtained by employing an implicit dual-time approach as proposed by Jameson [52]. This has the advantage, that the resulting linear system can be solved by the same implicit method as used for steady state problems.

Considering equation A.13 again, according to Jameson [52] the time derivative can be approximated by a second order backward difference discretisation as

$$\frac{3\mathbf{W}_{i,j}^{n+1} - 4\mathbf{W}_{i,j}^{n} + \mathbf{W}_{i,j}^{n-1}}{2\Delta t} + \mathbf{R}_{i,j}(\mathbf{W}_{i,j}^{n+1}) = 0 \tag{A.39}$$

The entire left hand side of this equation can be defined as a new, unsteady residual $\mathbf{R}^*$:

$$\mathbf{R}_{i,j}^*(\mathbf{W}^{n+1}) = \frac{3\mathbf{W}_{i,j}^{n+1} - 4\mathbf{W}_{i,j}^{n} + \mathbf{W}_{i,j}^{n-1}}{2\Delta t} + \mathbf{R}_{i,j}(\mathbf{W}_{i,j}^{n+1}) = 0 \tag{A.40}$$

This new equation can be seen as the solution of a steady state problem which can be solved with a time-marching method by introducing a derivative with respect to a fictitious pseudo-time, t^*,

$$\frac{\partial \mathbf{W}_{i,j}^{n+1}}{\partial t^*} + \mathbf{R}_{i,j}^*(\mathbf{W}^{n+1}) = 0 \tag{A.41}$$

Using an implicit time discretisation on the pseudo time t^*, equation A.41 becomes:

$$\frac{\Delta \mathbf{W}_{i,j}}{\Delta t^*} = \frac{\mathbf{W}_{i,j}^{m+1} - \mathbf{W}_{i,j}^{m}}{\Delta t^*} = -\mathbf{R}_{i,j}^*(\mathbf{W}^{m+1}) \tag{A.42}$$

where the superscript m+1 denotes the time level $(m+1)\Delta t^*$ in pseudo-time. Similar to the steady state case, the term $\mathbf{R}^*_{i,j}(\mathbf{W}^{m+1})$ is linearised with respect to the time variable t^*:

$$\begin{aligned} \mathbf{R}^*(\mathbf{W}^{m+1}) &= \mathbf{R}^*(\mathbf{W}^m) + \frac{\partial \mathbf{R}^*}{\partial t^*}\Delta t^* + O(\Delta t^{*2}) \\ &\approx \mathbf{R}^*(\mathbf{W}^m) + \frac{\partial \mathbf{R}^*}{\partial \mathbf{W}}\frac{\partial \mathbf{W}}{\partial t^*}\Delta t^* \\ &\approx \mathbf{R}^*(\mathbf{W}^m) + \frac{\partial \mathbf{R}^*}{\partial \mathbf{W}}\Delta W \end{aligned} \tag{A.43}$$

The term $\frac{\partial \mathbf{R}^*}{\partial \mathbf{W}}$ could be obtained by calculating the derivative of equation A.40:

$$\frac{\partial \mathbf{R}^*(\mathbf{W}^{n+1})}{\partial \mathbf{W}^{n+1}} = \frac{3}{2\Delta t}\mathbf{I} + \frac{\partial \mathbf{R}(\mathbf{W}^{n+1})}{\partial \mathbf{W}^{n+1}} \tag{A.44}$$

Substituting the above formula into equation A.43 and then the resulting expression into equation A.42 gives:

$$\left[\left(\frac{1}{\Delta t^*} + \frac{3}{2\Delta t}\right)\mathbf{I} + \frac{\partial \mathbf{R}}{\partial \mathbf{W}}\right]\Delta \mathbf{W} = -\mathbf{R}^*(\mathbf{W}^m) \tag{A.45}$$

Then, equation A.45 can be rewritten again in terms of the vector of primitive variables $\mathbf{P}$ and the flux residual components $\mathbf{R}_\xi$ and $\mathbf{R}_\eta$ to obtain:

$$\left[\left(\frac{1}{\Delta t^*} + \frac{3}{2\Delta t}\right)\frac{\partial \mathbf{W}}{\partial \mathbf{P}} + \frac{\partial \mathbf{R}_\xi}{\partial \mathbf{P}} + \frac{\partial \mathbf{R}_\eta}{\partial \mathbf{P}}\right]\Delta \mathbf{P} = -\mathbf{R}^*(\mathbf{W}^m) \tag{A.46}$$

Since the linear system of equation A.46 is similar to the one of equation A.38, it can be solved by the same method as that used for the steady state solver.

The rate of convergence between two consecutive time steps is monitored via a so-called pseudo-time tolerance, which is defined as

$$\frac{||\mathbf{W}^{n+1,m+1} - \mathbf{W}^{n+1,m}||_2}{||\mathbf{W}^{n+1,m+1} - \mathbf{W}^{n}||_2} \tag{A.47}$$

Based on previous experiences [53], [54] this value was set on 0.001 for all the results presented in this thesis.

A.6 Approximate Jacobians

An important feature of the PMB2D code is the use of approximate Jacobians. The idea of using an approximate approach instead of an exact one emerged from the following observation. The use of the MUSCL extrapolation for the higher order spatial accuracy means that the left and right states near a cell interface are extrapolated according to the following relations:

$$\begin{aligned} \mathbf{W}^{-}_{i+\frac{1}{2},j} &= \mathcal{F}\left(\mathbf{W}_{i-1,j}, \mathbf{W}_{i,j}, \mathbf{W}_{i+1,j}, \mathbf{W}_{i+2,j}\right) \\ \mathbf{W}^{+}_{i+\frac{1}{2},j} &= \mathcal{G}\left(\mathbf{W}_{i-1,j}, \mathbf{W}_{i,j}, \mathbf{W}_{i+1,j}, \mathbf{W}_{i+2,j}\right) \end{aligned} \tag{A.48}$$

As a result, the flux residual for cell (i,j) is a function of nine points (see Fig.A.2):

$$\mathbf{R}_{i,j} = \mathbf{R}\left(\mathbf{W}_{i-2,j}, \mathbf{W}_{i-1,j}, \mathbf{W}_{i,j}, \mathbf{W}_{i+1,j}, \mathbf{W}_{i+2,j}, \mathbf{W}_{i,j-2}, \mathbf{W}_{i,j-1}, \mathbf{W}_{i,j+1}, \mathbf{W}_{i,j+2}\right)$$

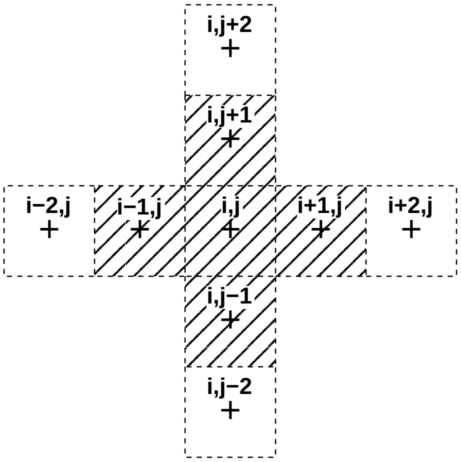

Figure A.2: *Flux residual dependency for exact/approximate derivation of the inviscid terms.*

Thus, when the Jacobian matrix $\frac{\partial \mathbf{R}}{\partial \mathbf{W}}$ has to be worked out for eqs.A.37 and A.45, then there will be nine non-zero entries per row in this matrix. However, an approximation to the exact Jacobian, gained by neglecting the influence of the MUSCL interpolation, could lead to significant reductions in terms of the memory, CPU time and also the ease of solving the matrix, since it will be more diagonally dominant

[55]. Because of the approximation, the left and right states are reduced to

$$\begin{aligned} \mathbf{W}^{-}_{i+\frac{1}{2},j} &= \mathcal{F}'\left(\mathbf{W}_{i,j}\right) \\ \mathbf{W}^{+}_{i+\frac{1}{2},j} &= \mathcal{G}'\left(\mathbf{W}_{i+1,j}\right) \end{aligned} \tag{A.49}$$

so the flux residual becomes a function of only five points (the dashed area in Fig. A.2):

$$\mathbf{R}_{i,j} = \mathbf{R}'\left(\mathbf{W}_{i-1,j}, \mathbf{W}_{i,j}, \mathbf{W}_{i+1,j}, \mathbf{W}_{i,j-1}, \mathbf{W}_{i,j+1}\right) \tag{A.50}$$

This approximation, which is applied only for the derivation of the Jacobian terms, reduces memory requirements and matrix-vector multiplication operation counts to 5/9 of the values using the exact Jacobians. The same idea was used for the

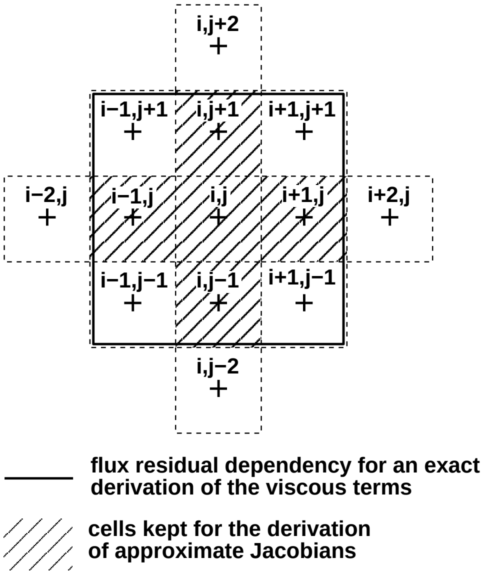

Figure A.3: *Flux residual dependency for exact/approximate derivation of the viscous terms.*

reduction of the Jacobians arising from the viscous fluxes. Because of using an auxiliary cell for these terms (see section A.3) a viscous flux residual will be the function of nine points (see Fig. A.3): $\mathbf{W}_{i-1,j-1}$, $\mathbf{W}_{i,j-1}$, $\mathbf{W}_{i+1,j-1}$, $\mathbf{W}_{i-1,j}$, $\mathbf{W}_{i,j}$, $\mathbf{W}_{i+1,j}$, $\mathbf{W}_{i-1,j+1}$, $\mathbf{W}_{i,j+1}$ and $\mathbf{W}_{i+1,j+1}$. An exact derivation of the inviscid and viscous Jacobians together would involve four more terms in addition to the nine above: $\mathbf{W}_{i-2,j}$, $\mathbf{W}_{i+2,j}$, $\mathbf{W}_{i,j-2}$ and $\mathbf{W}_{i,j+2}$ (the cells shown in Fig. A.3).

The approximation facilitated in the PMB2D code takes into account only the influence of the two cells situated on the either side of the considered edge for the derivation of the Jacobians. For example, in the case shown in Fig. A.1 the contributions of $\mathbf{W}_{i,j-1}$, $\mathbf{W}_{i,j+1}$, $\mathbf{W}_{i+1,j-1}$ and $\mathbf{W}_{i+1,j+1}$ are neglected and only the terms arising from $\mathbf{W}_{i,j}$ and $\mathbf{W}_{i+1,j}$ are kept. This yields savings of 8/13 in terms of the memory and the CPU time. The cells considered during the derivation of the approximate Jacobians are shown by the dashed area in Fig. A.3.

The above approximations were extensively tested and proved to be successful for a wide range of applications [55].

A.7 Deforming mesh algorithm

In order to enable the numerical simulation of the hysteresis phenomenon, which involves a moving spike, an algorithm of a continuous mesh deformation has to be applied. The method employed in the PMB2D code is a transfinite interpolation algorithm (TFI), based on the grid displacements. It consists of three main steps.

First, the details of the desired grid movements are read in from a separate file containing the type and direction of the motion for the four corners of each block. There are currently three types motion types facilitated in the code: pitch/plunge, rotational and translational motions. Once the corresponding motion type is identified, the block corner displacements are calculated (see Fig. A.4a,b).

Then, as a second step, the displacements of the four block corners are used to interpolate the displacement of all points along the block boundary. This is accomplished by employing a weighted formula as

$$d\mathbf{x} = \left(1 - \frac{a}{c}\right) d\mathbf{x}_A + \left(1 - \frac{b}{c}\right) d\mathbf{x}_B$$

where $d\mathbf{x}$ is the displacement of a selected point (P) on the block boundary, $d\mathbf{x}_A$ and $d\mathbf{x}_B$ are the displacements of the endpoints (block corners) of the edge on which P lies, and $a = ||\vec{AP}||$, $b = ||\vec{BP}||$ and $c = ||\vec{AB}||$ (see Fig. A.4c). If both endpoints are fixed, then the whole boundary face remains fixed. Finally, in the third step, the new location of the interior points is calculated. Following the original formulation of the TFI algorithm described by Gordon and Hall [56], the general transfinite interpolation method results in a recursive algorithm which is here applied to the grid point displacements :

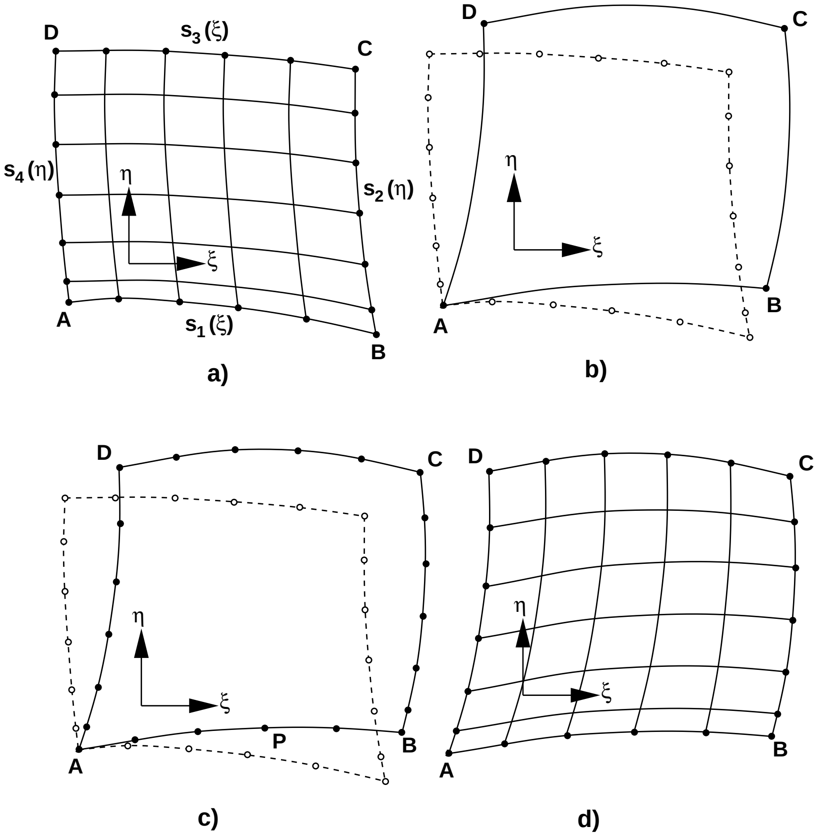

Figure A.4: *The TFI algorithm of grid deformation.*

$$d\mathbf{x}(\xi,\eta) = \mathbf{f}_1(\xi,\eta) + \phi_1^0(\eta)\,[d\mathbf{x}_{b1}(\xi) - \mathbf{f}_1(\xi,0)]$$

$$+\phi_2^0(\eta)\,[d\mathbf{x}_{b3}(\xi) - \mathbf{f}_1(\xi,1)]$$

where

$$\mathbf{f}_1(\xi,\eta) = \psi_1^0(\xi)d\mathbf{x}_{b4}(\eta) + \psi_2^0(\xi)d\mathbf{x}_{b2}(\eta)$$

and $d\mathbf{x}_{b1}$,$d\mathbf{x}_{b2}$,$d\mathbf{x}_{b3}$,and $d\mathbf{x}_{b4}$ are the interpolated displacements along the four block faces. The functions ψ and ϕ are the blending functions in the ξ and η directions respectively. These functions are given by the grid point distributions along each block face as

$$\begin{aligned}
\psi_1^0(\xi) &= 1 - s_1(\xi) \\
\psi_2^0(\xi) &= s_3(\xi) \\
\phi_1^0(\eta) &= 1 - s_4(\eta) \\
\phi_2^0(\eta) &= s_2(\eta)
\end{aligned}$$

where $s_1(\xi)$ is the stretching function on the block face $\eta = 0$, $s_2(\eta)$ on the block face $\xi = 1$, $s_3(\xi)$ on the block face $\eta = 1$ and $s_4(\eta)$ on the block face $\xi = 0$. The coordinates of the new grid points are then simply obtained by

$$\mathbf{x}(\xi,\eta) = \mathbf{x}_0(\xi,\eta) + d\mathbf{x}(\xi,\eta)$$

where $d\mathbf{x}$ is the interpolated displacement and $\mathbf{x}_0$ is the vector position for the initial undisturbed grid.

As a last note, a Geometric Conservation Law (GCL) is also implemented in the PMB2D code [54], which calculates the cell volume changes according to the area swept by the cell boundary.

Appendix B

Animations CD-ROM

A CD-ROM containing the animations of the analysed spiked body flows has been enclosed to aid the undersatnding of the flow features. Two movies are provided for each case: one shows the Mach contours overlapped by the streamlines (Mach regions only for the hysteresis cases) and the other the pressure regions. Each animation is provided in both .mv and .mov formats to enable their visualisation in either the Movieplayer (UNIX) or the Quicktime (WINDOWS) softwares. Further instructions are given in the 'Readme' file. The full contents of the CD-ROM is given in Table B.1.

Case	Mach contours/regions movie filename	Pressure regions movie filename
Oscillation at M=6.00	osc_M6_mach.mv osc_M6_mach.mov	osc_M6_press.mv osc_M6_press.mov
Pulsation at M=2.21	puls_M2_mach.mv puls_M2_mach.mov	puls_M2_press.mv puls_M2_press.mov
Pulsation at M=6.00	puls_M6_mach.mv puls_M6_mach.mov	puls_M6_press.mv puls_M6_press.mov
Hysteresis inward moving spike $v\_sp = 0.004[1]$, M=2.21	hyst_mach_inw.mv hyst_mach_inw.mov	hyst_press_inw.mv hyst_press_inw.mov
Hysteresis outward moving spike $v\_sp = 0.004[1]$, M=2.21	hyst_mach_out.mv hyst_mach_out.mov	hyst_press_out.mv hyst_press_out.mov

Table B.1: Contents of the CD-ROM of animations.

Bibliography

[1] Oswatitsch, K. Der Druckrückgewinn bei Geschossen mit Rückstossantrieb bei hohen Überschallgeschwindigkeiten. *Bericht Nr 1005, Forch. & Entwickl. Heereswaffenamtes*, 1944.

[2] Mair, W.A. Experiments on separation of boundary layer on probes in front of blunt nosed bodies in a supersonic stream. *Philosophical Magazine*, 43(342):593–601, July 1952.

[3] Bogdonoff, S.M., Vas, I.E. Preliminary investigations of spiked bodies at hypersonic speeds. *Journal of Aerospace Sciences*, 26(2):65–74, 1959.

[4] Maull, D.J. Hypersonic flow over axially symmetric spiked bodies. *Journal of Fluid Mechanics*, 8:584–592, 1960.

[5] Wood, C.J. Hypersonic flow over spiked cones. *Journal of Fluid Mechanics*, 12(4):614–624, 1961.

[6] Holden, M.S. Experimental studies of separated flows at hypersonic speeds. Part I - Separated flows over axisymmetric spiked bodies. *AIAA Journal*, 4(4):591–599, 1966.

[7] Album, H.H. Spiked blunt bodies in supersonic flow. *AFOSR TR 307*, 1961.

[8] Wyborny, W. Der Einfluss eines ausgelenkten Zentrastifes auf die aerodynamischen Beiwerte rotationsymmetrischer Hyperschallflugköorper. *DLR FB 69-37*, 1969.

[9] Roberts, B.G. An experimental study of the drag of rigid models representing two parachute designs at M=1.40 and 2.19. *RAE TN Aero 2734*, 1960.

[10] Maynard, J.D. Aerodynamic characteristics of parachutes at Mach numbers 1.6 to 3.0. *NASA TN D 752*, 1961.

[11] Robinson, M.L., Roberts, B.G., Sayer, A.M. An examination of the flow instability associated with spiked bluff body configurations. *WRE HSA TN 101*, 1964.

[12] Jones, R.A., Bushnell, D.M., Hunt, J.L. Experimental flow field and heat transfer investigation of several tension shell configurations at a Mach number of 8. *NASA TN D 3800*, 1967.

[13] Minges, M.L. Ablation phenomenology (a review). *High Temperatures - High Pressures*, 1, 1969.

[14] Kenworthy, M.A., Richards, B.E. A study of the unsteady flow over concave conic models at Mach 15 and 20. *AFML TR 138*, 1976.

[15] Abbett, M.J., Cooper, L., Dahm, T.J., Jackson, M.D. Flow characteristics about concave conic forebodies at high Mach numbers. *AIAA Paper 75-153*, 1975.

[16] Yoshikawa, K.K. Transient phenomena of shock-induced turbulent separation for a spikebody and stalling airfoil at transonic and supersonic speeds. *AIAA Paper 82-1362*, 1982.

[17] Candler, G.V., Nompelis, I., Holden, M.S. Computational Analysis of Hypersonic Laminar Viscous-Inviscid Interactions. *AIAA Paper 2000-0532*, 2000.

[18] Kenworthy, M.A. A study of unstable axisymmetric separation in high speed flows. *PhD Thesis, Virginia Polytechnic Institute and State University, USA*, 1978.

[19] Equations, tables, and charts for compressible flow. *NACA 1135*, 1953.

[20] Kabelitz, H.P. Zur Stabilität geschlossener Greznschichtablösegebeite an konischen Drehkörpern bei Hyperschallströmung. *DLR FB: 71-77*, 1971.

[21] Demetriades, A., Hopkins, A.T. Asymmetric shock-wave oscillations on spiked bodies of revolution. *Journal of Spacecraft and Rockets*, 13(11):703–704, 1978.

[22] Ericsson, L.E. Flow pulsations on concave conic forebodies. *Journal of Spacecraft and Rockets*, 15(5):287–292, 1978.

[23] Panaras, A.G. The high speed unsteady separation around concave bodies can be explained by an inviscid flow mechanism. *These Annexe, U. Libre de Bruxelles*, 1976, also 'Pulsating flows about axisymmetric concave bodies', AIAA Jornal, 19(6):804-806, 1981.

[24] Edney, B. Effects of shock impingement on the heat transfer around blunt bodies. *AIAA Journal*, 6(1):15–21, 1968.

[25] Calarese, W., Hankey, W.L. Modes of shock-wave oscillations on spike-tipped bodies. *AIAA Journal*, 23(2):185–192, 1985.

[26] Antonov, A.N., Gretsov, V.K., Shalaev, S.P. Unsteady supersonic flow past a body with a spike mounted in front. *Akademiia Nauk SSSR, Mekhanika Zhidkosti i Gaza*, pages 118–124, Sept-Oct 1976.

[27] Antonov, A.N., Gretsov, V.K. Experimental investigation of the characteristics of unsteady separated regions arising in the supersonic flow at a spiked body. *Akademiia Nauk SSSR, Mekhanika Zhidkosti i Gaza*, pages 98–104, 1977.

[28] Zapriagaev, V.I., Mironov, S.G. An experimental study of fluctuations in the front separation zone at supersonic flow velocities. *Zhurnal Prikladnoi Mekhaniki i Tekhnicheskoi Fiziki*, pages 116–124, Aug 1989.

[29] Shang, J.S., Hankey, W.L. Flow oscillations of spike-tipped bodies. *AIAA Journal*, 20(1):25–26, 1982.

[30] Sears, W.R., Telionis, D.P. Boundary-layer separation in unsteady flow. *SIAM Journal of Applied Mathematics*, 28(1):215–235, 1975.

[31] Mikhail, A.G. Spike-nosed projectiles with vortex rings: steady and nonsteady simulations. *Journal of Spacecraft and Rockets*, 33(1):8–14, 1996.

[32] Ingram, C.L., McRae, D.S., Benson, R.A. Time-accurate simulation of a self-excited oscillatory supersonic external flow with a multi-block solution adaptive mesh algorithm. *AIAA paper 93-3387-CP*, 1993.

[33] Yamauchi, M., Fujii, K., Highashino, F. Numerical investigation of supersonic flows around spiked blunt body. *Journal of Spacecraft and Rockets*, 32(1):32–42, 1995.

[34] Myshenkov, V.I. Numerical study of separated flow before a spiked cylinder. *Akademiia Nauk SSSR, Mekhanika Zhidkosti i Gaza*, (6):162–166, Nov-Dec 1981.

[35] Paskonov, V.M., Tseraneva, N.A. Numerical investigation of high-speed laminar flows around bodies with forward facing spike. *Akademiia Nauk SSSR, Mekhanika Zhidkosti i Gaza*, (2):126–131, Mar-Apr 1984.

[36] Kenworthy, M.A. Private communications with the author. 1999.

[37] Anderson, J.D. Modern compressible flow - with historical perspective. *McGraw-Hill*, 1990.

[38] East, R.A., Wilkinson, P.P. A study of the oscillating separated flow ahead of a forward facing step oscillating traversely to a hypersonic free stream. *AASU Rep. 263*, 1966.

[39] Karlowarskii, V.N., Sakharov, V.I. Numerical computation of supersonic flows around blunt bodies with retractable forward facing spike. *Akademiia Nauk SSSR, Mekhanika Zhidkosti i Gaza*, (3):119–127, 1986.

[40] Needham, D.A. Laminar separation in hypersonic flow. *PhD thesis, University of London*, 1965.

[41] Chapman, D.R. Laminar mixing of a compressible fluid. *NACA TR 958*, 1950.

[42] Nash, J.F.,. An analysis of two dimensional turbulent base flow including the effects of the approaching boundary layer. *NPL Aero R. 1036, ARC 24,000*, 1962.

[43] Holder, D.W., Gadd, G.E. The interaction between shock waves and boundary layers and its relation to base pressure in supersonic flows. *Symposium on Boundary Layer Effects in Aerodynamics, NPL*, 1955.

[44] Sirieix, M. Pression de culot et pression de melange turbulent en ecoulement sypersonique plan. *ONERA RA 78*, 1960.

[45] Cooke, J.C. Separated supersonic flow. *RAE TN Aero 2879*, 1993.

[46] Burggraf, O.R. Inviscid reattachment of a separated shear layer. *Proceedings of the 3rd International Conference on Numerical Methods in Fluid Mechanics, Vol. II*, 1972.

[47] B.J. Gribben. Application of the multiblock method in computational aerodynamics. *PhD Thesis, University of Glasgow*, 1998.

[48] Roe, P.L. Approximate Riemann solvers, parameter vectors and difference schemes. *Journal of Computational Physics*, 43:357–372, 1981.

[49] Hirsch, C. Numerical computation of internal and external flows. *John Wiley & Sons*, 1988.

[50] Gnoffo, P.A. Point-implicit relaxation strategies for viscous hypersonic flows. In *Computational Methods in Hypersonic Aerodynamics, edited by Murthy T.K.S., Kluwer Academic Publishers*, pages 115–151, 1993.

[51] Axelsson, O. Iterative Solution Methods. *Cambridge University Press*, 1994.

[52] Jameson, A. Time dependent calculations using multigrid, with applications to unsteady flows past airfoils and wings. *AIAA Paper 91-1596*, 1991.

[53] Badcock, K.J., Cantariti, F., Hawkins, I., Gribben, B., Dubuc, L., Richards, B.E. Simulation of unsteady turbulent flows around moving aerofoils using the pseudo time method. *International Journal of Numerical Methods in Fluids*, 32:585–604, 2000.

[54] Dubuc, L., Cantariti, F., Woodgate, M., Gribben, B., Badcock, K., Richards, B.E. Solution of the unsteady Euler equations using an implicit dual time method. *AIAA Journal*, 8:1417–1427, 1998.

[55] Cantariti, F., Dubuc, L., Gribben, B., Woodgate, M., Badcock, K., Richards, B.E. Approximate Jacobians for the solution of the Euler and Navier-Stokes equations. *University of Glasgow, Aero Report 5*, 1997.

[56] Gordon, W.J., Hall, C.A. Construction of curvilinear coordinate systems and applications of mesh generation. *International Journal of Numerical methods in Engineering*, 7:461–477, 1973.